A THESIS

FOR THE DEGREE OF DOCTOR OF PHILOSOPHY

Development of Intrinsic Self-Powered Photodetectors based on Piezo-Phototronic Effect

YUVASREE PURUSOTHAMAN

Department of Mechatronics Engineering

GRADUATE SCHOOL
JEJU NATIONAL UNIVERSITY

February 2019

Development of Intrinsic Self-Powered Photodetectors based on Piezo-Phototronic Effect

YUVASREE PURUSOTHAMAN

(Supervised by Professor Sang Jae Kim)

A thesis submitted in partial fulfillment of the requirement for the degree of
Doctor of Philosophy
2018.12.11

The thesis has been examined and approved.

Sooseok Choi

Thesis Director, Prof. Soo Seok Choi — Associate Professor, Department of Energy Engineering, College of Engineering, Jeju National University

Jong Hwan Lim

Thesis Committee Member, Prof. Lim Jong Hwan — Professor, Department of Mechatronics Engineering, College of Engineering, Jeju National University

Thesis Committee Member, Prof. Jeong Man Hee — Assistant Professor, Department of Energy Engineering, College of Engineering, Jeju National University

Thesis Committee Member, Dr. Nagamalleswara Rao Alluri — Research Professor, Department of Mechatronics Engineering, College of Engineering, Jeju National University

Thesis Committee Member, Prof. Sang Jae Kim — Professor, Department of Mechatronics Engineering, College of Engineering, Jeju National University

December 2018

Department of Mechatronics Engineering
GRADUATE SCHOOL
JEJU NATIONAL UNIVERSITY
Republic of Korea

Acknowledgement

This thesis becomes a reality with the kind support and help of many individuals. I would like to extend my sincere thanks to all of them.

Foremost, I want to offer this endeavor to God for the wisdom he bestowed upon me, the strength and peace of mind in order to finish this research.

I pay my deep sense of gratitude to my supervisor Prof. Sang Jae Kim for his valuable guidance, instructions and critical comments. His support made it possible for me to work on the topic that was of great interest to me. I am grateful to him for believing in me and the opportunities that he has extended to gain knowledge, explore my skills to go beyond the limits and dream for the best.

I express my sincere thanks to each member in Nano Materials and Systems Laboratory (NMSL) who travelled with me throughout this journey. Most above my lab seniors, for their endless support, kind and understanding spirit on every note of discussions which had contributed tremendously to this report. Your encouragements when the times got rough are much appreciated.

To family, my father Mr. M. Purusothaman, I know you are right here leading me to move forward with every step in life with your memories being my blessings. To my mom Mrs. K P Radhamani who is my strength and my bundle of joy Mr. P. Hariharasudhan, I am extremely grateful for all the things you have sacrificed and managed to bring me as what I am today. I won't have crossed this stage without your encouragement being the greatest support and the comfort I felt each time when my mobile flashes with your call.

Yuvasree Purusothaman

Thesis Overview

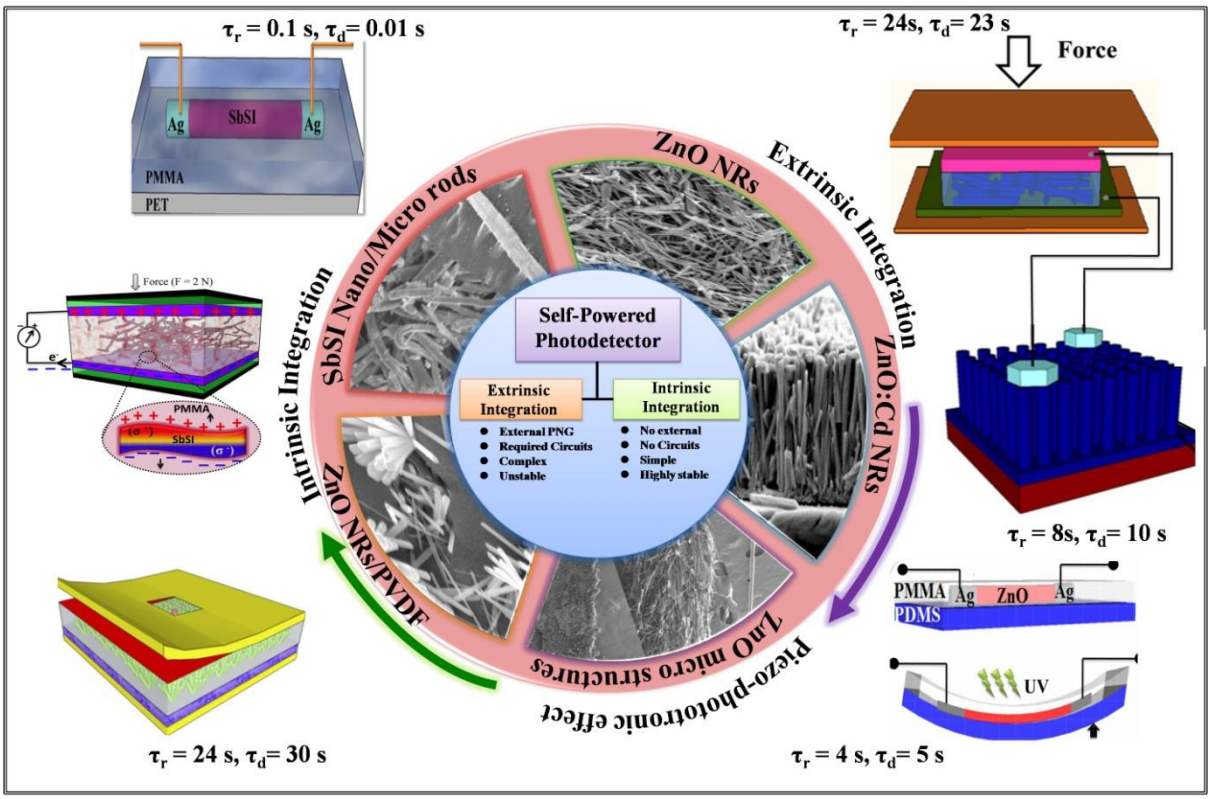

Contents

CHAPTER-1

Introduction

CHAPTER II

Materials, methods and measurement techniques

CHAPTER III

Ceramic based Piezoelectric Energy Harvester using $K_{0.5}Na_{0.5}NbO_3$ (KNN) Pigmented Composite

CHAPTER IV

Elucidation of Piezoelectric and Semiconducting Properties of ZnO Nanorods and Cd Doped ZnO Nanorods

CHAPTER V

Regulation of Charge Carrier Dynamics in ZnO Micro-Architecture Based UV/Visible Photodetector via Photonic-Strain Induced Effects

CHAPTER VI

Internally Hybridized Interfacial Quantification to Stimulate Highly Flexile Self-Powered Photodetector

CHAPTER VII

Photoactive Piezoelectric Energy Harvester Driven by Ternary Chalcohalides ($A_VB_{VI}C_{VII}$) towards Self-Powered Photodetection

CHAPTER VIII

Summary and Future Perspective

Nomenclature

PNG	Piezoelectric nanogenerator
PD	photodetector
SPPD	Self powered photodetector
SSR	Solid state reaction
MW	Micro wire
XRD	X-ray diffraction
FTIR	Fourier Transform Infrared Spectroscopy
FESEM	Field Emission Scanning Electron Microscope
XPS	X-ray Photoelectron Spectroscopy
EDS	Energy dispersive X-ray spectroscopy
EQE	External quantum efficiency
C-SBH	Change in Schottky barrier heights
MPB	Morphotropic phase boundary
SDOF	Single degree of freedom
UV	Ultraviolet
UV-S	UV sensor
M-S-M	Metal-semiconductor-metal
NR	Nanorods
CB	Conduction band
VB	Valence band
PVD	Physical vapor deposition
SPUV-S	Self-powered UV-Sensor
CVD	Chemical vapor deposition

VPT	Vapor phase transport technique
LED	Light emitting diodes
PVDF	Polyvinylidene difluoride
S-PVDF	Seeded-Polyvinylidene difluoride
PMMA	Polymethyl methacrylate
PDMS	Polydimethylsiloxane
PVA	Polyvinyl alcohol
DIW	De-ionized water
WCA	Water contact angle
SMR	Single micro rod
HFR	High frequency range
LFR	Low frequency range
LCD	Liquid crystal display

List of Tables

List of Figures

초록

나노 장치 / 센서의 개발을 위한 나노 기술의 적용 및 활용은 전자, 통신, 광학, 의료 및 국방 기술 분야의 차세대 시스템을 구축하는데 필요한 기반 기술중의 하나이다. 또한, 초소형의 나노 시스템이 배터리나 다른 전원공급 없이 자가발전과 동시에 작동하는 것은 매우 진전된 과학 기술의 발전에 해당한다. 광전자의 관점에서는 외부 바이어스 전압/배터리 / 전원공급 없이 작동하는 자가발전 광 검출기를 구성하는 것은 무선 및 독립적 감지 장치의 개발을 위하여 필요한 중요한 요소기술이다. 따라서, 본 연구에서는 광 검출기 (Photo Detector, PD)의 자가구동 전원의 역할을 할수 있는 압전 나노 발전기 (Piezo-electric Nanogenerator, PNG)의 개발을 시도하였다. PNG는 변형에 반응하는 비대칭성 물질의 압전 전위의 발생을 구동력으로 활용한다. 또한, 압전 재료의 전위에 의해서 유도된 변형은 피에조트로닉스를 기반으로 하는 금속–반도체–금속 (M-S-M) 인터페이스를 역학적으로 조절하는 역할을 한다. 또한, 광원의 추가적인 상호작용은 광전하 생성과 인터페이스 / 접점을 통한 이동을 제어하는 압전-광전자라 불리는 3방향 연결 메커니즘을 생성한다. 압전-광전자 효과를 이용하여, 향상된 광 검출성능의 제공을 위해 세라믹 (KNN), 2원산화물 (ZnO) 그리고 3차 칼코할라이드 (ternary chalcohalides, $A^{V}B^{VI}C^{VII}$)로 구성된 나노소재의 탐색을 통한 고유 자가발전 광 검출기 개발을 위한 PNG와 PD의 효과적인 일체화 방안을 제시한다.

본 논문의 III 장에서는 조성상 경계 (morphotropic phase boundary, MPB)가 x = 0.5 ($K_{0.5}Na_{0.5}NbO_3$)일 때 나오는, $K_{1-x}N_xNO_3$의 화학당량적비를 갖는 고체 상태 반응법 (SSR)에 따른 칼륨 니오브산 나트륨 (KNN)의 합성에 대하여 실험하였다. 압전

합성소재는 알키드 수지바인더에 충전제 / 안료로서 KNN 나노 입자와 함께 제작하였다. KNN의 기계적 에너지 수확 능력은 압전 나노 발전기 (PNG)로 작동하는 캔틸레버빔 진동시스템을 제작하여 조사하였다. 캔틸레버빔에 코팅된 KNN 충전복합체는 7.2g, 14.4g 및 21.6g의 서로 다른 크기의 검증질량 (proof mass, m_p)을 이용한 스프링 질량 모델을 사용하였다. 압전 복합체는 질량하중 21.6 g에서 캔틸레버빔에 가해지는 최대 응력하에서 1.4 V의 개방회로 전압 (V_{OC})이 발생하였다. 이 장에서는 저주파 진동에너지 (<10 Hz)를 수집하기 위한 고감도의 무연 압전 복합 시스템의 개발에 대하여 설명하였다.

다음 단계는 자가발전 광 검출기 (self-powered photodetectors, SPPD)의 개발을 위한 반도체 거동 및 압전 특성의 분석을 실시하였다. IV장에서는 기계적 및 광원에 민감한 다기능 소재에 대하여 연구하였으며, PNG및 PD와 같은 두가지의 다른 에너지 수확 유닛의 제작을 통해 카드뮴 (Cd)을 도판트(Dopant)로 사용한 수열성 1D-ZnO 나노 막대 (ZnO NRs)에 대한 압전 / 반도체 성질의 대칭 튜닝을 개발 및 분석하였다. ZnO NRs의 압전 특성은 V_{OC}=36V, I_{SC}=284μA (순수 ZnO NRs)에서 V_{OC}=15V, I_{SC}=178μA (1 wt% Cd가 첨가된 ZnO NRs)로 압전 출력을 감소시키는 Cd 원자에 의해 크게 영향을 받은 것으로 보인다. 하지만, Cd 1 wt%는 순수한 ZnO NRs ($D^*=5.4x10^{10}cmH^{1/2}W^{-1}$)보다 높은 $1x10^{11}cmH^{1/2}W^{-1}$의 검출성 한계치 (D^*)로 우수한 광 반응 특성을 보였다. 또한 PNG와 PD 간의 외부 병렬 연결을 통한 SPPD 개발을 시도하였다.

5장에서는 도핑 메커니즘을 통해 얻은 비대칭 효과와 PNG와 PD의 내부통합으로 SPPD의 개발을 목표로 하여, 장치의 성능을 제어하는 간단하면서도 효과적

인 피에조-포토트로닉 결합에 의한 소자를 제작하였다. 유연 PD는 마이크로와이어 (MW), 산호와 같은 마이크로스트립 (CMS) 및 근모와 같은 마이크로와이어 (F-MW)와 결합한 ZnO 마이크로-구조로 개발되었다. 압축 변형 (- ε_z = 0.37, 0.75, 1.13, 1.50 및 1.87 %)을 통한 고유 압전 전위의 미세조정은 금속-반도체 (M-S) 인터페이스에서 쇼트키 장벽의 크기(Φ_{SB1}, Φ_{SB2})를 효과적으로 변화시켰다. $6.72\times10^{10}cmH^{1/2}W^{-1}$의 검출범위 (D*)와 UV에서 가시영역 (365nm, 405nm 및 535nm)까지 확장된 스펙트럼의 변화에 따른 압전-반도체-광여기와 같은 세가지 매개변수를 동시에 조사 및 분석하였다.

6장에서는 5장에서 도출한 피에조-포토트로닉스에 기반한 PNG와 PD의 내부 통합에 의한 일체형 장치의 개발에 관하여 조사하였다. Zn^{2+}와 함께 뿌려진 강유전성 PVDF 폴리머는 꽃모양의 F-ZnO 나노 막대 (F-ZnO NRs)를 성장시켜 조립된 장치 (F-SPPD)의 유연성을 높이기 위해 프리스탠딩 기재로 사용하였다. F-SPPD는 회전력에 의한 기계적 변형에 충분히 반응하여 5V 및 60nA의 압전 출력을 생성하였다. 또한, 제작한 광 검출기는 인장 변형 조건 (+ε)하에서 75μA ($24mW/cm^2$)의 향상된 UV 광전류 (I_{Ph})특성을 보여주었다.

7장에서는 SbSI와 SbSeI와 같은 새로운 형태의 강유전성-반도체 물질인 3차 칼코할라이드 ($A^{V}B^{VI}C^{VII}$)소재의 다기능 특성을 갖는 SPPD의 개발을 위한 연구를 수행하였다. 또한, 폴리 디메틸실록산 (PDMS), 폴리 비닐리덴 플루오라이드(PVDF) 및 폴리 메틸 메타크릴레이트 (PMMA)와 같이 널리 선호되는 중합체 매트릭스를 갖는 기재를 사용하였다. 광활성 물질은 약 5V / 150nA(SbSI) 및 약 2V / 60nA (SbSeI)의 압전 반응 특성을 보여주었다. 또한, PNG 및 단일 SbSI 마이크로로드 (SMR-PNG)

에서의 광활성 반도체의 영향은 하이브리드화한 일체형 자가발전 광 검출기의 개발에 중요 요소인 피에조-포토트로닉 효과를 실현하였다.

본 논문에서는 전원 공급이나 배터리의 추가가 없는 다기능 재료를 이용한 차세대의 유연성있고 착용가능한 광전자 센싱 시스템의 설계를 위한 체계적인 연구를 수행하였다. 또한, 하나의 유닛에 두개의 다른 광 및 압전 특성을 집적화할때 발생하는 외부 연결의 구성요소, 회로장치의 복잡성, 유연성있고 인터페이싱 유닛의 최소화를 위한 중요한 대안을 제시하였다.

Abstract

Expansion of nanotechnology for the development of nanodevices/sensors is highly demanding to promote next-generation systems in the fields of electronics, communications, optical, medical and defense technologies. With the vast opportunities, it is extremely fascinating for nanosystems to operate self-powered without the requirement of batteries and other external power supplies. In the view of optoelectronics, constructing self-powered photodetectors that works without an external bias voltage/battery/power supply has gained significant attention to cultivate wireless and independent sensing devices. With the perspective, we have developed piezoelectric nanogenerator (PNG) that can serve as self-sufficient power sources for photodetectors (PD). The PNGs utilizes the piezoelectric potentials as a driving force which responds to influential straining of non-centrosymmetric materials. Moreover, the strain induced piezopotential in piezoelectric materials serves to dynamically modulate the metal-semiconductor-metal (M-S-M) interfaces based on piezotronics. Additional interaction of light sources produces a three-way coupling mechanism referred as piezo-phototronics which controls the photo charge generation and transportation across the interfaces/junctions. By using the piezo-phototronic effect, we exhibit the effective internal integration of PNG and PD for the development of intrinsic self-powered photodetectors with exploration of nanomaterials constituting ceramic (KNN), binary oxide (ZnO) and ternary chalcohalides ($A^{V}B^{VI}C^{VII}$) to provide improved photodetection performances.

Chapter III of this thesis covers the synthesis of potassium sodium niobate (KNN) under solid state reaction method (SSR) with stoichiometric ratio of $K_{1-x}N_xNO_3$, where the morphotropic phase boundary (MPB) occurs at x = 0.5 ($K_{0.5}Na_{0.5}NbO_3$). A piezoelectric composite system was formulated with KNN nanoparticles as filler/pigment in alkyd resin binder. The mechanical energy harvesting ability of KNN was studied through development

of a cantilever beam vibration system acting as piezoelectric nanogenerator (PNG). The KNN filled composite coated on the cantilever beam acted as a spring–mass model that was tested for different proof mass (m_p) loadings of 7.2 g, 14.4 g, and 21.6 g. The piezoelectric composite was capable of producing an open-circuit voltage (V_{OC}) of 1.4 V under maximum stress exerted on the cantilever beam, at a mass loading of 21.6 g. Through this chapter, a highly sensitive lead-free piezoelectric composite system for harvesting low-frequency vibration energy (<10 Hz) was explained by accounting to piezoelectric properties.

Next stage involves the analysis of piezoelectric property along with semiconducting behaviour for the development of self-powered sensors in optoelectronics specifically focussed on photodetectors (SPPD). For which, multifunctional materials are explored which are sensitive to mechanical as well as light sources. This motivates to proceed **Chapter IV** to develop and analyze the symmetric tuning of piezoelectric/semiconducting properties for hydrothermally grown 1D-ZnO nanorods (ZnO NRs) using cadmium (Cd) as the dopant through fabrication of two different energy harvesting units such as piezoelectric nanogenerators (PNG) and photodetectors (PD). The piezoelectric property of ZnO NRs was greatly affected by the Cd atom, which led to a reduction in the piezoelectric output from V_{OC}=36 V, I_{SC}=284 µA (pure ZnO NRs) to V_{OC}=15 V, I_{SC}=178 µA (1 wt% Cd-doped ZnO NRs). However, 1 wt % of Cd showed good photo response with a detectivity (D*) limit of $1x10^{11}cmH^{1/2}W^{-1}$, which is higher than that of pure ZnO NRs (D* = $5.4x10^{10}cmH^{1/2}W^{-1}$). Further, possible means to demonstrate SPPD was illustrated through external parallel connection between PNG and PD.

With the unsymmetrical effect obtained through doping mechanism and with aim to perform SPPD with internal integration of PNG and PD, simple yet effective route to control the device performance was established through three way coupling piezo-phototronic concept in **Chapter V**. A flexible PD was developed with ZnO micro-architectures such as

micro wire (MW), coral like micro strip (CMS), and fibril like clustered micro wire (F-MW). Fine tuning of intrinsic piezoelectric potentials through compressive strain (- ε_z = 0.37, 0.75, 1.13, 1.50 and 1.87 %) effectively changed the Schottky barrier heights (Φ_{SB1}, Φ_{SB2}) at metal – semiconductor (M-S) interfaces. The detectivity range (D*) of 6.72× 10^{10} $cmH^{1/2}W^{-1}$ and broadened spectral activity extending from UV to Visible region (365 nm, 405 nm and 535 nm) three parameters such as piezoelectric-semiconductor-photoexcitation was concurrently explored and analyzed.

Chapter VI of this thesis steps with an advancement of internal integration of PNG and PD into a single device with detailed piezo-phototronic information acquired through the previous chapters. As an approach, ferroelectric PVDF polymer seeded with Zn^{2+} was employed as a free-standing substrate to grow floral-like F-ZnO nanorods (F-ZnO NRs) promoting flexibility to the as-fabricated devices (F-SPPD). F-SPPD was able to produce piezoelectric output of ~ 5 V and 60 nA by sufficiently responding to the mechanical deformations under the rotational force. Also, the in-build photodetector showed an enhanced UV photocurrent (I_{Ph}) of 75 μA (24 mW/cm^2) under the tensile strain condition (+ε).

Through **Chapter VII**, new type of ferroelectric-semiconductor material, ternary chalcohalides ($A^VB^{VI}C^{VII}$) such as SbSI and SbSeI were synthesized and explored as an efficient candidate for SPPD with multifunctional properties. The possibilities of polymeric interface for developing SPPD modules with widely preferred polymer matrices, such as polydimethylsiloxane (PDMS), (Polyvinylidene fluoride) PVDF and polymethyl methacrylate (PMMA) were investigated. The photoactive material generates piezoelectrical responses of ~ 5 V/ 150 nA, SbSI and ~ 2 V/ 60 nA, SbSeI. Further, the influence of photoactive semiconducting properties in PNG and single SbSI micro rod (SMR-PNG) were demonstrated with realization of piezo-phototronic effect aiding to the development of intrinsic self-powered photodetectors. The systematic studies reported in this thesis enables

freedom for designing next generation flexible and wearable optoelectronic sensing systems using multifunctional materials that are devoid of additional power supplies or batteries. Moreover, pairing of two different systems in a single unit serves as a scale-down approach to minimize the components of external connection, complexity of the circuitry devices, interfacing units fronting the maturation of flexible optoelectronics.

CHAPTER I

Introduction

1.1 Background

In the technological direction of miniaturizing components for improved performances, the dominating roadmap to drive the advancement of electronic industries relies on integrating individual micro/nano devices with diversified functionalities into multifunctional micro/nano systems promoting the development of self-powered smart systems/sensors. Power sources are indispensable for independent, sustainable, maintain-free and continuous operations of implantable biosensors, ultrasensitive chemical and optical sensors, nano robotics, micro/nano electromechanical systems (MEMS/NEMS), remote and mobile environmental sensors, homeland security and even portable/wearable personal electronics. It is highly desired for sensors to be self-powered without the requirement of batteries or external power supplies.

Among the newly developed self-powered sensors for mechanical, optical, biological, and chemical characteristics, optoelectronic sensors have attracted attention from researchers in many fields because of their wide applications in modern/personal electronics, human–machine interfacing, wearable devices, health care, environmental monitoring, implantable and biomedical diagnosis/therapy. The concept of piezotronics and piezo-phototronics was invented for implementing the active flexible optoelectronics, which enables the novel approach for directly generating electronic/optical controlling signals using mechanical actuations, so that direct control of charge carrier generation, separation, transportation and recombination processes can be enabled in optoelectronic devices aiming at improving energy efficiency and sensitivity of light emitting diodes (LED), solar cells and photodetectors (PD) .

1.2 Origin and basics of piezo-phototronic effect

Piezoelectricity is a well known effect that involves the production of an electrical potential in a substance as the pressure on it changes. This effect has been widely used for fabricating electromechanical sensors, actuators, and energy converters. The most identified materials that has a piezoelectric effect are ceramic based compounds such as $Pb(Zr,Ti)O_3$ (PZT), $BaTiO_3$, $LiNbO_3$, and Bi_4TiO_{12}. However, these materials are electric insulator, and it is less useful for building electronic devices. Piezoelectric materials that are used for fabricating electronic and optoelectronic devices are required to be semiconductors, such as ZnO, GaN, InN, and ZnS.

By using multi functionality materials in optoelectronic applications (in 2006), the external gate voltage was replaced by the piezopotential in a piezoelectric-semiconducting material, such as ZnO, so that the charge carrier transport process can be tuned/ gated by applying a stress to the device. When a semiconductor crystal is strained, two typical effects are observed. One is the piezoresistance effect, which is introduced because of the change in band gap and possible density of states in the conduction band. This effect has no polarity; therefore, it has an equivalent effect on the source and drain of the FET. On the other hand, the piezopotential is created in the crystal if the material is also piezoelectric. Since the piezopotential has polarity, it can tune the effective heights of the Schottky barriers at the source and drain in opposite directions. This is a non-symmetric and is known as piezotronic effect. The type of devices fabricated by using the piezopotential as the gate voltage is called a piezotronic devices as it is triggered or driven by a mechanical deformation action[1-3].

Alternatively, for a device with Schottky contacts at either or both the source and drain, by introducing a laser excitation at the source/drain, a coupling has been demonstrated among

piezoelectricity, photoexcitation, and semiconductor characteristics, leading to the three way coupling mechanism referred to piezo-phototronics (in 2009) (**Figure 1.1**).

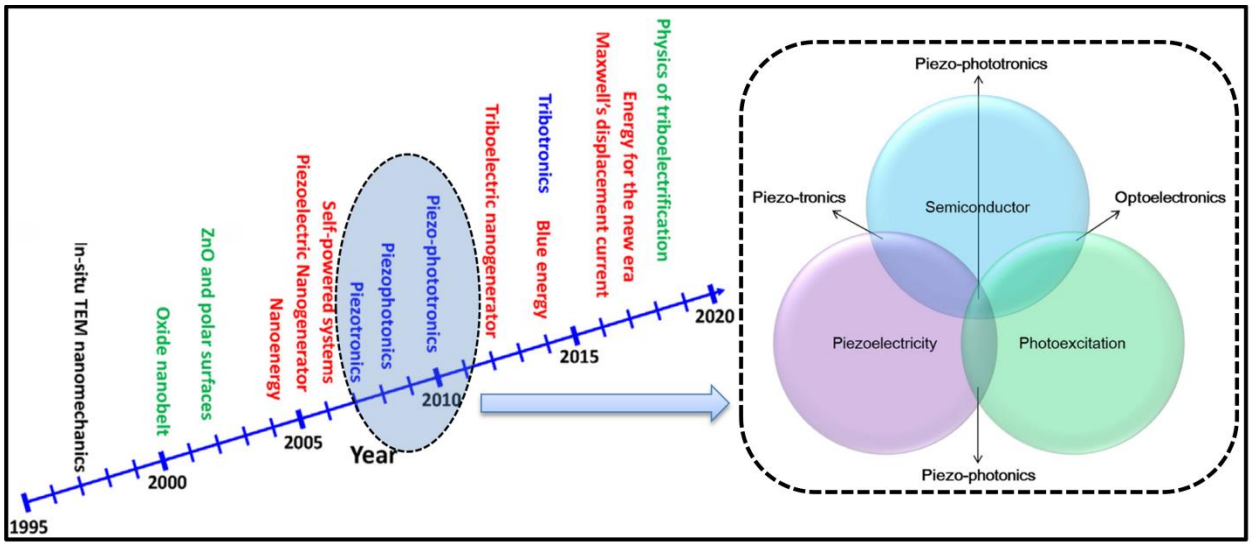

Figure 1.1 Origin of piezo-phototronic effect.

The strain can effectively increase the height of the Schottky barrier based device, allowing a fine tuning of the electric transport property of the device. In contrast, the effective height of the Schottky barrier can be lowered by shining a laser beam at the local contact with the excitation energy larger than the band gap, which increases the density of the local electron-hole pairs and the change of barrier profile due to charge separation/redistribution. By controlling the magnitude of the strain and the intensity of the laser beam, we can effectively tune the charge transport property from Schottky to Ohmic or from Ohmic to Schottky. The effect describing the tuning and controlling of electro-optical processes by a strain-induced piezopotential is referred as piezo-phototronic effect and the devices working with this effect is known as piezo-phototronic devices[1-3].

1.3 Piezo-phototronic devices and applications

As explained piezo-phototronic effect can effectively tune the electrical transport properties of the devices, it finds wide scope to be utilized in all the major energy harvesting and storage applications (**Figure 1.2**).

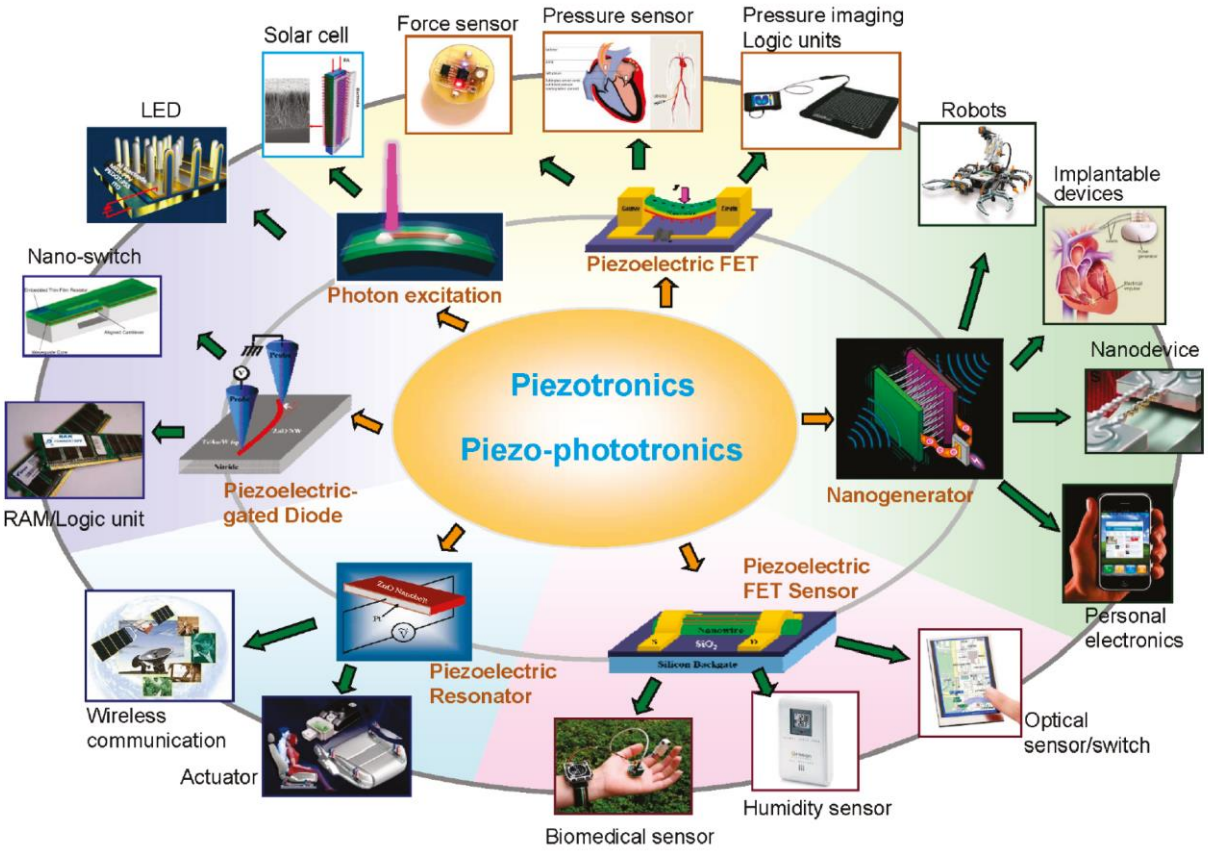

Figure 1.2 Overview of piezotronic and piezo-phototronic applications.

Researchers have developed photocell with aim of maximizing the power output through fine tuning of schottky barrier heights. The effect is well explored for the development of piezopotentially gated transistors. Recently, it has attracted attention in development and integrated self-charging power cell (SCPC)[4], which can be charged up by mechanical deformation and vibration from the environment, providing an innovative approach to provide a

new mobile power source for both self-powered systems and portable and personal electronics. Piezo-phototronic effect on photo electrochemical (PEC) processes exhibited an enhancement in the efficiency of PEC system made of semiconductors that are direct in contact with an electrolyte[5]. This thesis relates to the application of piezo-phototronic in optoelectronic devices and hence, we elaborate the application aspects in detail specifically focusing towards optoelectronic devices.

1.4 Piezo-phototronic effect in optoelectronic applications

1.4.1 Piezo-phototronic effect on solar cells

Experimental results consistent with the previous analytical discussions on the application of the piezo-phototronic effect in enhancing the solar cell performance were demonstrated using an n-CdS/p-Cu_2S coaxial NW based solar cell[6]. The performance of the device was enhanced when it was subjected to compressive strain up to -0.41%, and the I_{sc} is increased from 0.25 to 0.33 nA, while the V_{oc} varied between 0.26 and 0.29 V. The efficiency increased by 70% when -0.41% compressive strain was applied. For the P3HT-ZnO nanowire p–n heterojunction solar cell, V_{oc} increases and decreases with increasing the compressive strain and tensile strain, respectively, while I_{sc} almost showed a constant value of 0.035 nA under different strains[7]. When -0.35% strain was applied on the device, the V_{oc} enhanced by 38%, as compared to that without strain. Colloidal quantum-dot solar cell (QDSC) is also a promising candidate for effective solar energy harvesting. Recently, a novel strategy to modulate the interfacial band structure of ZnO/PbS QDSCs by piezoelectric polarization has been presented[8]. The reports suggest that piezo-phototronic plays a vital role in improving the efficiency of solar devices through simple strain approach.

1.4.2 Piezo-phototronic effect on LEDs

The piezo-phototronic effect has been utilized to effectively tune the LED intensity and enhance the external efficiency of LED fabricated using a ZnO (n-type) - GaN (p-type)[9]. The external efficiency of the LED can reach 7.82% after applying strain, which is comparable to that of the LED structures based on nanorods hybrid quantum well LED. It has also been reported that the piezo-phototronic effect can be utilized to effectively enhance the external efficiency of an inorganic/organic LED based on a single ZnO nanowire/polymer (PEDOT:PSS) core-shell structure[10]. Under the fixed forward bias above the turn-on threshold voltage, the current decreases step by step when the applied strain varies from 0.003% tensile strain to -0.008% compressive strain. The light emission intensity and EQE of the hybrid LED have been enhanced to 190% and 230%, respectively, after applying -0.008% compressive strain when the c-axis of ZnO NW was pointing away from the polymer. In addition, it is also reported that the electroluminescence (EL) properties of p-type GaN thin films can be tuned by the piezo-phototronic effect when strain was applied to the GaN film, EQE of the blue EL at 430 nm was changed by 5.84% under different straining conditions[11]. The piezo-phototronic effect has a more pronounced effect on the LED emission process[12].

1.4.3 Piezo-phototronic effect on photodetectors

1.4.3.1 Schottky contact photodetectors

In Schottky barrier based photodetectors, the SBH is therefore important for dictating the detection sensitivity. By tuning the SBH in a ZnO wire based UV sensor, which possesses the metal–semiconductor–metal (MSM) structure, through applying a strain, it has been demonstrated that the sensitivity of the UV detector can be significantly improved, especially when the illumination intensity is rather weak[13-15]. The responsivity of the photodetector was

enhanced by 530%, 190%, 9%, and 15% upon the UV light illumination of 0.75 μWcm^{-2}, 22μWcm^{-2}, 0.75 $mWcm^{-2}$, and 33 $mWcm^{-2}$, respectively, when the ZnO nanowire experiences compressive strain of -0.36%[16]. Piezopotential can be created in the wurtzite structured CdSe nanowires by applying external strain and thus, the piezo-phototronic effect was utilized to enhance the performance of the CdSe nanowire photodetector[16]. Piezo-phototronic enhanced on/off ratio of GaN film photodetector was reported with self-powered GaN membrane based MSM UV photodetector with a 1% tensile strain[17]. It exhibits a stable, fast, and wide range response to UV illumination with various intensities.

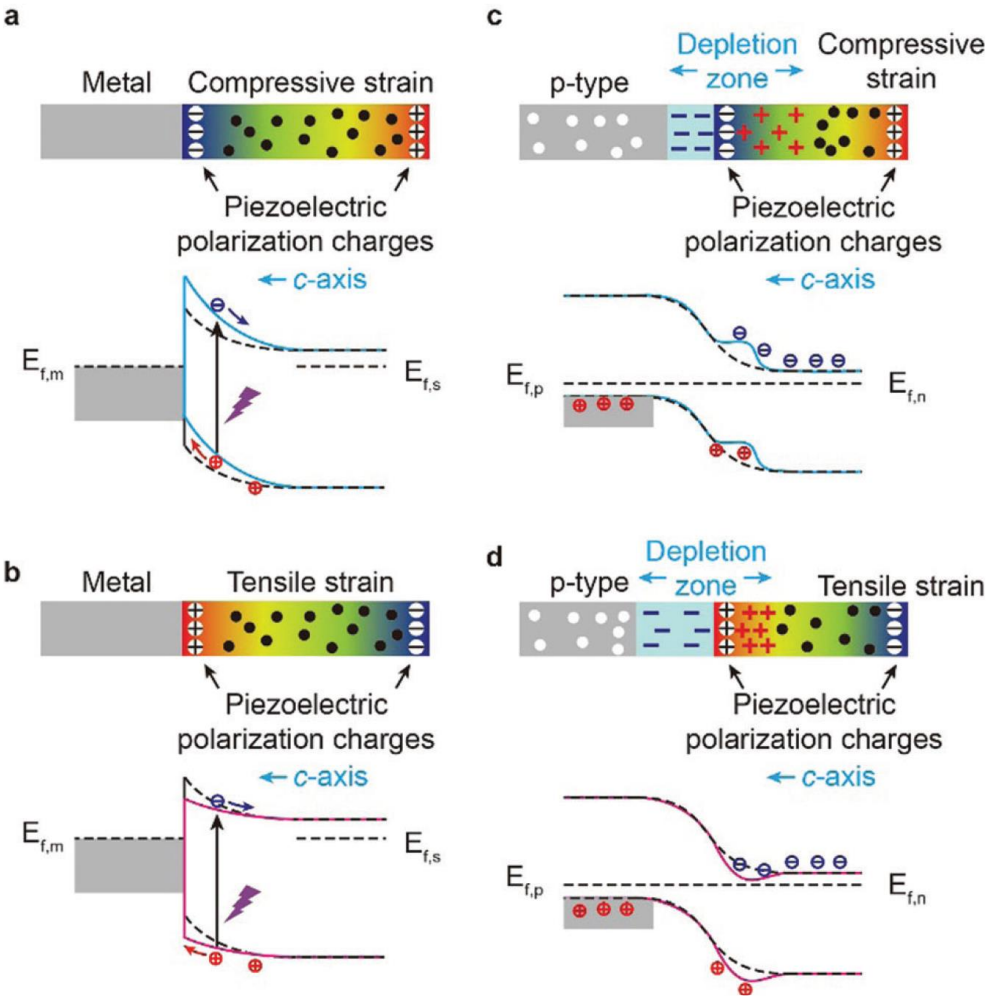

Figure 1.3 Schematic energy band illustration of tensile and compressive strain conditions on the MSM (a, b) and p-n junction (c, d) interfaces.

1.4.3.2 p-n junction photodetectors

Tremendous efforts have been devoted to improve the photoresponsivity and adjustability of silicon based nano/micro photodetectors. Inspired by the enhanced performance by introducing the piezo-phototronic effect, a p-Si/ZnO nanowire hybridized photodetector has been fabricated[18]. By introducing the piezo-phototronic effect, the photoresponsivity of the silicon based photodetector was enhanced by 177% and the response time was shortened to 87%[19]. Tuning the doping concentration of the semiconductors can enhance the piezoelectric coefficient to reduce the screening effect. Alloying is a feasible way to enhance the piezoelectric coefficient while maintaining the crystal structure. Reports are available on enhanced piezopotential of p-Si/n-$Mg_xZn_{1-x}O$ thin film photodetector with an external strain of -0.3%. Organic/inorganic hybrid photodetectors made of Tetrakis-(N,N-di-p-methoxyphenylamine) 9,90-spirobifluorene (spiro-MeOTAD) was demonstrated using piezo-phototronic effect with improved sensitivity[19]. Enhanced visible and ultraviolet photodetection using the ZnO-CdS core-shell micro/nanowire structures showed the modulation of the SBH at the two ends of the wire under strains at a bias of 2 V. The responsivity was enhanced by more than ten-fold when the strain was -0.4% compared to the strain free nanowire. Later, ZnO-CdS double-shell nanowire array was fabricated on carbon fiber (CF) with changes in photocurrent at 2 V bias voltages under different strains was reported. When the CF was under tensile strain along the axial direction, corresponding compressive strain was created in the ZnO nanowire, inducing negative piezo-charge in the ZnO/CdS interface. Conversely, when compressive strain along the wire introduces positive piezo-charge at the interface, and the barrier height decreases, this enhances the photogenerated electron transport from the excited ZnO, and in the excited CdS, the trapping of photogenerated holes was restrained, thus enhancing the performance. The direct integration of

branched ZnO-CdS double-shell nanowires and CF not only enables the 3D nanostructure array to sense the light but also introduces a flexible substrate with good stability. The literatures suggest that the performance of photodetectors can be enhanced by introducing the piezo-phototronic effect[19].

1.5 Self-powered nanosystems for photodetection

A self powered nanosystem is an integration of multiple nano devices/sensors that can operate without the requirement of external power supply or batteries. This system includes harvesting different forms of energies such as chemical energy, thermal energy, mechanical energy, and solar energy. Typically, a self-powered nanosystem for light detection is composed of three components: a light sensor, a power unit and an electrical measurement system. A photodetector (PD) can be coupled with an energy harvesting unit (a nanogenerator or solar cell) or be combined with an energy storage unit (a lithium ion battery or supercapacitor) to drive these components.

One such kind is piezoelectric nanogenerator (PNG), depending on the piezoelectric potential formed in the nanomaterials through applied load owing to the driving force for the generation of piezoelectric polarization. Various types of mechanical energy sources have been scavenged by nanogenerator, including air flow, liquid flow, and mechanical vibrations[20,21]. Z. L. Wang and co-workers reported the first demonstration of a self-driven nanosystem, in which a UV photosensor was powered by a nanogenerator[22]. They fabricated a vertically or laterally aligned ZnO nanowire array based high power output nanogenerator. This nanogenerator was coupled with an individual ZnO nanowire based UV photodetector to form a self-driven nanosystem, in which the two components were connected in series to create a loop. As illustrated in the above studies, PNG can be used as a power source to drive a PD. Alternatively; the nanogenerator can

be directly used as a sensor to detect light illumination. With the first realization of piezoelectric nanogenerator using ZnO nano wires which generated piezoelectric potentials when deformed using cantilever tip, there has been rapid growth in determining materials and device design to improve the energy conversion efficiency of PNGs. With the rapid development of portable devices and electronic products, multifunctional integrated nanodevices, which couple various functions into one device with miniaturized volume, have been rapidly developed in recent years. Significantly, the power units also need to be integrated into the PD to form self-powered nanosystems, which are especially favorable for next-generation optoelectronic devices.

Based on such ideas, through this thesis we demonstrated a self-powered sensor for optical energies through mechanical actuations. Furthermore, we fabricated a self-powered optical sensor based on the PNG and piezo-phototronic based PD, internally integrated in a single unit. The experiment demonstrates that not only we use piezo-phototronic effect to enhance the performance of photodetection but can also be used to develop self powered optical sensors. Also, through internal integration we demonstrated that PNG not only used as an energy harvester, but also as an active sensor for detecting a mechanical and optical signals from the environment.

1.6 Integrated self-powered photodetectors

In this section, the integration prospects for application in self-powered photodetectors are discussed. Conventional photo sensors require an additional power source acting as a bias voltage to detect and convert the optical energy into electrical signals. In self powered technology, the photo sensing is enabled without the requirement of any external power supply or batteries. In self-powered photo sensing, the PNG acts as a powering unit to function the photosensing behavior that can be classified into two modes i) external and ii) internal.

i) Extrinsic mode involves the requirement of PNG and PD devices connected in parallel to detect the optical energy considering the change in PNG response[19]. This mode has quite drawbacks with using two or more devices to enable self-powering operation. It increases the fabrication procedures, consumes more time for fabricating multiple devices, it requires proper interfacing units between two sensing units, increases the complexity of the connection circuitry, lowers the sensitivity, and not highly stable mode.

ii) In the intrinsic mode, there is usage of single device which can act as both PNG and PD i.e, the single unit can respond to mechanical as well as light actuations[23]. The internal mode reduces the usage of two different sensing units by combining two devices into single flexible module (F-SPPD) utilizing the coupling effects of piezoelectric-semiconducting-photoexcitation (piezo-phototronic concepts). **Figure 1.4** illustrates an overview of photosensing with conventional and self-powered operations.

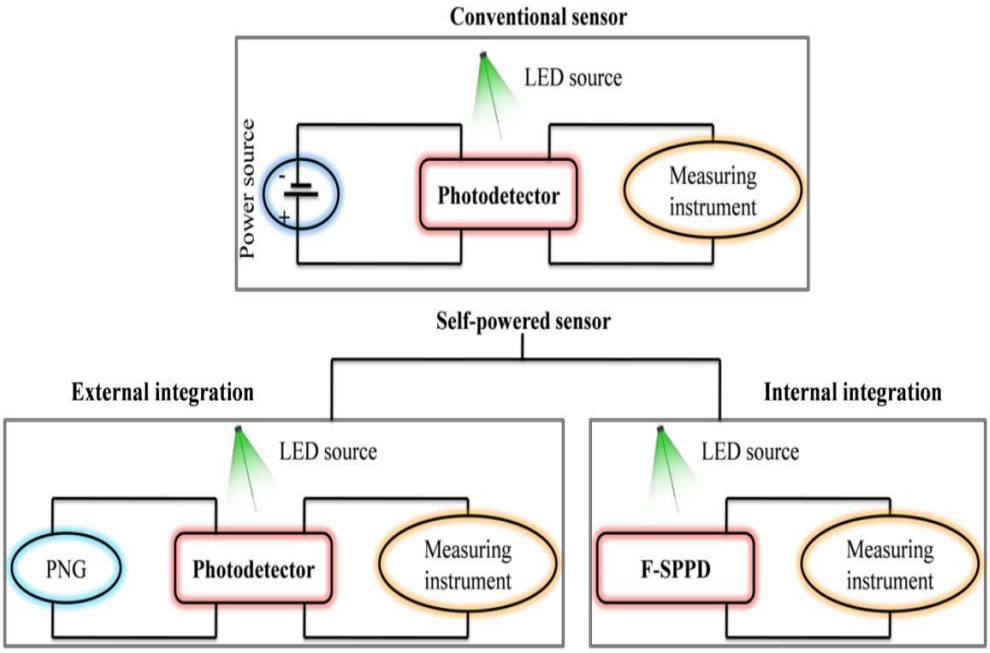

Figure 1.4 Conventional vs. self powered photo detection (external and internal).

1.7 Objective and scope of thesis

The literature reports depicts that the self-powered flexible optoelectronic sensing systems are expected to be the core of next-generation sensor networks due to their low weight, durability, and adaptability to different features of surfaces. Further, the multifunctional materials exhibiting superior semiconductor, piezoelectric and mechanical properties, makes them excellent candidates for novel electronic, opto-electronic devices and integrated systems. More importantly, the coupling between piezoelectric polarization, photo excited charge carriers and semiconductor properties had given rise to unique and unprecedented physical characteristics opening the doors for piezopotential modulated electronic and photonic devices. The available reports on piezo-phototronic focus particularly to utilize the effect in order to improve the sensitivity of photodetection[24].

In this regard, this work is aimed to realize piezo-phototronic effect to promote intrinsic self-powered devices. The perspective is to construct self-powered photodetector operating without bias voltage by implementing the principle and potential applications of piezotronic and piezo-phototronic effects. Thereby, we explored the mechanism of piezotronic and piezo-phototronic effects in the development of self-powered optical sensors through hybridization of piezoelectric nanogenerator and photodetector in a single module. The major parameters such as multifunctional materials (ceramics (KNN), binary oxide (ZnO) and ternary chalcohalides ($A^{V}B^{VI}C^{VII}$)), morphologies (micro and nano) and device configurations (extrinsic and intrinsic) are addressed through this work based on the coupling effects between piezoelectric-semiconducting-photoexcitation. The objective of this research are briefly outlined as,

- To prepare highly crystalline piezoelectric material KNN using low cost synthesis solid state reaction method

- To study the piezoelectric properties through PNG fabricated with KNN and its vibrational energy harvesting < 10 Hz
- To investigate the piezoelectric and semiconductor properties through synthesizing ZnO NRs using hydrothermal method. To examine the effect of using Cd as dopant in modulating the functional properties of ZnO NRs and demonstration of PNG and PD fabricated using ZnO NRs and Cd-ZnO NRs
- Demonstration of self-powered photo detector through parallel connections between ZnO NRs and Cd-ZnO NRs based PNG and PD
- To investigate three way coupling concept (piezo-phototronic) by concurrently analyzing the effect of piezoelectric and semiconducting along with photoexcitation behavior. To achieve efficient growth of ZnO micro-architectures such as micro wire (MW), coral like micro strip (CMS), fibril like clustered micro wire (F-MW) grown by one-step carrier gas/metal catalyst "free" vapor transport technique
- To determine the role of piezoelectric potentials in shifting the schottky contact and modulating the charge carrier generation, separation, transportation and recombination by piezo-phototronic effect through fabrication of MSM type PD using ZnO micro-architectures
- To investigate the self-powered photodetection through intrinsic integration of PNG and PD (SPPD) promoted through establishment of piezo-phototronic concepts in ZnO NRs grown on PVDF film synthesized using hydrothermal method through in-situ growth of Zn^{2+} seeded PVDF
- Finally exploration of emerging class of ternary chalcohalide materials to exhibit piezo-phototronic effect was studied. Synthesis and analysis of SbSI synthesized through solid

state reaction and examine for its functional properties, mechanical, optical energy harvesting capabilities, and its efficiency to work in intrinsic SPPD mode

The outcomes of this work present an ideal route enabling the internal integration of photo detector with nanogenerator through utilization of piezo-phototronic effect. In depth, it addresses the choice of material system from KNN which acts with high piezoelectric coefficient but poor semiconducting properties due to its ceramic insulating nature. Hence, there is necessity to switch over multifunctional materials like ZnO and next-generation emerging class of ternary chalcohalides ($A^{V}B^{VI}C^{VII}$) possessing three way piezoelectric-semiconductor-photoexcitation properties for the development of battery-free self-powered sensors for optoelectronic applications.

1.8 Structure of thesis

The presented thesis elaborates on the development of self-powered optical sensors based on the influential mechanism of piezotronic and piezo-phototronic effects. The key points revolving the work includes

- Investigation of coupling effects between piezoelectric-semiconducting-photoexcitation properties of multifunctional materials
- Demonstration of hybrid energy harvesting devices towards self-powered photo detectors through internal integration concepts

Based on the research focus the thesis is framed into eight chapters. An overview of each chapter is discussed below.

- **Chapter I** gives a broad knowledge on self-powered nano systems and its necessity for the development of next-generation of MEMS/NEMS devices. It summarizes the basic concept of piezotronics and piezo-phototronics in the field of optoelectronic. It briefly illustrates the performance of optoelectronic devices such as LED, solar cells, and photodetectors with respect to piezo-phototronic effects. Besides, modes in self-powered photodetection are explained with suitable graphical representation.
- **Chapter II** provides information on the reagents/chemical, apparatus, preparation and growth methodologies followed for efficient production of nanomaterials reported in this work. Measurement techniques adopted to analyze the synthesized materials are listed in detail along with the specification of the measuring instruments. Followed is the ideal device fabrication of energy conversion units such as PNG and PD, and electrical characterizations tools used to determine the working of the as-fabricated devices. This

chapter also gives a short summary on commonly used electrical parameters referring to the device characteristics.

- **Chapter III** reports the starting phase of the thesis in determining single parameter evaluation i.e. piezoelectric properties through synthesis of KNN nanomaterial using solid state reaction method. The energy harvesting capability of KNN to scavenge vibrational motions were determined through cantilever beam structured device oscillating at an exerted frequency. The piezoelectric resonance frequency of energy harvester is determined based on vibrational beam theories and correlated with experimental results. This chapter will provide the readers an overview of piezoelectric characteristics of a material to harness externally applied mechanical force respective to mass acting on the device.
- **Chapter IV** includes the demonstration of piezoelectric and semiconducting properties on an individual note through selection of material having multifunctional property. On the concern, ZnO nanorods (ZnO NRs) are examined for its piezoelectric and semiconducting behavior with influence of cadmium (Cd) as a dopant (Cd-ZnO NRs) into the crystal lattice of ZnO. The significance of ZnO NRs and Cd-ZnO NRs are studied with responsive effects to mechanical and optical energies. Here, self-powered photodetector is demonstrated through external connection between PNG and PD.
- **Chapter V** investigations on piezoelectric, semiconducting and photoexcitation effects are carried out demonstrating the piezo-phototronic effect. ZnO micro-architectures are synthesized using one step SSR method which produced three different morphologies of ZnO such as single micro wire (ZnO MW), micro strip (ZnO CMS) and fibril like micro wire (ZnO F-MW). Piezotronic and piezo-phototronic effects are examined through strain

induced modulations at MSM interfaces of PD device. This explains the behavior of piezoelectric potentials and the photo generated charge carriers when coupled together to construct an intrinsic self-powered photodetector.

- **Chapter VI** shows the development of PNG and PD integrated into a single module through in-situ growth of ZnO NRs in PVDF film. Flexible film consisting of ZnO NRs/PVDF is synthesized using hydrothermal treatment of Zn^{2+} seeded PVDF (S-PVDF) film. The processed film acts as an active layer which sense mechanical and optical energies promoting internally integrated self-powered photodetector (F-SPPD). Demonstration of F-SPPD is reported through mechanical force actuations and concurrent introduction of light sources acting at a wavelength of 365, 405, and 535 nm.
- **Chapter VII** from the above chapter's conceptualization of piezo-phototronic effects, this chapter includes the investigation of emerging class of ternary chalcohalides ($A^{V}B^{VI}C^{VII}$) as an efficiency energy harvesting material with multifunctional properties. Antimony sulfoiodide (SbSI) is synthesized with rod like morphology and single micro rod by optimization of temperature and time parameters. The polymeric interface of PVDF, PMMA and PDMS with SbSI are studied for the fabrication of devices. Antimony selenoiodide (SbSeI) is also reported with its PNG characteristics for comparability of performance. The semiconducting properties are analyzed under suitable wavelength of 630, 740, and 830 nm. Besides, the piezo-phototronic effect is realized using SbSI/PMMA composite and with single SbSI micro rod which performs as a SPPD.
- **Chapter VIII** summarizes the outcomes of the work produced, its salient features and suggestion/scope for future directions.

1.9 References

1 Z. L. Wang, *J. Phys. Chem. Lett.*, 2010, **1**, 1388–1393.

2 Z. L. Wang, *Nano Energy*, 2018, **54**, 477–483.

3 Z. L. Wang, *MRS Bulletin*, 2012, **37**, 814–827.

4 H. He, Y. Fu, T. Zhao, X. Gao, L. Xing, Y. Zhang, X. Xue, *Nano Energy*, 2017, **39**, 590–600

5 H. Li, Y. Yu, M. B. Starr, Z. Li, X. Wang, *J.* Phys. Chem. Lett., 2015, **6**, 3410–3416.

6 C. Pan, S. Niu, Y. Ding, L. Dong, R. Yu, Y. Liu, G. Zhu, Z. L. Wang, *Nano Lett.*, 2012, **12**, 3302–3307.

7 Y. Yang, W. Guo, Y. Zhang, Y. Ding, X. Wang, Z. L. Wang, *Nano Lett.*, 2011, **11**, 4812–4817.

8 M. Que, R. Zhou, X. Wang, Z. Yuan, G. Hu, C. Pan, *J. Phys.: Condens. Matter*, 2016, **28**, 433001.

9 Q. Yang, W. Wang, S. Xu, Z. L. Wang, *Nano Lett.*, 2011, **11**, 4012–4017.

10 Q. Yang, Y. Liu, C. Pan, J. Chen, X. Wen, Z. L. Wang, *Nano Lett.*, 2013, **13**, 607–613.

11 Y. Hu, Y. Zhang, L. Lin, Y. Ding, G. Zhu, Z. L. Wang, *Nano Lett.*, 2012, **12**, 3851–3856.

12 Y. Liu , S. Niu , Q. Yang , B. D. B. Klein , Y. S. Zhou , Z. L. Wang, *Adv. Mater.*, 2014, **26**, 7209–7216.

13 Y. Hu, J. Zhou, P. H. Yeh, Z. Li, T. Y. Wei, Z. L. Wang, *Adv. Mater.*, 2010, **22**, 3327.

14 J. Zhou, Y. Gu, Y. Hu, W. Mai, P. H. Yeh, G. Bao, A. K. Sood, D. L. Polla, Z. L. Wang, *Appl. Phys. Lett.*, 2009, **94**, 191103.

15 R. Yu, C. Pan, J. Chen, G. Zhu, Z. L. Wang, *Adv. Funct. Mater.*, 2013, **23**, 5868.

16 X. Han, M. Chen, C. Pan, Z. L. Wang, *J. Mater. Chem. C*, 2016, **4**, 11341.

17 M. Peng, Y. Liu, A. Yu, Y. Zhang, C. Liu, J. Liu, W. Wu, K. Zhang, X. Shi, J. Kou, J. Zhai, Z. L. Wang, *ACS Nano*, 2016, **10,** 1572–1579.

18 K. Q. Peng, S. T. Lee, *Adv. Mater*., 2011, **23**, 198.

19 W. Tian , Y. Wang , L. Chen , L. Li, *Small*, 2017, **13**, 1701848.

20 M. N. Li, A. L. Porter, Z. L. Wang, *Nano Energy*, 2017, **34**, 93.

21 F. R. Fan, W. Tang, Z. L. Wang, *Adv. Mater*., 2016, **28**, 4283.

22 S. Xu, Y. Qin, C. Xu, Y. Wei, R. Yang, Z. L. Wang, *Nat. Nanotechnol.*, 2010, **5**, 366.

23 Y. Purusothaman, N. R. Alluri, A. Chandrasekhar, V. Vivekananthan, S. J. Kim, *J. Phys. Chem. C*, 2018, **122**, 12177–12184.

24 R. bao, Y. Hu, Q. Yang, C. Pan, *MRS Bulletin*, 2018, **43**, 952–958.

CHAPTER II

Materials, methods and measurement techniques

This chapter gives a detailed overview of chemicals and apparatus used to carry out the experiments of the presented work. It also explains the synthesis techniques adopted to achieve the desired nanomaterials. Hydrothermal, solid state reaction and sonochemical methods are widely preferred methodologies in the present work. Further, this chapter provides the knowledge of standard characterization techniques such as XRD, Raman, FTIR, UV-Vis spectroscopy, XPS, FESEM, EDS, and ferroelectric P-E analysis adopted to examine the synthesized product. Besides, the measurement equipments employed for the device level performance evaluation and ideal characteristic terminologies used are discussed through this chapter.

2.1 Chemical details

The reagents preferred to synthesis highly pure nanomaterials reported in this thesis are listed in below **table 2.1**. All the chemicals used for the experiments are of laboratory grade and used without any further purifications.

Table 2.1 List of chemical used for the experiments.

Reagents	Molecular Formula	Purity	Details
Potassium cabonate	K_2CO_3	99.5%	Dae-Jung Chemical, Korea
Sodium carbonate	Na_2CO_3	99%	Dae-Jung Chemical, Korea
Niobium pentoxide	Nb_2O_5	99.9%,	Dae-Jung Chemical, Korea
Polyvinyl alcohol	$[-CH_2-CH(OH)-]_n$	99.5%	Dae-Jung Chemical, Korea
Alkyd resin	-	-	-
Cobalt naphthenate	$CoC_{22}H_{14}O_4$	11%	Dae-Jung Chemical, Korea
Zirconium oxide	ZrO_2	99%	High Purity Chemical, Japan
Zinc oxide	ZnO	99%	Dae-Jung Chemical, Korea
Aluminum stearate	$C_{18}H_{37}AlO_4$	99%	Dae-Jung Chemical, Korea
Turpentine oil	-	99%	Dae-Jung Chemical, Korea
Copper-beryllium sheet	-	-	Nilaco Corporation
Zinc acetate dihydrate	$[Zn(CH_3COO)_2.2H_2O]$	98%	Dae-Jung Chemical, Korea
Hexamethylenetetramine	$(CH_2)_6N_4$	99%	Yakuri chemicals, Japan
Cadmium acetate dihydrate	$[Cd(CH_3COO)_2 \cdot 2H_2O]$	98%	Dae-Jung Chemical, Korea
Sodium hydroxide	NaOH	98%	Dae-Jung Chemical, Korea

Polydimethylsiloxane	$(C_6H_6OSi)n$	-	Dow Corning Corporation
Indium tin oxide substrate	ITO	15ohm	Xinyan technology, China
Aluminium foil	Al	-	Samjin
Kapton film	-	-	Dupont
Ethanol	CH_3CH_2OH	99.9%	Dae-Jung Chemical, Korea
Acetone	C_3H_6O	99.8%	Dae-Jung Chemical, Korea
Copper leads	Cu	-	Nilaco Corporation, Japan
Monoethanolamine	C_2H_7NO	> 99%	Dae-Jung Chemical, Korea
Zinc (II) oxide (< 1 μm)	ZnO	99%	Dae-Jung Chemical, Korea
Graphite powder	-	-	Sigma Aldrich
Alumina crucible	Al_2O_3	-	Dae-Jung Chemical, Korea
p-type silicon substrate	p-Si	-	Nilaco Corporation, Japan
Silver paste	Ag	-	Dupont, 4922N
Polymethyl-methacrylate	$(C_5O_2H_8)_n$	99%	Sigma Aldrich
Polyvinylidene difluoride	$-(C_2H_2F_2)_n-$	99%	Alfa Aesar
N-Methyl-2-Pyrrolidone	$C_5H_9N_8$	99.5%	Dae-Jung Chemical, Korea
Antimony	Sb	99%	Cica reagents, Japan
Sulfur	S	99%	Dae-Jung Chemical, Korea
Iodine	I_2	99%	Dae-Jung Chemical, Korea
Selenium	Se	99%	Kanto chemical, Japan
Antistatic tape	-	-	Xinyan technology, China
Flexible PET sheet	-	-	Xinyan technology, China

The apparatus used to synthesis the nanomaterials and fabricate the piezoelectric nanogenerator and optical sensor devices are listed in below **table 2.2**.

Table 2.2 List of apparatus used in this work.

Apparatus	Model	Supplier
Oven	OF-02-GW	JIEO Tech
Magnetic stirrer and hot plate	MS300HS	M TOPS
Muffle furnace	CRF-M15	Ceber
Spin coater	SPIN 1200	Midas Syste,
Tubular furnace	-	Korea Furnace Development Co.Ltd
Bath sonicator	SONIC VCX 500 model (20 kHz, 500 W)	
Centrifuge	Gyrozen 580 MG	Gyrozen
Autoclave	PTFE container	Latech
Multimeter	73303	Yokogawa
LED light source	365, 405, 535, 630, 740, and 830 nm	Prizmatix
Thermal evaporator	JEE-4X	JEOL

2.2 Synthesis methodology

2.2.1 Solid state reaction (SSR)

A solid state reaction is an oldest and still most common method for preparing multicomponent solid materials. Solid state reactions offer reduced costs, and decreased amounts of chemical waste[1]. The advantage also includes ready availability of the precursors and low cost for powder productions on the industrial scale. It is an exothermic, direct reaction between or within solid reactants to yield a solid product of solvent free process at higher temperatures. It is performed in the absence of solvents by either grinding or melting the starting materials together or simply applying heat to a mixture of starting materials. This type of reaction is usually performed in order to obtain polycrystalline inorganic solids but may also be used in organic synthesis. In a solid-solid reaction, different reaction steps such as nucleation, transfer of matter across phase boundaries, and, most importantly, diffusion in the reaction product occur. In this course of study, ZnO micro-architectures such as micro wire (MW), coral like micro strip (CMS), fibril like clustered micro wire (F-MW) grown by one-step carrier gas/metal catalyst "free" vapor transport technique, highly-crystalline, rectangular-shaped potassium sodium niobate with equal stoichiometric ratio of $K_{0.5}Na_{0.5}NbO_3$, 'KNN' is prepared and ternary chalcohalide compound, antimony sulfoiodide, SbSI is synthesized by employing this method under higher temperature conditions depending on melting state of precursors used.

2.2.2 Hydrothermal method

Hydrothermal synthesis method is a pressure-temperature controlled heterogeneous chemical reaction in the presence of water, which is aqueous or non-aqueous above the room temperature and at pressure greater than 1 atm in a closed container. It offers the synthesis of

different dimensional nanomaterials with respect to the low costs for instrumentation, energy and precursors salt used. Hydrothermal synthesis includes the various techniques of crystallizing substances from high-temperature aqueous solutions at high vapor pressures. The principle of hydrothermal method is that an insoluble material at ambient temperatures could be made soluble using high temperatures and pressures[2]. The crystal growth is performed in an apparatus consisting of a steel pressure vessel called an autoclave, in which a nutrient is supplied along with aqueous or non-aqueous medium. A temperature gradient is maintained between the opposite ends of the growth chamber. At the hotter end the nutrient solute dissolves, while at the cooler end it is deposited on a seed crystal, growing the desired material. This method also offers a simple, low temperature, cost-effective route to synthesis nanomaterials of varied morphologies and grain sizes through regulation of solution composition, reaction temperature, pressure, solvent properties, additives and aging time. In this thesis, preparation of ZnO nanorods and its growth on glass, ITO/PET substrates were achieved by using hydrothermal synthesis technique.

2.2.3 Sonochemical method

Sonochemical method describes the chemical and physical processes occurring in solution through energy provided by ultrasound in the range from 20 kHz to 2 MHz resulting in agitation[3]. When a liquid is irradiated by high intensity ultrasound, high-energy chemical reactions occur. When sound waves with sufficient amplitude propagate through a liquid, the liquid is under dynamic tensile stress and the density changes with alternating expansive and compressive waves. The sonic waves create small vacuum bubbles or voids in the liquid, which then collapse violently (cavitations) during compression, creating very high local temperatures. It will produce free metal atoms generated by bond dissociation due to the high temperatures

created during bubble collapse. These atoms can be injected into the liquid phase and nucleate to form nanoparticles or other nano structured materials if appropriate templates or stabilizers are present in the solution. In presented thesis, this method is used to synthesize SbSeI with uniform morphology and also through probe sonication polymerization is initiated to form the polar beta phase of PVDF chains.

2.3 Measurement techniques and specifications

The synthesized nanomaterials are analyzed using standard characterization techniques[4] and the instrumentation details along with its specifications are elaborated in detail.

2.3.1 X-ray diffraction (XRD)

X-ray diffraction (XRD) provides detailed information on structures, phases, preferred crystal orientations (texture), chemical composition, average grain size, crystallinity, strain, and crystal defects when X-rays incident on the crystalline planes of an examined specimen according to Bragg's law. XRD from Rigaku, Japan, operated at 40 kV/40 mA using Cu-Kα radiation (λ = 1.5406 Å) at room temperature (2θ range: 0–90°) was used.

2.3.2 Raman spectroscopy

Raman spectroscopy is a vibrational spectroscopic technique based on inelastic scattering of monochromatic light, usually from a laser source providing submicron spatial resolution for light-transparent material without the requirement of sample preparation, making it suitable for in-situ experiments. It probes the chemical structure of a material and provides information about chemical structure, molecular vibrations and identity, phase and polymorphism, intrinsic stress/strain, contamination and impurity. Molecular vibrational modes was determined by using

Raman spectra recorded in the region of 100 - 3500 cm^{-1} at an excitation wavelength of 514 nm using high-throughput single-stage spectrometer (LabRAM HR Evolution; Horiba, Japan).

2.3.3 UV-Visible Absorption Spectroscopy

UV-Vis Absorption Spectroscopy is used to obtain the absorbance spectra of the crystalline samples based on the principles of Beer-Lambert law. An absorption spectrum will show a number of absorption bands corresponding to structural groups within the molecule useful for identification of optical band gap of the materials. The analysis was carried out using UV-Vis spectrophotometer from Cary300, Varian system, USA.

2.3.4 Fourier Transform Infrared Spectroscopy (FTIR)

Fourier Transform Infrared Spectroscopy (FTIR) reveals functional groups, vibrational stretch frequency chemical bonds in a molecule by producing an infrared absorption spectrum. The light is directed onto the sample of interest, and the intensity is measured using an infrared detector whereby the spectra produce a profile of the sample, a distinctive molecular fingerprint that can be used to screen and scan samples for many different components. FTIR spectra were measured with a Nicolet 6700 spectrophotometer (Thermo Scientific System) in the range of 400 to 4000 cm^{-1}**.**

2.3.5 X-ray Photoelectron Spectroscopy (XPS)

X-ray Photoelectron Spectroscopy (XPS) also known as Electron Spectroscopy for Chemical Analysis (ESCA) is a surface analysis technique providing valuable quantitative and chemical state information. It is useful to elucidate the electronic structure, elemental composition and oxidation states of elements in a material. The study is carried put using Theta Probe AR-XPS

System (Thermo Fisher Scientific, UK) operated with the X-ray monochromatic beam source of 1486.6 eV at 14 kV.

2.3.6 Field Emission Scanning Electron Microscope (FESEM)

The synthesized particle size distribution and shape of nanomaterials at a high resolution can be directly acquired from FESEM. The samples were sputtered with platinum (Pt) and measured using FE-SEM, Zeiss Supra-55vp, Germany with an acceleration voltage of 5 kV and filament current 10 μA. In this thesis, samples were also measured using JEOL JSM-6700F from Japan with resolution of 1.0 nm at an accelerating voltage 0.5 to 30 kV.

2.3.7 Energy Dispersive X-ray Spectroscopy (EDS)

Energy dispersive x-ray spectroscopy (EDS) with FE-SEM is used to determine the chemical composition and purity of synthesized nanomaterials. The compositional analysis were estimated under Zeiss FESEM instrument and EDAX, Bruker Nano GmbH Berlin, Germany with separate EDS detector connected to the FESEM instrument.

2.3.8 Ferroelectric hysteresis tester (P-E loop)

The measurements of properties such as permittivity (capacitance), dielectric loss, piezoelectric displacement, polarization, leakage current, remnant hysteresis, coercive field at driving voltages are enabled through polarization hysteresis loop (P-E) measurement system. The behavior of loop describes the polarization state of material possessing ferroelectric, capacitor or resistor characteristics. The synthesized materials reported in this work were analyzed using Precision +/-10kV HVI-SC, Radiant Technologies, Inc accessed using vision data acquisition software.

2.3.9 Water contact angle

The hydrophobic and hydrophilic nature of any surface can be identified through contact angle measurements between the surface and water droplet. In this work, the surface wetting properties of PVDF film was tested using water contact angle (WCA) instrument (Phoenix 300) to examine the property of KNN composite coated on copper beryllium substrates and to ensure the in-situ grown ZnO for the development of internally integrated devices.

2.4 Device fabrication techniques

The thesis involves two types of device characteristics such as piezoelectric nanogenerator (PNG) and photodetector (PD). PNG provides information of mechanical energy harvesting and PD illustrates the significance of optical sensing behavior and strain induced modulations at MSM interfaces. Development of PNG and PD include different device designs, configurations and electrode arrangements as discussed below.

2.4.1 Piezoelectric nanogenerator (PNG)

The mechanical energy harvesting capability of synthesized materials were determined through fabrication of piezoelectric nanogenerator (PNG) based devices. Typically PNG consists of an active energy scavenging layer (KNN, ZnO, and SbSI) sandwiched between two electrodes with two Cu leads attached to each electrode for efficient extraction of generated potential. Polymers such as PMMA and PDMS were used as a supporting matrix for the sensing layer which also promotes flexibility to the device. Aluminum (Al), gold (Au) and silver (Ag) were the preferred electrodes reported in this work for the fabrication of PNGs. After the electrode deposition the device is packed with antistatic tape, kapton or PDMS to ensure protection from environmental changes, external damages and interference from other effects.

2.4.2 Photodetector (PD)

The semiconducting parameters and optical characteristics of the synthesized materials were examined through development of photodetector (PD) with metal-semiconductor-metal (M-S-M) configurations to extracts and analyze the unique electrical characteristics such as IV (Current vs. Voltage) and time dependent switching nature (Current vs. Time). The semiconducting materials were deposited/grown as illustrated in detail through the following chapters. Silver (Ag) and gold (Au) electrodes were preferred as electrode contact depending on the work function of semiconductor material such as ZnO and SbSI. Two Cu conducting leads were attached to each M-S interface to which biasing voltage is applied for further studies on generation of charge carriers and strain induced modulations at each interfaces.

2. 5 Electrical characterizations

The device level measurements of developed PNG and PD were carried out using the following specified electrical instrumentations.

2.5.1 Piezoelectric measurements

The mechanical force was triggered by a linear motor system (LinMot-HF01-37) operated with variable acceleration with a moving shaft, and the results were recorded using a high-impedance electrometer (6514), a low-noise current pre-amplifier (SR570), picoammeter 6485, and nanovoltmeter 2184 which provides information on piezoelectrical voltage and piezoelectrical current, stability and load resistance.

2.5.2 Semiconductor analyzer

The semiconducting and photoelectric properties of materials were determined through semiconductor device parameter analyzer (Agilent-B1500A) (frequency variable CV-IV system) which can analyze voltage/current range: 0.5V to 100V, 1pA to 100mA (HRSMU), voltage/current range: 0.5V to 100V, 10pA to 100mA (MPSMU), voltage/current range: 2V to 200V, 1nA to 1A (HPSMU) with the frequency range: 1 kHz to 5 MHz. The instrument has excellent usability and scalability by using Modular type SMU (MPSMU, HPSMU, HRSMU), MFCMU and Window GUI for cap measurement.

2.6 Calculation of electrical parameters

Frequently referred electrical parameters to determine the performance of PNG and PD are discussed in detail with corresponding equation relationships [5-11].

2.6.1 Piezoelectric parameters

2.6.1.1 Resonant and vibrational frequency

The natural frequency of the vibrating substrate can be determined according to the beam theory of stiffness and the proof mass concept. The resonant frequency (f_0) of a vibrating rectangular beam system can be expressed by the following relationship:

$$f_0 = \frac{1}{2\pi}\sqrt{\frac{k_{eff}}{m_{eff}}} \quad - \quad (1)$$

where f_0 is the resonant frequency, k_{eff} is the effective spring/cantilever beam stiffness, and m_{eff} is the effective mass acting on the cantilever beam.

2.6.1.2 Power density

The power density can be evaluated by the following equation:

$$P_A = \frac{V^2}{R \times A} \quad -(2)$$

where *R* is the load resistance across the PNG, *A* is the surface area and *V* is the output voltage.

2.6.1.3 Spontaneous polarization

The electromechanical response of the PNG depends on the spontaneous polarization (P_s), which is given by the following equation:

$$d_{33} = 2Q_{eff}.\varepsilon_0.\varepsilon_r.P_s \quad -(3)$$

where Q_{eff} is the effective electrostriction coefficient, piezoelectric coefficient (d_{33}), ε_0 is the permittivity of free space and ε_r represents the relative permittivity.

2.6.2 Photoelectric parameters

2.6.2.1 Photo responsivity

The photo-responsivity (R_λ) at a specific wavelength, which is defined as follows:

$$R_\lambda = \frac{I_{ph} - I_D}{P_L \times S} \quad -(4)$$

where I_{ph} and I_D are dark and photocurrent, P_L is the illumination intensity and S is the illuminated device area.

2.6.2.2 External quantum efficiency

The external quantum efficiency (EQE, η) was estimated from R_λ as

$$\eta = \frac{1240 \times R_\lambda}{\lambda} \quad - (5)$$

2.6.2.3 Photoconductive gain

The sensor performance was estimated by determining photoconductive gain (G) which is given as:

$$G = \frac{\Delta I/q}{P/h\nu} \quad - (6)$$

2.6.2.4 Photo detectivity

Further the photo detectivity ($D*$) is calculated using,

$$D* = \frac{A^{1/2} \times R_\lambda}{(2q \times I_D)^{1/2}} \quad - (7)$$

where q is the elementary charge carrier; $\Delta I = I_{ph} - I_D$; P is the incident power and h is the Planck's constant.

2.6.2.5 Strain rate

The strain % (ε_z) exerted on the device is calculated using,

$$\varepsilon_z = 3 \frac{a}{l} \frac{D_{max}}{l} (1 - Z/l) \quad - (8)$$

where *a* and *l* are the thickness and length of PDMS substrate, D_{max} is the maximum deformation of the device and *z* is the distance moved by the device from rest position.

2.6.2.6 Schottky barrier heights

Change in Schottky barrier heights (C-SBH) can be observed directly from the deviations in I-V response under compressive strains, which can be theoretically estimated using the thermionic emission diffusion theory and the corresponding equation is[76],

$$-\Delta\phi_{Bn} = -kT\ ln\frac{I(\varepsilon_z)}{I(0)} \quad -(9)$$

where $\Delta\phi_{Bn}$ is the change in Schottky barrier height (C-SBH) at M-S-M interfaces, k is the Boltzmann constant (1.38064×10^{-23} $m^2kgS^{-2}K^{-1}$), T is the room temperature (25 °C) and $I(\varepsilon_z)$ and $I(0)$ are the dark currents under zero strain and applied strain conditions.

2.6.2.7 Gauge factor

The performance of PD upon strain conditions were estimated by the gauge factor i.e,

$$Gauge\ factor = \frac{\delta I/I_0}{\varepsilon} \quad -(10)$$

where δI is the normalized change in the current when the strain is applied, I_0 is the current at the unstrained condition and ε being the strain rate.

2.6.2.8 Young's modulus

The Young's modulus (E) can expressed theoretically as,

$$E = \frac{\sigma}{\varepsilon_z} \quad -(11)$$

where, σ is the stress factor that depends upon the applied force acting at a specific area ($4F/\pi d^2$) and ε_z is the strain exerted on the device.

2.7 References

1 G. Cohn, *Chem. Rev.*, 1948, **42**, 527–579.

2 K. Byrappa, T. Adschiri, *Prog. in Cry. Growth and Charac. Mater.*, 2007, **53**, 117–166.

3 H. Xu, B. W. Zeiger, K. S. Suslick, *Chem. Soc. Rev*., 2013, **42**, 2555–2567.

4 S. Mourdikoudis, R. M. Pallares, N. T. K. Thanh, *Nanoscale*, 2018, **10**, 12871–12934.

5 J. Zhou, Y. Gu, P. Fei, W. Mai, Y. Gao, R. Yang, G. Bao, Z. L. Wang, *Nano Letters*, 2008, **8**, 789–793.

6 Q. Liao, M. Mohr, X. Zhang, Z. Zhang, Y. Zhang, ***Nanoscale,*** 2013, **5**, 12350–12355.

7 D. Roylance, *Mechanical Properties of Materials*, 2008, 1–128.

8 Y. C. Yang, C. Song, X. H. Wang, F. Zeng and F. Pan, *Appl. Phys. Lett.*, 2008, **92**, 012907.

9 T. Mattila and A. Zunger, *J. Appl. Phys.*, 1999, **85**, 160–167.

10 J. Wang and Y. Zhang, *Sci. Rep.*, 2016, **6**, 24660.

11 Y. Purusothaman, N. R. Alluri, A. Chandrasekhar, V. Vivekananthan, S. J. Kim, *Small*, 2018, 1703044.

CHAPTER III

Ceramic based Piezoelectric Energy Harvester using $K_{0.5}Na_{0.5}NbO_3$ (KNN) Pigmented Composite

Highlights

- A highly sensitive lead-free piezoelectric composite system for harvesting low-frequency vibration energy (<10 Hz) was developed using highly-crystalline, rectangular-shaped potassium sodium niobate ($K_{0.5}Na_{0.5}NbO_3$, 'KNN') as a pigment in an alkyd resin binder
- The layered conductive copper beryllium cantilever/piezoelectric composite/aluminium acted as a device structure to obtain the electrical responses of a cantilever on various mass loadings (7.2 g, 14.4 g, and 21.6 g)
- A maximum open circuit voltage of 1.4 V was produced by the piezoelectric composite coated on the surface of the deflecting cantilever beam at a proof mass (m_p) of 21.6 g
- This suggests that the developed lead-free piezoelectric composite was capable of harvesting energy from the vibrating source and was also sensitive to the degree of mechanical strain exerted by the deflecting cantilever beam

Graphical Outline

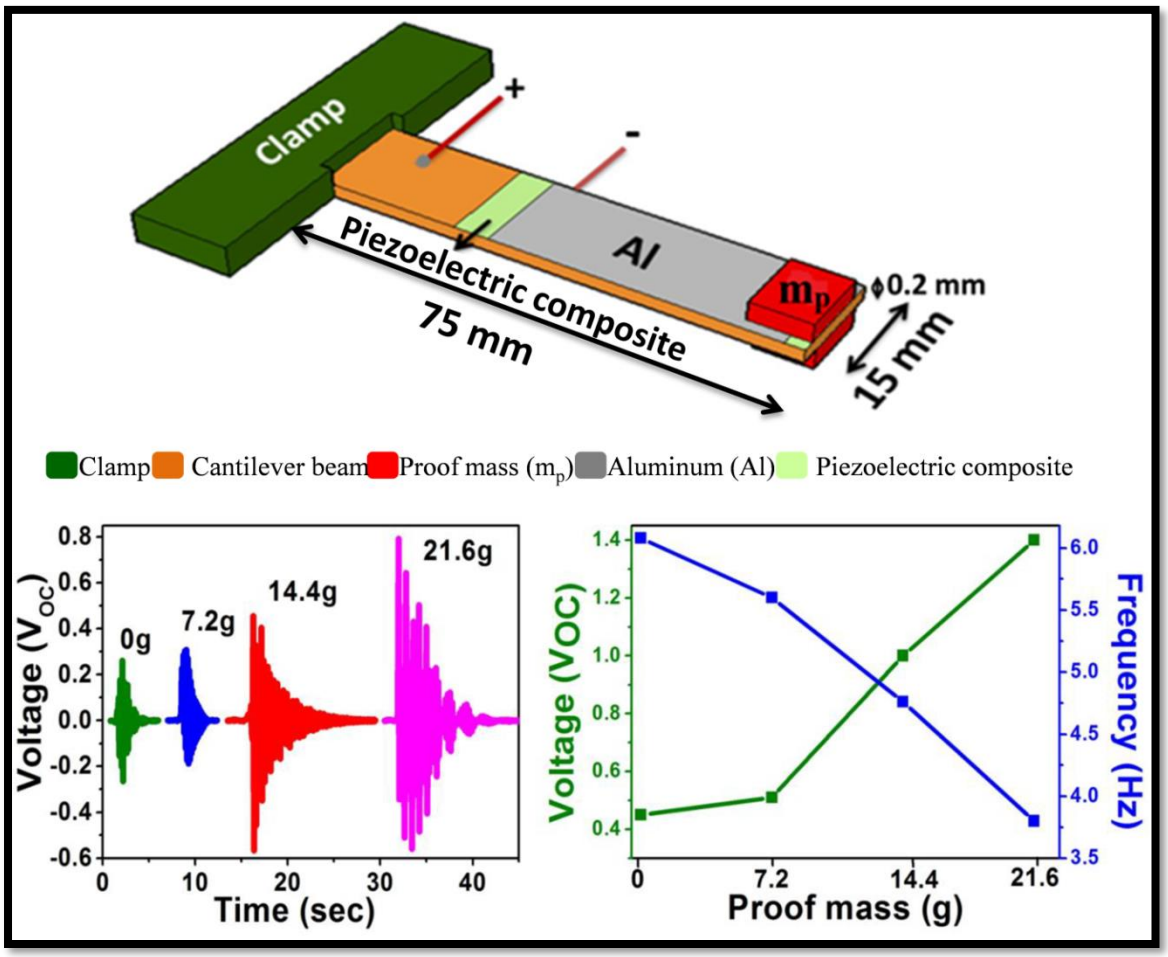

3.1 Introduction

Piezoelectric composites have wide uses in various fields such as actuators, transducers, non-destructive testing, structural health monitoring, and self-powered sensor applications, due to their multifunctional properties, adaptability on many substrates, flexibility, and easy processing. These composites are also useful for harnessing low-frequency mechanical energy from environmental vibrations, air (or water) motion, and human walking. Piezoelectric composites exhibit reasonable ferroelectric, piezoelectric, and dielectric properties, which can address the problem of the brittleness of inorganic nanoparticles based films, leakage current issues, and also improve the mechanical stability of the material.

Recent studies have shown the feasibility of piezoelectric composite as a strain-sensing unit, which was demonstrated experimentally using a lead zirconate titanate (PZT) ceramic in a water-based acrylic medium[1]. The PZT composite was then poled at 600 V for 1 h, exhibiting a piezoelectric coefficient (d_{33}) of 10–30 pC/N[2]. Milled composite powders of calcium-modified lead titanate and polyvinylidene fluoride-trifluoroethylene (PTCa/P(VDF-TrFE)) were used as a piezoelectric filler exhibiting a d_{33} of 33 pC/N for effective application as an acoustic emissions (AE) sensor in evaluating the frequency response in the range of 33 kHz to 50 MHz[3]. A sol-gel processed PZT coating system was developed that was deposited on an Al/steel substrate through a spraying technique, yielding a d_{31} coefficient of 30 pC/N[4]. PZT 5A in a water-based acrylic medium was studied with varying ratios (1:1, 4:1, and 7:3) of piezoelectric ceramic to acrylic resin[5,6,7]. Apart from the acrylic medium, PZT was used as a pigment along with an epoxy resin to form paint composites[8,9]. PZT 5H in an epoxy matrix was developed with a d_{33} of 17 pC/N, which acted as a wave sensor for damage detection in a carbon fibre-reinforced composite (E-glass) plate[8].

Most of the piezoelectric composite systems that have been developed use PZT as a pigment material in a polymer binder. The high dielectric coefficient exhibited by PZT ceramics has resulted in it as a non-replaceable material for piezoelectric sensors. However, lead oxide, which is a component of PZT, is highly toxic; its toxicity is further enhanced due to its volatilisation at high temperature, particularly during calcination and sintering, causing environmental hazards[10]. These problems paved the way for the development of lead-free piezoelectric materials, such as barium titanate ($BaTiO_3$), bismuth sodium titanate (BNT), bismuth potassium titanate (BKT), zinc oxide (ZnO), and potassium sodium niobate ($K_{0.5}Na_{0.5}NbO_3$, KNN). Among them, KNN is one of the most promising lead-free piezoelectric candidates, possessing piezoelectric behaviour similar to PZT ceramics[11]. KNN ceramics are ABO_x perovskite-structured materials, derived from the combination of $KNbO_3$ and $NaNbO_3$. KNN possesses a high piezoelectric and dielectric constant, with a remnant polarisation of 14 μC/cm and coercive field of 140 kV/cm[12].

In this study, KNN was used as a pigment (filler) to develop an alkyd-based piezoelectric composite system with stoichiometric ratio of $K_{1-x}N_xNO_3$ ($K_{0.5}Na_{0.5}NbO_3$). The morphotropic phase boundary (MPB) occurs at x = 0.5 (KNN); this refers to the phase transition from a tetragonal to a ferroelectric orthorhombic phase at which the maximum dielectric property is exhibited[13]. Here, a piezoelectric composite system was formulated using rectangular-shaped KNN nanoparticles synthesised by a solid-state reaction (SSR) method, where they were used as a pigment material in an alkyd resin. To determine the energy-harvesting ability of the KNN-based piezoelectric composite developed, a cantilever beam vibration system was studied. The cantilever structure was used because it has a large displacement and induces high stress in the presence of small vibrations[14]. Vibrations are a form of mechanical force in the low-frequency

range of 0–100 Hz[15,16]. In the present scenario, in which low-frequency energy harvesting from the host unit is limited, the piezoelectric composite developed served as a new form of energy-harvesting material, operating at a low frequency, <10 Hz. The piezoelectric composite coated on the cantilever beam acted as a spring–mass model that was tested for different proof mass (m_p) loadings of 7.2 g, 14.4 g, and 21.6 g. The piezoelectric composite was capable of producing an open-circuit voltage (V_{OC}) of 1.4 V under maximum stress exerted on the cantilever beam, at a mass loading of 21.6 g.

3.2 Experimental section

3.2.1 Synthesis of nano-sized piezoelectric pigment material (KNN)

A single-crystalline nano-sized KNN fine powder was synthesised through a high-temperature SSR method. In a typical procedure, the raw materials, such as K_2CO_3 (99.5%, Dae-Jung), Na_2CO_3 (99%, Dae-Jung), and Nb_2O_5 (99.9%, Dae-Jung) were used as a starting material and taken according to the atomic weight ratio of the target KNN solid composition. Before the reaction, the precursor mixture was dried at 200°C for 3 h and then finely ground using an agate mortar for 1 h with ethanol as a medium. The resulting slurry was dried at 100°C for 1 h and calcined at 850°C for 10 h. The calcined powder was then ground and pelletized using a mixture of 5 wt% polyvinyl alcohol (PVA) as a binder. The pellet discs were prepared with a diameter of ~9 mm and a thickness of ~1.5 mm under a uniaxial pressure of 40 MPa. The pellets were then sintered at 1100°C, with a raising time of 5 h and soaking time of 2 h. Next, the sintered pellets were crushed and ground using an agate mortar for 1 h, to obtain a fine nano-sized powder. The KNN powder obtained was used as a pigment material in an alkyd resin-based composite system and studied in terms of its energy-harvesting capabilities.

3.2.2 Formulation of lead-free KNN piezoelectric composite

The composite system consisted of three major components: the pigment, which determined the functionality of the composite; a polymer binder medium to hold the pigment; and appropriate additives to enhance the curing and coating properties of the composite on to any substrates. In a typical composite preparation procedure, the as-synthesised KNN piezoelectric material is used as the pigment that determines the piezoelectric performance of the composite, followed by addition of an alkyd resin as a polymer binder medium and additives, such as cobalt naphthenate (outer coat drier), nano-sized ZrO_2 (inner coat drier), nano-sized ZnO (stabiliser), PVA (thickener), aluminium stearate (anti-settling agent), and turpentine oil (solvent). The wt% ratio used was as reported elsewhere[17,18] and is listed in **Table 3.1**.

Table 3.1 Composition of as-prepared piezoelectric composite.

Materials	Function	Wt %
KNN	Pigment - provides piezoelectric functionality to composite	20
Alkyd resin	Binder – polymer medium to hold the pigment	60
Cobalt naphthenate	Outer coat drier	0.6
Nanosized ZrO_2	Inner coat drier	0.6
Nanosized ZnO	Stabilizer	0.6
PVA	Thickener	0.6
Aluminum stearate	Anti-settling agent	0.6
Turpentine oil	Solvent	17

The composite mixture of 20 wt% KNN pigment, 60 wt% alkyd resin, and 20 wt% additives and solvent were stirred magnetically for 24 h at high speed with occasional addition of solvent. If the stirring is too vigorous, the temperature rises, accelerating polymerisation of the binder. This is a key step in the preparation of the composite coating due to the balance required in trying to break up agglomerates but yet avoid premature polymerisation of the alkyd resin. Finally, KNN piezoelectric composite was obtained, which appeared light green in colour. The tendency of KNN particles to settle down was avoided by the use of additives, such as an anti-settling agent, which holds the pigment particles to avoid possible agglomeration. However, for good quality composite films, high-speed mixing should be performed for 30 min prior to coating on any substrate.

3.2.3 Design of an energy harvester using a lead-free piezoelectric composite

The most common vibration-based energy harvesters consist of a cantilever beam substrate with a piezoelectric material on the top of a conducting beam. A copper-beryllium sheet of size 75 × 15 × 0.2 mm was used, which has dual functionality, as a substrate and the 'bottom' electrode. The as-synthesised piezoelectric composite was coated on the top side of the copper-beryllium cantilever beam within a pre-defined area (50 × 15 mm) using a brush coating technique and was kept at room temperature for 24 h to cure the composite medium. To measure the piezoelectric response of the KNN-based composite system, thin aluminium foil (thickness: ~80 μm) was attached on the surface of the cured piezoelectric composite, to act as the 'top' electrode. Two copper wires were attached to the top of the Al foil and the bottom of the conductive substrate to collect the generated charge carriers from the piezoelectric composite through an external circuit. Next, one end of the cantilever was fixed to a clamp and the other

end was free to move; the movement/deflection depended on the vibration experienced by the copper beryllium sheet.

3.2.4 Measurement techniques

The phase composition of the as-prepared KNN particles was determined using X-ray diffraction (XRD, Rigaku, Japan), operated at 40 kV and a current of 40 mA using Cu-Kα radiation (λ = 1.5406 Å) at room temperature (2θ range: 20–70°). The morphological structure and particle size distribution of the perovskite-phased KNN was analysed by field-emission scanning electron microscopy (FE-SEM, Zeiss Supra-55vp, Germany and JEOL JSM-6700F, Japan). Raman spectra were recorded from 100 to 900 cm^{-1} at an excitation wavelength of 514 nm using a single-stage spectrometer (LabRAM HR Evolution; Horiba, Japan). Fourier-transform infrared (FTIR) spectra were measured with a Nicolet 6700 spectrophotometer. The surface wetting properties of the piezoelectric composite surface were measured using a water contact angle (WCA) instrument (Phoenix 300). Purity of synthesized KNN pigment was confirmed by Energy dispersive X-ray spectrometry (EDAX, Bruker Nano GmbH Berlin, Germany). To determine the P-E hysteresis loop, KNN pellet of diameter ~ 13 mm and thickness ~ 1 mm was measured on a Radiant precision LC II ferroelectric tester (Radiant technology, Inc) system. The piezoelectric performance of the formulated KNN-based piezoelectric composite system was assessed using a high-impedance electrometer (Keithley 6514, Keithley Instruments, Cleveland, OH, USA).

3.3 Results and Discussion

3.3.1 Structural and surface morphological analysis

The phase information of as-prepared KNN nanoparticles was evaluated by XRD and Raman spectroscopy (**Figure 3.1**). Figure 3.1(a) shows the pure perovskite-type structure with

no trace of any impurity phase for the calcined and then sintered KNN nanoparticles. This confirmed the 'ideal' diffusion of Na^+ ions into K^+ ion sites (A sites) in the ABX_3 perovskite structure[19,20]. The split nature of the diffraction peak at 45°, indexed as (220) and (002), represents the single orthorhombic phase of KNN nanoparticles[21] (Figure 3.1(b)). Also, it can be seen that the KNN powder samples calcined at 850°C showed broad peaks, indicating the fine crystallite size of KNN. During the period of sintering at 1100°C, the crystallisation of KNN nanoparticles improved, as confirmed by the stronger, sharper peaks. The size of the crystallite KNN nanoparticles was 26.61 nm, with an internal strain of 0.005 due to the diffusion of K^+ and Na^+ ions into the A-sites in the perovskite structure. The lattice parameters were as follows: a = 5.64 Å, b = 3.94 Å, and c = 5.67 Å, from which the volume of the unit cell (V = a × b × c, orthorhombic phase) was determined to be 125.9 $Å^3$. The formation of KNN, with the appropriate stoichiometric ratio, is given by

$$0.5K_2CO_3 + 0.5Na_2CO_3 + Nb_2O_5 \rightarrow 2[K_{0.5}Na_{0.5}NbO_3] + CO_2 \quad \text{- (1)}$$

The detailed dynamic symmetry and phase information of the perovskite-structured KNN was obtained through Raman analysis. The Raman spectrum of KNN nanoparticles was recorded at room temperature in the 100–900 cm^{-1} range (Figure 3.1(c)). The spectrum reveals the vibration characteristics of KNN nanoparticles related to the external modes (from cations) and internal modes (due to the NbO_6 polyhedron)[19]. The spectrum showed five major vibration bands, at 190, 262, 538, 606, and 843 cm^{-1}, which were identified as ν_6, ν_5, ν_2, ν_1, and ν_{1+5}, respectively[22]. These bands correspond to the stretching and bending vibrations of NbO_6. The bands ν_1 and ν_2 are stretching modes and ν_6 and ν_5 are bending modes, of which ν_1, ν_2, and ν_5 are due to internal vibrations of the polyhedron. The modes around 538 cm^{-1} and 843 cm^{-1} exhibited similar behaviours to pure $KNbO_3$[22]. The band at 843 cm^{-1} arises from short stretching of Nb=O

(ν_{1+5}). The band at 606 cm^{-1} is due to symmetric stretching of O-Nb-O (ν_1). The band at about 262 cm^{-1} arises from the stretching vibration of Nb-O bonds (ν_5)[19]. Also, the vibration mode ν_1 is related to the symmetric A_{1g} type, corresponding to the Nb-O bond, and ν_2 is related to the doubly degenerated E_g vibrations of the O-Nb-O bonds. All of these vibration modes confirm the 'perfect' formation of the perovskite phase of KNN nanoparticles.

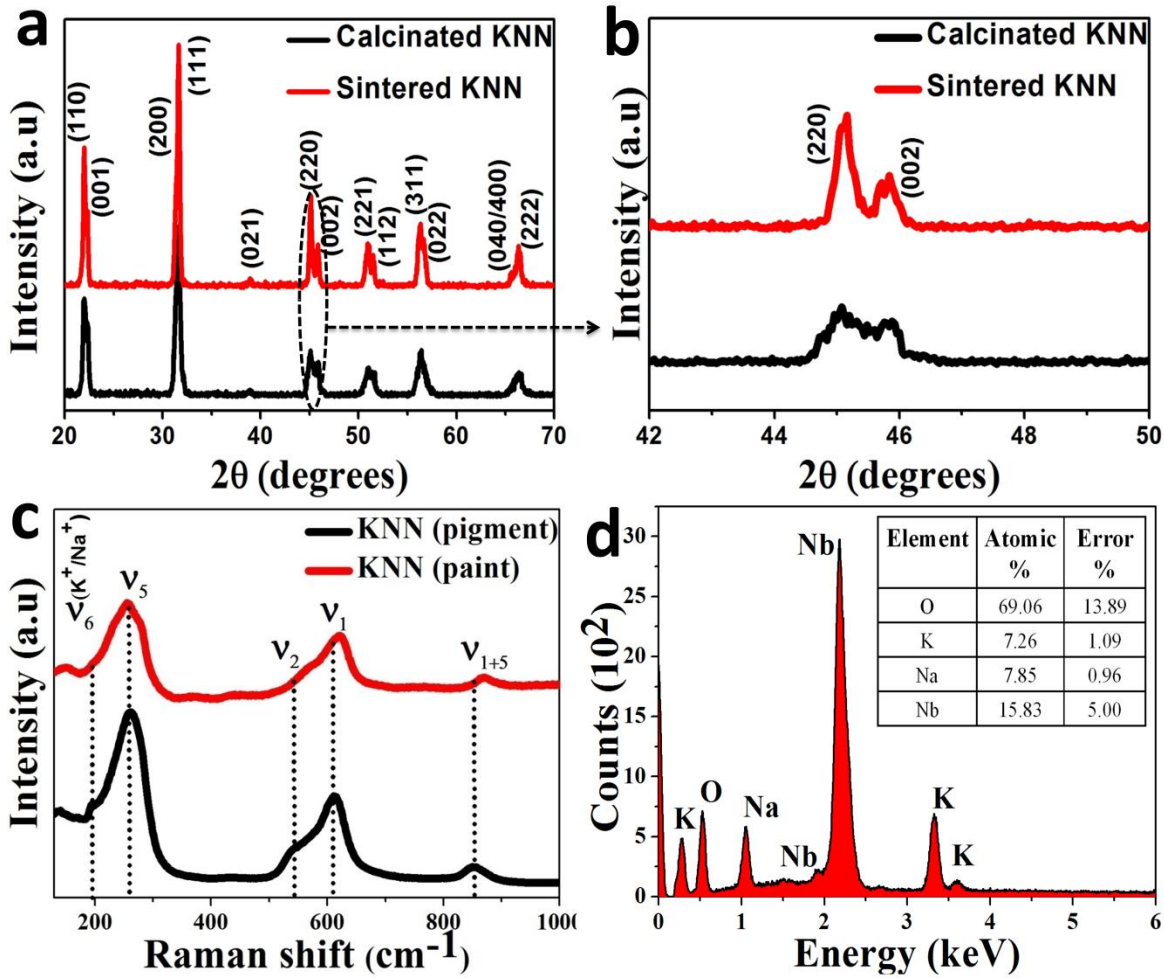

Figure 3.1 Structural confirmation of as-synthesised $K_{0.5}Na_{0.5}NbO_3$ (KNN) nanoparticles: **(a)** X-ray diffraction spectrum of KNN nanoparticles with a single-crystalline orthorhombic phase. **(b)** Enlarged portion of the diffraction peak at 45°, indexed as (220)/(002) planes. **(c)** Raman spectrum of KNN nanoparticles and KNN in composite medium. **(d)** Energy dispersive spectroscopy analysis of KNN nanoparticles (inset table is the quantitative ratio of O, K, Na, and Nb).

Furthermore, the formulated piezoelectric composite was analysed to determine the phase symmetry of the KNN pigment in the alkyd medium. The Raman spectrum (Figure 3.1(c)) indicated that the KNN nanoparticles in the composite experienced native vibrational modes. The slight shifts observed in peaks ν_2, ν_1, and ν_{1+5} arise due to changes in the stretching modes of the polyhedron (NbO_6). This shift behaviour was expected from the continuous stirring of KNN nanoparticles in the alkyd medium for 24 h at high speed, which affected O-Nb-O bond stretching. The EDAX analysis (Figure 3.1(d)) confirmed the presence of O, K, Na, and Nb in a ratio (inset table) close to the estimated stoichiometric level (for KNN). The peaks confirmed that the final KNN product was highly pure and carbonate-free. Calcined KNN nanoparticles showed an irregular morphology, due to abnormal grain growth at a temperature of 850°C (**Figure 3.2**). Upon sintering at 1100°C for 2 h, the KNN nanoparticles shrunk; this led to improved densification, fine grain growth, and the morphology of the as-synthesised KNN pigments.

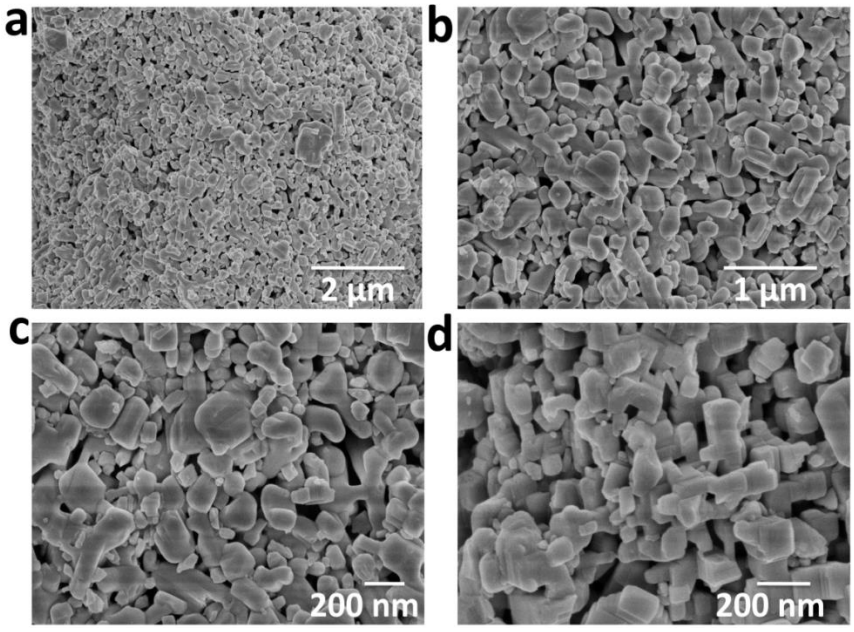

Figure 3.2 FESEM images at different scale rate (2 µm, 1 µm and 200 nm) of as-synthesized KNN nanoparticles calcinated at a temperature of at 850 °C for 10 h.

Figure 3.3 shows FE-SEM analysis results of as-synthesised KNN nanoparticles sintered at 1100°C. The KNN particles exhibited rectangular brick-like shapes, as expected for KNN-based ceramics, and showed an average size of ~300 nm. The incorporation of K^+ and Na^+ ions into the A-sites in the ABO_x (A-NbO_3) composition induces an evolution of grain morphology to the nearly rectangular-shaped grains. FE-SEM images also revealed the presence of small grain morphology. This is attributable to the secondary nucleation of small crystals to form further rectangular-shaped KNN nanoparticles. The presence of small grains helps to enhance the surface diffusion mechanisms that promote rectangular KNN nanograin formation.

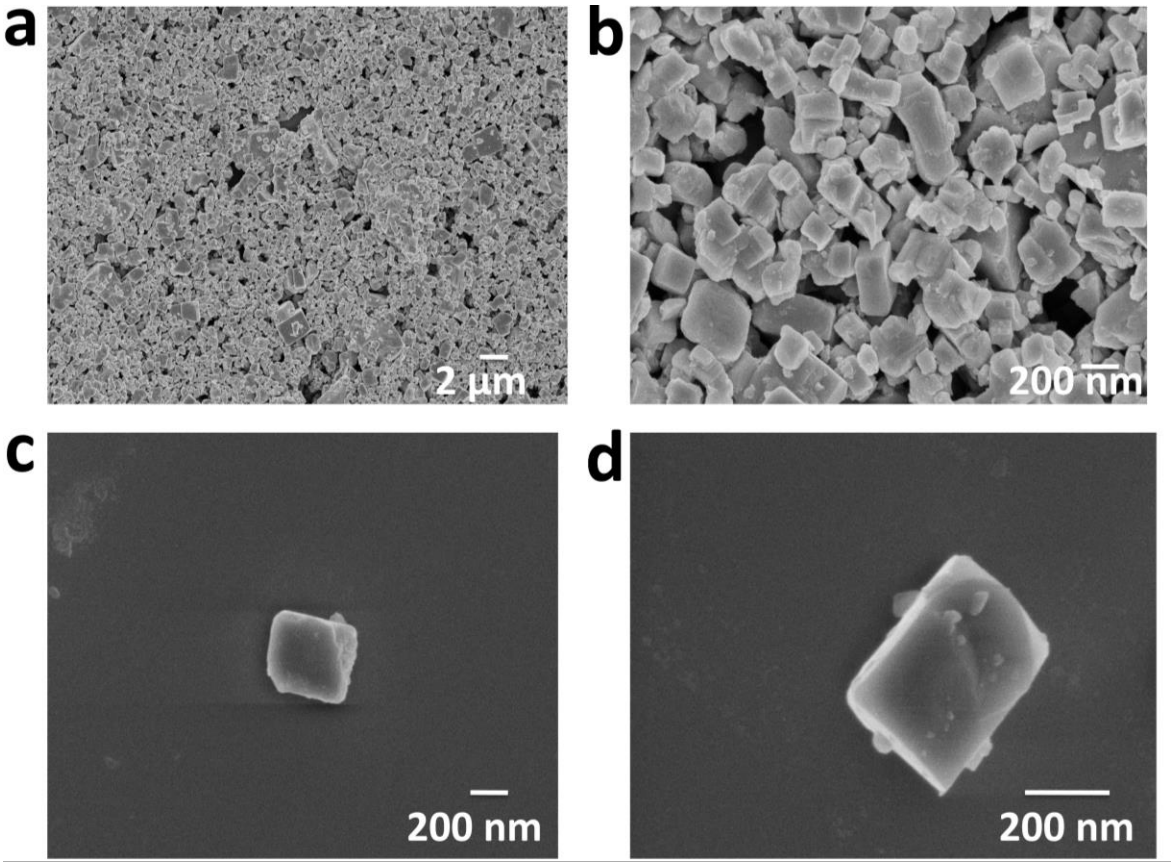

Figure 3.3 (a, b) Field-emission scanning electron microscopy (FE-SEM) images of as-synthesised KNN nanoparticles using a high-temperature solid-state reaction method at 2 µm and 200 nm scales. **(c, d)** Magnified images of the KNN nanoparticles showing different sizes of grains at a 200 nm scale.

Further, the ferroelectric property exhibited by $K_{0.5}Na_{0.5}NbO_3$ nano pigment sintered for about 2 h at 1120°C was confirmed through P-E hysteresis loop. **Figure 3.4** shows the polarization (P) vs. electric field (E) hysteresis loop at a frequency of 1 Hz, confirming the ferroelectric property exhibited by $K_{0.5}Na_{0.5}NbO_3$ sample sintered for 2 h at 1120°C. The hysteresis loop at a drive voltage of 1 kV/cm, demonstrates the existence of polarization with a lossy capacitance nature of as-synthesized KNN pigment[23]. This kind of inflated behavior is mainly due to the contribution of leakage current which depends upon various factors. Firstly, the presence of oxygen vacancies adds up to high leakage current and secondly, there is a size and geometrical effect as the dimension of the material is lowered[24, 25]. The reduced grain size of prepared KNN (~ 300 nm) affects the polarization, leaving it unsaturated. Despite these factors, the sintered KNN nanomaterial possesses reasonable piezoelectric properties with remnant polarization (P_r) of ~ 99 μC/cm^2 and coercive fields (E_c) of ~ 820 V/cm which are higher than reported in the literature[2, 4]. A further improvement in piezoelectric properties can be achieved by reducing the leakage current through suitable doping mechanism and processing temperature[26].

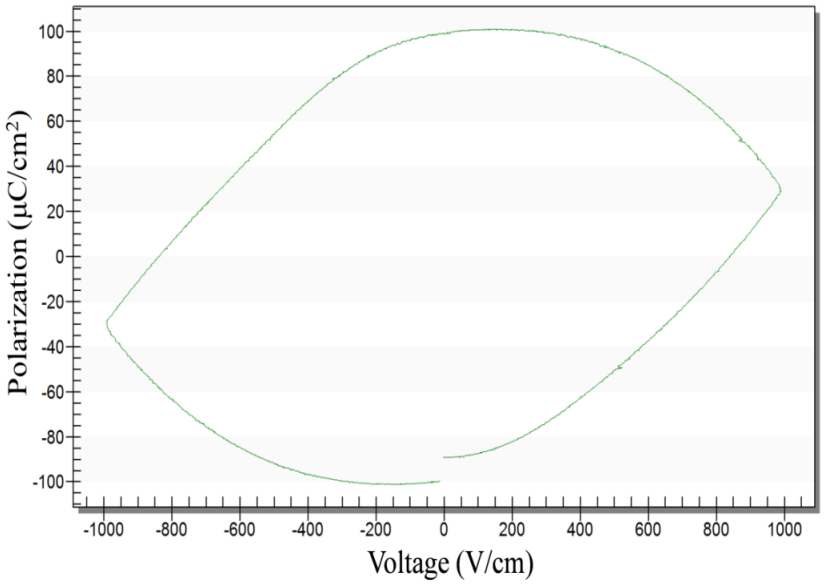

Figure 3.4 P-E hysteresis loop of as-prepared $K_{0.5}Na_{0.5}NbO_3$ sample sintered for 2 h at 1120°C.

Figure 3.5(a) shows optical images of formulated piezoelectric composite coated on a copper-beryllium substrate. Figure 3.5(b) shows the FE-SEM results of the piezoelectric composite; KNN nanoparticles as a pigment were dispersed uniformly in the alkyd resin medium, with minimal agglomeration. Figure 3.5(c) shows the FTIR spectrum of the KNN-based piezoelectric alkyd composite system.

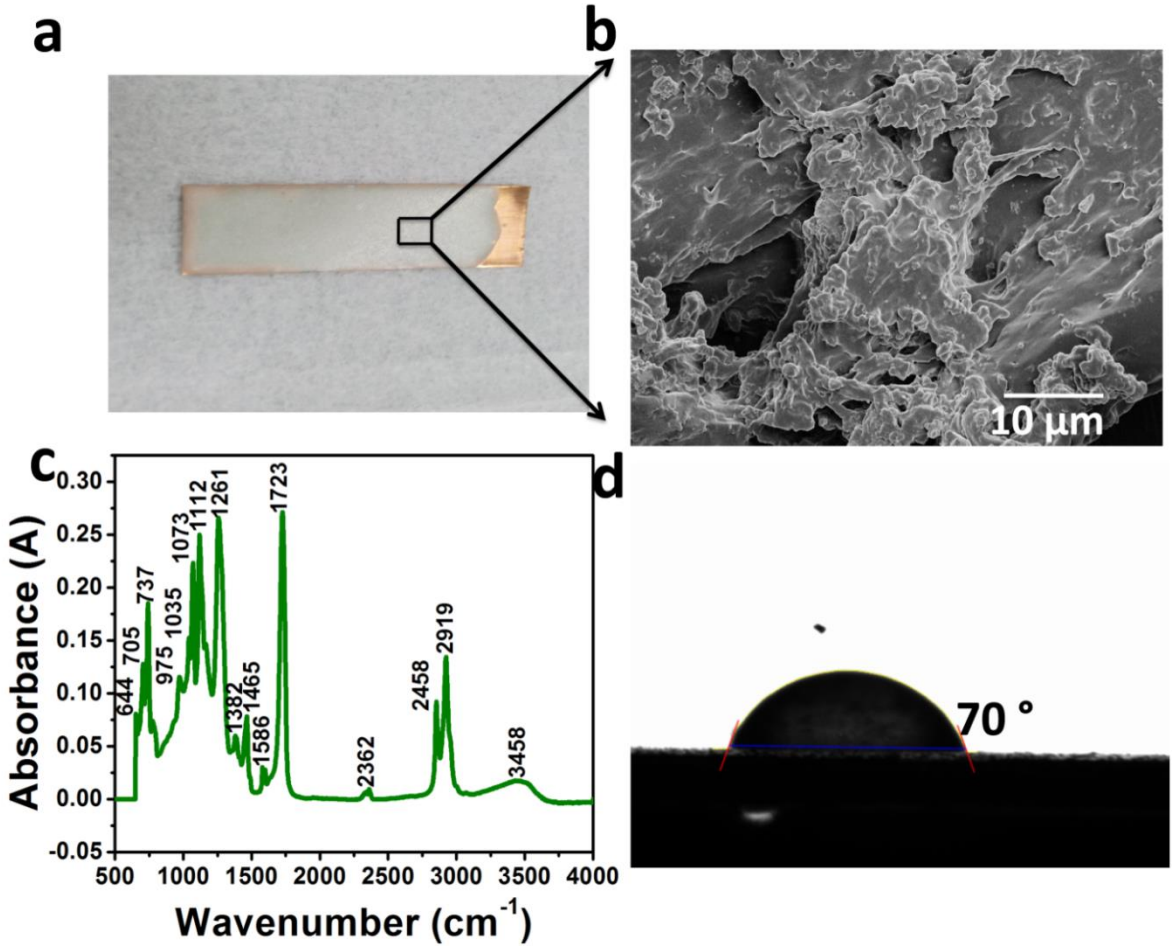

Figure 3.5 (a) Optical image of KNN-based piezoelectric composite coated on a copper-beryllium substrate. **(b)** FE-SEM image of the as-formulated piezoelectric composite, showing uniform dispersion of KNN pigment nanoparticles. **(c)** Fourier-transform infrared spectrum of piezoelectric composite consisting of an alkyd/KNN composition. **(d)** Water contact angle of the piezoelectric composite, brush-coated on the cantilever substrate.

The characteristic peaks obtained after natural oxidation in the piezoelectric composite system are as follows. The broad band at 3483 cm^{-1} was assigned to O-H stretching. The sharp peaks at 2928 cm^{-1} and 2850 cm^{-1} are attributable to C-H stretching. The strong peak at 1725 cm^{-1} coincides with C=O of the carboxyl groups[27]. The small peak at 1586 cm^{-1} was assigned to the aromatic ring, and C-H and C-R bending modes were observed at 1457 cm^{-1} and 1385 cm^{-1}, respectively[27]. The small peaks at 1069 cm^{-1}, 1126 cm^{-1}, and 1252 cm^{-1} are due to C-O groups, and the weak peak at 746 cm^{-1} corresponds to aromatic =C-H bending[27]. In the spectra, the band located at 644 cm^{-1} is due to a symmetrical stretching mode, arising from NbO_6 polyhedra[28, 29]. The KNN pigment was mixed homogeneously in the alkyd system and it was not altered by the properties of the alkyd polymer resin. The surface properties of the composite were determined through water contact angle (WCA) measurements. Figure 3.5(d) shows the wetting properties of the composite surface, measured in terms of WCA characteristics. A WCA of 70° was achieved, illustrating the hydrophilic nature of the piezoelectric composite. The hydrophilic nature of the piezoelectric composite surface showed good adhesive bonding and physical interaction due to intermolecular forces developed between the surface and the liquid. This also ensures that the piezoelectric composite coated on the surface is less rough. The thickness of piezoelectric composite coated on to the copper beryllium substrate was measured to be ~65 μm through FESEM observation (**Figure 3.6**).

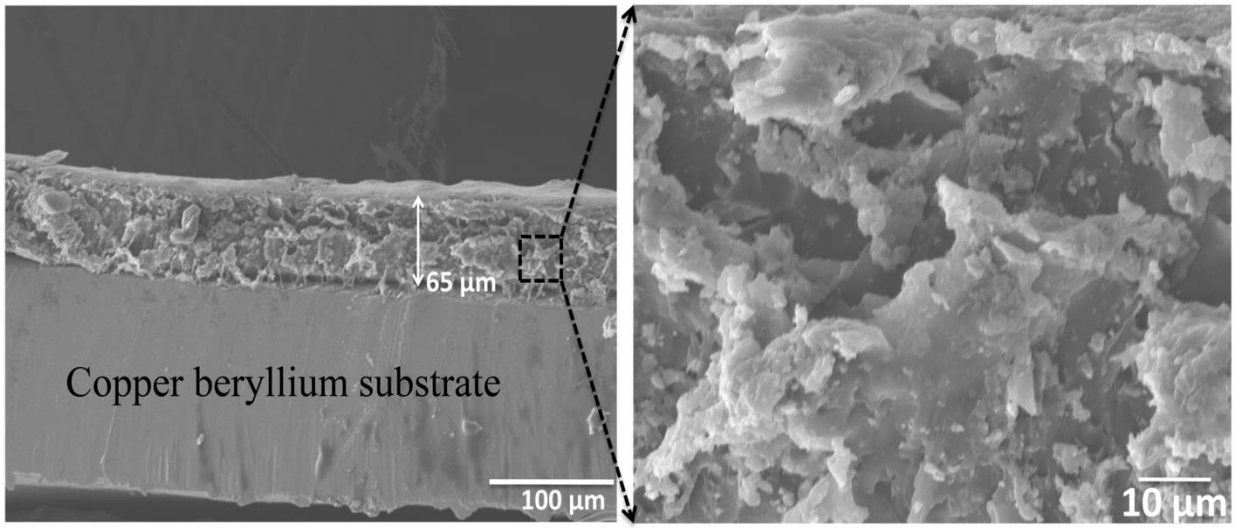

Figure 3.6 Cross-sectional FE-SEM analysis of KNN based piezoelectric composite coated on copper beryllium substrate.

3.3.2 Energy harvesting capability of the piezoelectric composite

3.3.2.1 Piezoelectric voltage response without proof mass (m_p)

To determine the ability for power generation from the piezoelectric composite, one end of the cantilever beam coated with piezoelectric composite was mounted on a fixed clamp. The other end was set free to move, depending on the vibrations exerted on the substrate. An optimum vibration harvester can be modelled as a spring–mass system consisting of three major parts: the substrate, the piezoelectric part, and the proof mass. **Figure 3.7**(a) shows a schematic illustration of the as-developed piezoelectric composite-based vibration system. As a cantilever beam substrate, a rectangular-shaped copper-beryllium thin sheet was used, which can respond to vibrations from the environment. The copper-beryllium substrate exhibits high mechanical strength and has a favourable elastic modulus, which acts as an ideal spring material that efficiently transfers the vibrations to the piezoelectric composite. Here, the KNN-based

piezoelectric composite developed was used to convert mechanical stress applied to the copper-beryllium substrate into an electrical signal.

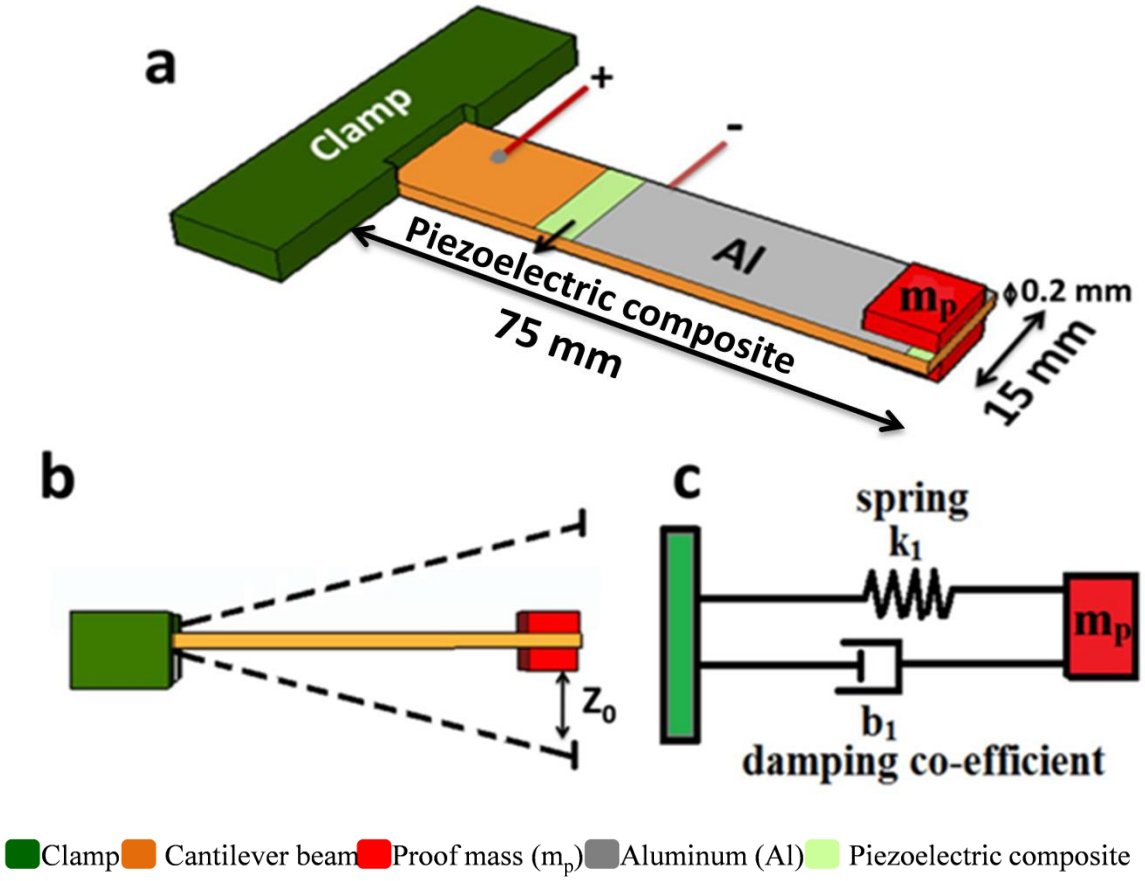

Figure 3.7 Schematic representations of **(a)** Cantilever-based vibration system. **(b)** Cantilever beam displaced to a distance, Z_0. **(c)** Typical spring–mass system.

To measure the vibrational response of the spring–mass model, the tip of the cantilever beam of length 75 mm was deflected manually to a distance (Z_0) and released (Figure 3.7(b) & **Figure 3.8**). This causes the beam to vibrate freely at the deflected end. The deflection of the beam produces similar stress in the piezoelectric composite coated on its surface, thus creating a piezopotential drop in the composite substrate, allowing a flow of electrons to transfer between the electrodes. Because the degree of stress exerted on the cantilever beam and the piezoelectric

composite is non-uniform, due to the beam structure, an electrode covering the entire region of the piezoelectric composite surface is necessary. Thus, an aluminium electrode was used to efficiently transfer the electrons produced throughout the vibrating system.

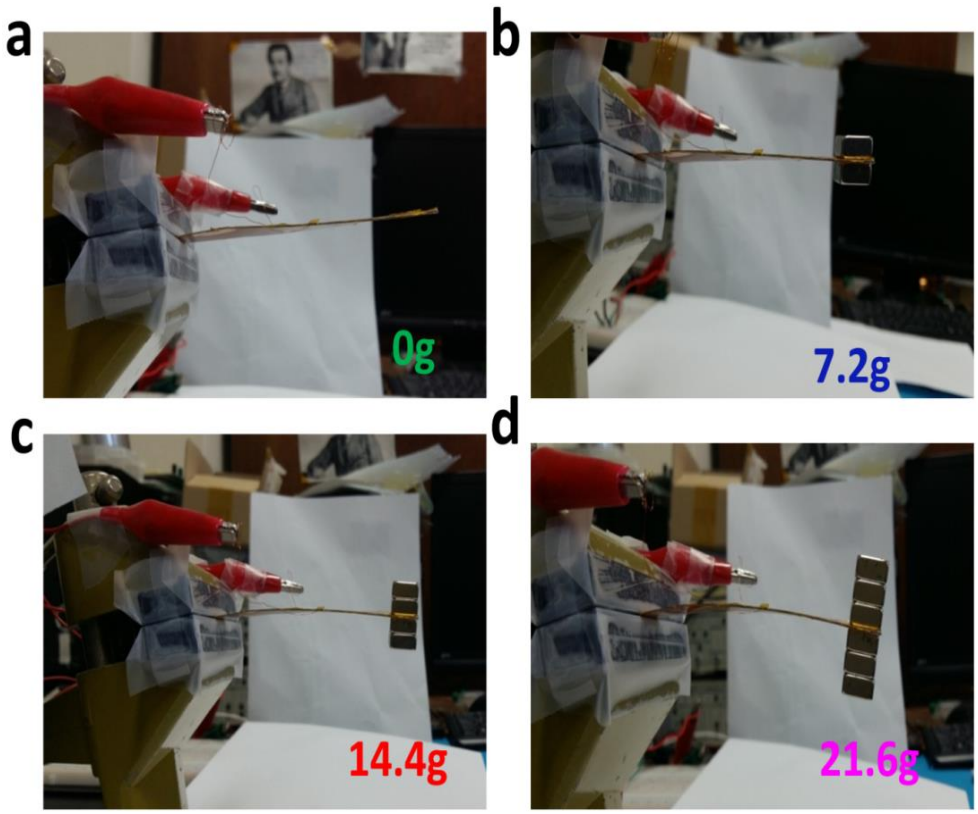

Figure 3.8 Optical images of copper beryllium beam with different loaded mass. **(a)** 0 g. **(b)** 7.2 g. **(c)** 14.4 g. **(d)** 21.6 g.

From **Figure 3.9**(a), the peak voltage produced due to the cantilever beam vibrating without any proof mass (m_p) was nearly 0.45 V. To measure the relative performance of the energy-harvesting system, a mechanical stress was applied parallel to the cantilever beam substrate coated with piezoelectric composite. The deviation of the cantilever causes the piezoelectric composite to experience similar stress. Due to the mechanical stress, a piezopotential was generated across the composite film, which serves as a driving force for electrons to flow between the top and bottom electrodes. The piezopotential produced is directly

proportional to the vibrating cantilever substrate. Thus, the output voltage/current signal of the piezoelectric composite is a direct measure of the vibration of the cantilever.

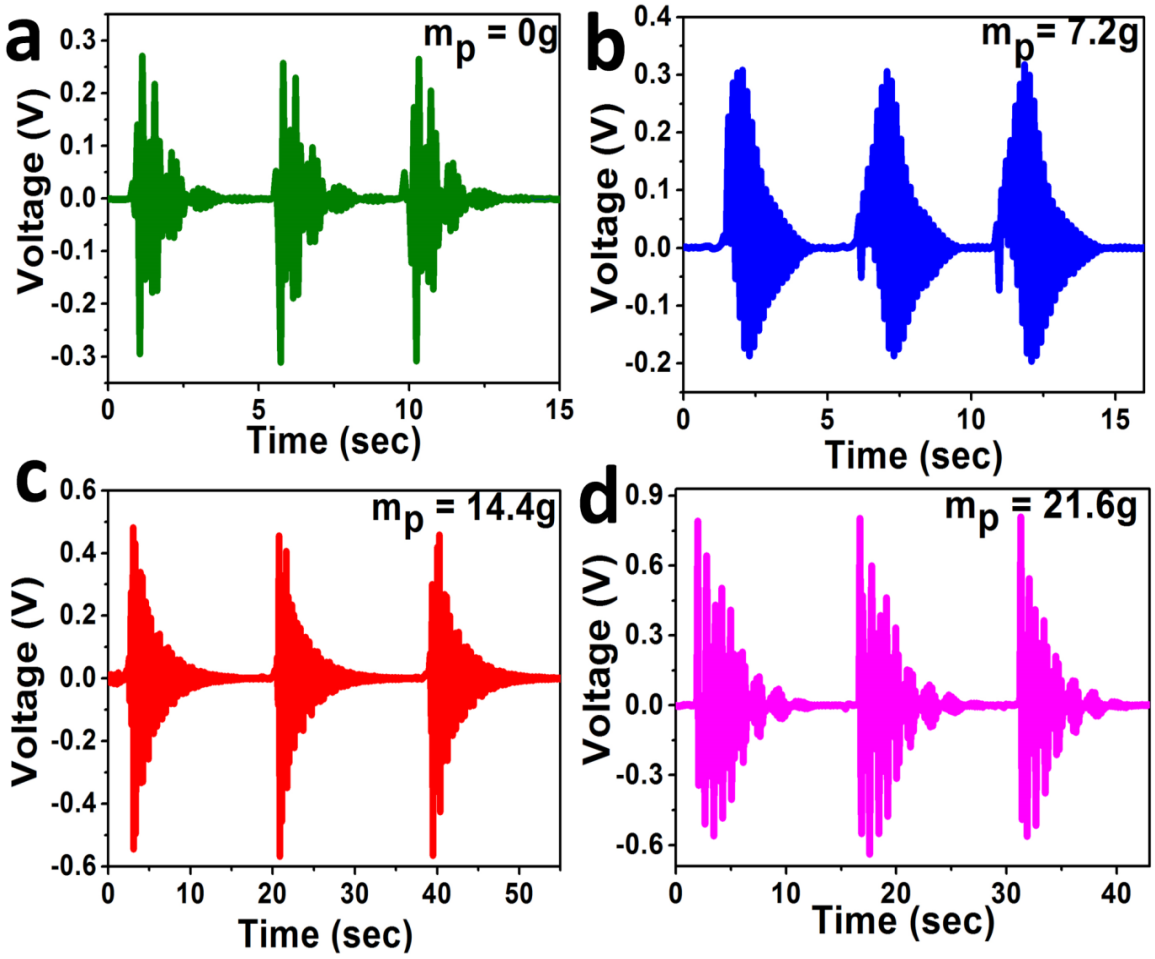

Figure 3.9 Electrical performance of the piezoelectric composite determined as a spring–mass system. **(a)** Output voltage response of cantilever beam with no mass loading. **(b)** 7.2 g proof mass. **(c)** 14.4 g proof mass. **(d)** 21.6 g proof mass.

The vibration response in Figure 3.9(a) is due to the initial mechanical stress applied to the beam followed by the restoring behaviour of the beam due to its damping effect. The maximum amplitude (0.45 V) obtained was due to the immediate response of the beam when deflected to a displacement distance (Z_0) of 2 cm. Further, the amplitude is minimised due to the damping effect, which restricts the vibration of any free-standing system. Thus, the vibration

ends after a certain time and the beam is restored to its original position after 2 s. The restoring effect of the beam can be observed in the amplitude of the voltage response (Figure 3.9(a)).

3.3.2.2 Piezoelectric voltage response with proof mass (m_p)

The resonance frequency is an important parameter that plays a key role in cantilever beam- structured energy harvesters. At the resonance frequency, the vibration of the cantilever is maximal, producing the maximum amplitude in the voltage signal. The frequency of any energy-harvesting vibration system can be modulated by addition of a proof mass (m_p). Depending on the weight and position of the proof mass added to the cantilever beam, the modes of vibration changes. To analyse the effect of the proof mass (m_p) on the piezoelectric voltage response, the cantilever beam was assessed with three masses (7.2, 14.4, and 21.6 g). Here, the position of the proof mass was fixed at the tip of the copper-beryllium beam and the weight of the proof mass was varied to determine the frequency response of the vibrating system. As shown in Figure 3.7(b), one end of the cantilever was fixed to a rigid clamp and the other end was set to vibrate freely on addition of the proof mass (m_p). Thus, this configuration resembles a spring–mass damping system operating with a single degree of freedom (SDOF) with a damping/restoring force, b_1; the stiffness of the flexible cantilever beam is given by the spring constant, k_1 (Figure 3.7(c)). Figure 3.8 shows images of the cantilever beam deflection loaded with various proof masses. The maximum load that the cantilever beam could withstand was limited to 21.6 g for the defined area of the beam (75 × 15 × 0.2 mm). With further addition of proof mass, the cantilever beam deforms, changing its position, thus reaching a maximum deflection point. The addition of proof mass determines the damping force of the vibrating beam, i.e. the restoring force to return the specific distortion of the body back to its equilibrium position[30]. Figures 3.9(b) and (c) show the effect of different mass loadings. As the proof mass increased, the

amplitude of the voltage increased. For a 7.2 g proof mass, the peak voltage obtained was 0.51 V (Figure 3.9(b)), which increased further to 1 V for a 14.4 g proof mass and 1.4 V with a 21.6 g mass loading (Figure 3.9(d)). It was observed that the voltage generated by the energy harvester with a proof mass was higher than that without a proof mass. **Figure 3.10** illustrates the piezoelectric output current obtained as a function of proof mass loading of the cantilever beam. A linear increase in the piezoelectric current was observed as the strain acting on the beam was varied by the addition of the proof mass (7.2, 14.4, and 21.6 g).

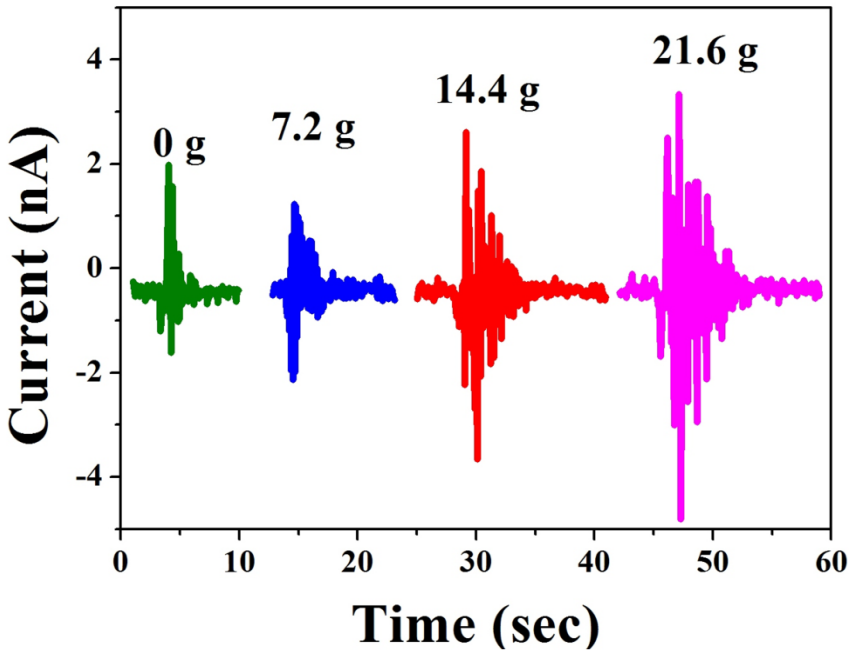

Figure 3.10 Piezoelectric current response as a function of increased proof mass (m_p = 0, 7.2, 14.4 and 21.6 g).

The energy harvester with a proof mass generated a higher voltage than the energy harvester with no proof mass, as more strain was produced at the fixed end of the beam. The voltages obtained of 0.45, 0.51, 1, and 1.4 V are from the piezoelectric potential generated across the composite coated on the cantilever beam substrate (**Figure 3.12**(a)). Additionally, the effect of output voltage as a function of tip displacement (Z_0) was tested. As the tip displacement was

varied to 1, 2, and 3 cm, the deflection of the beam was altered, which, in turn, changed the strain acting on the piezoelectric composite, thus causing a similar effect on the piezoelectric voltage produced from the composite. From Figure 3.12(b), a simultaneous increase in the peak voltage was observed as the displacement increased, whereas there was no change in the operating frequency of the cantilever beam. This also illustrates that the KNN-based piezoelectric composite system developed was capable of harvesting energy from the vibrating source and was also sensitive to the function of mechanical stress exerted by the vibrating surface.

3.3.3 Experimental and theoretical validation of piezoelectric resonance frequency

The fundamental frequency domains of the vibrating cantilever beam, with and without proof mass, are determined by Fourier transform (FT) analysis of the voltage response obtained[31]. **Figure 3.11** shows the frequency characteristics of the vibrating beam. Upon mass loading, the frequency eventually decreased, in accordance with a typical spring–mass effect. Upon addition of the proof mass, the strain exerted by the cantilever beam increased, which eventually increased the operating frequency of the vibrating beam. When the copper-beryllium substrate was deflected to a distance (Z_0) of 2 cm with no additional mass, the beam oscillated at a resonance frequency of 6.08 Hz (Figure 3.11(a)). When a proof mass of 7.2 g was added, the frequency was lowered to 5.6 Hz (Figure 3.11(b)). The beam vibrated at lower frequencies: 4.76 Hz with a proof mass (m_p) of 14.4 g (Figure 3.11(c)) and 3.8 Hz with a proof mass of 21.6 g (Figure 3.11(d)).

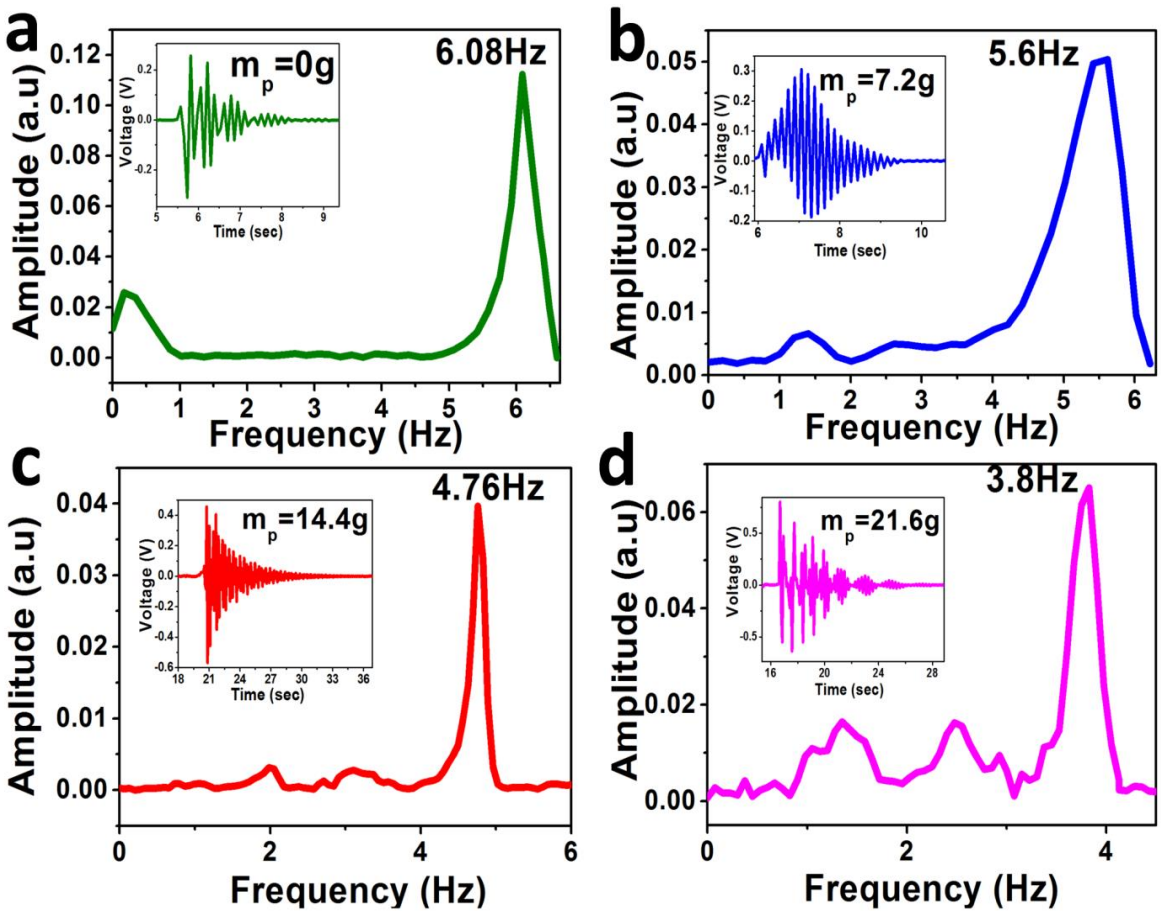

Figure 3.11 Frequency responses of the cantilever beam at various proof mass loadings. **(a)** No mass (0 g). **(b)** 7.2 g. **(c)** 14.4 g. **(d)** 21.6 g.

Theoretically, the natural frequency of the cantilever beam can be determined according to the beam theory of stiffness and the proof mass concept. The resonant frequency (f_0) of a vibrating rectangular beam system can be expressed by the following relationship[32,33]:

$$f_0 = \frac{1}{2\pi}\sqrt{\frac{k_{eff}}{m_{eff}}} \qquad \text{- (2)}$$

where f_0 is the resonant frequency, k_{eff} is the effective spring/cantilever beam stiffness, and m_{eff} is the effective mass acting on the cantilever beam. The effective stiffness depends on Young's modulus *(E)* and the moment of inertia *(I)* of the copper-beryllium substrate, and is given by the following equation:

$$k_{eff} = \frac{3EI}{L^3} \quad \text{- (3)}$$

where L is the length of the cantilever beam and the moment of inertia (I) is determined by the width and height of the cantilever beam as

$$I = \frac{bh^3}{12} \quad \text{- (4)}$$

The resonant frequency also depends upon the effective mass, m_{eff} , which can be expressed as

$$m_{eff} = 0.236\rho AL \text{ (without proof mass)} \quad \text{- (5)}$$

$$m_{eff} = 0.236\rho AL + m_p \text{ (with proof mass)} \quad \text{- (6)}$$

where m_p is 7.6 g, 14.4 g, or 21.6 g, L = 75 mm, h = 0.2 mm, b = 15 mm, the density (ρ) of copper-beryllium = 8260 kg/m^3, and Young's modulus (E) = 1.27×10^{11} N/m^2.

Using the relationship above, the effective spring/cantilever beam stiffness, k_{eff}, is 9.0311 N/m, and the effective mass acting on the vibrating system, m_{eff}, is 0.000438 kg (without m_p), and 0.00763 kg (m_p = 7.2 g), 0.01453 kg (m_p = 14.4 g), and 0.02203 kg (m_p = 21.6 g). Finally, the resonant frequency of the vibrating cantilever beam was determined theoretically to be 22.86, 5.47, 4.01, and 3.22 Hz with proof masses of 0, 7.2, 14.4, and 21.6 g, respectively. The resonant frequency decreased as the mass acting on the beam increased, consistent with the behaviour of a standard spring–mass damper system[34]. Figure 3.12(d) shows a comparative analysis of resonant frequency obtained experimentally versus that calculated theoretically, using the Euler–Bernoulli theory of beams. From the graph, the resonant frequency was approximately equal for the systems loaded with proof masses, whereas considerable variation was observed in the theoretical and experimental values in the frequency of the beam vibrating with no proof mass. The experimental frequency was much reduced, to 6.08 Hz versus the theoretical value of 22.86 Hz. This reduction in frequency is attributable to the effect of the mass acting on the

substrate with the piezoelectric composite. The piezoelectric composite coating the copper-beryllium substrate acted as an additional mass to the beam, which altered the natural resonance vibration frequency of 22.86 Hz by reducing it to 6.08 Hz.

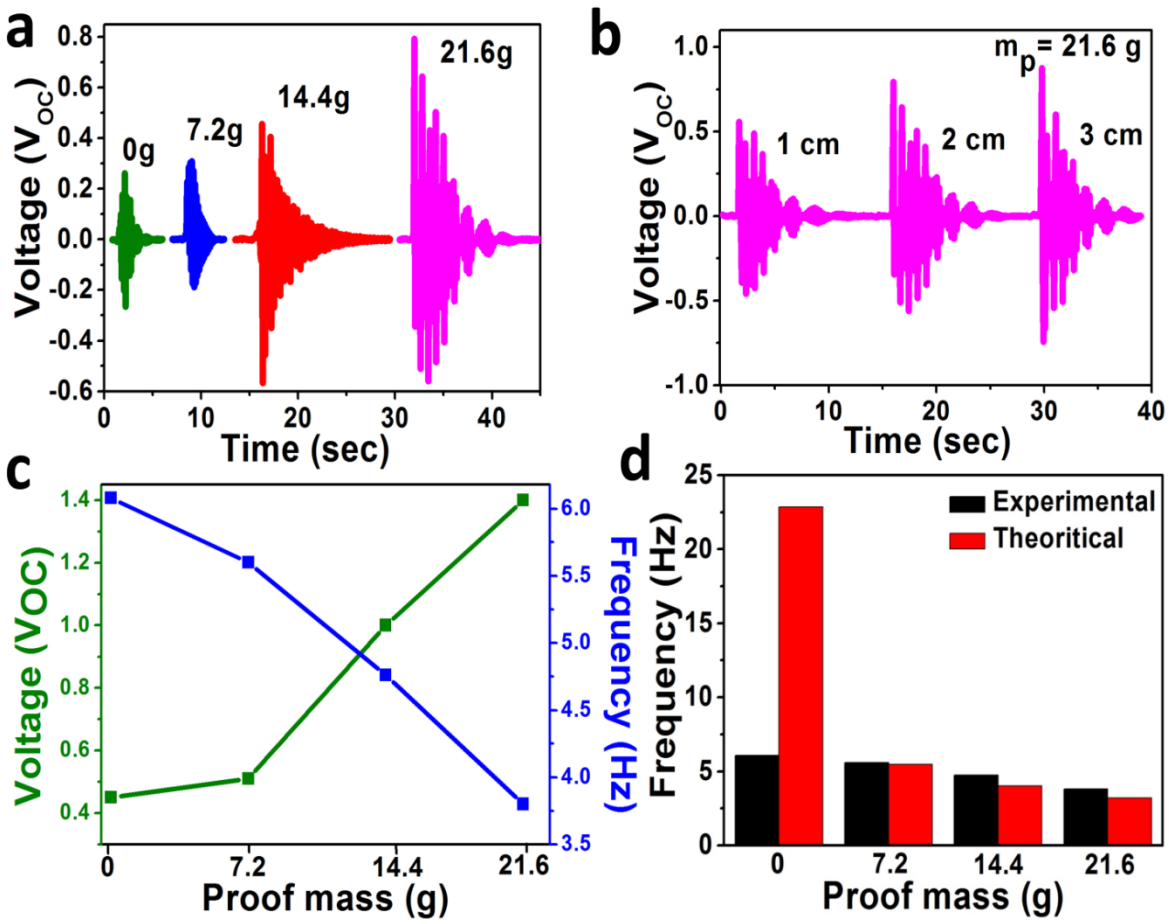

Figure 3.12 (a) Piezoelectric voltage response as a function of increased proof mass. **(b)** Behaviour of cantilever beam at different tip displacements (Z_0). **(c)** Dependence of open circuit voltage (V_{OC}) and resonance frequency of cantilever beam on proof mass loading. **(d)** Cumulative comparison of experimentally obtained resonance frequencies with theoretical calculations.

For further studies on mass loading, the frequencies of vibration were approximately the same because the mass of the piezoelectric composite was negligible compared with the proof masses of 7.2, 14.4, and 21.6 g. The output power of the energy harvester depends on the

effective mass rather than the total mass of the cantilever beam structure. These results suggest that the KNN-based piezoelectric composite system developed is capable of harvesting energy from a low-frequency vibrating environment and that it is highly sensitive to the degree of mechanical strain applied to it.

Table 3.2 Comparison on the cantilever configuration of proposed KNN based piezoelectric composite with other published reports.

Material	**Cantilever configuration**	**Dimension (mm)**	**m_p[a] (g)**	**V_{OC}[b] (V)**	**f_0[c] (Hz)**	**Ref**
PZT-5A	Bimorph	125 × 13.2 ×21.33	0.72	3.3	36	35
PZT	Bimorph	8 × 5 × 0.4	0.8	0.08	51	36
PZT	Bimorph	40 × 220 × 0.8	12	0.19 mW (P)	14.5	37
PZT-5A	Bimorph	90 × 40 × 24	-	2.47	-	38
PZT	Unimorph	11.5 × 12.7	0.7	0.32	60	39
PVDF	Unimorph	30 × 12.2 × 0.125	8600 kg/m^3	4.72	4 - 6	40
ZnO	Fiber	50 × 50	1	0.39 70 nA (I_{SC})	175	41
KNN	Unimorph	50 × 15	21.6	1.4 8 nA (I_{SC})	3.8	This work

[a] Proof mass; [b] Piezoelectric output voltage; [c] Resonant frequency

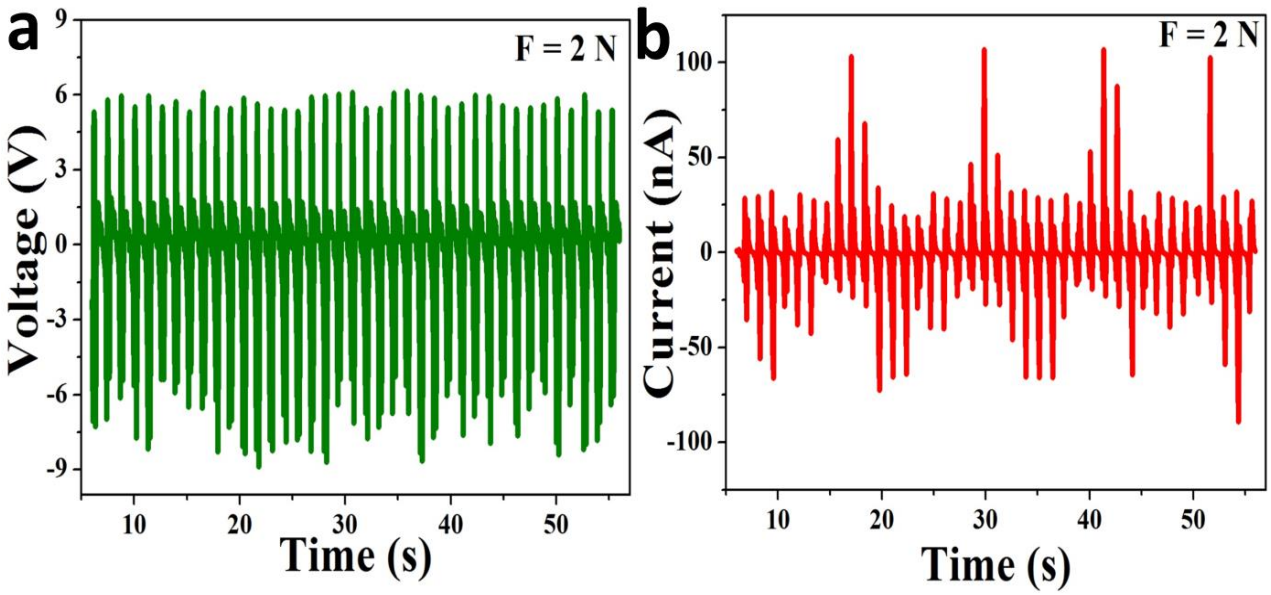

Figure 3.13 Piezoelectric performance of KNN based piezoelectric composite under a constant load of 2 N. **(a)** Electrical output voltage (V_{OC}). **(b)** Electrical output current (I_{SC}).

Besides, the reliability of the piezoelectric composite was examined under a constant mechanical load of 2 N (obtained by a linear motor shaft mass (2 kg) moving with acceleration of 1 m/s^2). The piezoelectric composite generated a maximum electrical output of $V_{OC} \approx 12$ V and $I_{SC} \approx 70$ nA (**Figure 3.13**).

Table 3.3 Performance comparison of piezoelectric KNN composite with published reports.

Material	Area (cm)	Force	V_{OC}[a] (V)	I_{SC}[b] (A)	Ref
$K_{0.5}Na_{0.5}NbO_3$/PDMS	2.5 × 4.5	Finger	0.17	4.48 n	42
$K_{0.6}Na_{0.4}NbO_3$ Nanorods	-	1 kgf	0.38	6.4	43
0.9525($K_{0.5}Na_{0.5}NbO_3$)-0.0475$LiTaO_3$/PDMS	2.1 × 1.7	140 N	53	15 μ	44
0.942($K_{0.480}Na0_{.535}$)NbO_3-0.058$LiNbO_3$/PDMS	3 × 3	0.33 % (strain)	12	1.2 μ	45
$K_{0.5}Na_{0.5}Nb_{0.995}Mn_{0.005}O_3$/Silk solution	-	500 μN	1.8	0.1 μ	46
0.96($K_{0.48}Na_{0.52}$)($Nb_{0.95}Sb_{0.05}$)O_3– 0.04$Bi_{0.5}$($Na_{0.82}K_{0.18}$)0.5ZrO_3/PDMS	2 × 2	-	10	-	47
$K_{0.5}Na_{0.5}NbO_3$/Alkyd (piezoelectric composite)	5 × 1.5	2 N	12	70 n	This work

[a] Piezoelectric output voltage; [b] Piezoelectric output current

3.4 Conclusion

In summary, we developed a piezoelectric composite system using alkyd resin as a binding polymer to hold KNN pigment nanoparticles. Highly crystalline, rectangular-shaped KNN piezoelectric nanoparticles with an orthorhombic phase were synthesised using a high-temperature SSR method. The performance of piezoelectric composite was evaluated by detecting the cantilever beam vibrations at mass loadings of 7.2, 14.4, and 21.6 g. The piezoelectric composite was capable of producing a maximum open circuit voltage (V_{OC}) of 1.4 V with a proof mass (m_p) of 21.6 g acting on the cantilever beam. The behaviour of

developed lead-free piezoelectric composite composition demonstrates its potential use as a sensitive energy-harvesting unit that can be used for large-area energy scavenging systems. The results above pave the way for composite and coating technologies, with various multifunctional nanomaterials, such as piezoelectric, magneto electric, pyroelectric, and thermoelectric, to promote efficient alternative energy-harvesting approaches to drive low power consumption sensors and electronics.

3.5 References

1 Y. Zhang, *J. Intell. Mater. Syst. Struct.*, 2006, **17**, 843–852.

2 J.M. Hale, J. Tuck, *Proc. Inst. Mech. Engrs C J. Mech. Engng Sci.*, 1999, **213,** 613–621.

3 X. Li, Y. Zhang, *Fatigue Fract. Eng. Mater. Struct*., 2008, **31,** 684–694.

4 T. Kaneko, K. Iwata, M. Kobayashi, *IEEE Trans. Ultra. Ferroelec. Freq. Cont.*, 2015, **62,** 1686–1695.

5 Y. Zhang, *Proc. SEM X Int. Congr*., 2004, **5765,** 1095–1103.

6 J.R. White, *J. Mater. Sci.*, 2004, **9**, 3105–3114.

7 L.-H. Kang, *Adv. Compos. Mater*., 2014, **23**, 73–84.

8 S. Egusa, N. Iwasawa, *J. Mater. Sci.*, 1993, **28**, 1667–1672.

9 J.M. Hale, R. Lahtinen, *Plast. Rubber Compos.*, 2007, **36,** 419–422.

10 I. Coondoo, N. Panwar, A. Kholkin, *J. Adv. Dielectr*., 2013, **3**, 1330002.

11 S. Priya, S. Nahm, *Springer new York*, 2013, **1,** 528.

12 J.F. Li, K. Wang, F.Y. Zhu, L.Q. Cheng, F.Z. Yao, *J. Am. Ceram. Soc.*, 2013, **96,** 3677–3696.

13 K. Wang, J.F., *J. Adv. Ceram*., 2012, **1,** 24–37.

14 S. Saadon, *Optoelectronics and Adv. Mater.*, 2010, **8**, 1219–1224.

15 H. Li, C. Tian, Z.D. Deng, *Appl. Phys. Rev.*, 2014, **1,** 0–20.

16 L. Dhakar, H. Liu, F.E.H. Tay, C. Lee, *A. Phys.*, 2013, **199,** 344–352.

17 K. Krishnamoorthy, K. Jeyasubramanian, M. Premanathan, G. Subbiah, H.S. Shin, S.J. Kim, *Carbon*, 2014, **72**, 328–337.

18 K. Krishnamoorthy, M. Premanathan, M. Veerapandian, S. Jae Kim, *Nanotechnology.*, 2014, **25**, 315101.

19 Z. Wang, H. Gu, Y. Hu, K. Yang, M. Hu, D. Zhou, J. Guan, *CrystEngComm.*, 2010, **12,** 3157.

20 K. Chen, J. Tang, Y. Chen, *Ceram. Int.*, 2016, **42,** 9949–9954.

21 X. Chen, F. He, J. Chen, Y. Wang, H. Zhou, L. Fang, *J. Mater. Sci. Mater. Electron.*, 2014, **25,** 2634–2637.

22 L.-Q. Cheng, K. Wang, Q. Yu, J.-F. Li, *J. Mater. Chem. C.*, 2014, **2,** 1519.

23 Z. Wang, Y. Hu, W. Wang, D. Zhou, Y. Wang, H. Gu, *Int. Ferroelec*, 2013, **42**, 24–30.

24 D. Zhou, H. Gu, Y. Hu, , Z. Wang, Z. Qian, Y. Wang, *J. App. Phys*., 2011, **109**, 114104.

25 M. U. Farooq, J. G. Fisher, J. H. Kim, D. Zhang, *J. Cer. Proc. Res.*, 2016, **17**, 304–312.

26 P. Zhao, B. P. Zhang, J. F. Li, *App. Phys. Letters,* 2007, **90**, 242909.

27 S.M. Cakić, L.B. Bošković, *Hem. Ind.*, 2009, **63,** 637–643.

28 M. b Dolhen, A. Mahajan, R. Pinho, M.E. Costa, G. Trolliard, P.M. Vilarinho, *RSC Adv.*, 2015, **5,** 4698–4706.

29 N. Duc Van, *Sci. World J.*, 2014, **2014,** 1–6.

30 B.P. Nabar, Z. Çelik-Butler, D.P. Butler, *Nano Energy.*, 2014, **10,** 71–82.

31 A.H. Danesh-Yazdi, N. Elvin, Y. Andreopoulos, *J. Sound Vib.*, 2014, 3092–3108.

32 D. Shen, J.H. Park, J. Ajitsaria, S.Y. Choe, H.C. Wikle, D.J. Kim, *J. Micromechanics Microengineering.*, 2008, **18,** 55017.

33 M.A. Halim, J.Y. Park, *Sensors Actuators. A Phys.*, 2014, **208,** 56–65.

34 A.E. Kubba, K. Jiang, *Sensors (Basel).*, 2013, **14,** 188–211.

35 L. Dhakar, H. Liu, F. E. H. Tay, C. Lee, *Sensors Actuators A. Phys.*, 2013, **199**, 344–352.

36 H. Liu, C. Lee, T. Kobayashi, C. J. Tay, C. Quan, *Sensors Actuators A. Phys.*, 2012, **186**, 242–248.

37 X. Jiang, Y. Li, J. Li, J. Wang, J. Yao, *J. Renewable Sus. Energy*, 2014, **6**, 1–16.

38 S Wei, H. Hu, S. He, *Smart Mater. Struct.*, 2013, **22**, 105020–105028.

39 E. Fernandes, S. Zarabi, H. Debéda, C. Lucat, *J. Phys.: Conf. Series*, 2016, **773,** 012109.

40 X. Ma, A. Wilson, C. D. Rahn, S. Trolier-mckinstry, *J. Vib. and Acous.*, 2016, **138,** 1–9.

41 M. H. Malakooti, B. A. Patterson, H. S. Hwang, H. A. Sodano, *Energy Environ. Sci.***,** 2016, **9**, 634–643.

42 Y. Zhuang, Z. Xu, F. Li, Z. Liao, W. Liu, *J. Alloys Compd.*, 2015, **629**, 113–117.

43 P. G. Kang, B. K. Yun, K. D. Sung, T. K. Lee, M. Lee, N. Lee, S. H. Oh, W. Jo, H. J. Seog, C. W. Ahn, I. W. Kim, J. H. Jung, *RSC Adv.*, 2014, **4**, 29799–29805.

44 Q. Xue, Z. Wang, H. Tian, Y. Huan, Q. Xie, Y. Yang, D. Xie, C. Li, Y. Shu, T. Ren, *AIP Advances*, 2015, **5**, 017102–017107.

45 C. K. Jeong, K. Park, J. Ryu, G. Hwang, K. J. Lee, *Adv. Funct. Mater.* **,** 2014, 1–10.

46 K. N. Kim, J. Chun, S. A. Chae, C. W. Ahn, I. W. Kim, S. Kim, Z. L. Wang, J. M. Baik, *Nano Energy*, 2015, **14**, 87–94.

47 R. Zhu, J. Jiang, Z. Wang, Z. Cheng, H. Kimura, *RSC Adv.*, 2016, **6**, 66451–66456.

CHAPTER IV

Elucidation of Piezoelectric and Semiconducting Properties of ZnO Nanorods and Cd Doped ZnO Nanorods

Highlights

- To overcome the drawback faced by ceramic based nanogenerator which are sensitive only to one form of energy (mechanical force), in this chapter piezoelectric energy harvesters were fabricated by adopting multifunctional material such as zinc oxide which has dual sensing capability i.e., mechanical and optical energies
- An asymmetrical effect on the functional (piezoelectric and semiconducting) properties of 1D-ZnO NRs by the doping of cadmium having a higher ionic radius (0.97 Å) was observed
- One fold reductions in the piezoelectric properties were determined due to Cd addition through successful fabrication of a nanogenerator, however enhancements in the semiconducting properties were observed with various wt% (0.1, 0.5, 1, 1.5 and 2 wt%) of Cd-doped into the ZnO NRs lattice
- Besides, a self-powered UV sensor (SPUV-S) was demonstrated using a parallel connection with the ZnO NRs based nanogenerator as an independent power source to drive the Cd-ZnO NRs UV sensor

Graphical Outline

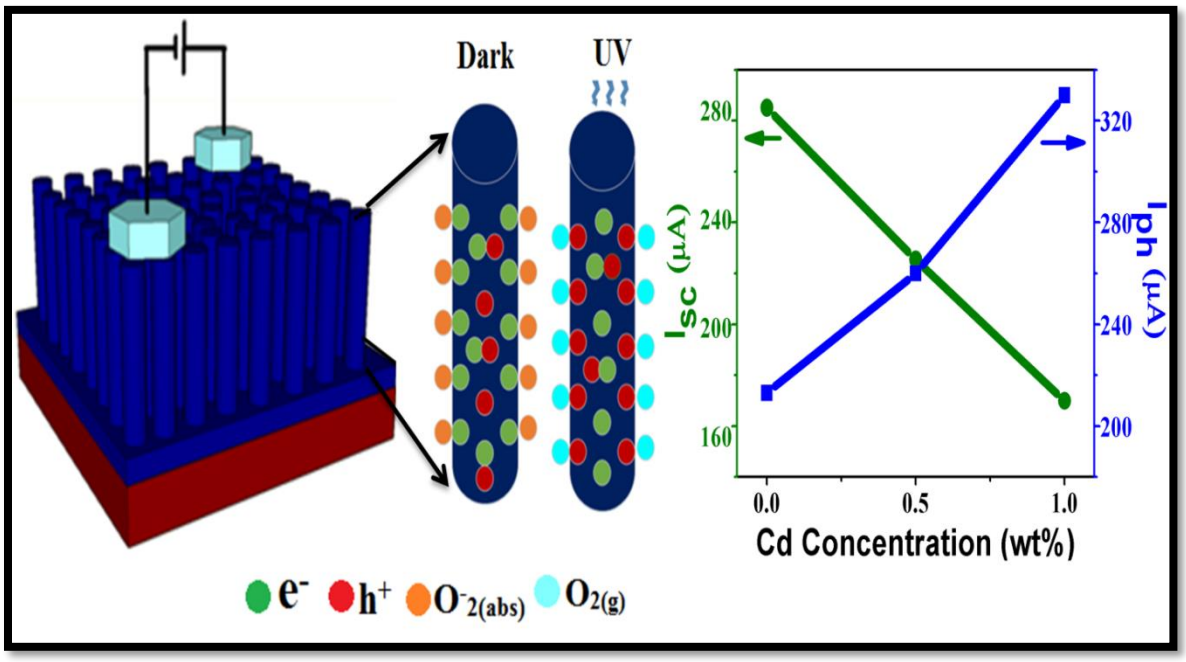

4.1 Introduction

The development of self-powered systems using energy harvesting technologies, such as piezoelectric[1], photoelectric[2], pyroelectric[3], electromagnetic[4], and triboelectric[1] devices, has attained great interest. Over the last decade, the piezoelectric nanogenerator (P-NG) technology has tremendously improved due to advances in the device structure[1], the growth of piezoelectric nanostructures on various flexible substrates[5-6], doping effects[7] and the use of composite devices (inorganic nanoparticles/polymer matrix)[8]. The P-NG can act as an independent power source to drive micro/nano devices, and in some cases, the P-NG itself acts as a self-powered device[9]. An extensive survey on the generation of power for these materials shows that the power density obtained using 1D or 2D-ZnO P-NGs lies between the $\mu W/cm^2$ to mW/cm^2 [10,11] range, and the power density of composite P-NGs lies between the mW/cm^2 to W/cm^2 range[12,13]. Currently, many researchers are focusing on the tuning of 1D-ZnO functional properties, such as piezoelectric, optical and semiconducting properties, for improving the sensor performance and energy generation. ZnO is a very versatile material, with an energy band gap of 3.2 eV, that exists in several nanostructure forms, such as nanowires, nanoflakes, nanotubes, nanoribbons and nanorods[14,15]. Here, the selection of a foreign atom or doping material for the ZnO nanostructures will play a key role in tuning its properties and controlling its suitability for the desired application[16,17]. Recent reports have demonstrated that the piezoelectric coefficient of ZnO can be improved using metals, such as Vanadium (V)[18], Magnesium (Mg)[19], Lithium (Li)[20], Palladium (Pd)[21], Iron (Fe)[22], Aluminum (Al)[23], Cobalt (Co)[24], Copper (Cu)[25], and Silver(Ag)[26], as doping materials, and non-metals, such as Sulfur (S)[27] and Phosphorus (P)[28], have induced ferroelectric behavior in ZnO-based P-NGs, resulting in high piezoelectric response. A few other reports have demonstrated that doping with group III elements can be used for different

applications as follows: Al-doped and In-doped ZnO thin films serve as an alternative to transparent conducting oxide (TCO), and Ga-doped ZnO (GZO) has been used in flat-panel displays and solar cells[29]. In addition to doping with transition metals (TM), rare earth elements, such as Erbium (Er)[30], Lanthanum (La)[31], and Europium (Eu)[32], have recently been widely used to improve the luminescence properties of 1D-ZnO nanomaterials. Despite the availability of many reports that focus specifically on the modification of a particular property, there is still a lack of studies that address the asymmetrical influence of the doping material on the semiconducting and piezoelectric nature of 1D-ZnO and its usefulness for electronic applications. This motivates us to develop and analyze the symmetric tuning of piezoelectric/semiconducting properties for hydrothermally grown 1D-ZnO nanorods (ZnO NRs) using Cadmium as the dopant. Cadmium chalcogenides are technically important class of material owing to its wide spread of utility in electronics and optoelectronic devices. For narrowing the band gaps, cadmium dopant would be an appropriate candidate which has a band gap of 2.38 eV[33]. Cd-ZnO NRs (with a Cd concentration of < 1 wt%) have a significantly improved UV response, and simultaneously, a reduced piezoelectric performance compared to undoped ZnO NRs. We also identified the Cd doping limit for ZnO, i.e., doping with ≤ 1 wt% of Cd^{2+} results in perfect diffusion of the dopant ions into the Zn^{2+} site and doping with > 1 wt% of Cd^{2+} creates a secondary or impurity phase in the ZnO NRs. The concentration of < 1 wt% Cd used is within the permissible exposure limit of 2.5 μg per cubic meter of air[34] and also within the level of median lethal dose of order Cd (890mg/kg^{-1}) < CdO (72mg/kg^{-1}) which is environmentally acceptable[35]. Here, vertically aligned (*c*-axis orientation) ZnO and Cd-ZnO NRs on glass substrates were used to investigate the semiconducting behavior. The reduction in the piezoelectric performance was analyzed using an ITO/Cd-ZnO NRs-PDMS/Al device. Finally,

we successfully developed a self-powered UV photo sensor (SPUV-S) using the parallel connection between two devices, e.g., Cd-ZnO NRs was used as a UV sensor and undoped ZnO NRs was used as a power source (nanogenerator). The proposed method is simple, cost effective and suitable for large scale fabrication.

4.2 Experimental

4.2.1 Synthesis of ZnO and Cd-ZnO NRs

The synthesis of ZnO NRs and cadmium-doped ZnO (Cd-ZnO) NRs were carried out using a hydrothermal method. To grow the ZnO NRs, a precursor solution was prepared using an equimolar ratio of zinc acetate dihydrate [$Zn(CH_3COO)_2.2H_2O$] as the starting material and hexamethylenetetramine (HMT) as a stabilizer, which also acts as the growth-directing agent, in an aqueous medium. A 0.2 M solution of [$Zn(CH_3COO)_2.2H_2O$] and HMT was poured into a container and stirred for 30 minutes at room temperature. Cd-ZnO NRs were synthesized by adding different concentrations (0.1, 0.5, 1, 1.5 and 2 wt%) of cadmium reagent, cadmium acetate dihydrate [$Cd(CH_3COO)_2 \cdot 2H_2O$] into the precursor solution. The pH value of the medium was adjusted to 10 by adding sodium hydroxide (NaOH), which in turn produces a clear solution. After 30 minutes of constant stirring, the as-synthesized precursor solution was transferred into a Teflon-lined stainless steel autoclave and soaked at a temperature of 150 °C for 24 h. A white precipitate was collected and washed several times using water and ethanol until it reached a neutral pH value. Next, the solution was dried overnight at 60 °C and calcinated at 500 °C for 1.5 h to improve the crystallinity of the NRs.

4.2.2 Growth mechanism of 1D-ZnO NRs

Figure 4.1 illustrates the growth mechanism of ZnO NRs formation. The precursor dissolved in aqeous medium forms $Zn(OH)_2$ which undergoes two types of reaction i) it reduces to a smaller extend forming ZnO that acts as a nucleation site ii) it form an ion-complex [Zn(OH)2-] which reacts with HMT to form ion-pair complex or polaron (NH_4^+-$[Zn(OH)_4]^{2-}$) due to electrostatic interaction. The presence of NH_4^+ leads to rod shape morphology by orienting the polaron on c-axis of ZnO crystal. Thus, HMT acts as a surfactant by regulating the growth direction of ZnO. Sodium acetate is formed as a by-product during the reaction between Zinc acetate dihydrate and NaOH[36]. Sodium acetate formed is water soluble and therefore it gets removed during the centrifugation and heat treatment (refer experimental section 3.2.1). Thus the final end product formed (ZnO NRs) were pure with no impurities or by-products residing in it.

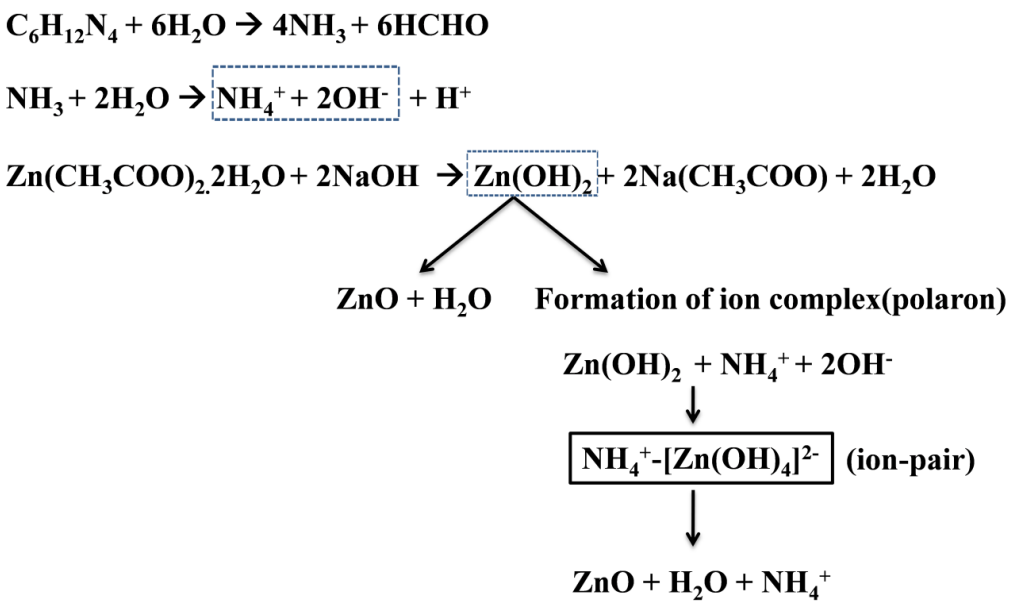

Figure 4.1 Growth mechanism of 1D-ZnO NRs.

4.2.3 Fabrication of randomly oriented Cd-doped ZnO NRs-based piezoelectric nanogenerator

The fabricated piezoelectric nanogenerator (P-NG) with a device area of 1.5 cm x 1.5 cm has the following four major parts: Cd-ZnO NRs (0, 0.1, 0.5 and 1 wt%) as the active material, Polydimethylsiloxane (PDMS) matrix as an insulating layer, ITO and Al foil as the bottom and top electrodes, and Kapton film as a protective frame from external environmental factors. Firstly, ITO-coated PET substrates were cleaned using ethanol, acetone and deionized (DI) water. Four devices were fabricated by depositing different active materials on the ITO/PET substrates, such as undoped ZnO NRs, 0.1 wt% Cd-ZnO NRs, 0.5 wt% Cd-ZnO NRs and 1 wt% Cd-ZnO NRs, which are designated as P-NG, P-NG1, P-NG2, and P-NG3, respectively. The as-synthesized NRs were sonicated, dispersed in 1 ml of ethanol, spin coated onto the cleaned PET/ITO substrates at 2500 rpm for 30 seconds and treated at 65 °C for 10 minutes. This process was repeated five times to ensure good uniformity and to achieve a substrate that was densely covered with the active material. A thin layer of fine PDMS (10:1) was spin coated on the NRs/ITO/PET substrate at 5000 rpm for 60 seconds and cured overnight at 80 °C in a hot oven. A low-cost flexible Al foil (15 μm) was attached on top of the PDMS/NRs/ITO/PET substrate to serve as atop electrode. Two copper conducting leads were glued with silver paste on the two electrodes (ITO & Al) and used for measuring the performance of the P-NGs. Finally, the flexible P-NGs, with a PET/ITO/NRs/PDMS/Al device structure, were covered with Kapton film to ensure their protection from environmental changes and external damages. To improve the polarization, all P-NG devices were electrically poled by applying an electric field of 4 kV for 24 h at room temperature; the dipoles were preferentially oriented with respect to the direction of

the applied electric field. **Figure 4.2** illustrates the schematic view of synthesis and fabrication processes.

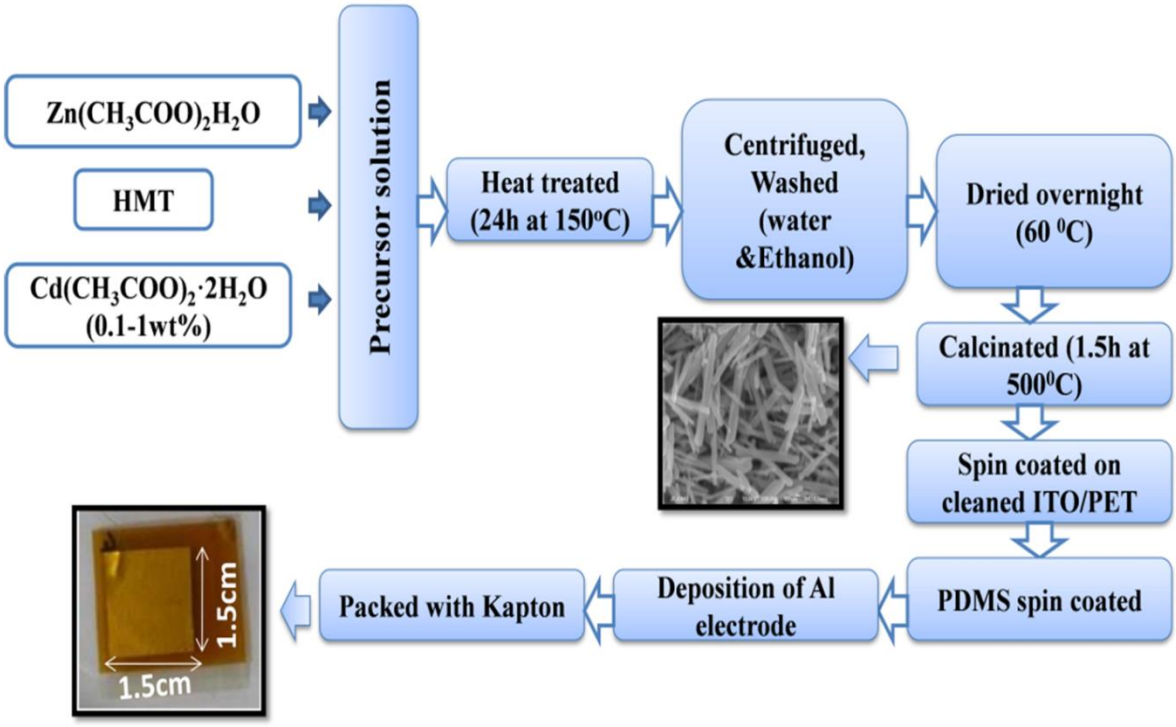

Figure 4.2 Schematic representation of fabrication process of P-NG devices.

4.2.4 Fabrication of vertically aligned Cd-doped ZnO NRs array-based UV-sensor (UV-S)

The glass substrates were initially cleaned by successive sonication in ethanol, acetone and DI water. To prepare the seed layer solution, zinc acetate dihydrate (0.5 M) was dissolved in aqueous medium and stirred for 2 h at 60 °C. The solubility of the precursor salt was improved by adding 1 M of monoethanolamine (C_2H_7NO, MEA), which acts as a stabilizer. The seed layer sol was aged for 24 h, and then it was spin coated on pre-cleaned glass substrates at 2500 rpm for 30 seconds followed by a heat treatment for 10 minutes at 200 °C. This coating process was repeated three times to obtain uniformity and to achieve the desired thickness of the seed layer. Then, the substrates were annealed for 1 h at 600 °C. ZnO NRs were hydrothermally grown at 90

°C for 6 h by immersing the seed-layered glass substrates into the nutrient solution consisting of equal moles of $Zn(CH_3COO)_2.2H_2O$ and HMT (0.2 M), which was adjusted to a pH of 10. For different concentrations of Cd-ZnO NRs, the same procedure was repeated with the addition of $Cd(CH_3COO)_2 \cdot 2H_2O$ into the nutrient solution, where the Cd to Zn precursor weight ratio was maintained at 0.1 wt%, 0.5 wt % and 1 wt%. After the reaction was completed, the glass substrates were rinsed with DI water and dried in an oven at 60 °C. Two copper wires, within a defined area of 0.5 cm x 0.5 cm, were attached using constant amount of Ag paste for the electrical measurements; this completed the fabrication of UV-S devices. The distance between the electrodes was 0.2 cm. **Figure 4.3** represents the synthesis and fabrication processes involved in UV-sensor devices.

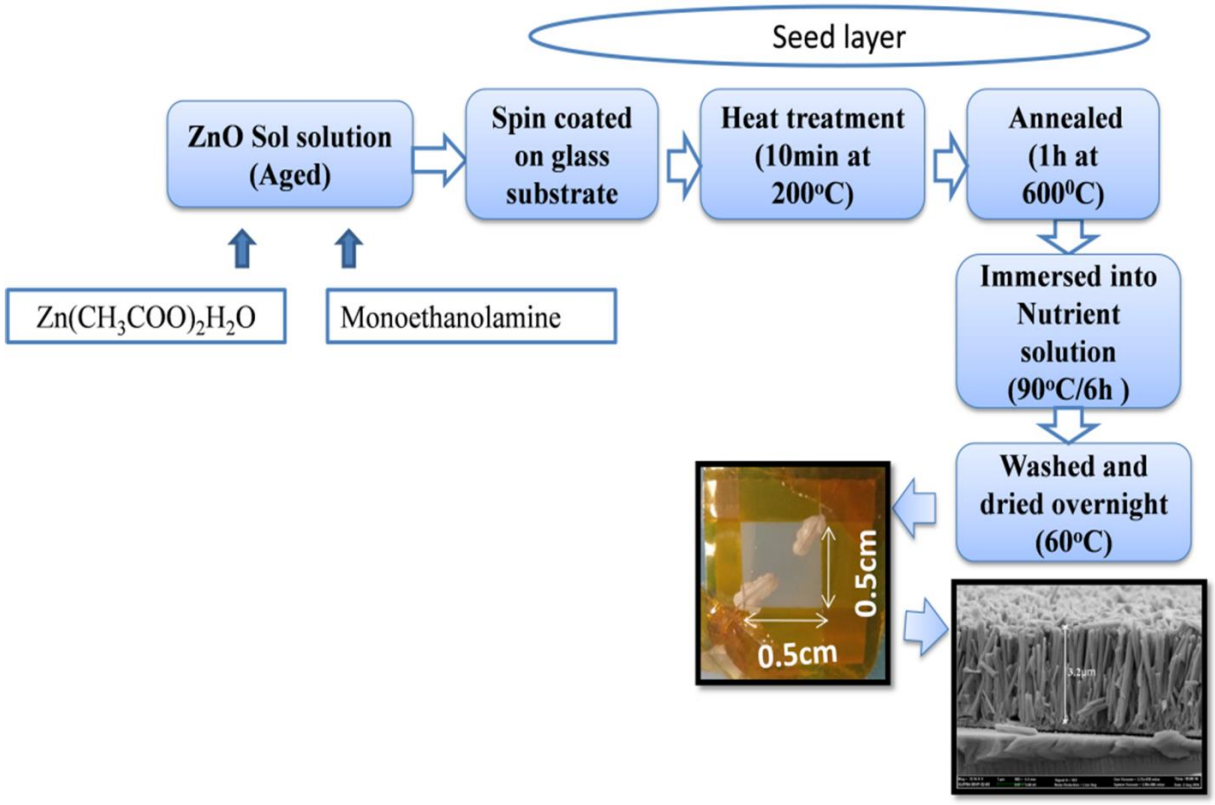

Figure 4.3 Experimental flow of UV-Sensor fabrication process.

4.2.5 Measurement system

The morphological structure, particle size distribution and layer thickness of ZnO and Cd-ZnO NRs were analyzed by field-emission scanning electron microscopy (FE-SEM, Zeiss Supra-55vp, Germany and JEOL JSM-6700F, Japan). The phase composition and the lattice strain induced by the Cd dopant in as-prepared ZnO NRs were determined by an X-ray diffractometer (XRD, Rigaku, Japan) operated at 40 kV and a current of 40mA using Cu-Kα radiation (λ=1.5406 Å) at room temperature (with a 2θ range from 20º to 80º). The absorbance spectrum in the range of 200-800 nm was recorded with a UV-Vis spectrophotometer (Cary300, Varian system, USA). Raman spectra were recorded from 200-800 cm^{-1} at an excitation wavelength of 514 nm using high-throughput single-stage spectrometer (LabRAM HR Evolution; Horiba, Japan). Elemental analysis of the samples was carried out using X-ray photoelectron spectroscopy (XPS, Theta Probe AR-XPS System). Piezoelectric measurements of P-NG devices were carried out using the mechanical force triggered by a linear motor system (LinMot-HF01-37) operated with an acceleration of 1 m/s^2, and the results were recorded using a high-impedance electrometer (6514) and a low-noise current pre-amplifier (SR570). The photo-responsive I-V measurements were recorded using a semiconductor device parameter analyzer (Agilent-B1500A) with the help of a Prizmatix multi-wavelength LED light source operated at wavelengths of 365 nm, 405 nm and 535 nm at different intensities.

4.3 Results and discussions

4.3.1 Structural and surface morphology analysis of Cd-ZnO NRs

The XRD patterns of Cd-doped crystalline ZnO NRs with Cd = 0, 0.1, 0.5 and 1 wt% are shown in **Figure 4.4**(a).

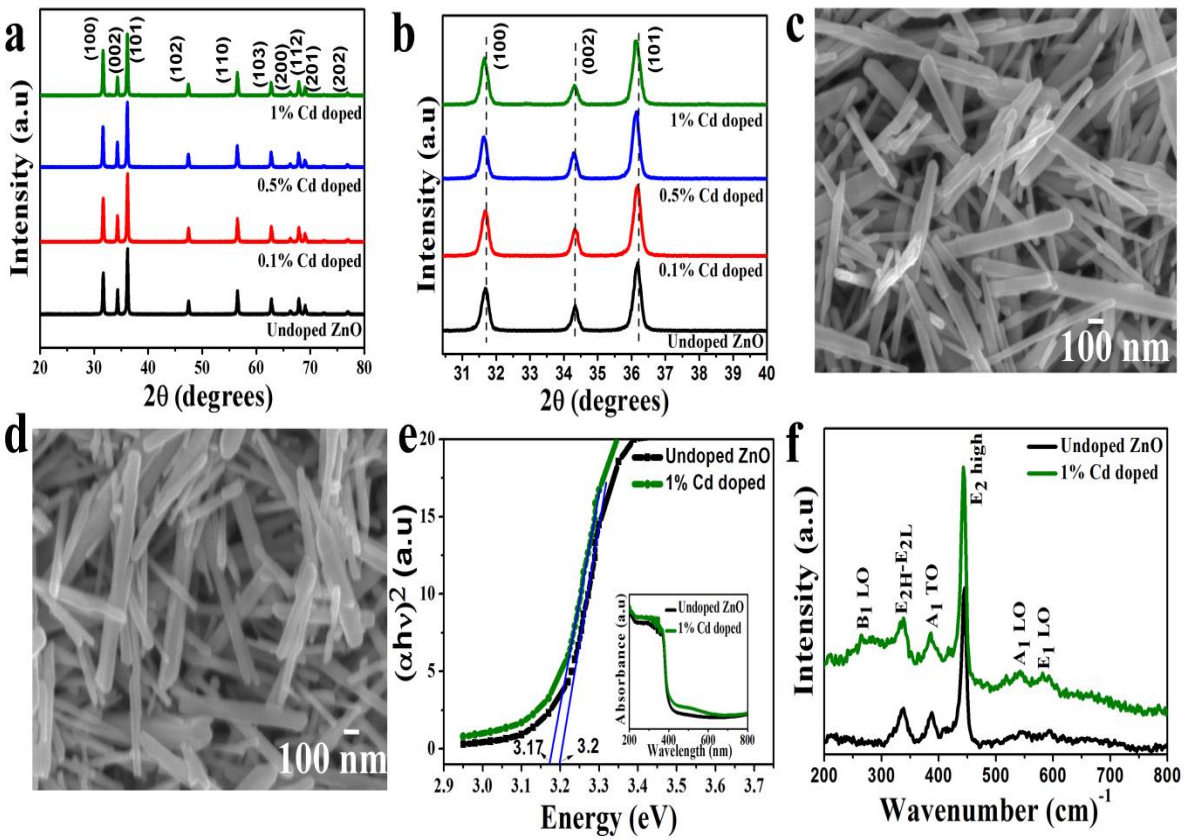

Figure 4.4 (a) XRD patterns of pure and Cd-doped ZnO NRs. **(b)** Enlarged portion showing shifts in the peaks. FE-SEM images of as-synthesized. **(c)** Pure ZnO NRs. **(d)** 1 wt% Cd-doped ZnO NRs. **(e)** The Tauc plot analysis from the UV-Vis absorption spectra (inset) of pure and 1 wt% Cd-doped ZnO NRs. **(f)** Raman spectra of pure and Cd-doped ZnO NRs.

All the peaks are indexed to the wurtzite structure of ZnO (space group $P6_3mc$) and the patterns exhibit a strong (101) peak with a *c*-axis orientation[37]. There are no secondary phases or clusters observed for the doping concentrations (0.1-1 wt%) of Cd, which indicates that Cd^{2+} ions are perfectly dissolved in the ZnO lattice. Figure 4.3(b) shows possible peak shifts in the (100), (002), (101) peaks towards lower angles, i.e., from 31.67º, 34.33º, 36.16º to 31.65º, 34.31º, 36.14º, respectively, as the Cd concentration increased. This is due to the substitution of the higher ionic radius of Cd^{2+} (0.97 Å) in Zn^{2+} (0.74 Å) ionic sites. Changes in the diffraction

peaks towards lower angles indicate that Cd is incorporated into the wurtzite lattice also confirming the increase in wt% of Cd in 1D-ZnO NRs. In the case of higher Cd doping concentrations of 1.5 wt% and 2 wt%, the strongest reflection of the cubic Cd phase appeared with low intensity (**Figure 4.5**), which indicates phase separation due to the formation of CdO.

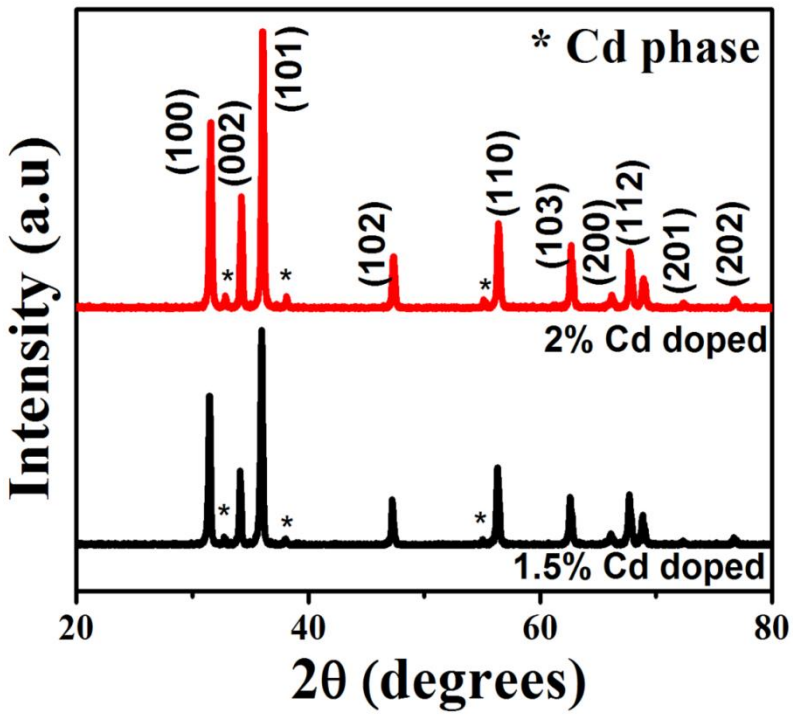

Figure 4.5 XRD patterns of 1.5 wt % and 2 wt % Cd doped ZnO NRs.

The expansion of the unit cell as a result of Cd^{2+} substitution creates an internal strain of approximately 0.28 % on the grown NRs, which reduces the crystallite size from 46.5 nm to 43.14 nm. The calculated lattice parameters are a=b=3.25 Å, and c=5.20 Å (undoped ZnO NRs), and a=b=3.26 Å, and c=5.22 Å (1 wt% Cd doped ZnO NRs). The c/a ratio confirms the perfect hexagonal wurtzite structure of the NRs. The increase in the lattice parameters is due to the expansion of the unit cell volume, which is an effect of the ionic radii mismatch between Zn^{2+} and Cd^{2+}.

Low- and high-magnification FESEM images of undoped ZnO NRs and synthesized 1 wt% Cd-ZnO NRs are shown in Figure 4.3(c) and 4.1(d). The images reveal that as-prepared NRs are uniformly grown, and they exhibit a good rod-shaped morphology after the hydrothermal treatment. The diameter of NRs ranges between 100 – 150 nm and the length of the NRs is approximately 1 µm. It should be noted that the controlled concentration of Cd doping (< 1 wt%) does not hinder the morphological structure of NRs, whereas phase separation occurs as the Cd concentration increases (> 1 wt%), which leads to deterioration of NRs due to more replacement of smaller Zn^{2+} ions (0.74 Å) by larger Cd^{2+} ions (0.97Å) (**Figure 4.6**).

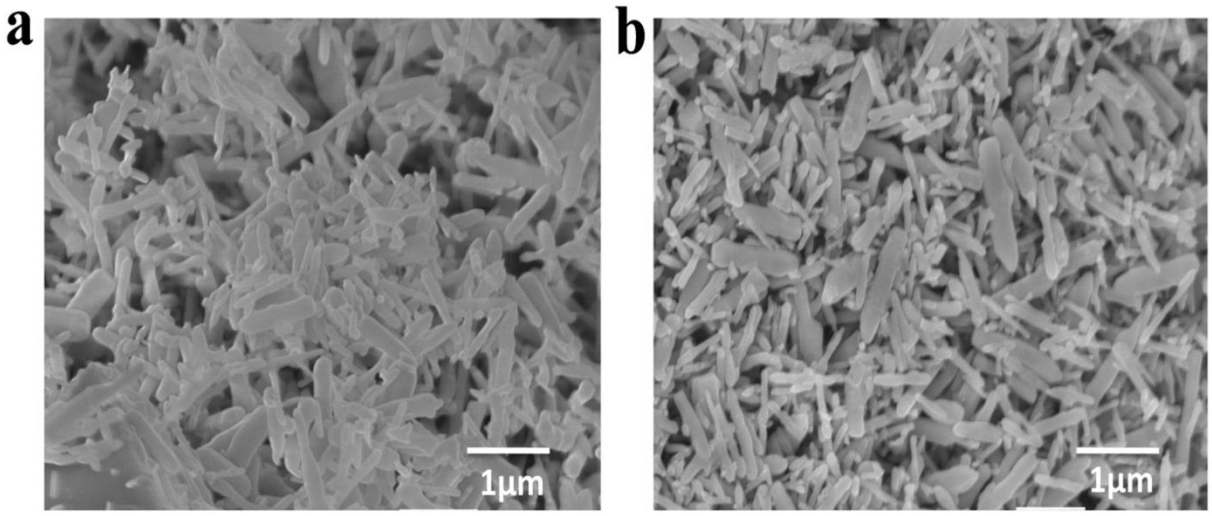

Figure 4.6 FESEM images showing the deterioration in ZnO NRs when doped with higher Cd concentration. **(a)** 1.5 wt %. **(b)** 2 wt %.

Figure 4.7 shows the seed layered growth of hexagonal wurtzite NRs, which are vertically well aligned and densely packed on the glass substrates along the homogeneous growth direction with a layer thickness of ~ 3 µm (Figure 4.11(d)).

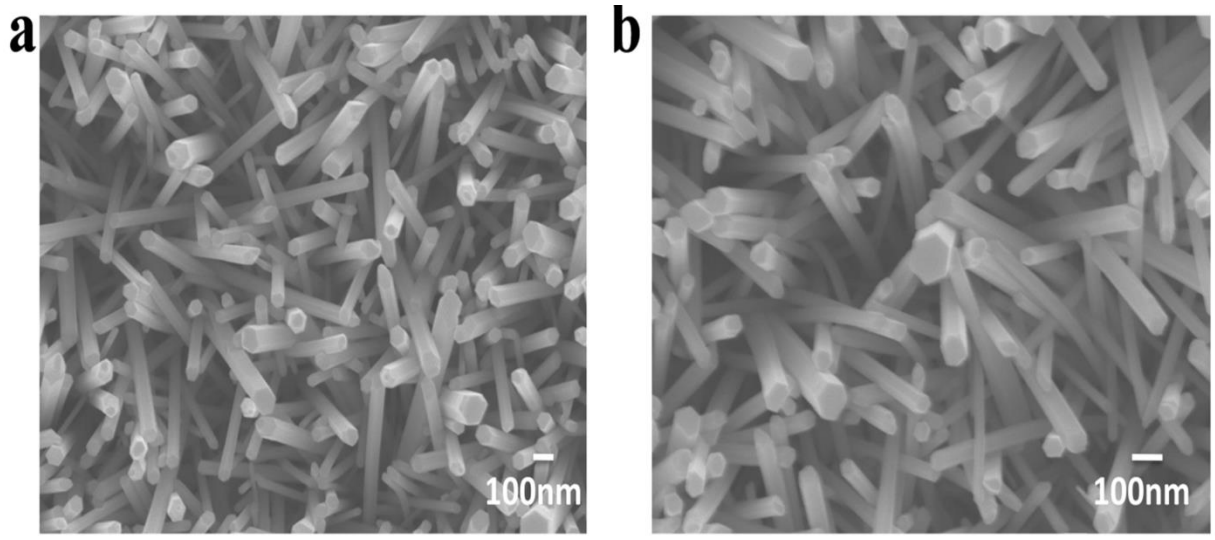

Figure 4.7 Top view of FESEM images of vertically grown **(a)** ZnO NRs. **(b)** 1 wt % Cd ZnO NRs on glass substrate.

The absorbance spectrum was recorded using the UV–Vis spectrometer to obtain the optical energy band gap (E_g) from the Tauc plot. The variation of the absorption coefficient (α) with the photon energy ($h\nu$) is given by the following equation:

$$(\alpha h\nu)^2 = C(h\nu - E_g) \quad \text{- (1)}$$

where C is a constant, h is the Planck's constant, and ν is the photon frequency. Figure 4.4(e) shows the absorbance spectra and Tauc plots of undoped ZnO NRs and 1 wt% Cd-doped ZnO NRs. Extrapolating the linear region of the $(\alpha h\nu)^2$ vs. ($h\nu$) plot on the x-axis gives the value of the optical band gap, (E_g). The absorption edge of the ZnO NRs clearly shifts to the red region due to Cd substitution, which results in a band gap reduction from 3.2 to 3.17 eV. This is because Cd doping increases the contribution of Cd-5s states in the conduction band, which have lower energy than Zn-4s states. The predominant existence of the Zn-4s state is altered by Cd-5s, which in turn leads to the reduction in the band gap of Cd-ZnO NRs[38]. The red shift of the optical band gap after Cd doping can also be attributed to the Moss-Burstein effect where doped

elements cause a shift in the Fermi energy level as a result of electrons generated by oxygen vacancies. The band gap tuning is confirmed by both the shift in the (002) XRD peaks and the red shift in the UV-Vis spectrum.

Further vibration properties of undoped and Cd-doped ZnO NRs were analyzed using Raman spectroscopy with excitation at a wavelength of 514 nm. From Figure 4.4(f), strong peaks are observed for undoped ZnO NRs at 386 cm^{-1}, 445 cm^{-1}, and 340 cm^{-1}. The peak at 386cm^{-1} is assigned to the A_1(TO) mode, the peak at 445 cm^{-1} corresponds to the optical photon E_2(high) mode, and the peak at 340 cm^{-1} (E_{2H}-E_{2L}) represents the secondary multi-photon scattering mode, which appears due to dimensional confinement (1D-NRs) of the synthesized ZnO. A low intensity peak that contributes to the E_1(LO) mode exists at 583 cm^{-1}; it represents the defect sites in ZnO NRs[38,39].

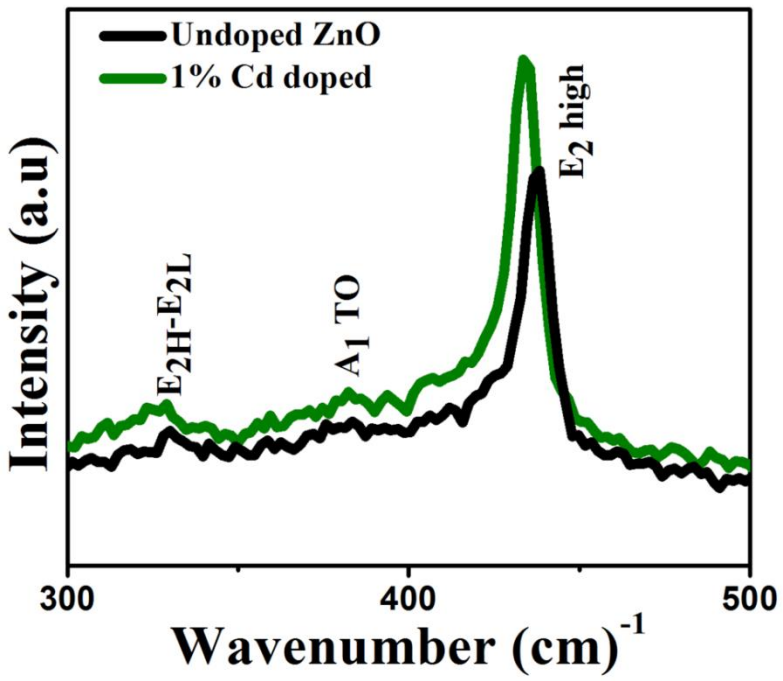

Figure 4.7 (c) Raman spectra of undoped and 1 wt% Cd-doped ZnO NRs grown vertically.

With the addition of Cd dopants, the peak at 583 cm^{-1} broadens along with a shift of the E_2(high) mode to 443 cm^{-1}, which is associated with the replacement of Zn^{2+} ions by larger size

Cd^{2+} ions; this subsequently induces crystallite stress and creates more defect zones, such as oxygen vacancies (V_o) and zinc interstitials (Zn_i). Similar effect is observed for vertically grown undoped and 1 wt% Cd doped ZnO NRs (Figure 4.7(c)). The elemental composition and chemical states due to Cd doping in the ZnO matrix are identified by determining the line energies (binding energies) in the XPS spectra. **Figure 4.8**(a) and 4.8(b) shows the peaks of C, O, Zn and Cd in the XPS spectra of undoped ZnO NRs and 1 wt% Cd-ZnO NRs.

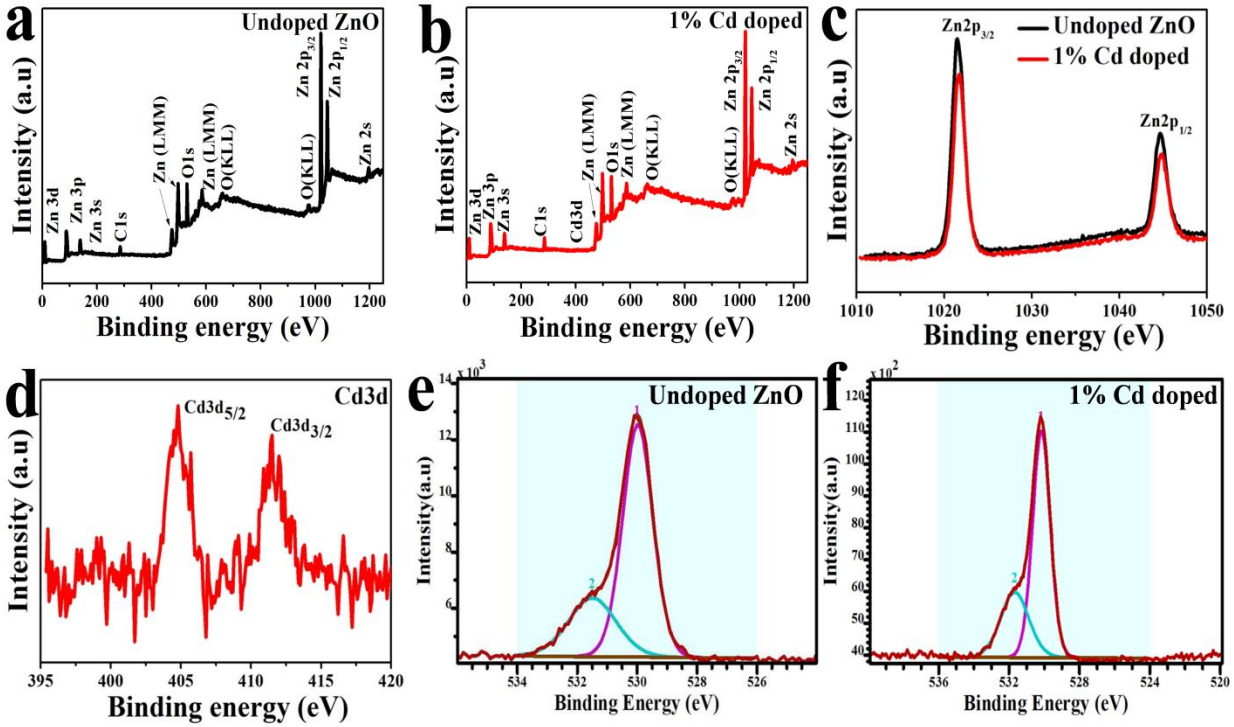

Figure 4.8 XPS spectrum for Cd, Zn and O distribution **(a)** Spectra of undoped ZnO NRs. **(b)** Spectra of 1 wt% Cd-ZnO NRs. **(c)** Zn region of undoped ZnO NRs and 1 wt% Cd-doped ZnO NRs. **(d)** Cd region ($3d_{5/2}$ and $3d_{3/2}$) of 1 wt% Cd-ZnO NRs. Gaussian-fitted O region for **(e)** undoped ZnO NRs. **(f)** 1 wt% Cd-ZnO NRs.

The elemental results show that there is no appearance of additional peaks in the final end product. This confirms that the synthesized ZnO NRs are highly pure and free from other impurities. The presence of elemental carbon was identified from the C1s peak at 284.6 eV,

which appears due to the exposure of materials in the environment. The appearance of two strong peaks at 1021.5 eV and 1044.6 eV represents the formation of Zn−O bonds[40] (Figure 4.8(c)). Upon addition of 1 wt% of Cd dopant, the Zn $2p_{3/2}$ peak shifted from 1021.5 eV to 1021.8 eV and Zn $2p_{1/2}$ peak shifted to higher binding energy from 1044.6 eV to 1044.9 eV. The increased binding energy (0.3 eV) is due to the interaction between electronic states of Zn^{2+} by Cd^{2+} ions. Figure 4.8(d) shows the high-resolution Cd 3d XPS spectra of 1 wt% Cd-ZnO NRs. The peaks at the binding energy of 404.8 eV and 411.5 eV are assigned to Cd 3d, and they can be attributed to Cd $3d_{5/2}$ and Cd $3d_{3/2}$, respectively[41,42]. Figure 4.8(e) and 4.8(f) presents the analysis of Gaussian fitting curves of the O1s spectra of undoped ZnO and 1 wt% Cd-doped ZnO NRs. The O1s peak at 529.9 eV is attributed to O_2^- ions on the wurtzite structure of the Zn^{2+} ion array, which are surrounded by Zn, while the higher binding energy O_2 species, centered at 531 eV, belong to the oxygen-deficient region caused by the oxygen vacancies[42,38]. The Cd-doped ZnO NRs have more donor content (such as oxygen vacancies) than the undoped ZnO[38]. The Cd content of as-grown ZnO NRs is estimated from the integrated peak areas to be approximately 0.38 atomic %, is indicative of a larger donor level compared to undoped ZnO NRs.

4.3.2 Significance of Cd doping in 1D ZnO NRs

4.3.2.1 Degradation of piezoelectric response

The P-NG (1.5 cm x 1.5 cm) made using spin coated NRs on a bottom PET/ITO electrode and a low-cost Al foil/Kapton top electrode is shown schematically in **Figure 4.9**(a).

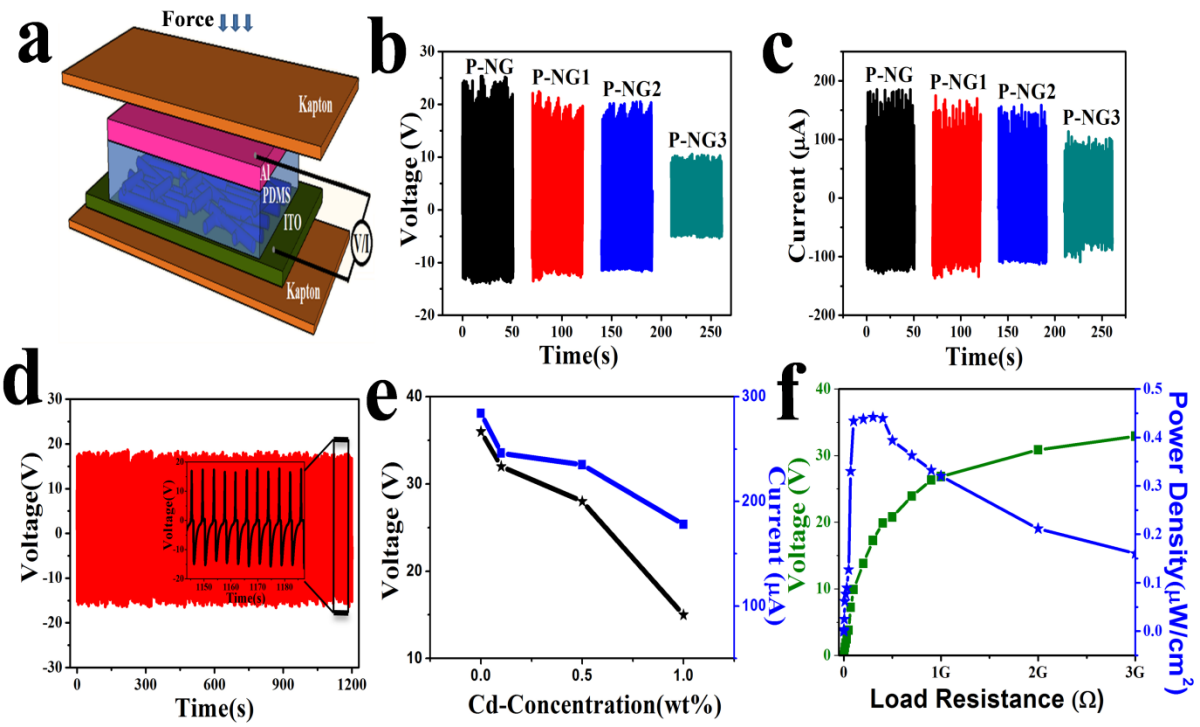

Figure 4.9 (a) Schematic diagram of the P-NG device. **(b)** Open-circuit voltage. **(c)** Short-circuit current of P-NG with varied Cd wt% under a 2 N load. **(d)** Stability analysis of P-NG for a time interval of 1200 seconds (under a 2 N load). **(e)** Electrical voltage and current as a function of Cd concentration. **(f)** Load resistance analysis and power density evaluation for P-NG device under a constant load of 2 N.

A thin layer of PDMS was used between the top Al electrode and the top of the NRs to prevent electrical breakdown during poling, and it also provides flexibility and reliability to the P-NG under excessive mechanical force. Cross-sectional FESEM analysis reveals that the fabricated PNG devices are approximately 332 μm in thickness. The spin coated ZnO/PDMS layer together form a thickness of ≈ 36 μm (**Figure 4.10**). Similarly, we fabricated Cd-doped ZnO NRs-based devices with different Cd concentrations of 0.1, 0.5 and 1 wt% in the ZnO NRs, which are referred to as P-NG1, P-NG2 and P-NG3, respectively. The electrical response (V_{OC}, I_{SC}) of the poled P-NG device under a constant mechanical load 2 N (obtained by a linear motor

shaft mass (2 Kg) moving with an acceleration of 1 m/s^2) is shown in Figure 4.9(b) and 4.9(c). Initially, the P-NG device generates a maximum output, e.g., $V_{OC} \approx 36$ V and $I_{SC} \approx 286$ μA, for 2 N loads. This output is high and comparable to that in many published reports[11,16,43,44]. Figure 4.9(d) shows the durability test, which proves that the P-NG is capable of producing a stable output performance during a 1200 second time interval under a load of 2 N. Next, we obtained the electrical response of Cd-doped ZnO NRs-based devices (0.1, 0.5 and 1 wt% of Cd in the ZnO NRs) and the corresponding output shows a decreasing trend with respect to the Cd concentration, as observed in Figure 4.9(b) and 4.9(c). The Cd dopant screens the piezoelectric output potential by producing excessive holes and defect sites, which results in a gradual decrease in the performance of the P-NG. The results show that the ferroelectric property is still induced in the Cd-doped P-NG; however, the dopant Cd element is unsuitable for improving the piezoelectric output. To further investigate the optimum output power density of the P-NG device (without doping), we conducted electrical measurements for various load resistance values ranging from 10 kΩ to 3 GΩ. Here, the output voltage increases with respect to the load resistance value for a constant load of 2 N; in contrast, the output current decreases with respect to the load resistance, as shown in Figure 4.9(f). The maximum power density obtained is approximately 0.41 μW/cm^2 at 300 MΩ; it can be evaluated by the following equation:

$$P_A = \frac{V^2}{R \times A} \qquad -(2)$$

where R is the load resistance across the P-NG, A is the surface area and V is the electrical output voltage obtained.

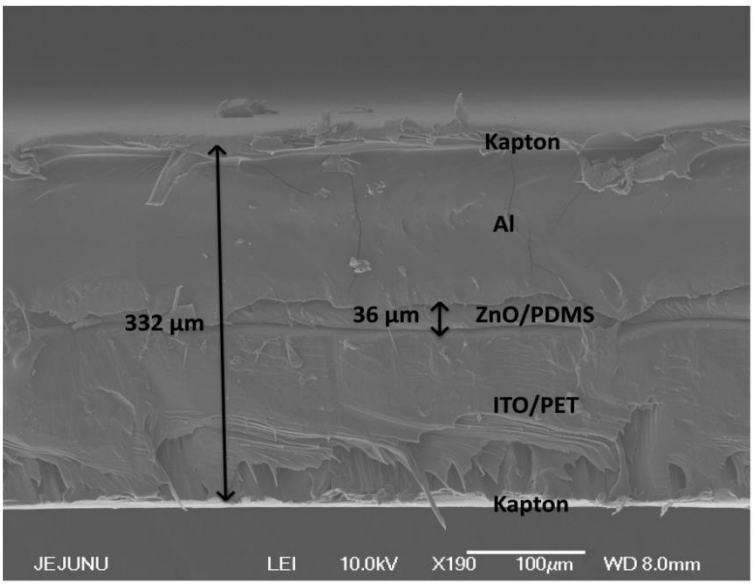

Figure 4.10 Cross-sectional FESEM analysis of fabricated PNG device.

By introducing a very small amount of Cd, the crystallographic alignment of the unit cell of the ZnO crystal is distorted. When the Cd doping concentration is further increased, there is a high loss in the symmetry of the unit cell, which results in a reduction in the piezoelectric response. This may be attributed to the difference in the ionic radii, where the ionic radius of Cd^{2+} (0.97 Å) is larger than that of Zn^{2+} (0.74 Å). Therefore, the lattice parameter (c) is increased when Cd^{2+} substitutes Zn^{2+}, which leads to deformation in the crystallinity and *c*-axis orientation of ZnO NRs. In addition to the induced effect of stress by the Cd atoms, the electromechanical response of the P-NG depends on the spontaneous polarization (P_s)[45], which is given by the following equation:

$$d_{33} = 2Q_{eff}.\varepsilon_0.\varepsilon_r.P_s \qquad -(3)$$

where Q_{eff} is the effective electrostriction coefficient, ε_0 is the permittivity of free space and ε_r represents the relative permittivity. From this equation, we find that the piezoelectric response

(d_{33}) in ferroelectrics such as ZnO is directly dependent on P_s. The polarization of the domain is mainly governed by the rotation and bending of non-collinear bonds formed between transition metals and oxygen along the *c*-axis[45] (here, the transition metals are Zn and Cd). In Cd-doped ZnO NRs, few of Zn^{2+} ions are replaced by Cd^{2+} ions which induces a strain due to the difference in ionic radii between Cd^{2+} (0.97 Å) and Zn^{2+} (0.74 Å). In order to balance the strain, Cd^{2+} move towards the existing point defect sites (V_o) in ZnO crystals, thereby increasing the bond between Cd and O[46]. The volume of ZnO NRs unit cell system gets expanded due to the elongation in Cd-O bond length[47]. This increase in bond length restricts the switching of Cd^{2+}-O1 towards the *c*-axis. Even under an applied electric field, the rotation of the Cd^{2+}-O1 bond is difficult compared to that of the Zn^{2+}-O1 bond, which reduces the switching polarization and contributes to a poor piezoelectric co-efficient (d_{33}). As the length of the bond corresponds parallel to the c-axis orientation in wurtzite crystals, we determined the bond length (b) with its relationship between internal parameter (u=3/8) and lattice parameter (c) given by the following equation[48, 49],

$$b = \frac{3}{8}c \qquad -(4)$$

The bond length of Cd^{2+}-O1 is calculated to be 1.957 Å which is higher than Zn^{2+}-O1 (1.950 Å). This has credited for the decrease in the electromechanical response of P-NG1, P-NG2 and P-NG3.

4.3.2.2 Enhancement of UV-photo response

To investigate the electrical performance, Metal (M)-Semiconductor (S)-Metal (M) type UV-Sensors (UV-S) were developed using 0, 0.5 and 1 wt% Cd-doped ZnO NRs; the device structure is schematically shown in **Figure 4.11**(a). The UV-S performance was analyzed under different environments, including a dark environment and under various light sources with wavelengths of 365 nm, 405 nm and 535 nm. An Ohmic electrical contact was obtained for UV-

S (ZnO NRs), UV-S0.5 (0.5 wt% of Cd) and UV-S1 (1 wt% of Cd), which can be analyzed by the dark currents (I_D) of both devices under an applied dc bias voltage of 10 V. Since the work function of Ag is 4.26 eV which is less than that of ZnO (5.2 eV), the barrier at the interface of metal-semiconductor-metal (M-S-M) is reduced; thus, the contact between ZnO and Ag is likely to be Ohmic[50]. Also Cd doping enhances the n-type charge carrier concentration in ZnO NRs and reduces the barrier height (Φ_B) for the charge carriers to tunnel through the M-S-M interface resulting in the formation of ohmic contacts[51].

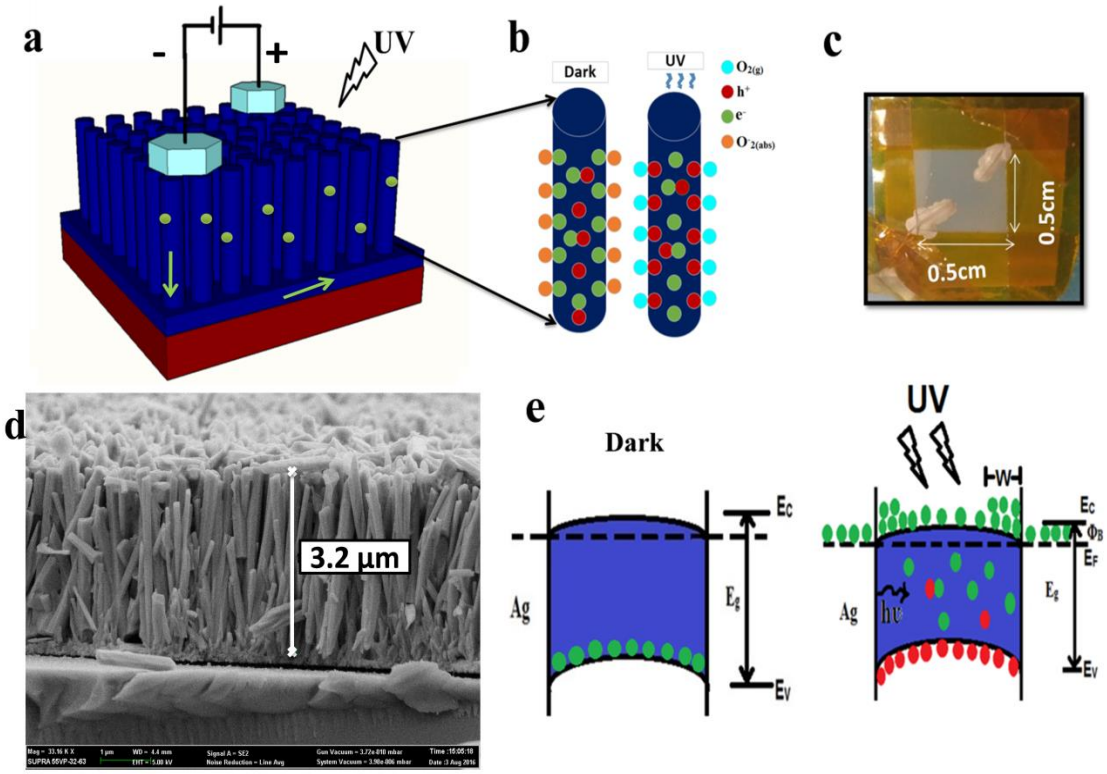

Figure 4.11 (a) Schematic illustration of the UV-Sensor device. **(b)** Transport route for photogenerated electron and hole in the dark and under UV-light. **(c)** Optical photograph of the UV-S device with an area of 0.5 cm x 0.5 cm. **(d)** Cross-sectional FE-SEM image of vertically grown ZnO NRs on seeded glass substrate. **(e)** Schematic energy level diagram of the UV-S with ZnO NRs in the dark and under UV-illumination.

In **Figure 4.12**(a), the dark current (I_D) decreases gradually with increase in Cd concentration (UV-S1 (2 µA) < UV-S0.5 (2.5 µA) < UV-S (2.9 µA)) which shows that Cd is been effectively doped into the lattice of ZnO NRs. This confirms that more oxygen vacancy sites are created by Cd doping, which favored the adsorption of more oxygen molecules on the surface of Cd-ZnO NRs[52]. This in turn reduced the number of free charge carriers that contribute to the generation of I_D. During UV light source (8 mW/cm^2), the photocurrent response of devices varies proportionally with respect to the Cd-doping concentrations.

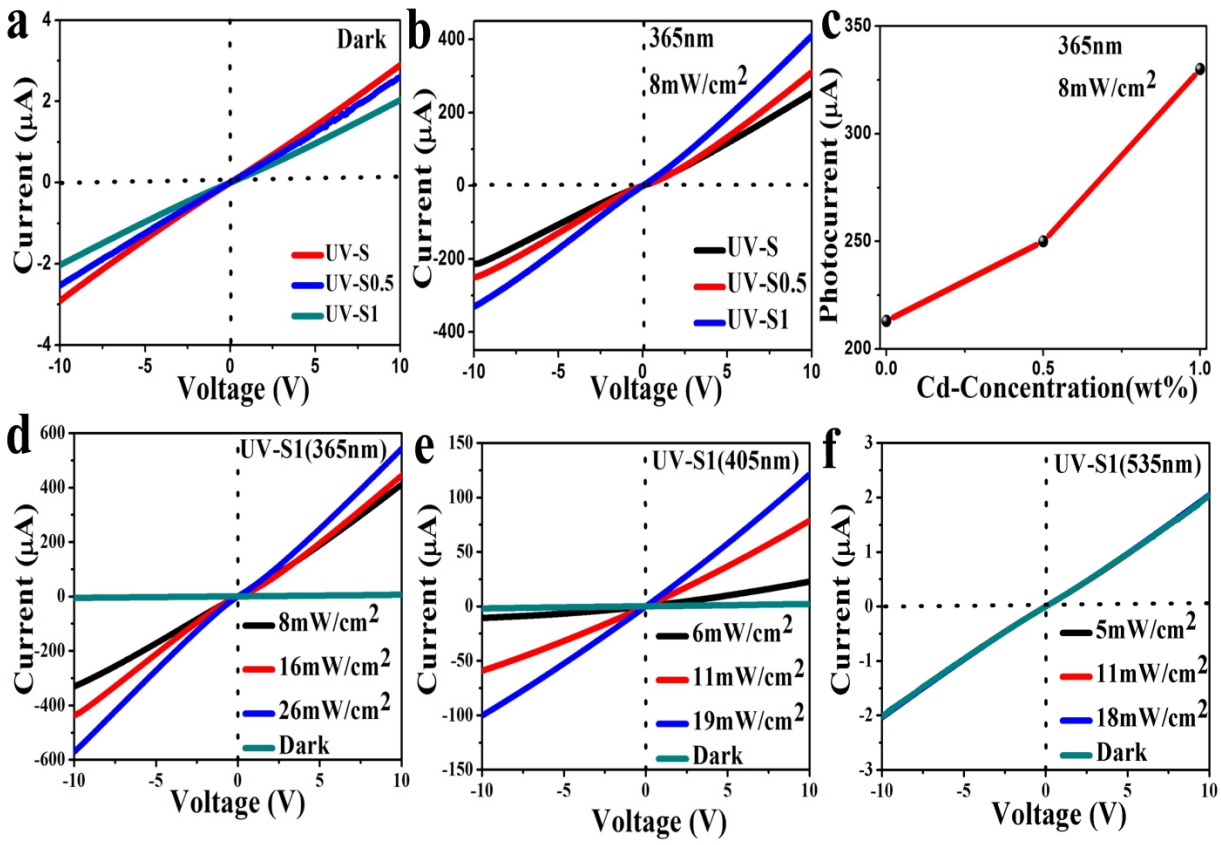

Figure 4.12 Electrical characterization of the UV-Sensor devices under UV-illumination. I-V measurements of undoped, 0.5 wt% and 1 wt% Cd-doped ZnO NRs **(a)** in the dark and **(b)** under UV illumination. **(c)** Photocurrent response as a function of Cd-concentration. I-V measurements of 1 wt% Cd-doped ZnO NRs at various wavelengths and illumination intensities **(d)** 365 nm, **(e)** 405 nm and **(f)** 535 nm.

Figure 4.12(b) shows the photo response spectra of UV-S under UV illumination at a wavelength of 365 nm and with an optical light intensity of 8mW/cm^2. The photocurrent of UV-S is 213 µA, which steadily increases to 250 µA as the Cd concentration increases to 0.5 wt% and reaches 330 µA for 1 wt% Cd-ZnO NRs (UV-S1). The dependence of photocurrent response as a function of Cd presence in the vertically grown ZnO NRs is illustrated in Figure 4.12(c). A one fold increment of the photocurrent (I_{ph}) response was observed for UV-S1, which makes it more suitable for fabricating high performance photodetectors. The dependence of the light intensity on the photocurrent of UV-S was analyzed by varying the intensity of the light source (8, 16 and 27 mW/cm^2) at 365 nm. The increase in the light intensity across UV-S1 will increase the I_{ph} response due to the generation of more photogenerated charge carriers in UV-S1. This clearly demonstrates that the as-fabricated sensor is highly sensitive for various light intensities of the 365 nm UV-source (Figure 4.12(d)). Then, the selectivity of UV-S1 was analyzed by investigating its performance under 405 nm (blue) and 535 nm (green) excitation light sources at different light intensities, and the results are summarized in Figure 4.12(e) and 4.12(f).The results indicate UV-S1 is completely inactive for the source with a wavelength of 535 nm, but a linear I_{ph} response was observed for UV-S1 under the 405 nm source for various light intensities. This I_{ph} response is much lower than the I_{ph} response of UV-S1 under the 365 nm source. A similar analysis was performed for UV-S, UV-S0.5 and its corresponding results are given in **Figure 4.13**. The behavior of UV-S1 is attributed to the difference in the photon energy of various excitation sources. This illustrates that the UV-S1 is highly selective to the wavelength of 365 nm, and further analyses are carried out at this specific wavelength. The performance of this sensor is estimated by its photo-responsivity (R_λ) at a specific wavelength, which is defined as follows:

$$R_\lambda = \frac{I_{ph} - I_D}{P_L \times S} \qquad - (5)$$

where I_{ph} and I_D are currents when the photodetector is under illumination and in the dark, P_L is the illumination intensity and S is the illuminated device area. The calculated maximum photo-responsivity (R_{365nm}) of the fabricated UV-S is 105 mA/W, which is less than the UV-S1 photo-responsivity (164 mA/W) at 8 mW/m^2.

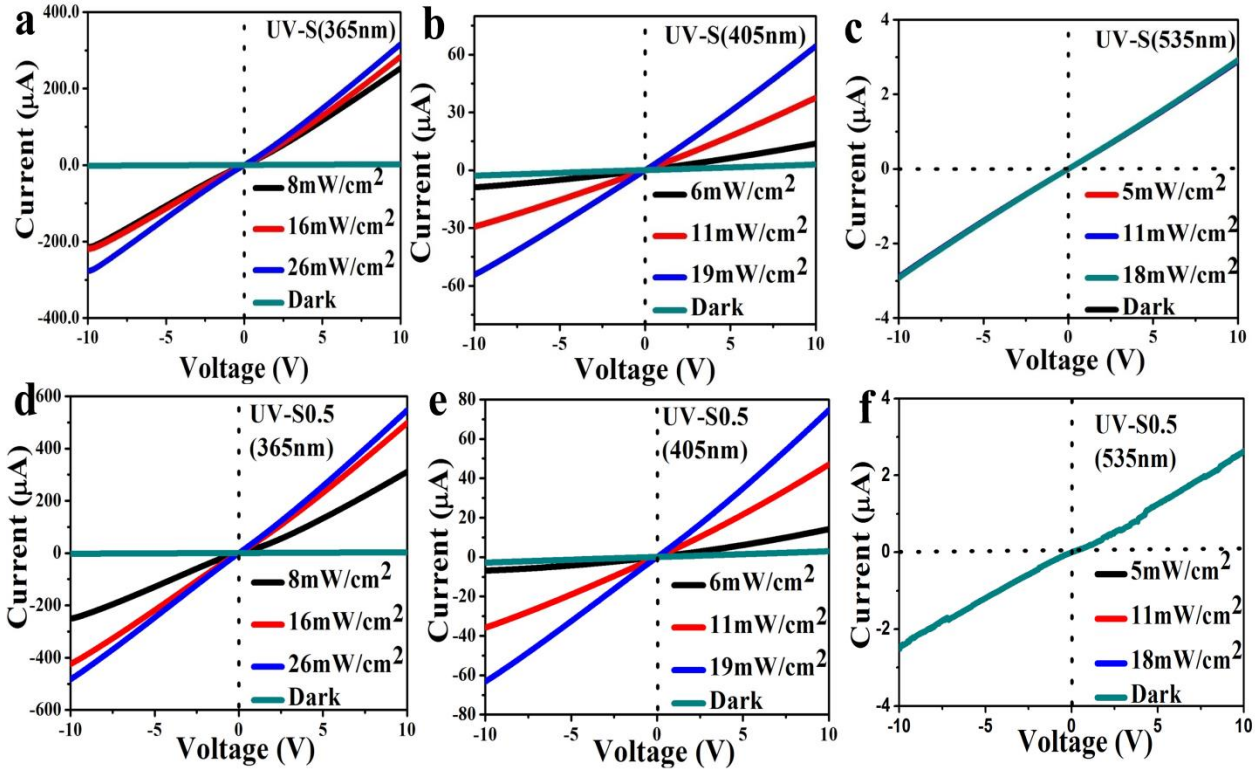

Figure 4.13 I-V measurements at various wavelengths and illumination intensities. Undoped ZnO NRs **(a)** 365 nm, **(b)** 405 nm **(c)** 535 nm and 0.5 wt% Cd-doped ZnO NRs **(d)** 365 nm, **(e)** 405 nm and **(f)** 535 nm.

Figure 4.14(a) and 4.14(b) show the effect of photo-responsivity as a function of the varied light intensities, and the photo-responsivity is fitted by a power law as follows: $I_{ph} = AP^{\theta}$ where I_{ph} is the photocurrent, A is a constant at a particular wavelength, P is the light intensity, and θ is a parameter that determines the photocurrent response of the devices. It is observed that an increase in the light intensity will result in a decrease in the responsivity factor at 365 nm (R_{365nm}). The higher exponent value of UV-S1 compared to UV-S indicates that Cd atoms induced more trap defect sites and higher recombination of electron-hole pairs, which contributed to the large I_{ph}.

The external quantum efficiency (EQE) was estimated from R_{λ} as $\eta = \frac{1240 \times R_{\lambda}}{\lambda}$ - (6) and fitted with a suitable power law, as shown in Figure 4.14(c) and 4.14(d). The sensor performance was further estimated by determining the parameters such as photoconductive gain (G) and detectivity ($D*$), which are given by the following:

$$G = \frac{\Delta I/q}{P/h\nu} \qquad -(7)$$

$$D* = \frac{A^{1/2} \times R_{\lambda}}{(2q \times I_D)^{1/2}} \qquad -(8)$$

where q is the elementary charge carrier; $\Delta I = I_{ph} - I_D$; P is the incident power and h is the Planck's constant. A higher detectivity of 1 x 10^{11} $cmH^{1/2}W^{-1}$ is estimated for UV-S1, which decreases as the light intensity increases. This indicates that the fabricated M-S-M based sensor is highly UV-sensitive for low-power measurements.

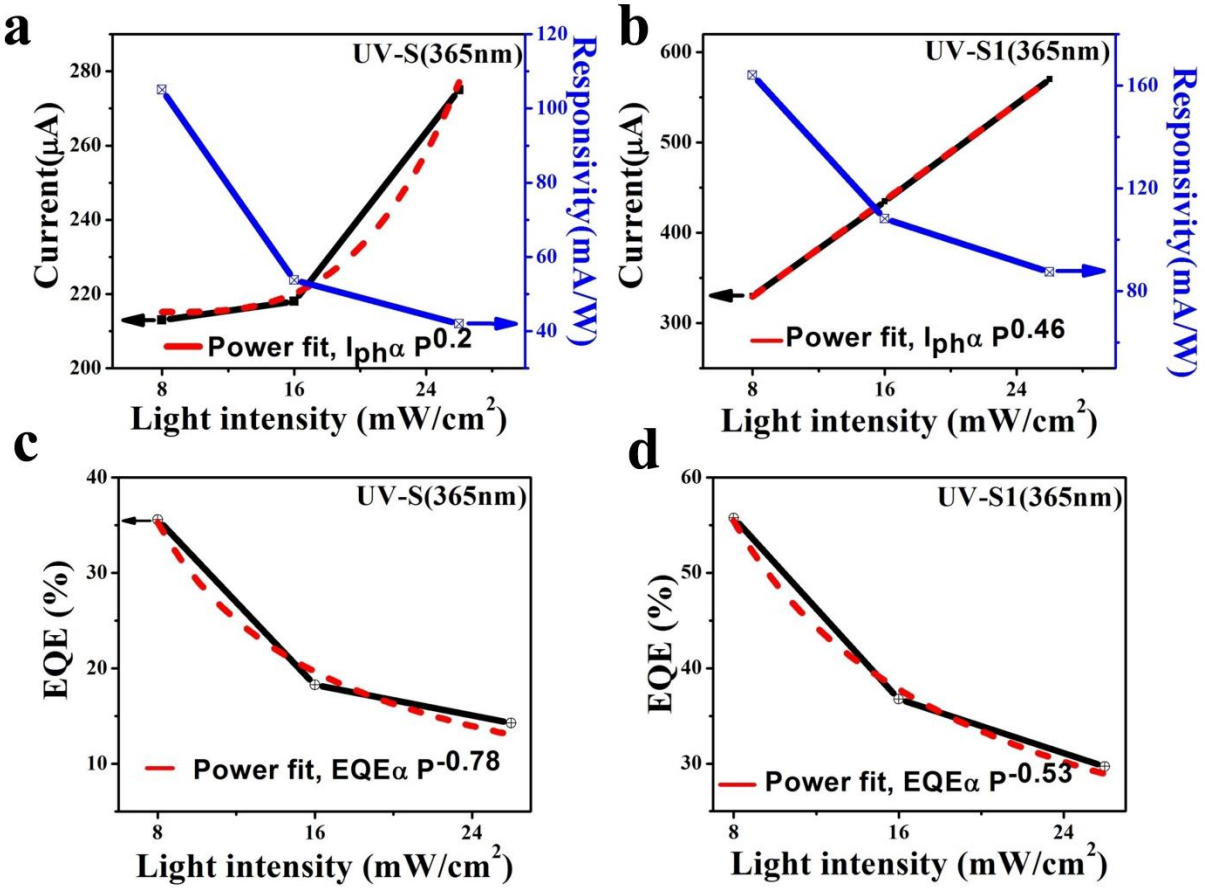

Figure 4.14 Response parameter analysis of UV-S and UV-S1 fitted with suitable power law($I_{ph}=AP^{\Theta}$). Photo-responsivity curves of UV-S based on **(a)** undoped ZnO NRs and **(b)** 1 wt% Cd-doped ZnO NRs. Light intensity-dependent EQE of **(c)** undoped ZnO NRs and **(d)** 1 wt% Cd-doped ZnO NRs.

The proposed UV-S1 response parameters are examined with those reported for UV-S and the values are summarized in **Table 4.1**. Besides, a comparative performance analysis of UV-S1 with other reports is listed in **Table 4.2**.

Table 4.1 Calculated response parameters for UV-S and UV-S1 for UV-illuminated at wavelength of 365 nm and 405 nm.

λ [a] nm	P_L [b] (mW/cm^2)	R_λ [c] (mA/W)		η [d] (%)		G [e]		D* [f] ($cmH^{1/2}W^{-1}$)	
		UV-S	UV-S1	UV-S	UV-S1	UV-S	UV-S1	UV-S	UV-S1
365	8	105	164	35.6	55.7	0.36	0.56	5.4×10^{10}	1.0×10^{11}
365	16	54	108	18.3	36.7	0.18	0.36	2.8×10^{10}	6.7×10^{10}
365	26	42	87	14.3	29.7	0.14	0.29	2.1×10^{10}	5.4×10^{10}
405	6	4.2	6.1	1.3	1.9	0.01	0.02	2.17×10^{9}	3.78×10^{9}
405	11	9.23	19.9	2.8	6.1	0.03	0.06	4.78×10^{9}	1.23×10^{9}
405	19	10.8	20.8	3.3	6.4	0.03	0.06	5.60×10^{9}	1.29×10^{9}

[a]*Wavelength,* [b]*Light intensity,* [c]*Photoresponsivity,* [d]*External quantum efficiency,*

[e]*Photoconductive gain,* [f]*Detectivity*

Table 4.2 Comparison of the Proposed UV-Sensor Device Performance with other reports.

Material	V^a (V)	$I_{ph}{}^b$ (A)	$\tau_R{}^c$ (s)	$\tau_D{}^d$ (s)	$R_\lambda{}^e$ (A/W)	Ref
ZnO:Mn	5	0.2 m	2.75	16.8	0.065	[53]
ZnO:Ti	5	102 μ	-	135	0.05	[54]
ZnO:Fe	8	1.13 m	-	-	3.66	[55]
ZnO:Sb	3	28.3 μ	7.3	20.3	-	[56]
ZnO:Mg	5	44.6 μ	-	-	22.33m	[57]
ZnO:Co	5	14 μ	-	-	0.0033	[58]
ZnO:Ag	5	40 m	80m	3.27	-	[59]
ZnO:C	14	-	2.97n	2.97n	$1.7x10^6$	[60]
ZnO:GO	10	1 μ	69	56	-	[61]
ZnO:Cd	10	330 μ	8	10	164m	This work

[a]Bias Voltage , [b] Photocurrent , [c]Response time, [d] Recovery time, [e]Photoresponsivity.

Figure 4.15(a) shows the time-dependent response and recovery spectra of UV-S and UV-S1. The high I_{on}/I_{off} ratio for the UV-S1 device shows that charge transport is enhanced by the replacement of Zn^{2+} by Cd^{2+} ions (Figure 4.15(b)).

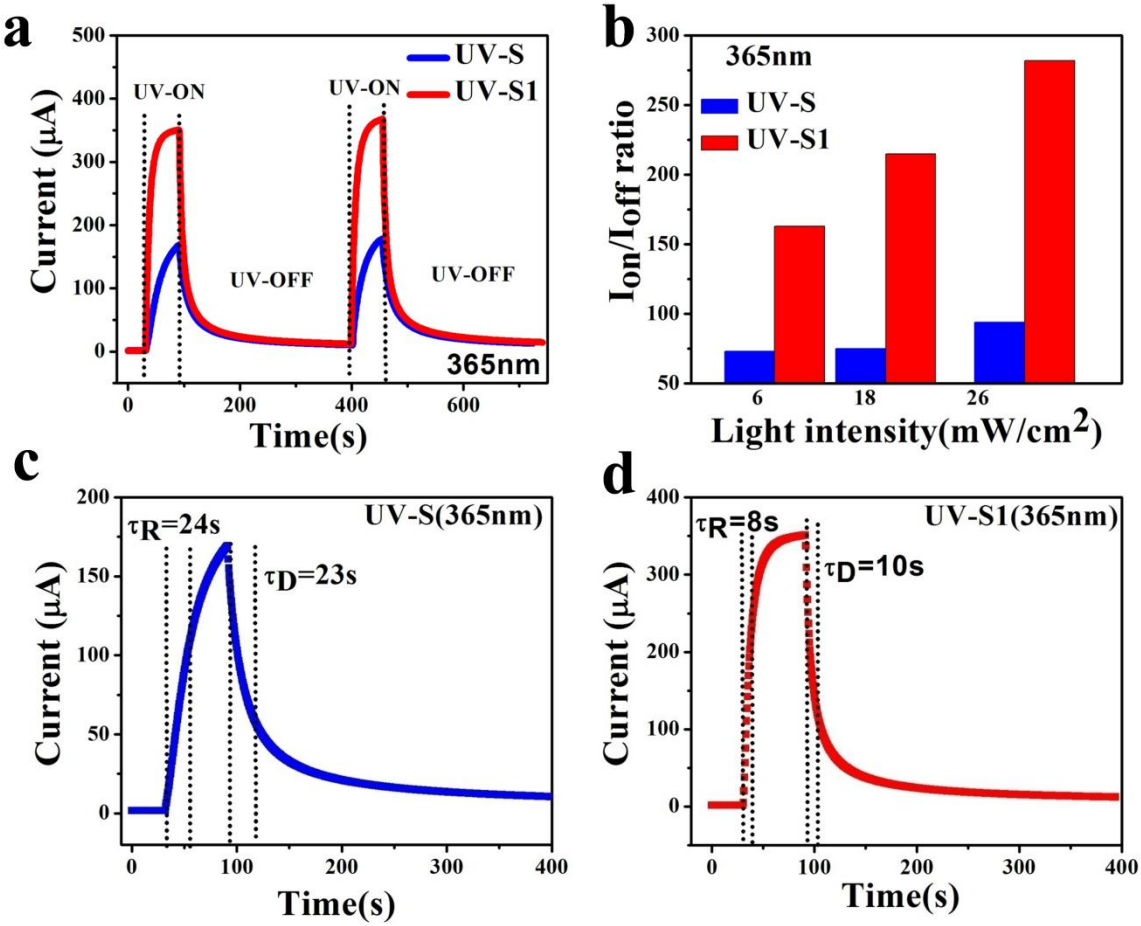

Figure 4.15 (a) Time-dependent UV photo response of UV-S and UV-S1 under a bias voltage of 10 V. **(b)** I_{on}/I_{off} ratio of undoped ZnO NRs and 1 wt% Cd-ZnO NRs. Time-resolved photocurrent rise and decay of **(c)** undoped ZnO NRs (UV-S) and **(d)** 1 wt% Cd-ZnO NRs (UV-S1).

The fabricated sensors were reversibly turned on/off during a 60 seconds time interval by switching the UV illumination (365 nm) with a light intensity of 8 mW/cm^2 at an applied bias of 10 V. The I_{ph} of UV-S and UV-S1 increases as the UV light was turned on for a time interval of

60 seconds and the I_{ph} decreases slowly once the UV source is switched off. The generation of I_{ph} for UV-S1 is much higher than the I_{ph} of UV-S for a limited time, which demonstrates the effect of the Cd dopant on ZnO NRs. A long decay time is observed for both UV-S and UV-S1 due to the presence of oxygen vacancy sites and the re-adsorption of O_2 molecules on the surfaces of NRs[62]. The response time (τ_R) and recovery time (τ_D) are determined by estimating the time required to approach 63 % ($\sim 1 - e^{-1}$) of the maximum I_{ph} from I_D and the time required for the recovery to 37 % ($\sim e^{-1}$) of the maximum I_{ph}. Figure 4.15(c) and 4.15(d) illustrates the calculated rise time (τ_R) and decay time (τ_D) as 24s and 23s, respectively, for UV-S and 8s and 10s, respectively, for UV-S1. The faster response time is achieved for UV-S1 based on 1 wt% Cd-ZnO NRs, which illustrates the effect of the Cd dopant in modulating the trap sites on the surface of nanorods.

4.3.2.3 Mechanism of Cd dopant modulated semiconductor properties of ZnO NRs

The role of Cd in modulating the semiconducting properties is discussed by considering the charge transport model (Figure 4.11(b)). When the bias voltage 10 V is applied to UV-S at ambient room temperature, oxygen molecules from the environment are absorbed on the surface of ZnO NRs [$O_{2_{(g)}} + e^- \rightarrow O^-_{2_{(abs)}}$][63]. This results in lower electron density and mobility of charge carriers, which are controlled by the formation of a depletion layer near the surface of ZnO NRs. Upon illumination by UV light, electrons (e^-) and holes (h^+) are generated across the surface of UV-S [$ZnO\ NRs + h\nu \rightarrow e^-(CB) + h^+(VB)$]. Due to the difference in the surface potential, the photogenerated holes migrate to the surface to react with $O^-_{2_{(abs)}}$, thereby releasing the trapped electrons to the conduction band (CB) [$h^+ + O^-_{2_{(abs)}} \rightarrow O_{2_{(g)}}$][63]. In this condition, the excess e^- available inside the NRs have a lower chance of recombining with the

holes because insufficient h^+ is are available due to the liberation of $O_{2_{(g)}}$. This increases the movement of electron charge carriers and consequently leads to higher photocurrent (I_{ph}) compared to I_D ~ 2.9 µA (Figure 4.12). In the case of the UV-S1 device comprising 1 wt% Cd-ZnO NRs as the sensing layer, the I_{ph} generated is double the magnitude of the photocurrent from UV-S. The replacement of Zn^{2+} by Cd^{2+} contributes to more donor defects, which act as a source for improving the n-type carrier concentration of ZnO and thus create more zinc interstitials (Zn_i) and oxygen deficiency sites (V_o). This increase in the vacancy defect zones produces a platform for the adsorption of more O_2 molecules on the surface of NRs, thus lowering the I_D (~ 2 µA) of UV-S1. When exposed to UV-illumination, excess amounts of $e^-$are released that are trapped by the formation of $O_{2_{(abs)}}^-$ molecules, thus increasing the electron intensity inside the Cd-ZnO NRs.

When UV-light is turned off, the photocurrent degrades gradually due to recombination of the excess $e^-$with h^+ and the re-adsorption of O_2 molecules on the surface by the capture of few e^-. The slow recovery time for the sensor is due to slow recombination of the $e^- - h^+$ pair. In addition to the adsorption and desorption mechanism, the sensor performance depends on the band gap modulation due to Cd doping. Figure 4.11(e) shows the energy band diagram of the sensor. Due to a higher work function of ZnO (Φ_S = 5.2 eV) than Ag (Φ_M = 4.2 eV), which is used as an electrode, the energy band bends at the Metal-Semiconductor-Metal interface, which indicates the tunneling of e^- from the conduction band of ZnO NRs to the Ag electrode to achieve the equilibrium Fermi-level (E_F), whereas the h^+on the surface of NRs establishes a strong Ohmic contact[50]. When Cd doping occurs, the band gap of ZnO NRs is red-shifted from 3.2 eV to 3.17 eV (Figure 4.4(e)). This reduced the barrier height, Φ_B, of the ZnO material, which ensures that the barrier width becomes thin enough for tunneling

of electrons at the Metal-Semiconductor-Metal interface and produces high conductivity and photocurrent from the UV-S1 device.

4.3.3 Realization of a self-powered UV-Sensor (SPUV-S)

The SPUV-S was developed using the parallel connection between the UV-S1 (1 wt% of Cd-doped ZnO NRs) and P-NG (only ZnO NRs) devices. The voltage drop across the sensor was measured to estimate the performance of the SPUV-S at various wavelengths (365 nm, 405 nm) and UV-illumination intensities. To determine the effect of Cd doping, measurements were conducted using UV-S for an effective comparison with UV-S1. Initially, when sensor devices (UV-S and UV-S1) are not connected, the P-NG delivers the maximum peak voltage (20 V), which then shows a considerable voltage drop from 20 V to ~ 17 V when the sensors are connected in parallel to P-NG (**Figure 4.16**(a) and 4.16(b)). This indicates that the internal resistance of UV-S and UV-S1 are much less than the internal resistance of P-NG. Upon irradiation of a 365 nm UV light, the UV-S1 resistance drops and the peak voltage reduces to 40 mV when the illuminated light intensity increases, as shown in the inset of Figure 4.16(b). The voltage drop for UV-S1 is higher than that for UV-S indicating that more free charge carriers are produced by Cd doping in ZnO NRs, which reduces the resistance across the sensor and thus results in an obvious increase in the voltage drop for UV-S1. Further the sensitivity of the self-powered performance of UV-S under blue (405 nm) light was examined. When the wavelength is increased to 405 nm, UV-S shows a small variation in voltage due to less absorption of photon energy from the light source, while UV-S1 is still highly responsive due to tuning of the band gap (3.17 eV) in Cd-ZnO NRs (Figure 4.16(c) and 4.16(d)). Our experimental results demonstrate that the substitution of Cd dopants into ZnO NRs will symmetrically decrease the piezoelectric properties while improving the UV-photo response behavior.

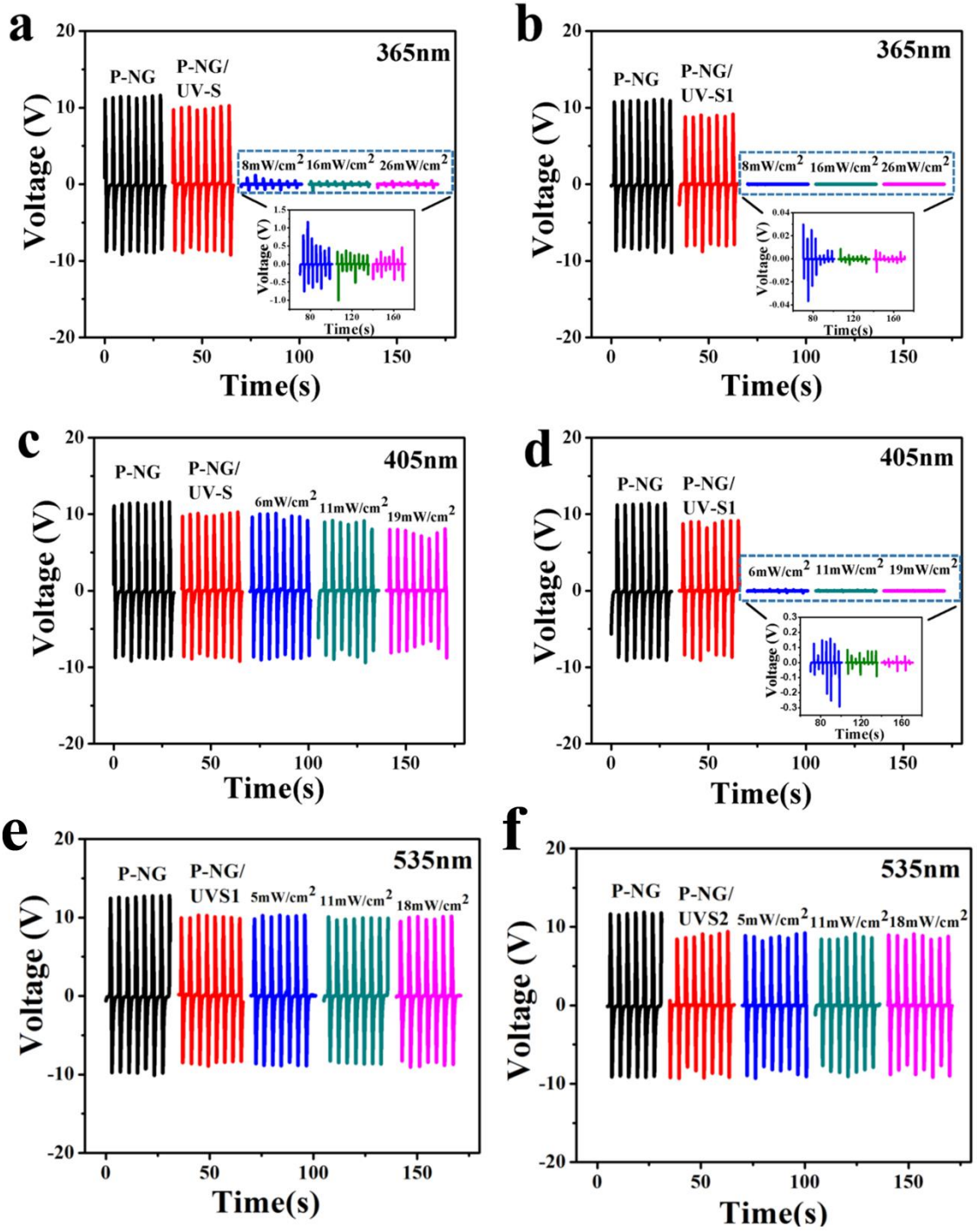

Figure 4.16 Measured electrical output voltage of self-powered UV-sensor (SPUV-S) at $\lambda_{365\ nm}$ operated at a light intensity of 8 mW/cm^2. **(a)** UV-S (undoped ZnO NR-based device) and **(b)** UV-S1 (1 wt% Cd-doped ZnO NRs-based device). Performance of SPUV-S at $\lambda_{405\ nm}$ operated at light intensity of 6 mW/cm^2**(c)** UV-S and **(d)** UV-S1. (**e, f**) Performance at $\lambda_{535\ nm}$.

4.4 Conclusion

In summary, the asymmetrical effect of the reduction in piezoelectric properties and the increase in the semiconducting behavior of ZnO NRs due to the substitution of Cd dopants was reported. UV-S1 (1 wt % of Cd) showed good photo response with a detectivity (D*) limit of $1x10^{11}cmH^{1/2}W^{-1}$, which is higher than that of UV-S (pure ZnO NRs) (D* = $5.4x10^{10}cmH^{1/2}W^{-1}$). In addition, the sensitivity of the UV-S1 device for various excitation light sources and power intensities was examined, and it confirms the enhanced UV sensing efficiency (η) and responsivity (R_λ) at 365 nm. Moreover, the ferroelectric property of ZnO NRs was greatly affected by the Cd atom, which led to a simultaneous reduction in the piezoelectric output from V_{OC}=36 V, I_{SC}=284 μA (pure ZnO NRs) to V_{OC}=15 V, I_{SC}=178 μA (1 wt% Cd-doped ZnO NRs).These finding shows that Cd doping in ZnO is unsuitable for energy conversion applications, such as applications that convert mechanical to electrical energy; In contrast, Cd doping enhances the semiconducting properties of ZnO, which is highly useful in the development of optoelectronic devices. In addition, the pure ZnO NRs-based nanogenerator and Cd-ZnO NRs photo-sensor are useful in the development of next-generation self-powered devices.

4.5 References

1 F. R. Fan, W. Tang, Z. L. Wang, *Adv. Mater.*, 2016, 4283–4305.

2 J.-H. Lee, J. Kim, T. Y. Kim, M. S. Al Hossain, S.-W. Kim, J. H. Kim, *J. Mater. Chem. A*, 2016, **4**, 7983–7999.

3 C. R. Bowen, J. Taylor, E. LeBoulbar, D. Zabek, A. Chauhan, R. Vaish, *Energy Environ. Sci.*, 2014, **0**, 1–21.

4 F. Invernizzi, S. Dulio, M. Patrini, G. Guizzetti, P. Mustarelli, *Chem. Soc. Rev.*, 2016, **45**, 5455–5473.

5 B. Lee, B. Park, H. Yang, J. W. Han, C. Choong, J. Bae, K. Lee, W. Yu, U. Jeong, U. Chung, J. Park, O. Kim, 2014. ACS Appl. Mater. Interfaces, 2014, **6**, 3520–3527.

6 K. Il Park, S. Xu, Y. Liu, G. T. Hwang, S. J. L. Kang, Z. L. Wang, K. J. Lee, *Nano Lett.*, 2010, **10**, 4939–4943.

7 Y. Wang, T. Hou, S. Tian, S. Lee, Y. Li, 2011, 7706–7716.

8 B. Saravanakumar, K. Thiyagarajan, N. R. Alluri, S. SoYoon, K. Taehyun, Z. H. Lin, S. J. Kim, *Carbon N. Y.*, 2015, **84**, 56–65.

9 Z. L. Wang, W. Wu, *Angew. Chemie - Int. Ed.*, 2012, **51**, 11700–11721.

10 K.-H. Kim, B. Kumar, K. Y. Lee, H.-K. Park, J.-H. Lee, H. H. Lee, H. Jun, D. Lee, S.-W. Kim, *Sci. Rep.*, 2013, **3**, 2017.

11 G. Zhu, R. Yang, S. Wang, Z. L. Wang, *Nano Lett.*, 2010, **10**, 3151–3155.

12 N. R. Alluri, B. Saravanakumar, S. J. Kim, *ACS Appl. Mater. Interfaces*, 2015, **7**, 9831–9840.

13 K. Il Park, J. H. Son, G. T. Hwang, C. K. Jeong, J. Ryu, M. Koo, I. Choi, S. H. Lee, M. Byun, Z. L. Wang, K. J. Lee, *Adv. Mater.*, 2014, **26**, 2514–2520.

14 Z. L. Wang, *J. Phys. Condens. Matter*, 2004, **16**, R829–R858.

15 Z. L. Wang, *MRS Bull.*, 2007, **32**, 109–116.

16 Y. Zhang, C. Liu, J. Liu, J. Xiong, J. Liu, K. Zhang, Y. Liu, M. Peng, A. Yu, A. Zhang, Y. Zhang, Z. Wang, J. Zhai, Z. L. Wang, *ACS Appl. Mater. Interfaces*, 2016, **8**, 1381–1387.

17 C. Liu, A. Yu, M. Peng, M. Song, W. Liu, Y. Zhang, J. Zhai, *J. Phys. Chem. C*, 2016, **120**, 6971–6977.

18 M. K. Gupta, J. H. Lee, K. Y. Lee, S. W. Kim, *ACS Nano*, 2013, **7**, 8932–8939.

19 R.C. Wang, Y.-X. Lin, J.J. Wu, *J. Phys. Chem. C*, 2015, **119**, 29186–29192.

20 S. H. Shin, Y. H. Kim, M. H. Lee, J. Y. Jung, J. H. Seol, J. Nah, *ACS Nano*, 2014, **8**, 10844–10850.

21 Y. Lin, P. Deng, Y. Nie, Y. Hu, L. Xing, Y. Zhang, X. Xue, *Nanoscale*, 2014, **6**, 4604–10.

22 D. Zhu, T. Hu, Y. Zhao, W. Zang, L. Xing, X. Xue, *Sensors Actuators, B Chem.*, 2015, **213**, 382–389.

23 W. Zang, W. Wang, D. Zhu, L. Xing, X. Xue, *RSC Adv.*, 2014, **4**, 56211–56215.

24 W. Zang, P. Li, Y. Fu, L. Xing, *RSC Adv.*, 2015, **5**, 84343–84349.

25 Y. Fu, Y. Zhao, P. Wang, L. Xing, X. Xue, *Phys. Chem. Chem. Phys.*, 2015, **17**, 2121–2126.

26 S. Lee, J. Lee, W. Ko, S. Cha, J. Sohn, J. Kim, J. Park, Y. Park, J. Hong, *Nanoscale*, 2013, **5**, 9609–9614.

27 C.-L. Hsu, I.L. Su, T.J. Hsueh, *RSC Adv.*, 2015, **5**, 34019–34026.

28 M. P. Lu, J. Song, M. Y. Lu, M. T. Chen, Y. Gao, L. J. Chen, Z. L. Wang, *Nano Lett.*, 2009, **9**, 1223–1227.

29 M.C. Jun, S.U. Park, J.H. Koh, *Nanoscale Res. Lett.*, 2012, **7**, 639.

30 X. Huang and J. L. Coffer, *Cryst. Growth Des.*, 2012, **12**, 2362–2366.

31 C. L. Hsu, H. H. Li, T. J. Hsueh, *ACS Appl. Mater. Interfaces*, 2013, **5**, 11142–11151.

32 C. S. Oliveira, J. Bettini, F. A. Sigoli, I. O. Mazali, *Cryst. Growth Des.*, 2015, **15**, 5246–5253.

33 S. Gowrishankar, L. Balakrishnan, N. Gopalakrishnan, *Ceram. Int.*, 2014, **40**, 2135–2142.

34 S. Satarug, M. R. Haswell-Elkins, M. R. Moore, *Br. J. Nutr.*, 2000, **84**, 791–802.

35 H. Services, *Toxicol. Ind. Health*, 1999, **15**, 655–701.

36 J. N. Hasnidawani, H. N. Azlina, H. Norita, N. N. Bonnia, S. Ratim, E. S. Ali, *Procedia Chem.*, 2016, **19**, 211–216.

37 W. E. Mahmoud, A. M. Al-Sanoosi, *Superlattices Microstruct.*, 2012, **51**, 506–511.

38 Y. Wang, Y. Yang, X. Zhang, X. Liu, A. Nakamura, *CrystEngComm*, 2012, **14**, 240.

39 Z. J. Othman, S. Ayed, A. Matoussi, H. Khemakhem, *Vib. Spectrosc.*, 2016, **85**, 208–214.

40 R. Ahmad, N. Tripathy, M. Y. Khan, K. S. Bhat, M. Ahn, Y.B. Hahn, *RSC Adv.*, 2016, **6**, 54836–54840.

41 A. Gulino, F. Castelli, P. Dapporto, P. Rossi, I. Fragalà, *Chem. Mater.*, 2002, **14**, 704–709.

42 Y. Dou, R. G. Egdell, T. Walker, D. S. L. Law, G. Beamson, *Surf. Sci.*, 1998, **398**, 241–258.

43 C. Ou, P. E. Sanchez-Jimenez, A. Datta, F. L. Boughey, R. A. Whiter, S.-L. Sahonta, S. Kar-Narayan, *ACS Appl. Mater. Interfaces*, 2016, **8**, 13678–13683.

44 M. R. Hasan, S. H. Baek, K. S. Seong, J. H. Kim, I. K. Park, *ACS Appl. Mater. Interfaces*, 2015, **7**, 5768–5774.

45 Y. C. Yang, C. Song, X. H. Wang, F. Zeng, F. Pan, *Appl. Phys. Lett.*, 2008, **92**, 012907.

46 X. Tang, H. Lü, Q. Zhang, J. Zhao, Y. Lin, *Solid State Sci.*, 2011, **13**, 384–387.

47 M. K. Yadav, M. Ghosh, R. Biswas, A. K. Raychaudhuri, A. Mookerjee, S. Datta, *Phys. Rev. B - Condens. Matter Mater. Phys.*, 2007, **76**, 1–9.

48 T. Mattila, A. Zunger, *J. Appl. Phys.*, 1999, **85**, 160–167.

49 J. Wang, Y. Zhang, *Sci. Rep.*, 2016, **6**, 24660.

50 L. J. Brillson, Y. Lu, *J. Appl. Phys.*, 2011, **109**, 121301.

51 H.-M. Chiu, J.-M. Wu, *J. Mater. Chem. A*, 2013, **1**, 5524.

52 T. S. Lin, C. H. Chen, C. T. Lee, *IEEE Photonics Technol. Lett.*, 2015, **27**, 759–762.

53 C. O. Chey, X. Liu, H. Alnoor, O. Nur, M. Willander, *Phys. Status Solidi - Rapid Res. Lett.*, 2015, **9**, 87–91.

54 P. S. Shewale, N. K. Lee, S. H. Lee, K. Y. Kang, Y. S. Yu, *J. Alloys Compd.*, 2015, **624**, 251–257.

55 R. Azimirad, A. Khayatian, S. Safa, M. Almasi Kashi, *J. Alloys Compd.*, 2014, **615**, 227–233.

56 W. Dai, X. Pan, S. Chen, C. Chen, W. Chen, H. Zhang, Z. Ye, *RSC Adv.*, 2015, **5**, 6311–6314.

57 P. S. Shewale, Y. S. Yu, *J. Alloys Compd.*, 2016, **654**, 79–86.

58 H. S. Al-Salman, M. J. Abdullah, *J. Mater. Sci. Technol.*, 2013, **29**, 1139–1145.

59 Y. Liu, X. Zhang, J. Su, H. Li, Q. Zhang, Y. Gao, *Opt. Express*, 2014, **22**, 30148–55.

60 D.-Y. Guo, C.X. Shan, S.-N. Qu, D.Z. Shen, *Sci. Rep.*, 2014, **4**, 7469.

61 Z. Wang, X. Zhan, Y. Wang, S. Muhammad, Y. Huang, J. He, *Nanoscale*, 2012, **4**, 2678.

62 C.H. Chen, C.T. Lee, *J. Electron. Mater.*, 2016, **45**, 4854–4858.

63 C. Soci, A. Zhang, B. Xiang, S. A. Dayeh, D. P. R. Aplin, J. Park, X. Y. Bao, Y. H. Lo, D. Wang, *Nano Lett.*, 2007, **7**, 1003–1009.

CHAPTER V

Regulation of Charge Carrier Dynamics in ZnO Micro-Architecture Based UV/Visible Photodetector via Photonic-Strain Induced Effects

Highlights

- A feasible, morphological influence on photoresponse behavior of ZnO micro-architectures such as micro wire (MW), coral like micro strip (CMS), fibril like clustered micro wire (F-MW) grown by one-step carrier gas/metal catalyst "free" vapor transport technique is reported
- The unique structural alignment of ZnO F-MW has enhanced the I_{Ph} from 14.2 to 186, 221, 290 μA upon various light intensities such as 0 to 6, 11, 17 mW/cm^2 at λ_{405nm}
- Herein, the nature of as-fabricated ZnO photodetector (PD) modulated by tuning the inner crystals piezoelectric potential through piezo-phototronic effect is demonstrated
- The current behavior observed at the two interfaces acting as the source (S) and drain (D) are carefully investigated by analyzing the Schottky barrier heights (Φ_{SB})
- This work can pave the way for the development of geometrically modified strain induced performances of PD to promote next generation self-powered optoelectronic integrated devices and switches

Graphical Outline

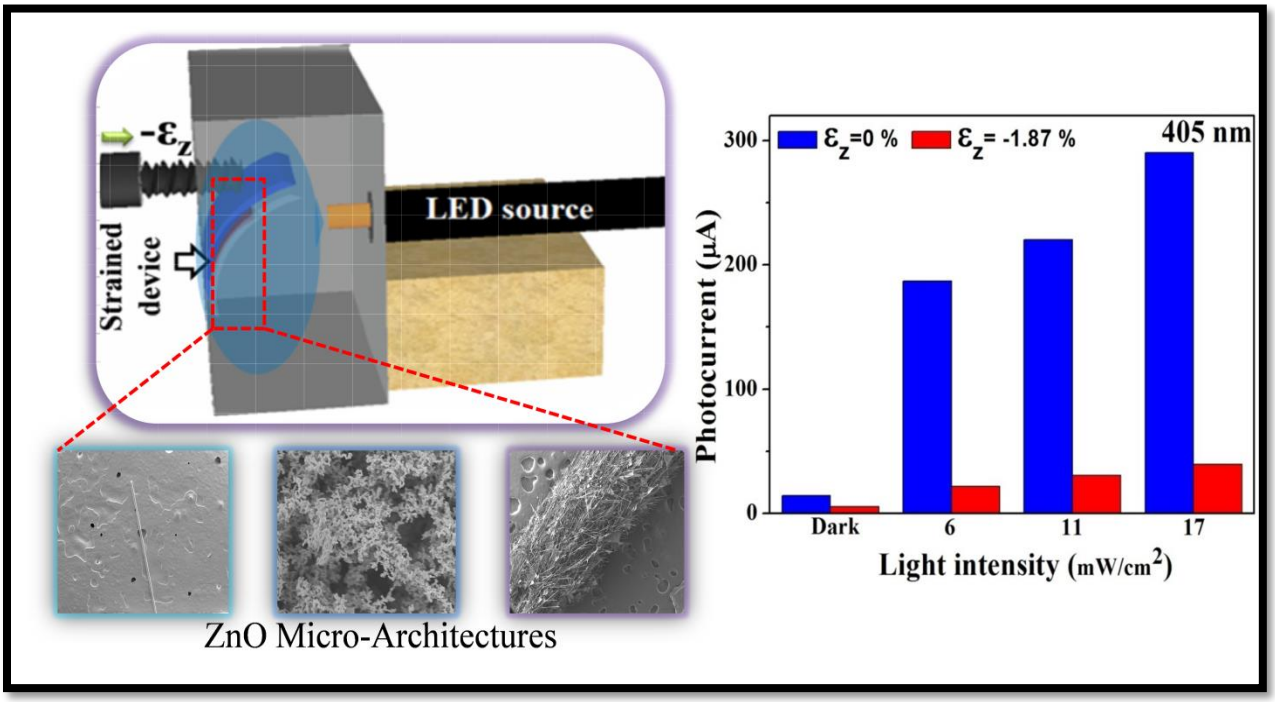

5.1 Introduction

ZnO is an inorganic II-VI semiconductor with a direct bandgap (3.37 eV) and highly accepted nanomaterial in the field of photocatalysis[1], batteries[2], solar cells[3,4] , light emitting diodes (LED)[5,6], photodetector[7-8], piezoelectric nanogenerators[9,10], bio-medical devices[11], optical sensors[12,13], chemical sensors[14] and gas sensors[15,16] due to its unique intrinsic properties. Over the last decade, multi-shaped ZnO micro/nanostructures in the form of rods[17], tetrapods[18-23], brush[24], wires[25], sheet[26], tubes[27], tower[28], disk[29], spheres[30], fern[31], peanut[32] and flower[33] has been produced by various synthesis strategies such as hydrothermal[34], sol-gel[35], solvothermal[36], ultrasonication[37], microwave[38], chemical vapor deposition (CVD)[39], physical vapor deposition (PVD)[40] and molecular beam epitaxy (MBE)[41], magnetron sputtering[3] methods. Literature reports suggest that the ZnO micro/nanostructures widens our knowledge on the dependency of the device performances as a function of geometrical factors such as structural architecture, particle size, surface to volume ratio and its crystallinity.

Recently, ZnO nanostructures are widely utilized and investigated to explore the concepts of piezoelectric effect, piezotronic effect, piezo-phototronic effect, and piezo-photocatalysis by the internal coupling of functional factors such as piezoelectric, semiconducting and photonic properties. Specifically in the case of flexible optoelectronic systems, controlling the morphological parameter broadens the spectral wavelength of light detection, sensitivity and performance of the devices by piezo-phototronic effect[42]. Here, the ZnO photodetector (PD) current response has been tuned by introducing the induced piezoelectric potentials across the metal-semiconductor (M-S) interface upon external compressive/tensile strains. Latterly, the photocurrent responsivity, gain factor and broadband wavelengths of ZnO PDs were improved drastically by various ways such as: (i) growth of novel pure nanostructures of ZnO (3D

branched type[43], comb[44] and crown-capped[34]) (ii) foreign elements doping into ZnO nanostructures and (iii) core-shell type organic/inorganic hybrid structures[42], respectively. Till now, sodium (Na)[45], gallium (Ga)[46], cadmium (Cd)[47], lithium (Li)[48], cobalt (Co)[49] and gold (Au)[50] elements were substituted into ZnO to improve the photonic properties. Similarly, many organic polymers along with ZnO structure were investigated such as poly(3,4-ethyleneioxythiophene):polystyrenesulfonate(PEDOT:PSS)[51],poly(3hexylthiophene)(P3HT)[4], polyaniline (PANI)[52] and poly[2-methoxy-5-(2-ethylhexyloxy)-1,4-phenylenevinylene] (MEH-PPV)[53] to enhance the photosensitivity. Other than these approaches, the ZnO PDs response can be improved or tuned by the strain induced behaviors in balancing the electronic transportations *via* piezotronic and piezo-phototronic effects towards the realization of flexible and rollable optoelectronic sensing systems[39,42,51,54]. Tuning the inner piezoelectric potential of ZnO micro wire PD has improved the photoresponsivity upon light illumination and strain conditions, respectively[8]. The published reports on these concepts are limited, and thorough investigation is necessary to explore the photosensing capability by synchronizing the factors like morphology, broadband spectral detection, piezotronic and piezo-phototronic effects.

In this work, a flexible photodetector was developed with various morphologies of ZnO micro-architectures such as micro wire (MW), coral like micro strip (CMS), and fibril like clustered micro wire (F-MW) that were obtained through a simplified carrier gas/catalyst-free vapor phase transport technique (VPT). The as-fabricated devices showed a broadband UV/Visible photo sensing capability at wavelengths 365 (UV), 405 (blue light emission) and 535 nm (green light emission). It was noteworthy that the photocurrent response and detectivity of the PD made of ZnO F-MW exhibited higher light harvesting potential compared to ZnO-MW and ZnO-CMS. Through this work, the performance of photodetection as a function of

morphological modification was evaluated. Further, the metal – semiconductor (M-S) interface behavior by finely tuning the intrinsic piezoelectric charge potentials *via* piezotronic and piezo-phototronic effect through externally applied compressive strain (- ε_z = 0.37, 0.75, 1.13, 1.50 and 1.87 %) was explored. This detailed mechanism enables freedom for designing next generation flexible and wearable optoelectronic sensing systems with superior performance.

5.2 Experimental section

5.2.1 One-step synthesis of vapor phase transport (VPT) technique for ZnO micro-architectures

ZnO micro-architectures (MW, CMS and F-MW) were synthesized by carrier gas/metal catalyst "free" VPT technique. In general procedure, zinc (II) oxide (< 1 μm) and graphite powder (< 20 microns) were obtained from Sigma-Aldrich and used without any further purification. Equal mass ratio (1: 1) of the source materials were blended together in mortar and pestle for about 30 min using ethanol as a solvent. Homogeneously mixed ZnO: graphite powder was loaded into an alumina (Al_2O_3) crucible and p-type silicon substrate was used to grow ZnO microstructures. Before the chemical reaction, the substrate has been pre-cleaned using RCA/HF treatment and located on loaded Al_2O_3 crucible in upside down manner and placed exactly at the center of the quartz tube. The temperature of the tubular furnace was elevated up to 1100 °C at a heating ramp of 190 °C/h and soaked at the same temperature for 1 h. Later, the furnace was allowed to cool down naturally to ambient room temperature. Finally, highly crystalline ZnO microstructures (MW, CMS and F-MW) were obtained inside and at the corners of the crucible. Notably, there was no observed growth of ZnO microstructures on the surface of the substrate (**Figure 5.1** (a)). The observed structural effect is expected to result from the modified conditions

in vapor transport method that was processed in the absence of carrier gas and catalyst-free target substrate.

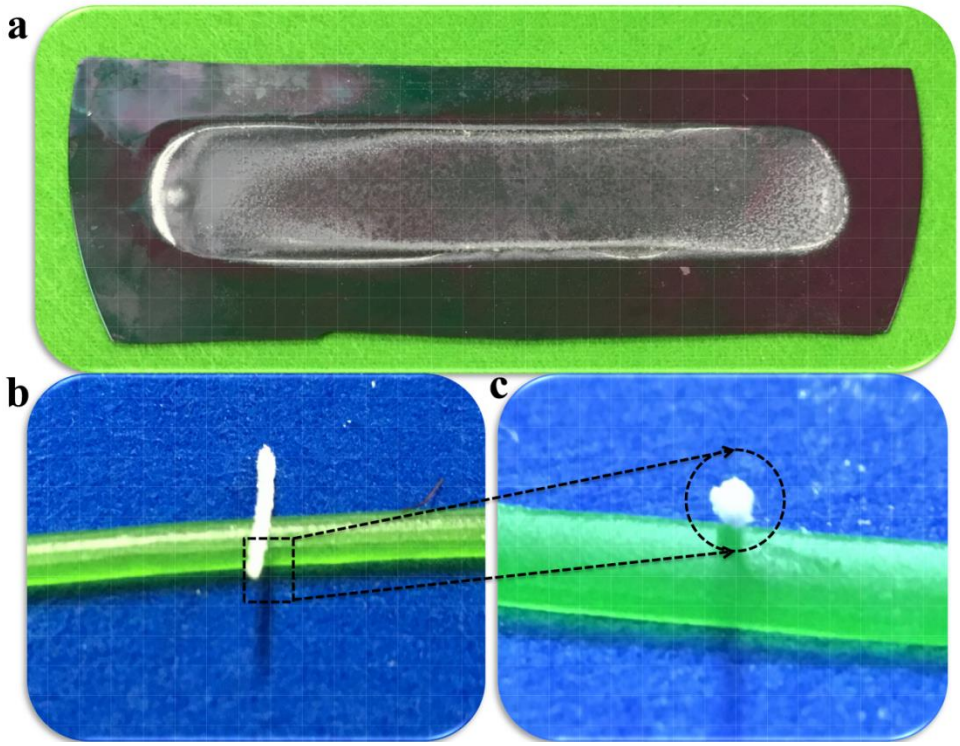

Figure 5.1 (a) Optical image of p-Si substrate after carrier gas/ metal catalyst-free VPT process signifying no substrate growth of ZnO microstructures. **(b, c)** Cylindrical clustered growth of ZnO F-MW.

5.2.2 Fabrication of flexible ZnO microstructures based photodetector

As-grown ZnO MW, CMS and F-MW were measured to a length of 4 mm and were carefully bonded onto a poly-dimethylsiloxane (PDMS) substrate to make the device flexible under different mechanical strain. Copper (Cu) wires were connected at the two ends of ZnO microstructure using silver (Ag) paste to form metal (M) - semiconductor (S) - metal (M) type PD. Lastly, optically transparent, flexible polymethyl-methacrylate (PMMA) layer was deposited on Ag/ZnO/Ag interfaces which also serves as a protecting layer for the PD device.

5.2.3 Characterization system

ZnO micro-architectures were analyzed using field-emission scanning electron microscopy (FE-SEM, Zeiss Supra-55vp, Germany and JEOL JSM-6700F, Japan). The purity of as-synthesized ZnO microstructures was confirmed by Energy dispersive X-ray spectrometry (EDAX, Bruker Nano GmbH Berlin, Germany). Molecular vibrational modes of ZnO was determined by using Raman spectra recorded from 200 - 800 cm^{-1} at an excitation wavelength of 514 nm using high-throughput single-stage spectrometer (LabRAM HR Evolution; Horiba, Japan). The bandgap was determined by the absorbance analysis (200 – 800 nm) using UV-Vis spectrophotometer from Cary300, Varian system, USA. High voltage enabled precision material analyzer (Precision 10kV HVI-SC, Radiant Technologies, Inc) was used to record the ferroelectric property. Various compressive strains (- ε_z) such as 0.37, 0.75, 1.13, 1.50 and 1.87 % were generated on ZnO PD using the manually designed 3D rotational setup, and the corresponding optical images are given in the supporting information file. The strain induced photo-responsive I-V measurements were recorded using a semiconductor device parameter analyzer (Agilent-B1500A) with the help of a Prizmatix multi-wavelength LED light source operated at wavelengths of 365 nm, 405 nm and 535 nm at different light intensities.

5.3 Results and discussion

5.3.1 Structural and surface morphology of ZnO micro-architectures

The morphological structures of as-synthesized ZnO micro-architectures were carefully collected from the Al_2O_3 crucible and observed through FESEM analysis. **Figure 5.2** illustrates three different morphologies of as-synthesized ZnO structures in the form of MW, CMS and F-MW. **Figure 5.2**(a, d) shows the single strand of ZnO MW with an average diameter of ≈ 20 μm.

Removal of carrier gas/catalyst in the synthesis procedure yields ZnO in the form of CMS and F-MW as shown in Figure 5.2(b, c). ZnO CMS arises due to the formation/collection of ZnO nanoparticles branched together in the form of a single strip having a diameter of ≈ 250 μm as shown in Figure 5.2(e). Similarly, ZnO F-MW formed due to the collective interaction and random bundling of n-numbered single strands of ZnO MWs having an average diameter ≈ 1 mm, as shown in Figure 5.2(c, f).

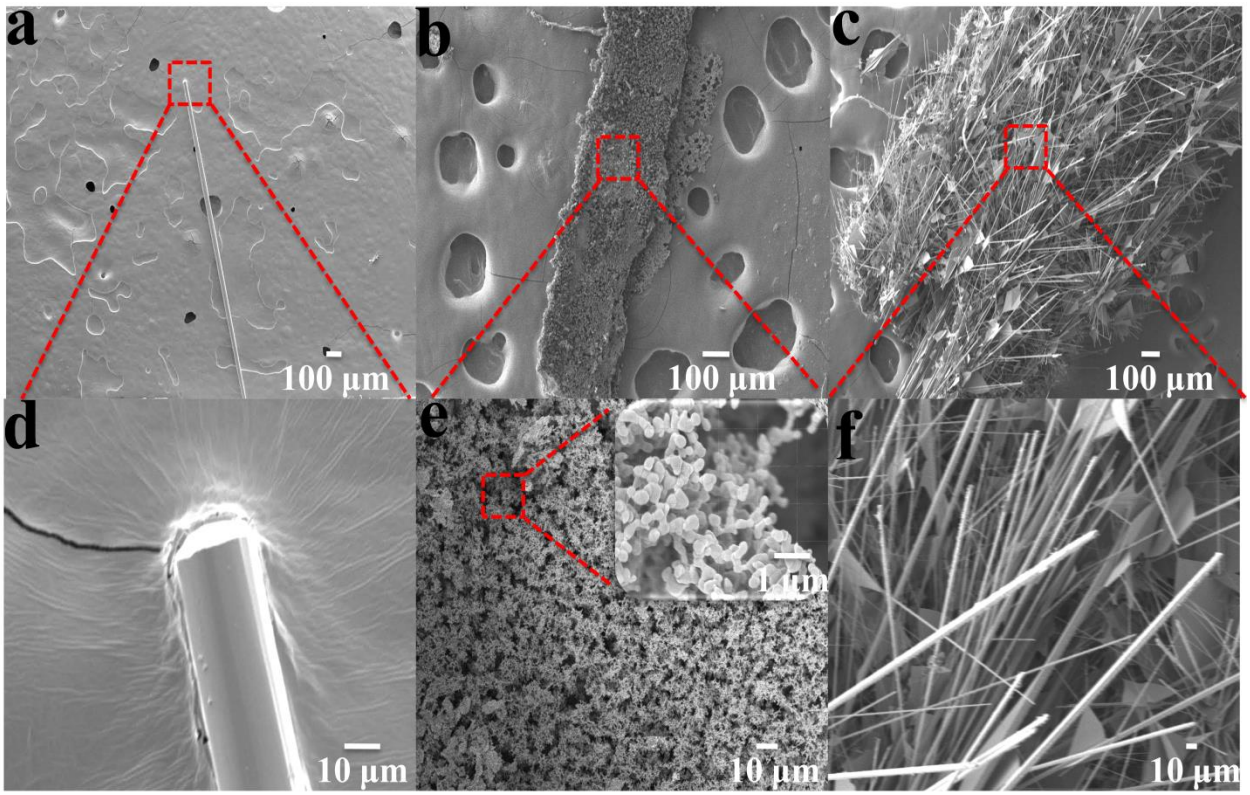

Figure 5.2 Field-emission scanning electron microscopy (FE-SEM) images of as-synthesised ZnO micro-architectures. **(a)** ZnO microwire (ZnO MW). **(b)** ZnO coral like microstrip (ZnO CMS). **(c)** ZnO fibril like clustered microwire (ZnO F-MW). **(d, e, f)** Magnified images of the respective ZnO micro-architectures at 10 μm scale.

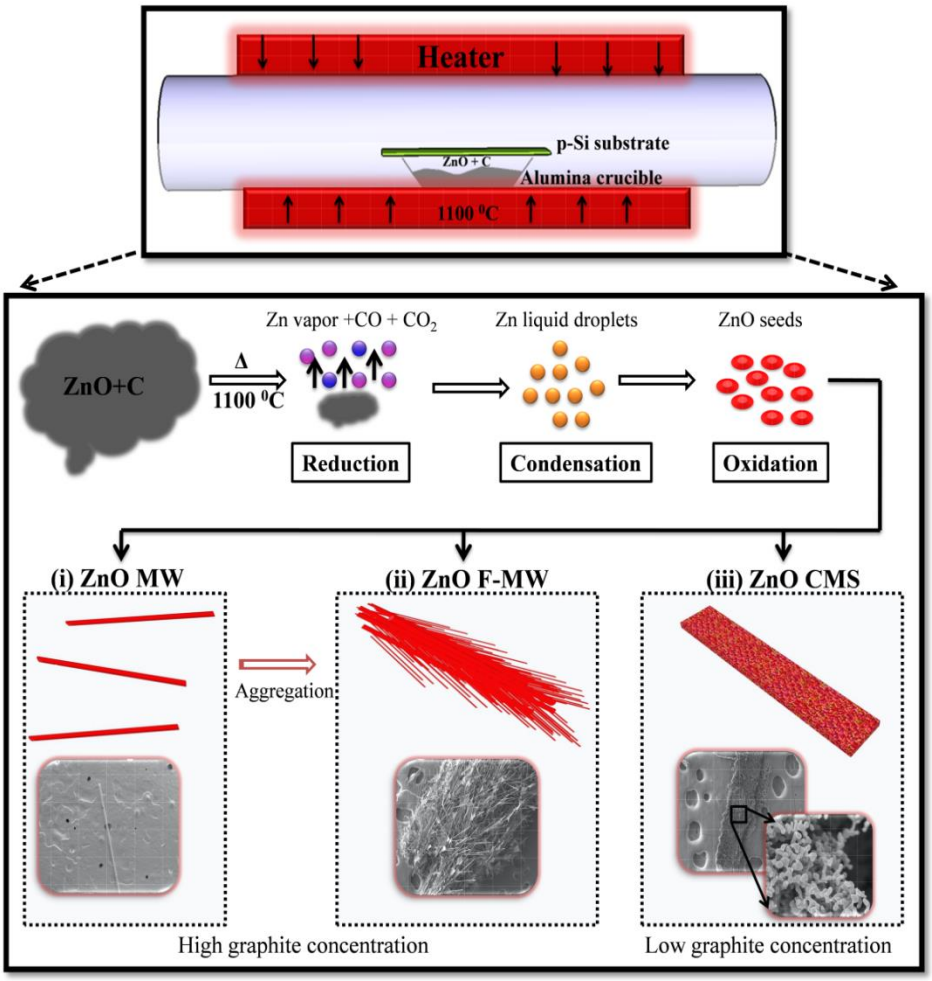

Figure 5.3 Schematic illustration of ZnO micro-architecture growth mechanism.

Figure 5.3 illustrates the growth mechanism of ZnO micro-architectures through a one-step VPT technique. The process that drives the formation of ZnO can be categorized as (i) reduction, (ii) transportation, (iii) absorption, (iv) condensation, (v) oxidization and (vi) solidification/crystallization[55]. When the reactant mixture (ZnO: Graphite powder) is treated at a higher temperature of 1100 °C it undergoes carbothermal decomposition ($ZnO + C \rightarrow Zn + CO$; $ZnO + CO \rightarrow Zn + CO_2$) and gets reduced to Zn vapor or its sub-oxide vapor ($ZnO_{x<1}$) along with producing oxidizing gases like CO, CO_2[56]. In the modified VPT technique, the transportation of produced Zn vapor is restricted as there is no influence of the carrier gas, and the catalyst-free p-Si substrate hinders the absorption of vaporized Zn owing to its poor sticking

co-efficient [57]. Thus the produced Zn vapor gets maintained within the crucible. The substrate freest Zn vapor itself acts as a catalyst[58] governing its condensation into Zn liquid droplets and further gets oxidized by the oxidizing gas (CO/CO_2) that was produced during thermal decomposition of reactant ZnO. Finally, the crystallization occurs at the interface of Zn vapors/oxidizing gas forming ZnO seeds serving as a nucleation zone for the growth of micro-structures. The orientation of micro-structures can be explained based on the following concepts,

(i) **ZnO MW:** At the beginning of the reaction when there is a high concentration of graphite, the growth process takes place faster leading to largely sized nucleation zone[2]. Therefore, micro wire (MW) structure is likely to form due to the faster crystallographic plane (001) growth of ZnO[58].

(ii) **ZnO F-MW:** The architectural arrangement of fibril like clustered micro wire (F-MW) is anticipated from the vapor solid process (VS) contributing to an anisotropic growth of ZnO where the growth rate is unequal. This may lead to dislocation or accumulation of as-formed micro wires. Also, the micro wires are trapped within the crucible as there is no Zn vapor mass transportation. Hence, as-grown micro wires gradually involves aggregation among itself mediated through self-organization leading to the development of F-MW[59].

(iii) **ZnO CMS:** As observed from FESEM results, coral like micro strips (CMS) are formed by conjugation of many ZnO nanoparticles under a single strip line. This is expected due to the insufficient concentration of graphite (as the reaction is proceeded) leading to slow growth speed thus hindering the micro wire pattern of ZnO[56].

The microstructure/size of peculiarly ordered ZnO F-MW closely depends on the conditions of vapor phase transport technique such as elevation temperature and homogeneous

mixture of ZnO: graphite raw powder thus forming perfect cylindrical fibrils like structure (Figure 5.1(b, c)). Here, the mass transportation of ZnO at its evaporation zone is altered as there is no use of carrier gas. Also, the catalyst-free p-Si substrate provides no nucleation point for the growth of ZnO on the substrate. Hence, free-standing ZnO micro-architectures are obtained due to the modified synthesis methodology resembling the structure of naturally existing corals and fibrils (**Figure 5.4**).

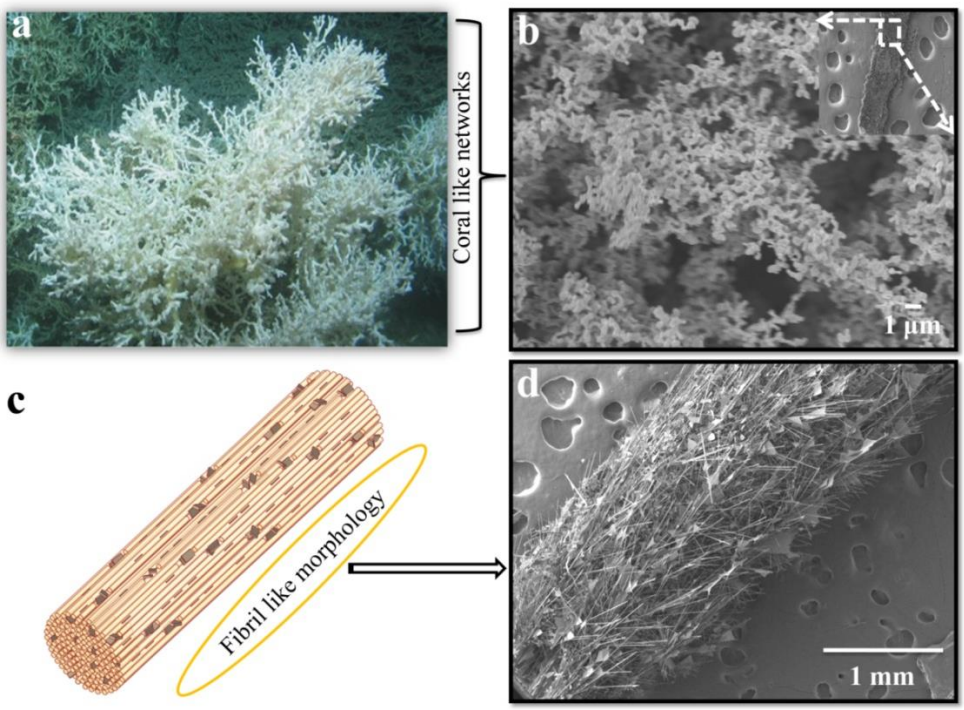

Figure 5.4 Comparison of ZnO micro-architectures with naturally existing materials. **(a, b)** Structure of ZnO CMS resembling coral species like morphology (Reference: http://www.xray-mag.com/content/coral-populations-north-atlantic-under-threat-climate-change). **(c, d)** Structure of ZnO F-MW similar to fibril like morphology (Source *DOI: 10.1038/nmat4089*).

The purity of as-prepared ZnO micro-architectures was confirmed through Energy dispersive X-ray analysis (EDAX). **Figure 5.5** represents the EDAX spectrum of ZnO MW, ZnO CMS and ZnO F-MW. It confirms that the formation of final product is ZnO and is highly free

from traces of impurities and constituents only Zn and O close to the atomic stochiometric ratio of 1:1 (inset table).

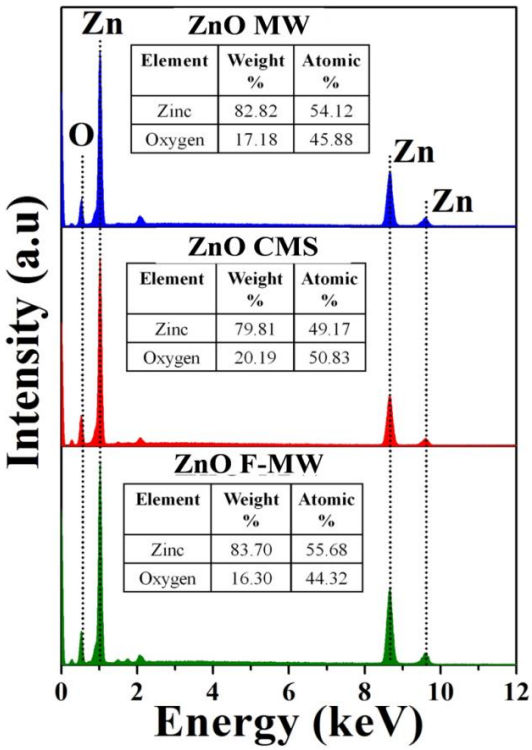

Figure 5.5 Elemental composition of Zn and O present in ZnO MW, ZnO CMS and ZnO F-MW.

Molecular vibrational properties of as-synthesized ZnO micro-architectures were investigated using the Raman spectroscopy operated at an excitation wavelength of 514 nm and an operating power ≈ 10 mW, respectively. **Figure 5.6**(a) represents the room-temperature Raman spectrum in the spectral range of 100 – 800 cm^{-1} for ZnO MW, ZnO CMS and ZnO F-MW. The spectrum consists of five major peaks located at 108, 342, 391, 446 and 589 cm^{-1}, which corresponds to respective phonon modes of wurtzite ZnO. The Raman peak located at 108 cm^{-1} is assigned to E_2 (low) phonon mode. The additional Raman peaks located at about 342, 391, 446 and 589 cm^{-1} are assigned to E_{2H} - E_{2L}, A_1 (TO), E_2 (high) and E_1 (LO) secondary multi-photon scattering modes, respectively[47]. Generally, E_1 (LO) represents the defect sites containing

zinc interstitial (Zn_i) and oxygen vacancy (V_O) in ZnO. All the three morphologies of as-synthesized ZnO exhibit similar vibrational properties though ZnO CMS has a drastic reduction in the intensity of phonon modes. This might be due to the translation of crystallographic symmetry from micro wire like structure to coral branches of ZnO nanoparticles.

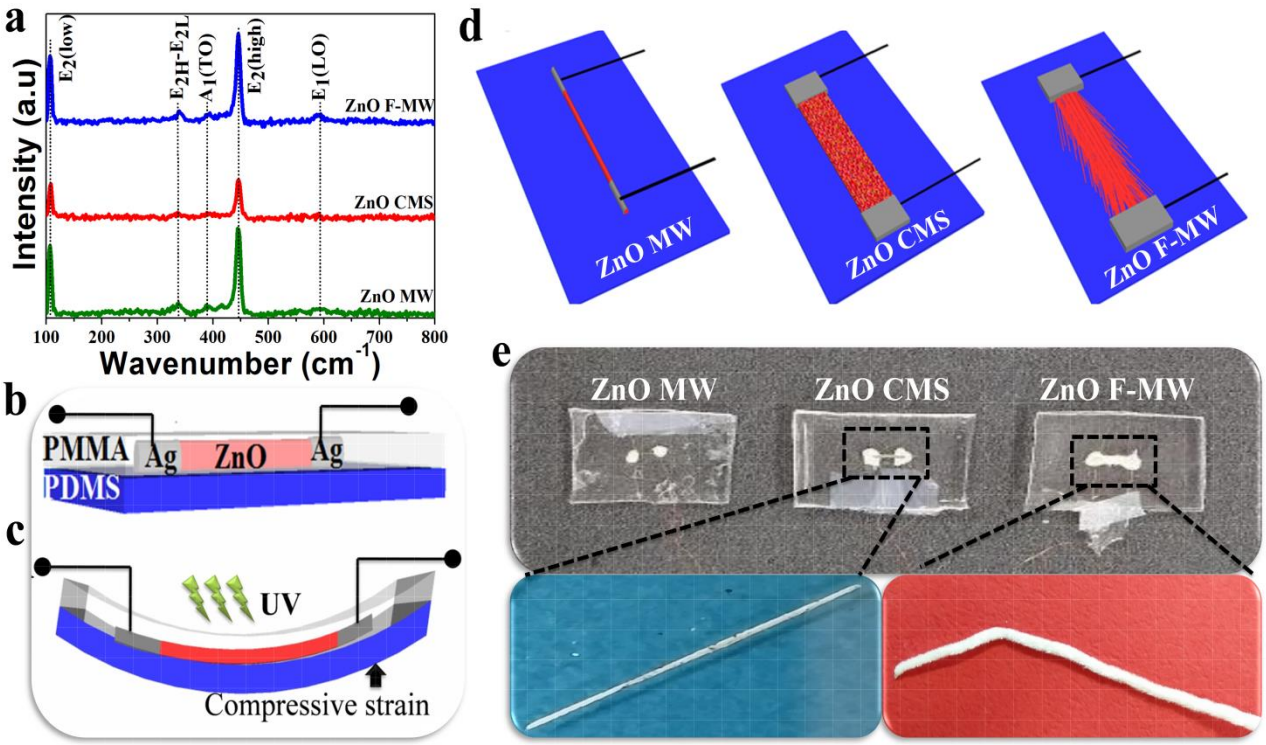

Figure 5.6 (a) Raman spectrum of ZnO micro-architectures. **(b)** Schematic representation of as-fabricated PD. **(c)** Compressive strain induced behaviour of PD. **(d)** Schematic view of ZnO device architectures. **(e)** Optical images of as-fabricated PD devices using ZnO MW, ZnO CMS and ZnO F-MW.

5.3.2 Photodetection capabilities of ZnO MW, ZnO CMS and ZnO F-MW

Influence of morphology on photo sensing behavior of ZnO was briefly studied through fabricating M-S-M based PD. An individual ZnO micro-architecture based PDs were constructed by the standard procedure as discussed in the experimental section. The as-fabricated ZnO PD

structure is schematically shown in Figure 5.6(b). Figure 5.6(c) represents the bending behavior of the device when a compressive strain (- ε_z) is exerted on it. Further, the scheme of fabricated PD with various morphologies (ZnO MW, CMS and F-MW) is illustrated in Figure 5.6(d). Also the optical images of as-fabricated devices are shown in Figure 5.6(e). Typical I-V analysis was carried out by placing the device inside a black box which is highly opaque to the environmental light effects (**Figure 5.7**)

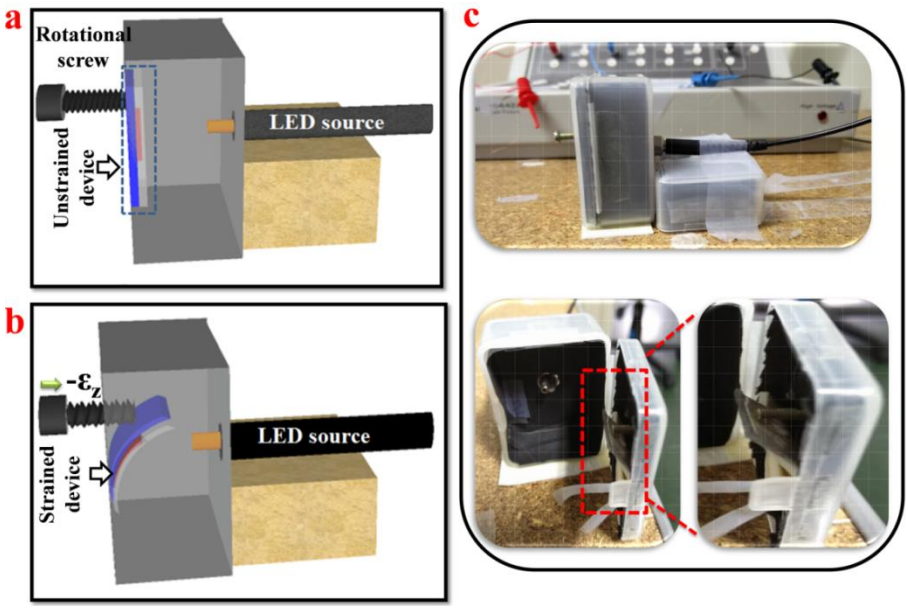

Figure 5.7 Schematic representation of as-designed strain measurement setup. **(a)** Under the unstrained condition. **(b)** Under the strained condition. **(c)** Optical images of the LED light source, PD placed inside the black box and magnified view of strain induced bending nature of the device.

Firstly, the photosensing performance of ZnO MW based PD under blue light illumination (λ = 405 nm) is studied. **Figure 5.8**(a) shows the I-V characteristics of the ZnO MW in the dark and under illumination at different light intensities of 6 mW/cm^2, 11 mW/cm^2 and 17 mW/cm^2.

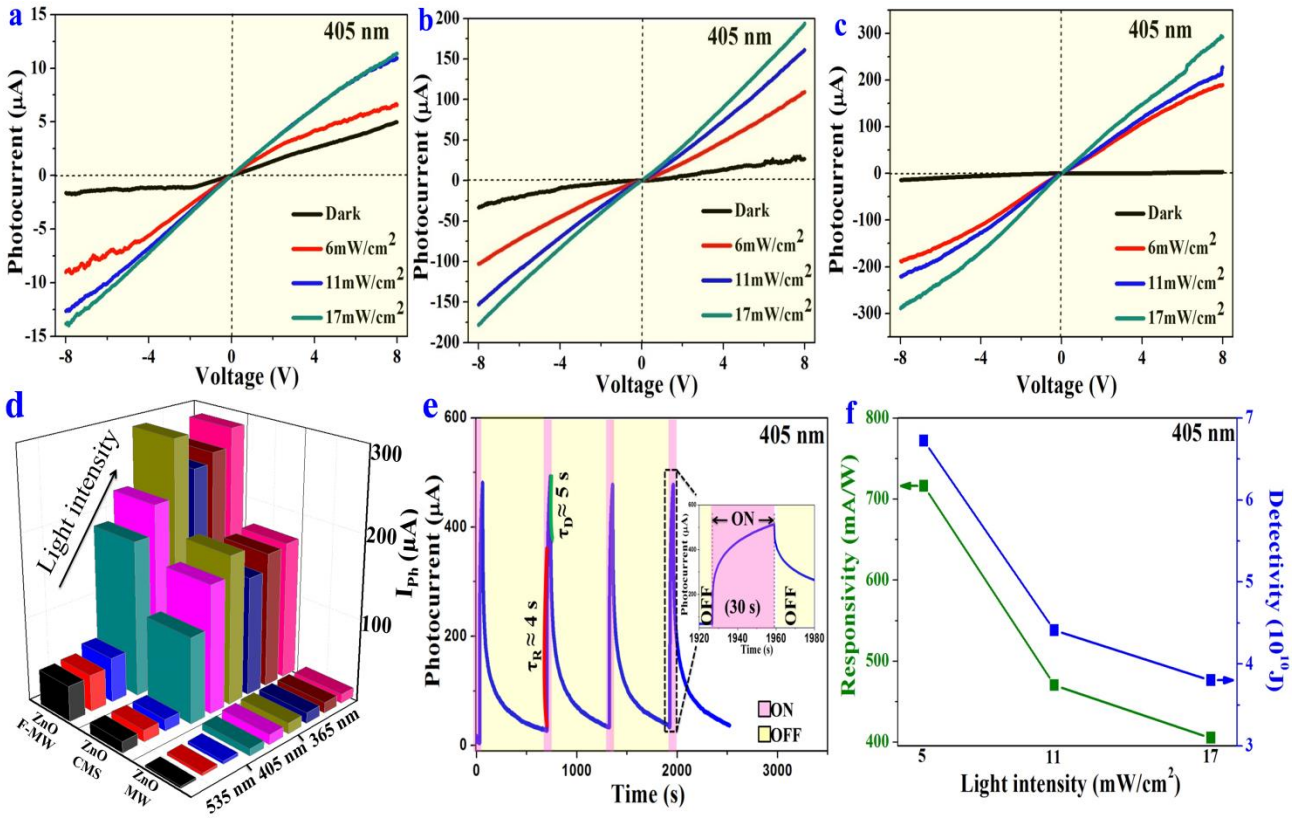

Figure 5.8 Photoresponsive analysis of ZnO PD at 405 nm. **(a)** ZnO MW. **(b)** ZnO CMS. **(c)** ZnO F-MW. **(d)** Comparative analysis of current responses at 365, 405 and 535 nm wavelengths. **(e)** Time responsive ON/OFF switching behaviour of ZnO F-MW. **(f)** Responsivity and detectivity of ZnO F-MW at $\lambda_{405\ nm}$.

The photocurrent response (I_{Ph}) increased from 1.64 μA (dark current, I_D) to 9.04 μA (6 mW/cm^2), 12.67 μA (11 mW/cm^2) and further to 13.83 μA (17 mW/cm^2) at an applied biasing voltage of $\pm$ 8 V. The working of PD depends on the mechanism where the sensing material (ZnO) generates charge carriers (e^- and h^+) upon adsorbing the incident photon energy (hν)[47]. The photogenerated charge carriers tunnel through the Schottky barrier (SB) contacts formed at M-S interfaces contributing to the photocurrent (I_{Ph}) of the device. Subsequently, the performance of ZnO CMS and ZnO F-MW were tested under the same wavelength with varied light intensities (6 mW/cm^2, 11 mW/cm^2 and 17 mW/cm^2). ZnO CMS produces the dark current

of ≈ 33.2 μA (at bias voltage of ± 8 V) and further, could observe a linear increment in the I_{Ph} response such as 103, 153 and 178 μA with respect to the illumination intensities as shown in Figure 5.8(b). Figure 5.8(c) illustrates the measured I-V characteristics of ZnO F-MW based PD at a wavelength of 405 nm. Under the light illumination, the current response increased from 14.2 μA (I_d) to 186 μA (6 mW/cm^2), which further enhanced to 221 μA (11 mW/cm^2) and 290 μA (at 17 mW/cm^2) upon varying the light irradiation. The ability to sense at broad spectral ranges was tested using light sources of wavelength 365 nm (**Figure 5.9**) and 535 nm (**Figure 5.10**) at varied light intensities, and a comparative plot is shown in Figure 5.8(d). The light intensity dependence of photocurrents (I_{Ph}) of ZnO F-MW at λ_{365}, λ_{405} and $\lambda_{535\ nm}$ is plotted in **Figure 5.11**. It can be noticed that the I_{Ph} increased concerning the optical illumination exhibiting the capability of wide operating spectral ranges.

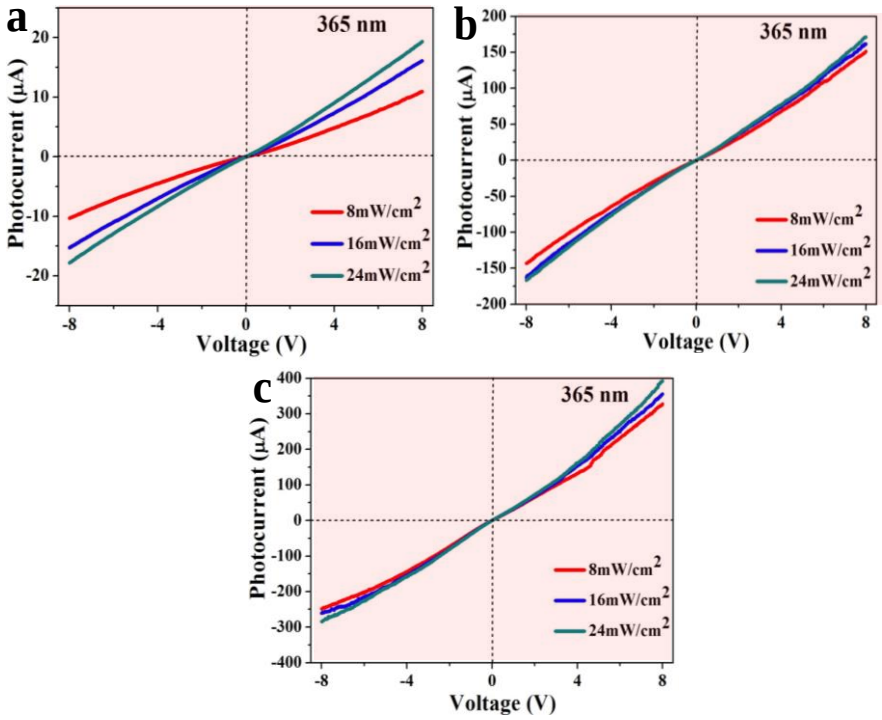

Figure 5.9 I-V characteristics at a wavelength of 365 nm under varied light intensities. **(a)** ZnO MW. **(b)** ZnO CMS. **(c)** ZnO F-MW.

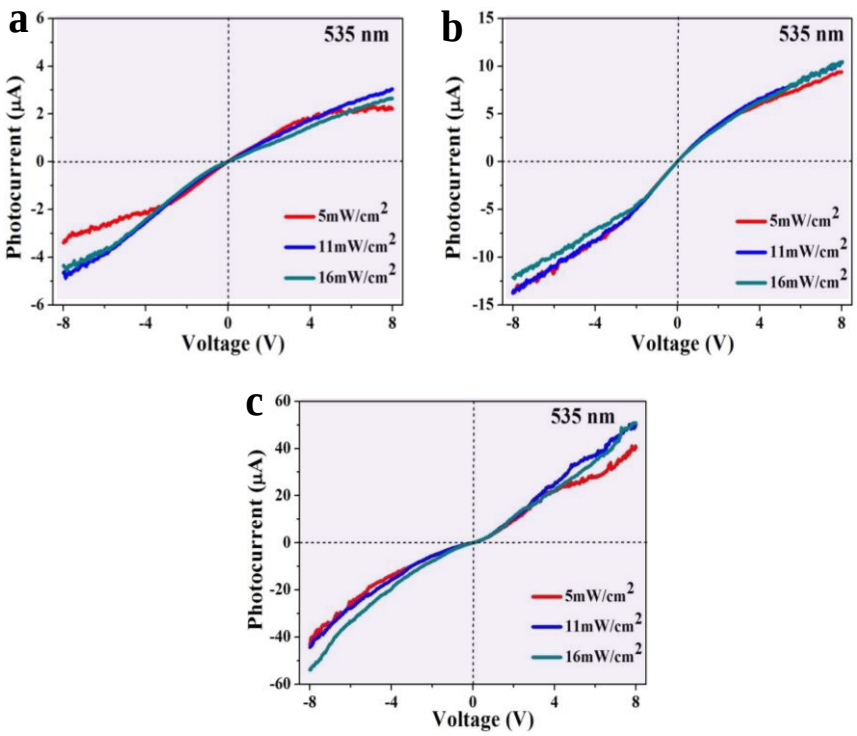

Figure 5.10 I-V characteristics at a wavelength of 535 nm under varied light intensities. **(a)** ZnO MW. **(b)** ZnO CMS. **(c)** ZnO F-MW.

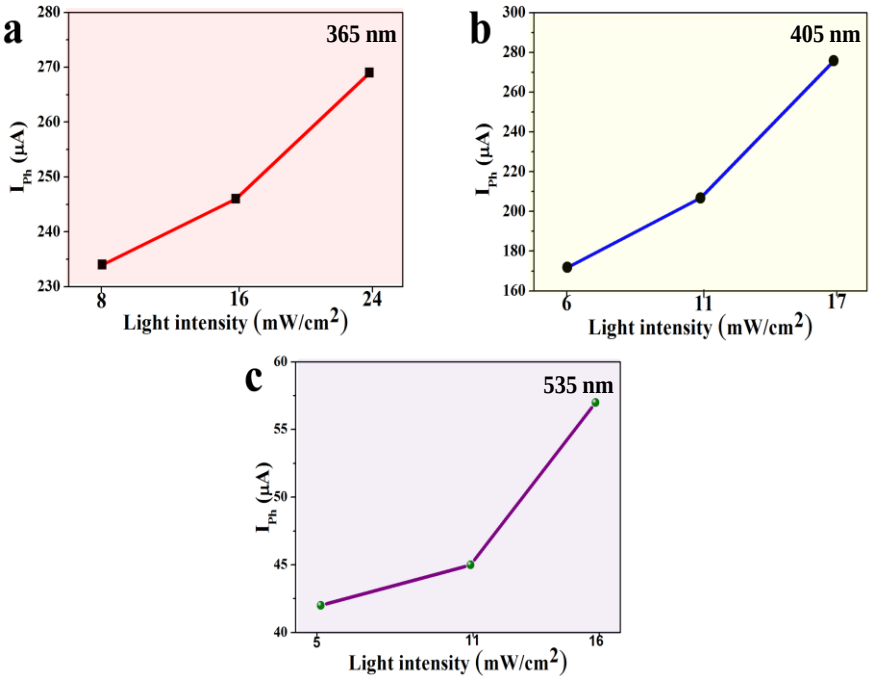

Figure 5.11 Dependence of photocurrent of ZnO F-MW with increase in light intensities at a biasing voltage of ± 8 V for wavelengths. **(a)** 365 nm. **(b)** 405 nm. **(c)** 535 nm.

Of the all micro structured devices, ZnO F-MW exhibited higher photocurrent response than ZnO MW and ZnO CMS. Significant variation in the I-V characteristics is observed depending on the geometrical effect of ZnO material (I_{Ph} ≈ ZnO F-MW > ZnO CMS > ZnO MW). In addition to UV light (365 nm), as-synthesized ZnO F-MW is sensitive to green light (535 nm) and also showed a higher response at blue light emission (405 nm) (The mechanism of broadband spectral activity is briefed in **Figure 5.12** through bandgap analysis). The higher current response from ZnO F-MW is due to the volumetric effect which increases the active surface area of the sensing material which in turn drives the generation of more charge carriers. Hence, further analysis and studies were carried out using ZnO F-MW based PD at $\lambda_{405\ nm}$.

Figure 5.8(e) represents the time responsive periodic ON/OFF switching behavior of the as-fabricated ZnO F-MW photodetector (PD). The analysis was performed at a biasing voltage of 8 V, where the PD was exposed to a light source ($\lambda_{405\ nm}$) for a period of 30 s and then the source illumination is turned OFF (inset). When the visible light source ($\lambda_{405\ nm}$) is ON, I_{Ph} of the ZnO F-MW device raised steadily. While the source is turned OFF (after an exposure period of 30 s), the I_{Ph} gradually drops with a longer decay time. The time response parameters (τ_R, τ_D) were calculated by estimating the exponential rise to 63 % ($\approx 1 - e^{-1}$) of I_{Ph} and exponential decay to 37 % ($\approx e^{-1}$) of I_{Ph}[47]. Also, Figure 5.8(e) illustrates the switching behavior of ZnO F-MW based PD with a rise time (τ_R) of ≈ 4 s and decay time (τ_D) of ≈ 5 s. Besides, the characteristics parameter of PDs were calculated such as responsivity ($R_{405\ nm}$), photoconductive gain (G), detectivity (D ∗) and are summarized in **Table 5.1**.

Table 5.1 Characteristic parameters of ZnO micro-architectures based PD.

Architecture	λ [a] (nm)	P_L [b] (mW/cm^2)	D* [c] ($cmH^{1/2}W^{-1}$)	G [d]	R [e] (mA/W)
ZnO MW	405	6	6.02×10^{10}	4.72	1542
		11	4.95×10^{10}	3.84	1253
		17	3.49×10^{10}	2.74	896
ZnO CMS	405	6	3.58×10^{10}	3.54	1167
		11	3.36×10^{10}	3.35	1095
		17	2.62×10^{10}	2.61	854
ZnO F-MW	405	6	6.72×10^{10}	2.19	716
		11	4.41×10^{10}	1.44	470
		17	3.80×10^{10}	1.24	406

[a] Wavelength ,[b] Light intensity, [c] Detectivity, [d] Photoconductive gain, [e] Responsivity

The as-fabricated ZnO micro-architecture based PD exhibits comparable performance to that of earlier reports as shown in Table **5.2**.

Table 5.2 Comparison of proposed ZnO microstructure based photodetector with other published reports.

ZnO Micro structure	Type	V [a]	R [b] (A/W)	I_{Ph} [c] (A)	D* [d] ($cmH^{1/2}W^{-1}$)	G [e]	Ref
Rod	MSM	5	4×10^{4}	45 μ	-	1.5×10^{5}	60
Comb	MSM	5	-	-	-	-	61
Wire	p - n	5	200 m	-	-	-	62
Wire	MSM	1	7.5×10^{6}	-	3.3×10^{17}	2.6×10^{7}	63
Tube	p - n	15	-	5 m	-	-	64
Wire	p - n	9	-	15 μ	-	-	65
Wire	MSM	5	4.5×10^{4}	1.9 μ	-	1.5×10^{5}	66
Core-shell	p - n	2	11	37.6 n	-	-	67
MW	MSM	8	1542 m	9.04 μ	6.02×10^{10}	4.72	This work
CMS	MSM	8	1167 m	103 μ	3.58×10^{10}	3.54	This work
F-MW	MSM	8	716 m	186 μ	6.72×10^{10}	2.19	This work

[a] Bias voltage, [b] Responsivity, [c] Photocurrent, [d] Detectivity, [e] Photoconductive gain

The bandgap of as-synthesized ZnO micro-architectures were determined through absorbance analysis and represented in Figure 5.12 along with its equivalent tauc plot. The photoresponse at various spectral wavelengths (mechanism of photoresponse) are discussed below

(i) **405 nm:** The bandgap of ZnO F-MW is found to be 3.05 eV and that of ZnO CMS is 3.08 eV (Figure 5.12(a)). If we theoretically calculate the respective wavelengths of the bandgap energies (using $E_g = hc/\lambda$), it corresponds to 406.5 nm (ZnO F-MW, 3.05 eV) and 402.5 nm (ZnO CMS, 3.08 eV). The bandgap narrowing results from the increase in crystallite size of as-synthesized ZnO micro-architectures *via* high temperature VPT process[68]. Hence, the reduction in the bandgap is the major factor responsible for the spectral activity of ZnO micro-architectures to highly respond for 405 nm wavelength.

(ii) **365 nm:** From the photonic energy principles, the charge carriers are generated when the supplied photon energy (hν) is equal to or greater than the bandgap of the material. According to Shockley and Queisser limit, there is a possibility of spectral losses when a greater amount of energy is supplied to the optically active material[69]. When an energy of 365 nm is illuminated on to the as-fabricated ZnO micro-architectures the e^- gets excited to the CB with higher energy by absorbing the photon; but the excited e^- are highly unstable by gaining more amount of energy, which tends to relax back to its original state by emitting/losing the absorbed energy before reaching the Ag/ZnO interface. So when compared to $E_g \approx h\nu$ case, the recombination rate of e^--h^+ pair is high when $E_g > h\nu$[69]. Since the thermalization (heat dissipation) is less when $E_g \approx h\nu$, the efficiency of photocurrent generation is high at 405 nm than 365 nm.

(iii) **535 nm:** The narrowed bandgap (3.05 - 3.08 eV) using VPT technique is due to high temperature (1200 °C) processing which had induced more vacancy sites adding to the native defect levels[70] of ZnO such as oxygen and zinc (V_O, V_{Zn}, O_i, Zn_i) vacancy/interstitial sites[71]. The E_1(LO) peak response at 589 cm^{-1} in Raman analysis (Figure 5.6(a)) confirms the presence of defect levels exhibited by the as-synthesized ZnO micro-architectures. Generally, these defective energy levels lies above the maximum of the valence band (VB) and minimum of the conduction band (CB) leading to tune the spectral activity of ZnO to absorb light of visible range. Figure 5.12(b) represents the energy band level as a position of the defective states. The defective vacancy sites near CB are majorly responsible for the visible activity (535 nm) of ZnO. Therefore, the spectral response of ZnO micro-architectures at 535 nm occurs from the defect level photogenerated charge carrier transition i.e. from the V_O^{-1}/V_{Zn}^{-1} to the CB[71, 72].

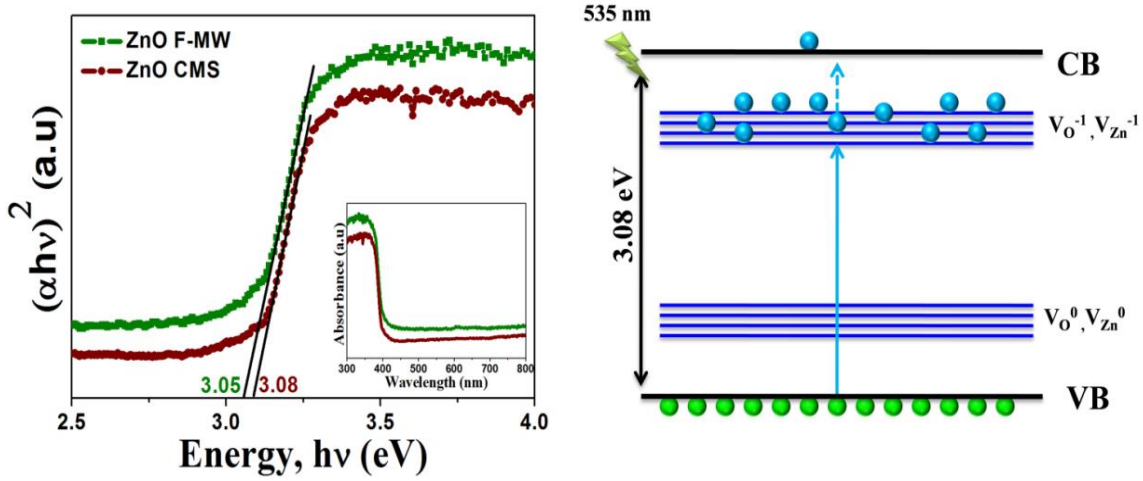

Figure 5.12 (a) Tauc plot analysis for the bandgap estimation of as-synthesized ZnO micro-architectures (inset shows the corresponding absorption spectra). **(b)** Energy band level of ZnO F-MW illustrating defect state induced charge carrier transition.

5.3.3 Piezotronic effect of ZnO F-MW based PD

The photoresponse of ZnO F-MW can be tuned by precisely modulating the charge transport and separation process at the M-S-M interfaces. The spontaneous internal polarization (**Figure 5.13**) exhibited by ZnO is utilized to investigate the performance of as-fabricated PD under various strain conditions.

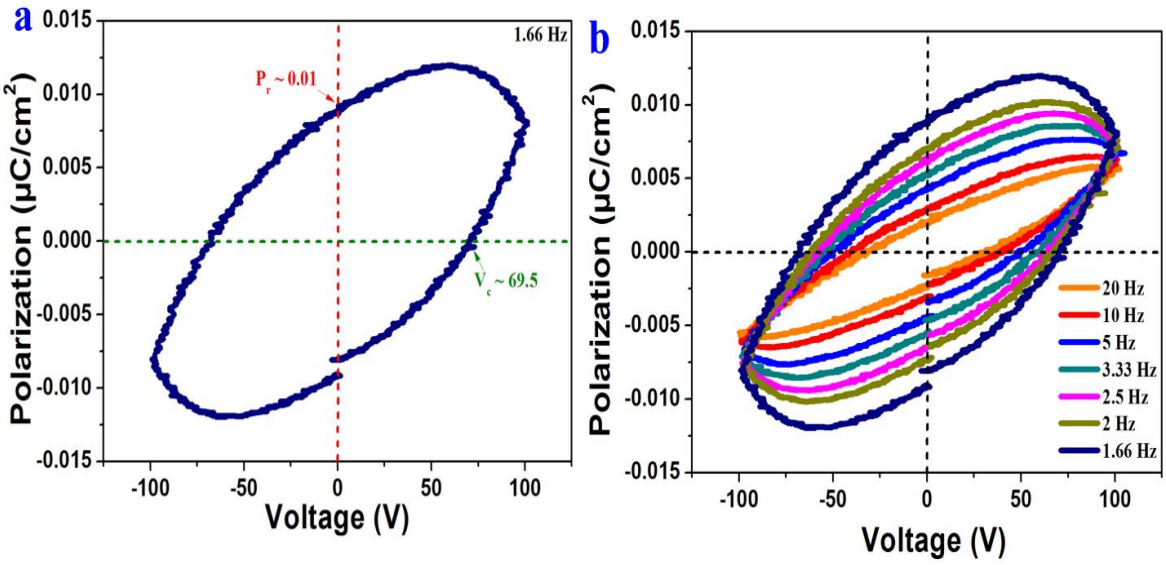

Figure 5.13 (a) P-V hysteresis loop of as-synthesized ZnO F-MW under an applied electric field (V) of 100 V. **(b)** Frequency dependence of remanent polarization (1.66 – 20 Hz, 100 V).

Figure 5.13 illustrates the ferroelectric behavior of ZnO F-MW through P-V loop analysis. The shape of P-V loop determines the lossy capacitive nature of the material with the remanent polarization (P_r) of 0.01 μC/cm^2 and coercive field (V_c) of 69.5 V for a period of 600 ms (1.66 Hz) (Figure 5.13(a)). The polarization at the negative electric field is attributed to the small leakage current existing in the material which also suggests the rectified (Schottky) formation of contacts between Ag/ZnO F-MW[73, 74]. Figure 5.13(b) represents P-V loop of ZnO F-MW upon increased frequency between the ranges of 1.66-20 Hz suggesting strong frequency

dependent as the characteristic nature of intrinsic ferroelectric property (spontaneous polarization) inherited by as-synthesized ZnO F-MW.

The compressive strains were applied to the ZnO PD in a precise manner by the rotating screw set up in the 3D-rotating stage. The nature of the PD under compressive strain (- ε_z) conditions are examined by emphasizing on piezo-phototronic effect. Initially, I-V characteristics of ZnO F-MW device was investigated in the absence of light source under various compressive strain conditions and the corresponding results were shown in **Figure 5.14**(a). It shows the rectification behavior under strained conditions. The ZnO F-MW device placed exactly at the center of the box, where one side of the device is fixed and the other end experiences to bend freely by rotating the screw setup as shown in Figure 5.7. Here, the number of screw rotations is proportional to the changes in the compressive strain induced on the ZnO F-MW PD. The strain % exerted on the device is calculated to be 0.37, 0.75, 1.13, 1.50 and 1.87 % which is given by[75]

$$\varepsilon_z = 3\,\frac{a}{l}\frac{D_{max}}{l}(1 - Z/l) \qquad \text{- (1)}$$

where *a* and *l* are the thickness and length of PDMS substrate, D_{max} is the maximum deformation of the device and *z* is the distance moved by the device through rotating screw. The dark current decreases steadily upon increasing the strain rate from - 0.37 % to - 1.87 % (Figure 5.14(b)).

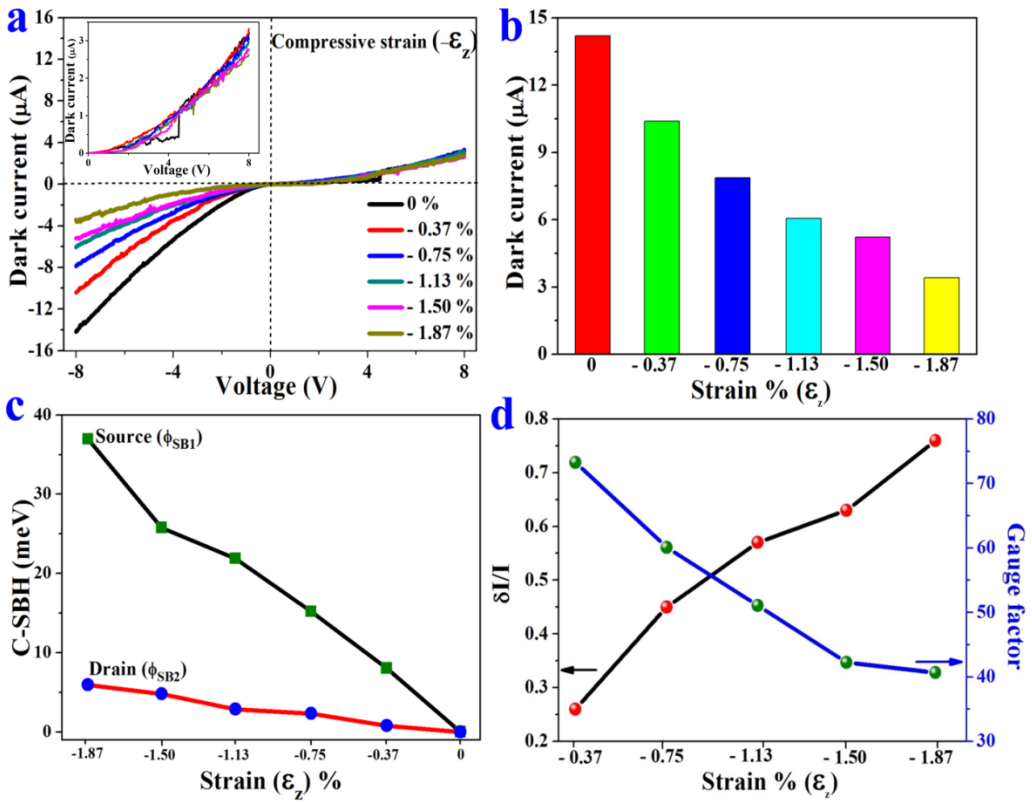

Figure 5.14 Piezotronic effect of ZnO F-MW based PD. **(a)** Dark current response under increased compressive strains (inset represents magnified view of forward bias condition). **(b)** Significance of compressive strain on PD performance. **(c)** Characteristic change in the Schottky barrier heights (C-SBH). **(d)** Normalized change in current (δI) and its gauge factor as a function of compressive strain.

A well established unsymmetrical Schottky contact is observed between the M-S-M interfaces which serves as two Schottky diodes connected back to back. The Schottky barrier height (Φ_{SB}) at one M-S interface (source, Φ_{SB1}) is lower than the other M-S interface (drain, Φ_{SB2}) thus leading to a non-linear current response from the device. Whenever strain is applied to the device, the Schottky barrier heights (SBH) are modulated thus altering the piezopotential charges generated at the M-S-M interfaces. Change in Schottky barrier heights (C-SBH) can be observed directly from the deviations in I-V response of ZnO F-MW device under compressive

strains, which can be theoretically estimated using the thermionic emission diffusion theory and the corresponding equation is[76],

$$-\Delta\phi_{Bn} = -kT\ ln\frac{I(\varepsilon_z)}{I(0)} \quad \text{- (2)}$$

where $\Delta\phi_{Bn}$ is the change in Schottky barrier height (C-SBH) at M-S-M interfaces, *k* is the Boltzmann constant (1.38064×10^{-23} $m^2kgS^{-2}K^{-1}$), T is the room temperature (25 °C) and $I(\varepsilon_z)$ and $I(0)$ are the dark currents under zero strain and applied strain conditions. Using this relationship, C-SBH at dark current under varied strain conditions (- 0.37, - 0.75, - 1.13, - 1.50 and - 1.87 %) are calculated to be 8.02, 15.20, 21.89, 25.76, 36.96 meV (source, Φ_{SB1}) and 0.77, 2.32, 2.85, 4.77, 5.93 meV (drain, Φ_{SB2}). Figure 5.14(c) represents the observed asymmetrical change in SBH at M-S-M interfaces (Φ_{SB1} andΦ_{SB2}). The performance of ZnO F-MW PD upon various strain conditions were estimated by the gauge factor[75] i.e,

$$Gauge\ factor = \frac{\delta I/I_0}{\varepsilon} \quad \text{- (3)}$$

where δI is the normalized change in the current when the strain is applied, I_0 is the current at the unstrained condition and ε being the strain rate (- 0.37, - 0.75, - 1.13, - 1.50 and - 1.87 %). The calculated gauge factors at different strains were shown in Figure 5.14(d) and notably achieved the highest gauge value of ≈ 73.27 at - 0.37 % strain. This gauge value decreases to 60.09, 51.10, 42.25 and 40.67 upon increased strain conditions - 0.75, - 1.13, - 1.50 and - 1.87 %, respectively. It is highly desirable to consider that the estimated gauge factor is higher than previous reports[77,76]. Further, the Young's modulus (E) of as-synthesized ZnO micro wire (ZnO MW) and ZnO fibril like clustered micro wire (ZnO F-MW) are expressed theoretically as[78],

$$E = \frac{\sigma}{\varepsilon_z} \quad \text{- (4)}$$

where, σ is the stress factor that depends upon the applied force acting at a specific area[79] ($4F/\pi d^2$) and ε_z is the strain exerted on the device through rotational screw based measuring setup. The Young's modulus of ZnO micro wire (ZnO MW) with an average diameter (d) of ≈ 250 μm is determined to be 62.56, 30.866, 20.48, 15.43 and 12.37 GPa for an induced compressive strain (- ε_z) of 0.37, 0.75, 1.13, 1.50 and 1.87 % (**Figure 5.15**(a)). Similarly, the Young's modulus of 1 mm diameter (d) sized ZnO fibril like clustered micro wire (ZnO F-MW) is computed as 2.5, 1.23, 0.82, 0.62 and 0.5 MPa at the same increased strain conditions (Figure 5.15(b)).

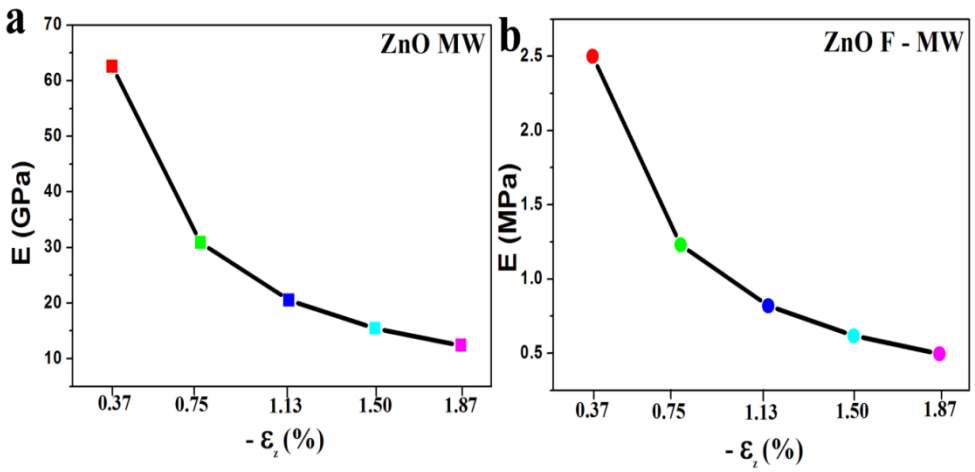

Figure 5.15 The relative effect of compressive strain on the Young's modulus. **(a)** ZnO micro wire (ZnO MW). **(b)** ZnO fibril like clustered micro wire (ZnO F-MW).

Observed non-linear nature of Young's modulus-strain is associated with the contributions from two major factors (i) the strain applied is compressive in nature showing negative behaviour,[80] and (ii) the increase in the deflection rate alters the pore distribution causing possible formation of cracks in the ZnO micro-architecture[80]. Due to these factors, residual strain is experienced by the device leading to the decrease in its modulus of elasticity.

Also, the variation in Young's modulus range (MPa - GPa) clearly justifies the surface to volumetric effect revealing that elasticity increases as the size (diameter) decreases[81].

5.3.4 Piezo-phototronic effect of ZnO F-MW PD

Finally, the piezo-phototronic effect was studied through the I-V responses from the PD at the maximum strain rate of - 1.87 % using 405 nm light source at varied light intensities (**Figure 5.16**). The pictorial image of the measurement setup under light illumination is shown in Figure 5.16(a). The photocurrent of ZnO F-MW PD increased monotonically by increasing the light intensities of 405 nm source under fixed strained condition (- 1.87%) (Figure 5.16(b)). This is due to the photogenerated charge carriers which get diffused at the M-S-M interfaces. It clearly demonstrates that the photoresponse of the strained device is much lower than that of unstrained condition as shown in Figure 5.16 (c, d).

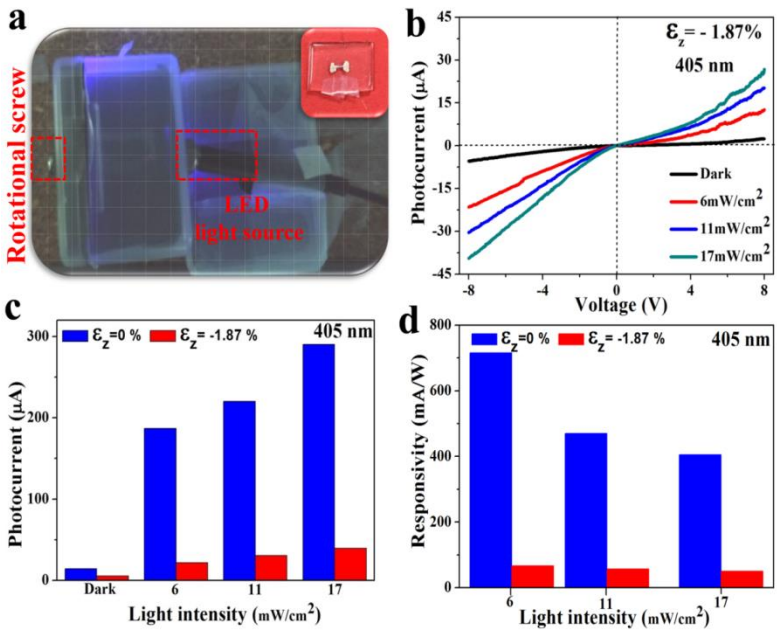

Figure 5.16 Piezo-phototronic effect of ZnO F-MW PD. **(a)** Optical image of 3D rotational measurement setup (inset showing as-fabricated PD). **(b)** I-V response of PD under various light intensity at a maximum strain condition. **(c)** Effect of strain on photogenerated current response. **(d)** Responsivity (R_{405}) under piezo-phototronic effect.

The strain induced piezoelectric potential and its corresponding C-SBH at the source and drain interfaces are illustrated schematically in energy band diagram (**Figure 5.17**). Figure 5.17(a) shows the asymmetrical energy band alignment at the M-S-M interfaces. From the I-V curves, it is evident that the two Schottky contacts ($\Phi_{SB1,}$ Φ_{SB2}) are established with differences in its barrier heights with the drain being higher than the source ($\Phi_{SB2} > \Phi_{SB1}$). This kind of behavior is usual in semiconducting materials due to the difference in carrier concentrations arising from growth instability such as point defects at Zn_i and O interstitial sites. At zero strain condition, the dark current at Φ_{SB1} is 14.2 μA and at Φ_{SB2} is 3.3 μA, which is in accordance with the existing differences in SBH. The non-linear characteristic of I-V curves determines the unequal distribution of piezoelectric potential in ZnO F-MW. When ZnO F-MW PD is subjected to a minimum compressive strain of - 0.37 %, the device bends proportionally altering the SBH at the M-S interfaces as illustrated in Figure 5.17(b). The strain applied at compressive conditions produces a negative piezopotential (σ^-) near the M-S interface thereby increasing the energy band from Φ_{SB1} to $\Delta\ \Phi_{SB1}$. As the strain is further increased (- 1.87 %), the more negative potential is created thus shifting the SBH to a higher level ($\Delta\ \Phi'_{SB1}$, Figure 5.17(c)). This is attributed to the accumulation of piezoelectric potential causing widening of the space charge (depletion) region thus altering the energy band alignment. In other words, the free charge carriers get neutralized by the negative piezoelectric charges (σ^-) produced under compressive strain by which the internal built-in potential decreases. Therefore fewer charge carriers are transported to the M-S interfaces leading to a linear decrease in dark current upon increasing the rate of compressive strain. This piezotronic effect acts predominantly at the free end of the device, whereas the fixed other end experiences negligible strain.

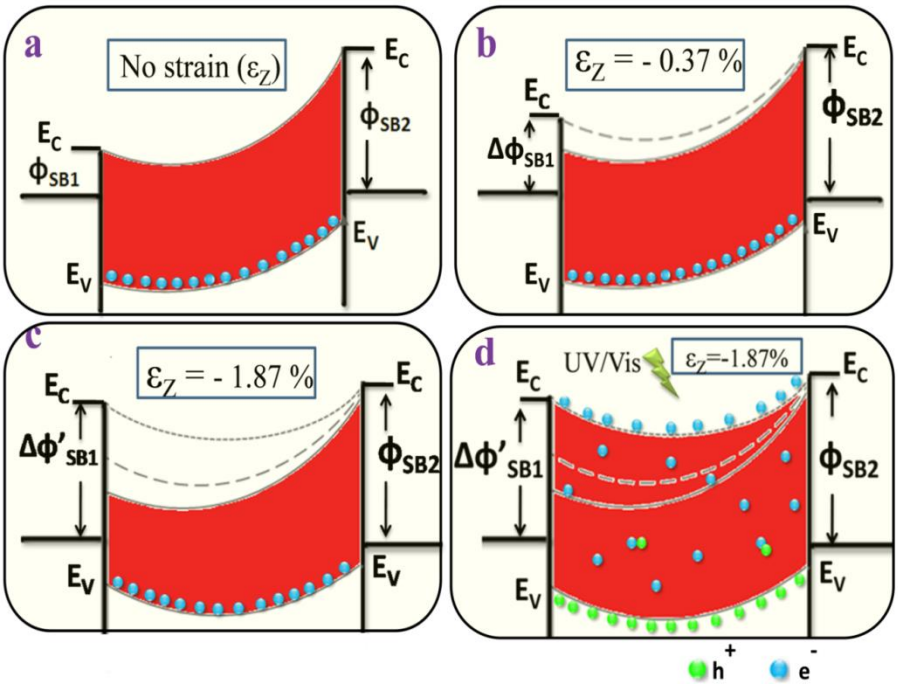

Figure 5.17 Schematic energy band diagram of M-S-M based PD. **(a)** At zero strain condition. **(b)** Initial strain of -0.37%. **(c)** Maximum strain of – 1.87 %. **(d)** Photogenerated charge carriers in the presence strain and light source.

The current response changes abruptly in the presence of light source even when the device is maintained at a maximum strain of -1.87%. Figure 5.17(d) illustrates the energy band characteristics of ZnO F-MW modulated by piezo-phototronic effect. Stimulated photo generated charge carriers tunnel through the M-S-M interfaces when the light source acts on the device. The photogenerated charge carriers with higher energy are capable to overcome the SB effect created due to the exerted compressive strain. This clearly demonstrates that the light illumination producing higher carrier concentration becomes the dominating factor which readily neglects the strain induced piezopotential. Also, as an effect of induced piezopotential charges (σ^-), the performance of the PD showed less response (Figure 5.16 (c & d)) compared to unstrained conditions due to piezo-phototronic effect via compressive strain. Thus strain and incident photon energies significantly influences the electrical transport characteristics at the M-S-M

interfaces and henceforth offering a qualitative strategy to precisely tune the properties of piezoelectric semiconducting materials for its practical applications in self-powered optoelectronic sensing systems and transmitter/receiver communication systems.

5.4 Conclusion

In summary, we synthesized highly crystallized ZnO micro-architectures (ZnO MW, ZnO CMS and ZnO F-MW) through a simplified vapor transport technique (carrier gas/catalyst-free). Fully packed flexible PDs were developed by transferring the microstructured ZnO onto a flexible PDMS substrate along with Ag as an electrode and PMMA as the packaging layer. Rectified I-V response behavior was observed for all PDs and varied symmetrically due to the large volumetric changes in the morphological structures such as ZnO MW, ZnO CMS and ZnO F-MW, respectively. As-fabricated ZnO F-MW PD exhibits excellent working characteristics with higher $I_{Ph} \approx 290$ μA at 17 mW/cm^2 and comparable responsivity ($R_{405\ nm}$) of ≈ 716 mA/W. The ability of photodetection was suppressed by applying external compressive strains (- ε_z = 0, 0.37, 0.75, 1.13, 1.50 and 1.87 %) which had effectively changed the Schottky barrier heights (Φ_{SB1}, Φ_{SB2}). Compared with reported micro-architectures, the unique fibril like clustered morphology (F-MW) of micro-sized ZnO exhibited superior photo sensing behavior with a detectivity range (D*) of 6.72×10^{10} cmH$^{1/2}$W^{-1} and broadened spectral activity extending from UV to Visible region (365 nm, 405 nm and 535 nm). All the results demonstrate that the piezo-phototronically tuned devices provide a promising way to develop flexible self-powered optical communication systems and sensors.

5.5 References

1 L. Wang, S. Liu, Z. Wang, Y. Zhou, Y. Qin, Z. L. Wang, *ACS Nano,* 2016, 10, 2636–2643.

2 N. Li, S. Jin, Q. Liao, C. Wang, *ACS Appl. Mater. Int.*, 2014, 6, 20590–20596.

3 Z. Tseng, C. Chiang, C. Wu, *Scientific Reports,* 2015, **5**, 13211.

4 Y. Yang, W. Guo, Y. Zhang, Y. Ding, X. Wang, Z. L. Wang, *Nano Letters,* 2011, **11**, 4812–4817.

5 D. I. Son, B. W. Kwon, D. H. Park, W. Seo, Y. Yi, B. Angadi, C. Lee, W. K. Choi, *Nature Nanotechnology*, 2012, **7**, 465–471.

6 N. Kirkwood, B. Singh, P. Mulvaney, *Adv. Mater., Int.,* 2016, 1600868.

7 D. Guo, C. Shan, S. Qu, D. Shen, *Scientific Reports*, 2014, **4**, 7469.

8 J. Dai, C. Xu, X. Xu, J. Guo, J. Li, G. Zhu, Y. Lin, *ACS Appl. Mater. Int.*, 2013, **5**, 9344–9348.

9 S. Baek, I. Park, *Nanotechnology*, 2017, **28**, 095401.

10 C. Liu, A. Yu, M. Peng, M. Song, W. Liu, Y. Zhang, J. Zhai, *J. Phy. Chem. C,* 2016, **120**, 6971–6977.

11 H. Xiong, *Adv. Mater.,* 2013, 25, 5329–5335.

12 B. Renganathan, A. R. Ganesan, *Opt. Fib. Tech.*, 2013, **20**, 48–52.

13 K. Wang, J. Zhou, L. Yuan, Y. Tao, J. Chen, P. Lu, Z. L. Wang, *Nano Letters,* 2012, **12**, 833–838.

14 N. L. Hadipour, A. A. Peyghan, H. Soleymanabadi, *J. Phys. Chem. C,* 2015, 119, 6398–6404.

15 M. Drobek, J. Kim, M. Bechelany, C. Vallicari, A. Julbe, S. S. Kim, *ACS Appl. Mater.*

Int., 2016, 8, 8323–8328.

16 J. Zhang, S. Wang, M. Xu, Y. Wang, B. Zhu, S. Zhang, W. Huang, S. Wu, *Crystal Growth Design*, 2009, 9, 3532–3537.

17 S. G. Ullattil, P. Periyat, B. Naufal, M. A. Lazar, *Ind. Eng. Chem. Res.*, 2016, 55, 6413–6421.

18 M. Thepnurat, T. Chairuangsri, N. Hongsith, P. Ruankham, S. Choopun, *ACS Appl. Mater. Int.*, 2015, 7, 24177–24184.

19 Y. K. Mishra, S. Kaps, A. Schuchardt, I. Paulowicz, X. Jin, D. Gedamu, S. Freitag, M. Claus, S. Wille, A. Kovalev, S. N. Gorb, R. Adelung, *Part. Part. Syst. Charact.*, 2013, ***30***, 775–783.

20 D. Gedamu, I. Paulowicz, S. Kaps, O. Lupan, S. Wille, G. Haidarschin, Y. K. Mishra, R. Adelung, *Adv. Mater.*, 2014, ***26***, 1541–1550.

21 Y. K. Mishra, G. Modi, V. Cretu, V. Postica, O. Lupan, T. Reimer, I. Paulowicz, V. Hrkac, W. Benecke, L. Kienle, R. Adelung, *ACS Appl. Mater. Interfaces*, 2015, 7, 14303–14316.

22 V. Postica, J. Grottrup, R. Adelung, O. Lupan, A. K. Mishra, N. H. de Leeuw, N. Ababii, J. F. C. Carreira, J. Rodrigues, N. B. Sedrine, M. R. Correia, T. Monteiro, V. Sontea, Y. K. Mishra, *Adv. Funct. Mater.*, 2017, 1604676 (1) –1604676 (15).

23 O. Lupan, V. Postica, J. Groottrup, A. K. Mishra, N. H. de Leeuw, J. F. C. Carreira, J. Rodrigues, N. B. Sedrine, M. R. Correia, T. Monteiro, V. Cretu, I. Tiginyanu, D. Smazna, Y. K. Mishra, R. Adelung, *ACS Appl. Mater. Interfaces*, 2017, 9, 4084–4099.

24 Y. Zhang, J. Xu, Q. Xiang, H. Li, Q. Pan, P. Xu, *J. Phys. Chem. C*, 2009, **113**, 3430–3435.

25 X. Fu, C. Li, L. Fang, D. Liu, J. Xu, D. Yu, Z. Liao, *ACS Nano*, 2016, 10, 11469–11474.

26 W. B. Ko, S. H. Lee, N. Myoung , J. P. Hong, ***J. Mater. Chem. C,*** 2016, **4**, 142–149.

27 Q. Wang, Y. Yan, Y. Zeng, Y. Lu, L. Chen, Y. Jiang, *Scientific Reports*, 2016, **6**, 27341.

28 H. Dong, Y. Liu, J. Lu, Z. Chen, J. Wang , L. Zhang, *J. Mater. Chem. C*, 2013, **1**, 202–206.

29 P. Rai, S. Raj, I. Lee, W. Kwak, Y. Yu, *Cer. Int.*, 2013, **39**, 8287–8291.

30 K. Foe, G. Namkoong, T. M. Abdel-fattah, H. Baumgart, M. S. Jeong, D. Lee, *Thin Solid Films*, 2013, **534**, 76–82.

31 Q. L. Ma, R. Xiong, B. Zhai, Y. M. Huang, *Applied Surface Science*, 2015, **324**, 842–848.

32 Z. Huang, C. Chai, B. Cao, *Crystal Growth Design*, 2007, **7**, 1686–1689.

33 W. Yuan, Z. Lu, C. M. Li, *J. Mater. Chem. A*, 2013, **1**, 6416–6424.

34 L. Zhang, X. Liu, C. Geng, H. Fang, Z. Lian, X. Wang, D. Shen, Q. Yan, *Inorg. Chem.*, 2013, 52, 10167–10175.

35 C. Yeh, H. Liu, M. Chuang, J. Denzer, D. Berling, H. Zan, O. Soppera, *Adv. Mater. Int.*, 2016, 1600373.

36 B. F. Lu, W. Cai, Y. Zhang, *Adv. Funct. Mater.*, 2008, **18**, 1047–1056.

37 G. D. Bellis, P. Ballirano, S. K. Balijepalli, S. Kaciulis, L. Caneve, F. Sarto, M. S. Sarto, ***RSC Adv.,*** 2015, **5**, 49861–49870.

38 D. Nunes, P. Duarte, J. C. Rodrigues, F. M. Costa, T. Monteiro, E. Fortunato, *J. Phys. Chem. C*, 2014, 118, 14629–14639.

39 Q. Yang, X. Guo, W. Wang, Y. Zhang, S. Xu, D. H. Lien, Z. L. Wang, *ACS Nano*, 2010, 4, 6285–6291.

40 A. Hadi, H. Hajghassem, M. Dousti, *J. Kor. Phy. Soc.*, 2013, **62**, 800–803.

41 C. Chang, H. Huang, Y. Lan, T. Lu, L. Tu, W. Hsieh, *Crystal Growth Design*, 2013, **13**,

3098–3102.

42 Q. Yang, W. Wang, S. Xu, Z. L. Wang, *Nano Letters*, 2011, **11**, 4012–4017.

43 X. Zhang, B. Liu, W. Yang, W. Jia, J. Li, C. Jiang, X. Jiang, ***Nanoscale,*** 2016, **8**, 17573–17580.

44 A. Manekkathodi, Y. Wu, L. Chu, S. Gwo, L. Chen, *Nanoscale*, 2013, **5**, 12185–12191.

45 L. Jianguo, D. Jielin, Z. Jianbo, S. Xueping, S. Zhaoqi, *J. Tech. Mat. Sci. Ed*., 2011, **26**, 23–27.

46 H. Wang, S. Baek, J. Song, J. Lee, S. Lim, *Nanotechnology*, 2008, **19**, 075607.

47 Y. Purusothaman, N. R. Alluri, A. Chandrasekhar, S. Kim, *J. Mat. Chem. C*, 2016, **5**, 415–426.

48 M. Salah, S. Azizi, A. Boukhachem, C. Khaldi, M. Amlouk, J. Lamloumi, *J. Mat. Sci.*, 2017, **52**, 10439–10454.

49 H. S. Al-salman, M. J. Abdullah, *J. Mat. Sci. Tech.*, 2013, **29**, 1139–1145.

50 L. Chang, T. Hsueh, ***RSC Adv.,*** 2016, **6**, 74201–74208.

51 P. Lin, X. Yan, Z. Zhang, Y. Shen, Y. Zhao, Z. Bai, Y. Zhang, *ACS Appl. Mater. Int.*, 2013, **5**, 3671–3675.

52 R. A. Talib, M. J. Abdullah, S. M. Mohammad, N. M. Ahmed, N. K. Allam, *J. Sol. State Sci. Tech.*, 2016, **5**, 305–308.

53 Q. Yang, Y. Liu, C. Pan, J. Chen, X. Wen, Z. L. Wang, *Nano Letters*, 2013, **13**, 607–613.

54 S. Bhowmick, V. Hrkac, H. Guo, O. L. Warren, J. Adam, L. Kienle, A. M. Minor, R. Adelung, Y. K. Mishra, *ACS Omega*, 2017, **2**, 2985–2993.

55 R. B. Saunders, S. Garry, D. Byrne, M. O. Henry, E. McGlynn, *Cryst. Growth. Des.*, 2012, **12**, 5972–5979.

56 M. Biswas, E. Mcglynn, M. O. Henry, *Microelectronics*, 2008, **40**, 259–261.

57 R. T. Zaera, M.C. M. Tomaz, S. Hassani, R. Triboulet, V.M. Sanjose, *J. Crys. Growth*, 2004, **271**, 711–721.

58 C. X. Xu, X. W. Sun, *Jpn. J. Appl. Phys.*, 2003, **42**, 4949–4952.

59 F. Ye, Y. Peng, G. Chen, B. Deng, A. Xu, J. *Phys. Chem. C*, 2009, **113**, 10407–10415.

60 J. Dai, C. Xu, X. Xu, J. Guo, J. Li, G. Zhu, Y. Lin, *ACS Appl. Mater. Interfaces*, 2013, **5**, 9344–9348.

61 A. Manekkathodi, Y. Wu, L. Chu, S. Gwo, L. Chen, *Nanoscale*, 2013, **5**, 12185–12191.

62 L. Shi, F. Wang, B. Li, X. Chen, B. Yao, D. Zhao, D. Shen, *J. Mater. Chem. C*, 2014, **2**, 5005–5010.

63 X. Liu, L. Gu, Q. Zhang, J. Wu, Y. Long, Z. Fan, *Nature Communications*, 2014, **5**, 1–9.

64 Q. Wang, Y. Yan, Y. Zeng, Y. Lu, L. Chen, Y. Jiang, *Scientific Reports*, 2016, **6**, 27341.

65 Q. Yang, W. Wang, S. Xu, Z. L. Wang, *Nano lett.*, 2011, **11**, 4012– 4017.

66 Q. Yang, X. Guo, W. Wang, Y. Zhang, S. Xu, D. H. Lien, Z. L. Wang, *ACS Nano*, 2010, **4**, 6285–6291.

67 F. Zhang, Y. Dong, Y. Zhang, X. Zhang, Z. L. Wang, *ACS Nano*, 2012, **6**, 9229–9236.

68 S. Rehman, R. Ullah, A. M. Butt, N. D. Gohar, *J. Hazardous Mat.*, 2009, **170**, 560–569.

69 P. Krogstrup, H. I. Jørgensen, M. Heiss, O. Demichel, J. V. Holm, M. Aagesen, J. Nygard and A. Fontcuberta, *Nature Photonics*, 2013, **7**, 306–310.

70 L. Schmidt-mende, J. L. Macmanus-driscoll, *Materials Today*, 2007, **10**, 40–48.

71 H. R. Khosroshahi, K. Edalati, J. Wu, Y. Nakashima, M. Arita, Y. Ikoma, M. Sadakiyo, Y. Inagaki, A. Staykov, M. Yamauchi, Z. Horita, M. Fuji, *J. Mater. Chem. A*, 2017, **5**, 20298.

72 T. Bora, P. Sathe, K. Laxman, S. Dobretsov, J. Dutta, *Catalysis Today*, 2017, **284**, 11–18.

73 D. Roy, S. B. Krupanidhi, *App. Phys. Letters*, 1992, **61**, 2057–2059.

74 S. Surthi, S. Kotru, R. K. Pandey, *J. Mater. Sci. Letters*, 2003, **22**, 591–593.

75 J. Zhou, Y. Gu, P. Fei, W. Mai, Y. Gao, R. Yang, G. Bao, Z. L. Wang, *Nano Letters*, 2008, **8**, 789–793.

76 Q. Liao, M. Mohr, X. Zhang, Z. Zhang, Y. Zhang, ***Nanoscale,*** 2013, **5**, 12350–12355.

77 H. Gullapalli, V. S. M. Vemuru, A. Kumar, A. Botello-mendez, R. Vajtai, M. Terrones, S. Nagarajaiah, P. M. Ajayan, *Small*, 2010, **6**, 1641–1646.

78 D. Roylance, Mechanical Properties of Materials, 2008, 1–128.

79 S. Hoffmann, F. Ostlund, J. Michler, H. J. Fan, M. Zacharias, S. H. Christiansen, C. Ballif, *Nanotechnology*, 2008, **18**, 1–5.

80 T. Oku, T. Usui, M. Eto, Y. Fukuda, *Carbon*, 1977, **15**, 30–38.

81 G. R. Patel, T. C. Pandya, *Amer. Inst. Phys.*, 2017, **1837**, 040024.

CHAPTER VI

Internally Hybridized Interfacial Quantification to Stimulate Highly Flexile Self-Powered Photodetector

Highlights

- In contrary to the existing externally powered photodetectors, a reliable approach for self-powered photodetection is designed for the first time through an internally integrated concept via coupling of piezotronic with photonic effects
- A flexile self-powered photodetector (F-SPPD) developed by one-dimensionally (1D) grown floral-like F-ZnO nanorods (F-ZnO NRs) on a PVDF substrate conjointly performs the tunability of optical properties through the exploitation of strain-induced piezoelectric potentials (σ^+, σ^-) at the electrode interfaces
- The experimental observation showed an ideal photodetector characteristics with a one-fold increment in photoresponsivity ($R_{365\ nm}$ ~ 22.76 mA/W) by lowered schottky barrier heights (Φ^T_{SB1}, Φ^T_{SB2}) through externally governed tensile strain (+ε)
- Further, the self-powered operation mode of F-SPPD exhibited higher spectral sensitivity (5.69 mA/W.cm^{-2}) than that of the photodetector (3.47 mA/W.cm^{-2}) operated under unstrained condition
- This work effectively brings in the direct integration ideology of two different systems into a single module towards the downscaling of device size and weight.

Graphical Outline

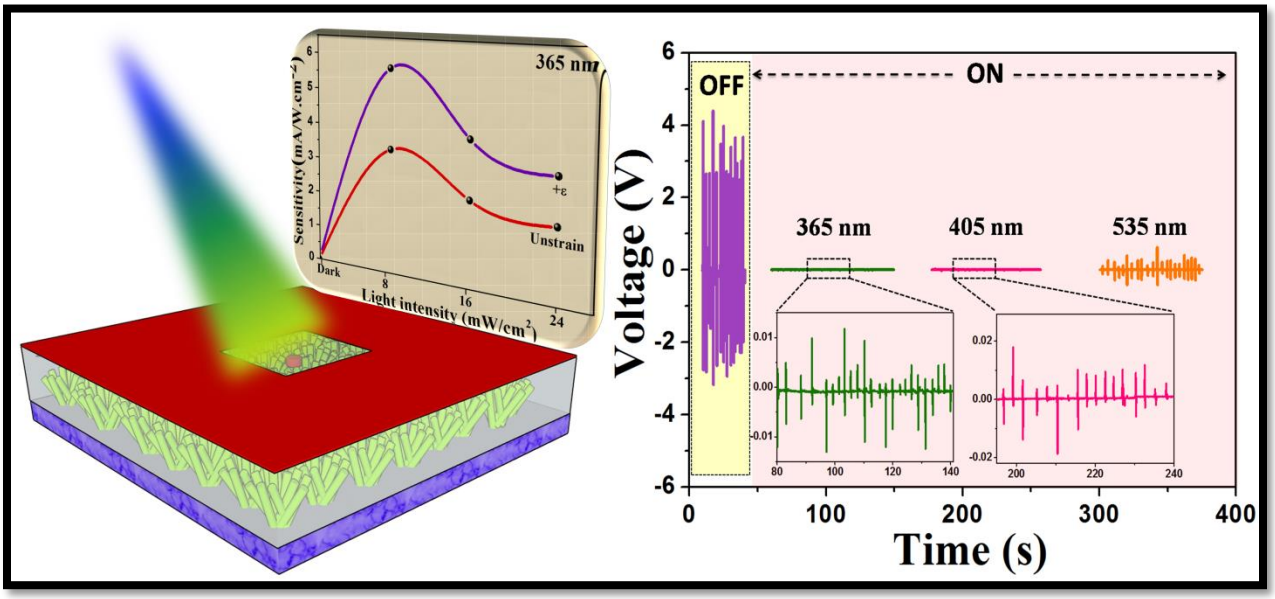

6.1 Introduction

Progression in IV generation of photodetectors (PD) endures the new conceptual insights inhibited with the effect of piezo-phototronic favoring the expansion of stretchable and self-powered integrated modules.[1,2] Heretofore, many efforts have been reported in the development of PD by the conjugation of photo electrochemical[3,4,5] photovoltaic,[6,7] pyroelectric,[8] piezoelectric,[2,9] and triboelectric[10,11] effects to meet the requirements of self-powered operation. Remarkably, self-powered PD with piezoelectric effect has gained much attention over utilizing the abundantly available mechanical energies to endorse the key functionality with a needless supply of external power units.[12,9] The integrated self-powered devices can be used as an intelligent sensing medium in various applications such as wireless communication networks,[13] chemical sensors, biosensors, pressure/speed sensor, tool for medical diagnostics, strain imaging, and future human-electronic interfacing.[14-19] The ability of multifunctional dual sensing was communicated by means of the photoconductive mechanism through which the harvested piezoelectric amplitude changes upon realizing the external light energies. Apparently, the available reports on the self-powered photodetection were based on the prototype wherein the PD was externally integrated with the nanogenerator for the power supply.[12,20-23] The external integration methodology had met the practical need to evade the additional electric power source, nevertheless; it has raised the challenge to run-over the added up mass to the overall sensing system. On the other hand, PD with spectroscopic sensitivity at zero bias (0 V) condition was manifested as a potential platform as a passive mode of self-detection.[24-27] Despite the available research directions in self-powered PD, it has become certainly necessary to rely on the architectural designs in exploring the direct detection modes conjointly reducing the weight and complexity of the circuitry device.

As an approach, we have demonstrated a simple, cost-effective way in developing a flexile self-powered photodetector (F-SPPD) by internally hybridizing the piezoelectric nanogenerator with the optical sensor. Highly ferroelectric polymer, PVDF was employed as a free-standing substrate which promotes flexibility to the as-fabricated device and together acts as a root holding the growth of floral-like F-ZnO nanorods (F-ZnO NRs). The photo sensing competency of F-ZnO NRs was studied by irradiating a LED light source operated at an UV wavelength of 365 nm. Besides, the selectivity of spectral active zone was determined by shifting the wavelength to near end visible regions (405 and 535 nm). As-fabricated F-SPPD was highly active in UV region displaying the attainable photoresponsivity ($R_{365\ nm}$) of 22.76 mA/W and detectivity (D*) of 2.72×10^{10} $cmH^{1/2}W^{-1}$ enhanced through the piezo-phototronic effect. The F-SPPD was able to produce piezoelectric output of ~ 5 V and 60 nA by sufficiently responding to the mechanical deformations under the rotational force. The intrinsic piezoelectric property coupled with the semiconducting features of the hydrothermally grown F-ZnO NRs was utilized to establish the self-integrated ideology favoring the development of in-built photodetection within the piezoelectric nanogenerator. This supports the working of F-ZnO NRs based PD with the capability to operate without any external power source. Moreover, pairing of two different systems in a single unit serves as a scale-down approach to minimize the components of external connection fronting the maturation of flexible optoelectronics.

6.2 Experimental Section

6.2.1 Synthesis of F-ZnO NRs grown in PVDF film

4 g of as-purchased Polyvinylidene difluoride (PVDF, Alfa Aesar) was dissolved in 32 ml of the N-Methyl-2-Pyrrolidone (NMP): acetone solvent composition measured at a

volumetric ratio of 5: 3 through probe sonicating the mixture for 1 h at an amplitude of 35 %. Later, the solution was transferred to a petri dish and polymerized at a temperature of 70 °C overnight. In order to obtain Zn^{2+} seeded film, PVDF solution was sonicated with the addition of zinc acetate dehydrate, $Zn(CH_3COO)_2.2H_2O$ (0.4 g) for 1 h followed by drying at 70 °C overnight. The F-ZnO nanorods (F-ZnO NRs) were grown on to the prepared PVDF films via the low-temperature hydrothermal process. An aqueous solution of 0.2 M of $Zn(CH_3COO)_2.2H_2O$ and hexamethylene tetramine (HMT) was stirred at 60 °C for a period of 1 h to obtain a well-dispersed solution. The as-prepared PVDF films were immersed in the precursor solution and treated hydrothermally at 80 °C for 12 h. After the reaction, the films were washed with ethanol and water and then dried overnight in the oven maintained at 60 °C.

6.2.2 Fabrication of flexile self-powered photodetector (F-SPPD) device

The as-synthesized PVDF films (pristine, Zn^{2+} seeded, F-ZnO NRs) were cut into the desired size of 2 × 2 cm representing the device area. 3 % (w/v) of PMMA in toluene was spin coated (2000rpm/ 60 sec) onto the PVDF films and then dried at 70 °C/ 1h. To establish electrodes, silver (Ag) paste (Dupont, 4922N) was finely coated on the PVDF/PMMA films followed by attachment of two copper (Cu) wires for the electrical measurements. To enable the photodetection part, a specific region (0.5 × 0.5 cm) was masked before the electrode deposition. Finally, PDMS (10:1) was used as a protecting package layer which completes the fabrication of flexile self-powered photodetector (F-SPPD) devices.

6.2.3 Instrumentation details

FE-SEM from JEOL JSM-6700F, Japan was used to examine the morphology and the distribution of F-ZnO NRs in PVDF film. Molecular vibrational modes were recorded through

LabRAM HR Evolution; Horiba from Japan using 514 nm laser operated in the range of 200 - 800 cm^{-1}. FTIR spectra were analyzed employing a Nicolet 6700 spectrophotometer in the range of 700 - 1500 cm^{-1}. The surface properties of the PVDF films were determined using the Phoenix 300 modeled contact angle analyzer with an angle range of 0° to 180°. Ferroelectric behaviors of PVDF films were observed using high voltage enabled precision material analyzer (Precision 10kV HVI-SC, Radiant Technologies, Inc). Manually designed rotary setup was operated to induce an external force (strain) on the as-fabricated F-SPPD devices. The piezoelectric performances were evaluated through a high impedance electrometer (Keithley 6514, Keithley Instruments, Cleveland, OH, USA). I - V measurement was carried out using Agilent-B1500A (semiconductor device parameter analyzer). Wavelength-dependent photoresponse was studied with Prizmatix multi-wavelength LED source, supplying the UV - Visible lights of wavelengths 365 nm, 405 nm and 535 nm at different intensities.

6.3 Results and Discussion

6.3.1 Structural analysis of in-situ grown F-ZnO NRs/PVDF film

The development of the proposed hybrid device architecture is illustrated schematically in **Figure 6.1**(a). The F-SPPD comprises of F-ZnO NRs grown on the S-PVDF film (Zn^{2+} seeded PVDF) acting as an active layer for concurrently harvesting mechanical and light energies. The top layer comprises of an optically involved PMMA; serving to avoid the distortions/damages to the F-ZnO NRs when treated for the electrode (Ag) deposition. The as-synthesized S-PVDF film appears with micro-sized pothole like morphology forming a contact angle (Θ_C) of 85 ° (Figure 6.1(b) & inset). The porosity of the film can be explained due to the usage of acetone that finds to evaporate much earlier than the film solidification. The F-ZnO NRs germinate out from the

holes during its hydrothermal growth process. Figure 6.1(c) represents the grasslands of F-ZnO NRs grown efficiently in the S-PVDF film for about a length ~ 2 μm and diameter of ~ 100 nm. The grown F-ZnO NRs has abruptly changed the surface property of the S-PVDF film which is eventually observed through the increase in its contact angle (Θ_C - 118 °, Figure 6.1(c) (inset)). The potholes permits the sprouting of F-ZnO NRs and hence grown where ever the cavities are present (Figure 6.1(d)). Also, the NRs are observed internally in the S-PVDF film grown in a zigzag manner (Figure 6.1(e)).

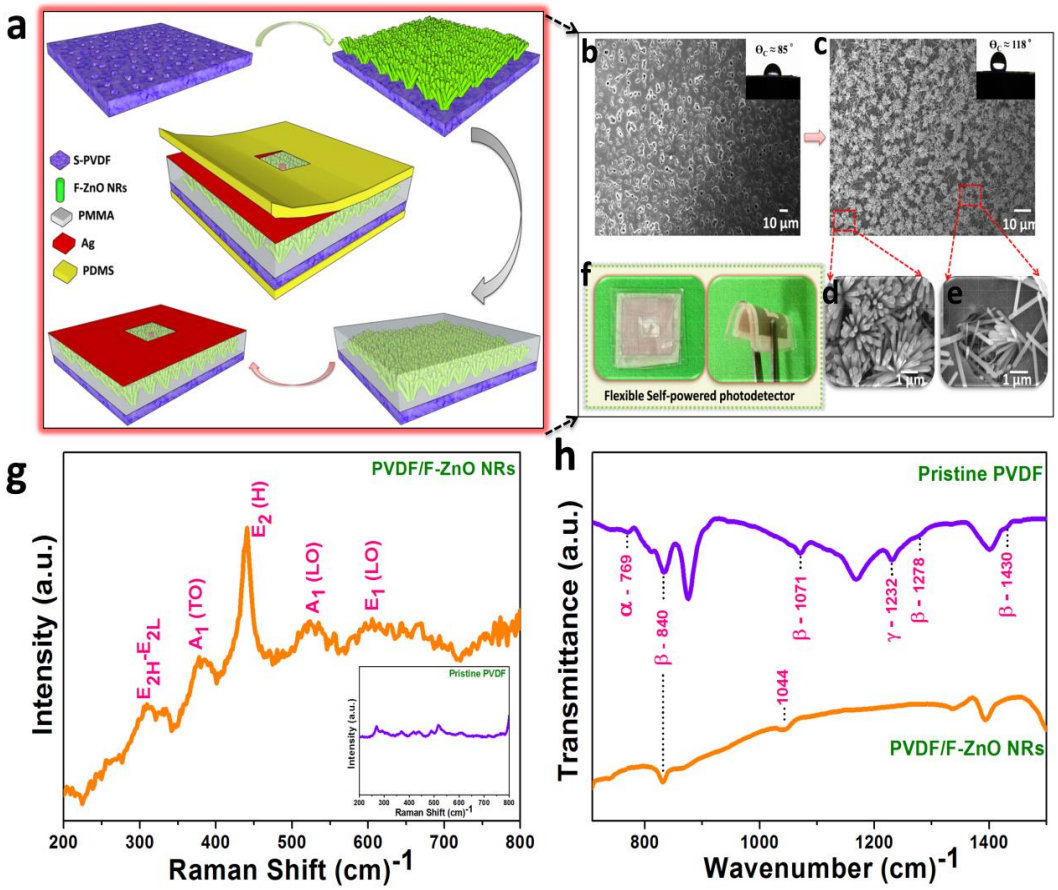

Figure 6.1 (a) Schematic illustration on fabrication of flexile self-powered photodetector (F-SPPD), FESEM images. **(b)** Untreated PVDF film. **(c)** Hydrothermally grown F-F-ZnO NRs throughout the PVDF film. **(d, e)** Magnified view of F-F-ZnO NRs. **(f)** Optical images of as-fabricated F-SPPD device. **(g)** Raman spectrum. **(h)** FTIR analysis.

Besides to verify the ionic (Zn^{2+}) seed effects, pristine PVDF film was treated hydrothermally which produced no significant growth of F-ZnO NRs on the film (**Figure 6.2**). This accounts to the beneficial use of S-PVDF over the plain PVDF film. Figure 6.1(f) shows the optical device images of the as-fabricated F-SPPD and its flexible nature to any kind of bending force. The average thickness of the active layer is noted to be ~ 60 μm (**Figure 6.3**).

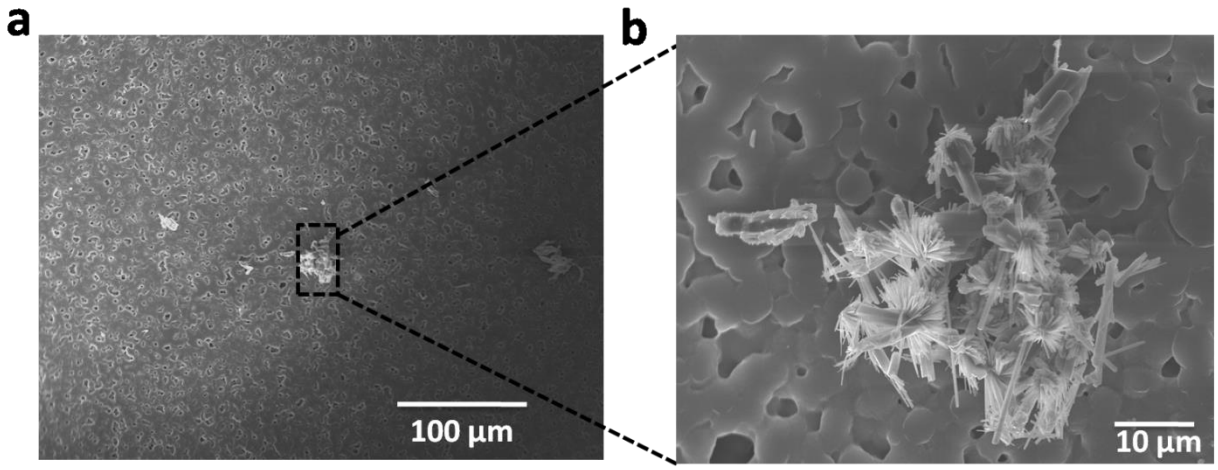

Figure 6.2 (a) FESEM of hydrothermally treated seedless PVDF film illustrating the poor growth of NRs. **(b)** Magnified view of ZnO NRs randomly attached on PVDF film suggesting weak adhesion.

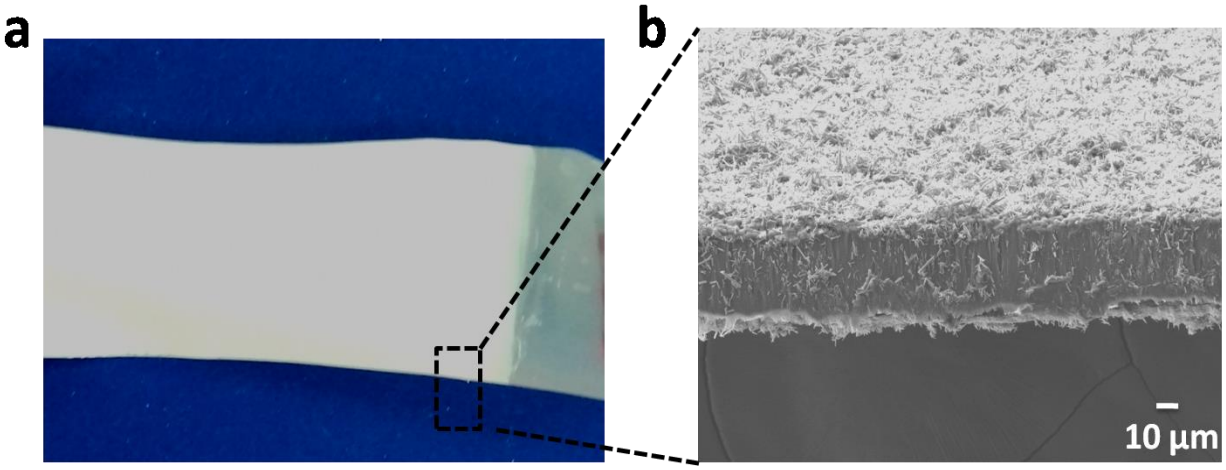

Figure 6.3 (a) Optical image of S-PVDF film after hydrothermal treatment. **(b)** FESEM image representing the thickness profile (~ 60 μm).

The characteristic Raman active mode of the as-synthesized F-ZnO NRs is shown in Figure 6.1(g). The peak at about 310 cm^{-1} corresponds to the difference between E_{2H} and E_{2L} mode and a sharp peak at 440 cm^{-1} attributes to the c-axis orientation of the NRs. The low-frequency peak at 330 cm^{-1} originates from the second/ multi-order phonon scattering modes typically observed for a F-ZnO wurtzite crystal lattice. Peaking at 378 and 528 cm^{-1} represents the A mode oscillations such as A_1(TO) and A_1(LO), respectively. The F-ZnO NRs exhibits the native defect states such as oxygen vacancy (V_o) and zinc interstitial (Zn_i) sites which are quantified from the vibration at 590 cm^{-1}.[22]

Figure 6.1(h) spectrally represents the crystallite phases (α, β and γ) formed in the as-processed PVDF films (pristine, Zn^{2+} seeded and F-ZnO NRs). The peak at 769 cm^{-1} represents the non-polar α phase, and 1232 cm^{-1} corresponds to the semi-polar γ phase. The polar β phase is confirmed through exclusive strong band at 840 cm^{-1} along with observable peaks at 1071, 1278 and 1430 cm^{-1} confirming the ferroelectric existence of the as-synthesized PVDF films.[28] Further, the F-ZnO NRs grown on the film surface and also intrinsically had altered the PVDF dipole polymeric chains $[-CH_2-/-CF_2-]_n$ thus suppressing the existence of the non-polar and semi-polar phases. The strong β phase content (840 cm^{-1}) is preserved in the processed PVDF film; however, the minor band (1430 cm^{-1}) has diminished. Further, it is expected that the intrinsic growth of the NRs may have contributed to the β band shift of 1071 cm^{-1} to 1044 cm^{-1}. **Figure 6.4** represents the measured FTIR for the plain PVDF film treated hydrothermally at 80 °C. The spectrum exhibits similar bands to that of untreated PVDF film confirming zero impact of the temperature treatment (80 °C), and hence the grown F-ZnO NRs are the prime factor to influence the changes in the PVDF chain ordering.[29]

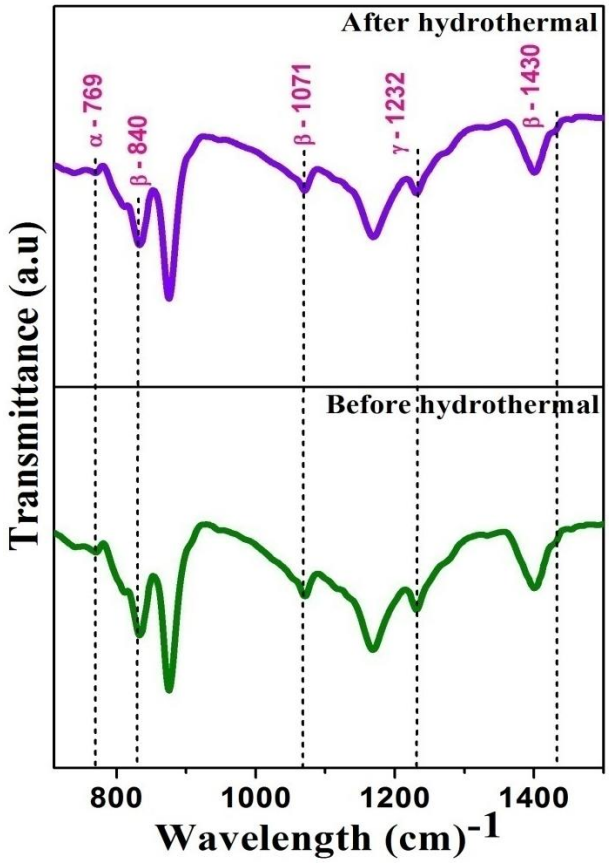

Figure 6.4 FTIR spectrum of the pristine film confirming no influence of heat treatment in altering the PVDF phases properties.

6.3.2 I-V characteristics of internally developed F-SPPD

In order to estimate the light sensing capability, the as-fabricated F-SPPD device is subjected to an UV source acting at a wavelength of 365 nm. **Figure 6.5**(a) represents the current-voltage characteristics of the dark (I_D) and photocurrent response (I_{Ph}) from the F-SPPD constituting of a self-integrated photodetector along with the piezoelectric nanogenerator. Observed I-V curve illustrates the formation of schottky type (Φ_{SB1}, Φ_{SB2}) behavior of the device. Upon UV illumination the generation of photo charge carriers (e^- - h^+) takes place increasing the dark current of 0.55 μA (I_D) to photocurrents (I_{Ph}) of 28, 39 and 50 μA at corresponding intensities of 8, 16 and 24 mW/cm^2. The linearity with the photocurrent response

upon increasing the light intensities is in accordance with an ideal photodetector consistent with the principles of the power law, $I_{Ph} = AP^{\Theta}$.[22]

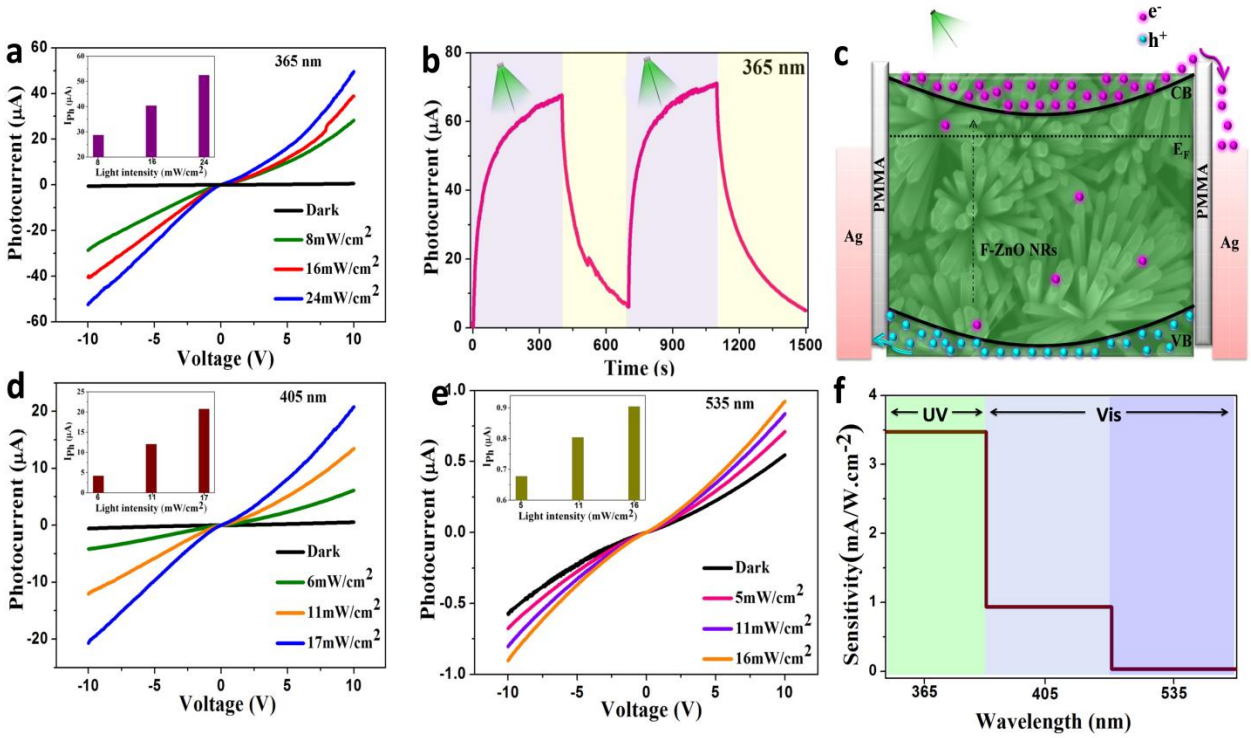

Figure 6.5 I-V characteristics of internally developed F-SPPD, **(a)** Photocurrent response at 365 nm (inset – linearity behaviour). **(b)** Time responsive ON-OFF switching studies. **(c)** Energy band diagram with photogenerated charge carriers. **(d)** Photocurrent performance at 405 nm. **(e)** Photoresponse under 535 nm irradiation. **(f)** Spectral sensitivity (S) at varied wavelengths.

The reproducibility performance is determined through periodic time responsive ON-OFF switching analysis where the device is irradiated to 8 mW/cm^2 intensity at 10 V bias. From the Figure 6.5(b), the rise and decay time of the photodetector is observed to be 24s (τ_r) and 30s (τ_d) using the exponential rise and decay factors ($\tau_r \sim 1 - e^{-1}$, $\tau_d \sim e^{-1}$).[22] The given energy band diagram in Figure 6.5(c) schematically represents the mechanism of photodetector upon UV illumination. In the absence of light, the dark current response from the devices arises from the inbuilt potential of F-ZnO NRs due to the free charge carriers. When the UV light is irradiated, it

produces the charge carriers where the electrons (e^-) in the valence band (VB) hops to the conduction band (CB) by absorbing the energy of the incident photons (hν).[30,31] The sensitivity of the photodetector to other spectral ranges is determined by exposing to the near end visible ranges. The response obtained at 405 nm is smaller than that the photocurrent observed for 365 nm (Figure 6.5(d)) and became negligible upon further shift of visible region to 535 nm (Figure 6.5(e)). Hence, it is evident that the as-fabricated SPPD device is highly selective and possesses distinguishable sensitivity (S) with two-fold deviations to the electromagnetic spectral zones (Figure 6.5(f)). The as-fabricated PD exhibits good responsivity ($R_{365\ nm}$ ~ 13.9 mA/W) under UV region (365 nm) given by[33],

$$R_\lambda = \frac{I_{Ph} - I_D}{P_L \times S} \quad \text{- (1)}$$

To clarify on the approach of self-powered photodetection, we demonstrated experiments on the strain based analysis by which the generation of piezoelectric potentials is promoted through the effect of piezotronic.[32] To rely on this concept, the as-fabricated F-SPPD is bend from its original unstrained position using manually designed rotary setup as shown in **Figure 6.6**.

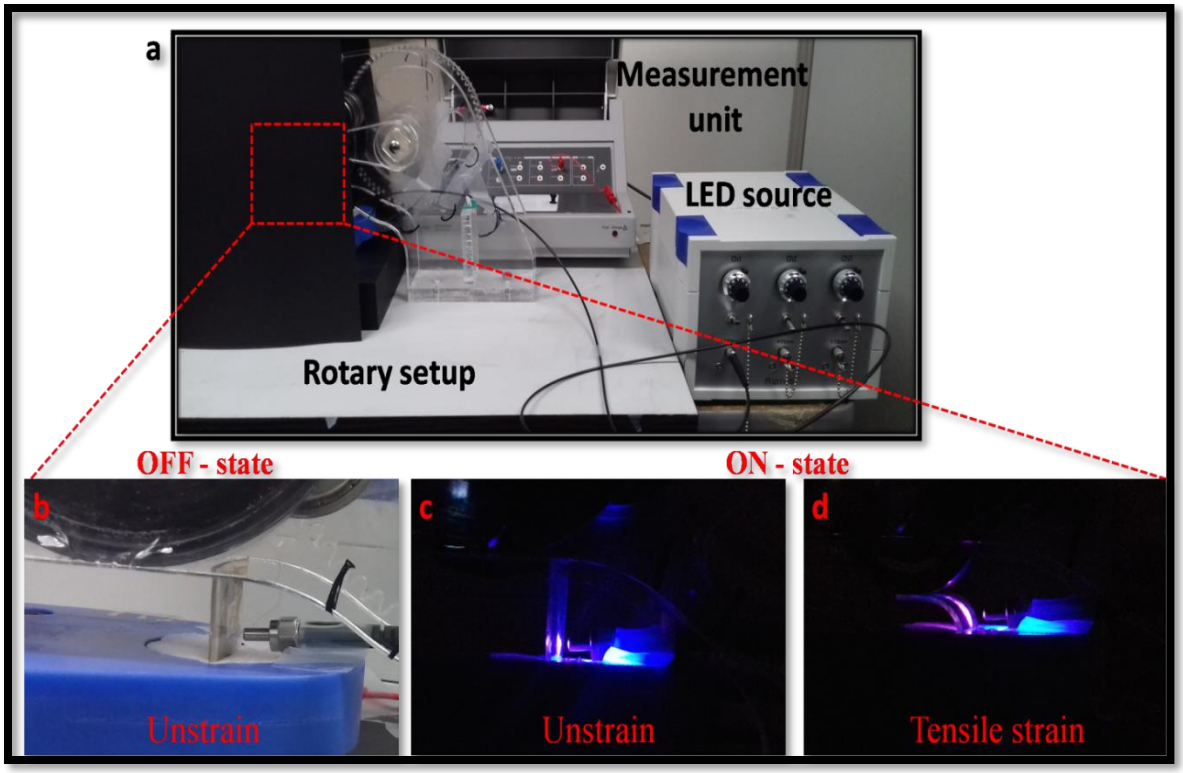

Figure 6.6 (a) Experimental setup for I-V analysis. **(b)** UV-OFF state, UV-ON state. **(c)** Under unstrain position. **(d)** Realization of piezo-phototronic effect governed by tensile strain condition.

6.3.3 Piezotronic modulated optical performance of F-SPPD

The response of the photodetector is determined under two conditions (i) tensile and (ii) compressive depending upon the nature of the strain applied. Under (i) tensile strain condition (+ ε) (**Figure 6.7**(a)), the piezoelectric potentials get distributed in a manner such as positive potential (σ^+) is accumulated at the electrode interfaces. The induced positive potential (σ^+) attracts the free electrons (e^-) present in the F-ZnO NRs towards the zone of the interface; which lowers the schottky barrier heights (Φ_{SB1}, Φ_{SB2}). This promotes more free charge carriers to cross the potential barriers with reduced schottky barrier heights (Φ^T_{SB1}, Φ^T_{SB2}) therefore increasing dark current response (Figure 6.7(c)). Alternatively under (ii) compressive strain (- ε) (Figure

6.7(a)), negative piezoelectric potential (σ^-) is generated which increases the schottky barrier heights (Φ^C_{SB1}, Φ^C_{SB2}) consequently lowering the transportation of free charge carriers due to the raised potential barriers at the interfaces (Figure 6.7(d)).[33] Specifically determining the charge of potential distribution acting on each NRs are quite tedious as the F-ZnO NRs are grown in an irregular manner representing both vertical and horizontal direction (Figure 6.1(b)). So when the device is strained, some of the NRs experiences positive potential and other few experience the negative potential near the interface. From the current response, we represent the net piezoelectric potential (as either positive or negative) depending upon the majority of the charges accumulated at the electrode interface. By indulging the piezo-photronic effect, the photocurrent response is enhanced to the order of one-fold upon applying the tensile strain on to the F-SPPD (inset Figure 6.7(b)). The observed symmetrical enhancement in both the schottky contacts is from the device structure where both the electrodes are placed on the top. So when a strain is induced, both the electrodes experience the same piezoelectric potential leading to mutual increase or decrease in the current responses.[34] Figure 6.7(e) brings a comparative plot portraying the enhanced performance of photodetection due to the piezotronic effect (tensile strain). Besides, the induced strain has led to a one–order sensitivity improvement in optical detection (Figure 6.7(f)). The generated piezoelectric potentials paves the way for tuning the performance of the as-fabricated PD through externally governed strain induced factors. **Table 6.1** summarizes the effect of tensile strain through evaluating the characteristic parameters of an ideal PD such as Detectivity ($D*$) and Photoconductive gain (G) represented as[33],

$$G = \frac{\Delta I/q}{P_L/h\nu} \quad \text{- (2)}$$

$$D* = \frac{A^{1/2} \times R_\lambda}{(2q \times I_D)^{1/2}} \quad \text{- (3)}$$

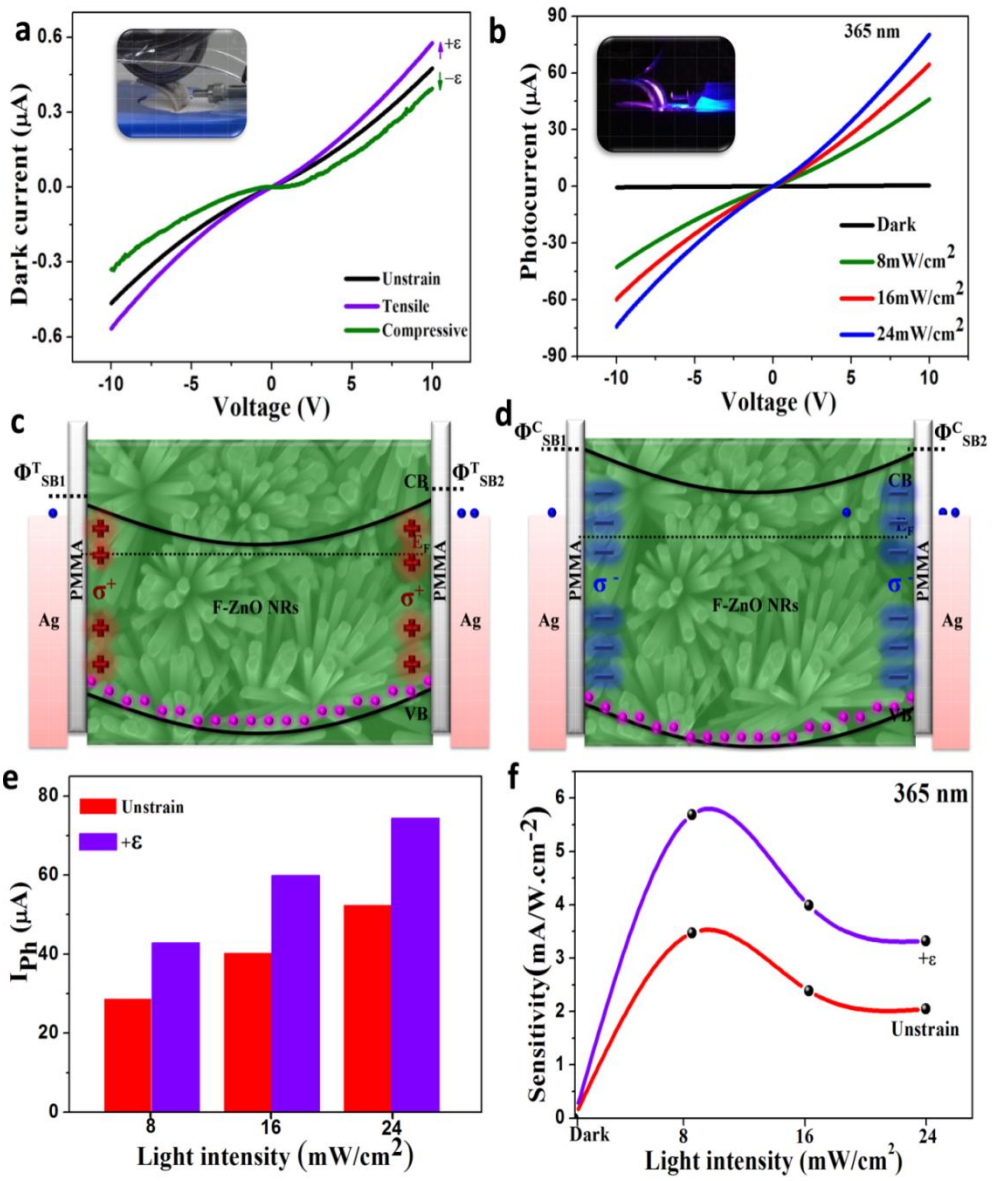

Figure 6.7 Piezotronic modulated PD performance. **(a)** Analysis of tensile and compressive strain on dark current response. **(b)** Enhanced photodetection under tensile strain (365 nm). Alignment of energy band **(c)** Accumulation of positive piezoelectric potential (σ^+) (lowered Φ_{SB}). **(d)** Compressive strain induced negative piezoelectric potential (σ^-) (increased Φ_{SB}). **(e)** Photocurrent response as an effect of tensile strain. **(f)** Improved sensitivity of internally integrated PD under tensile strain condition.

Table 6.1 Calculated photodetector performance characteristics as an effect of tensile strain (+ε) at the source irradiation of 365 nm.

P_L [a]	R [b]		D* [c]		G [d]		S [e]	
(mW/cm^2)	(mA/W)		($\times 10^{10}$ $cmH^{1/2}W^{-1}$)				($mA/W.cm^{-2}$)	
	Unstrain	**+ε**	**Unstrain**	**+ε**	**Unstrain**	**+ε**	**Unstrain**	**+ε**
8	13.89	22.76	1.66	2.72	0.047	0.077	3.47	5.69
16	9.55	15.96	1.14	1.91	0.032	0.054	2.39	3.99
24	8.18	13.29	0.98	1.59	0.027	0.045	2.05	3.32

Power intensity [a], Responsivity [b], Detectivity [c], Photoconductive gain[d] , Sensitivity [e]

6.3.4 Conceptualization of self-integrated through piezoelectric characteristics

To further simplify the conceptualization of self-integrated theory, the exhibited ferroelectric behavior is determined through the saturation of polarization (P) to the externally applied voltage (V). **Figure 6.8**(a) illustrates the P-V loop at a potential of 1500 V for pristine PVDF, S-PVDF and PVDF/F-ZnO NRs films of thickness ~ 60 μm. The hysteresis curve resembles the typical ferroelectric characteristics of the as-prepared films with a lossy capacitive nature. The nonzero remanent polarization (P_r) at zero applied voltage confirms the presence of spontaneous polarization exhibited at the room temperature. The determined remanent polarization (P_r) of the pristine PVDF is 0.031 $\mu C/cm^2$, which upon seeding of Zn^{2+} increases to 0.099 $\mu C/cm^2$. Further, P_r shows drastic improvement of 0.304 $\mu C/cm^2$ from the ferroelectric contribution of grown F-ZnO NRs. Similarly, PVDF/F-ZnO NRs shows better coercive field

(V_c) of 1170 V compared to pristine and S-PVDF films (Figure 6.8(b)). Followed is the demonstration of mechanical energy harvesting ability of the as-fabricated F-SPPD in the absence of UV light source. The F-SPPD is mounted in a rotary setup so that the device is subjected to continuous mechanical force by rotating the shaft. As shown in Figure 6.8(c), the piezoelectric voltage (V_{P-P}) of F-ZnO NRs grown on the PVDF film acquires higher response of ~ 5 V compared to that of plain PVDF and S-PVDF. Similar behavior is observed in the current profile, where the PVDF/F-ZnO NRs produces a peak to peak value (I_{P-P}) of ~ 60 nA.

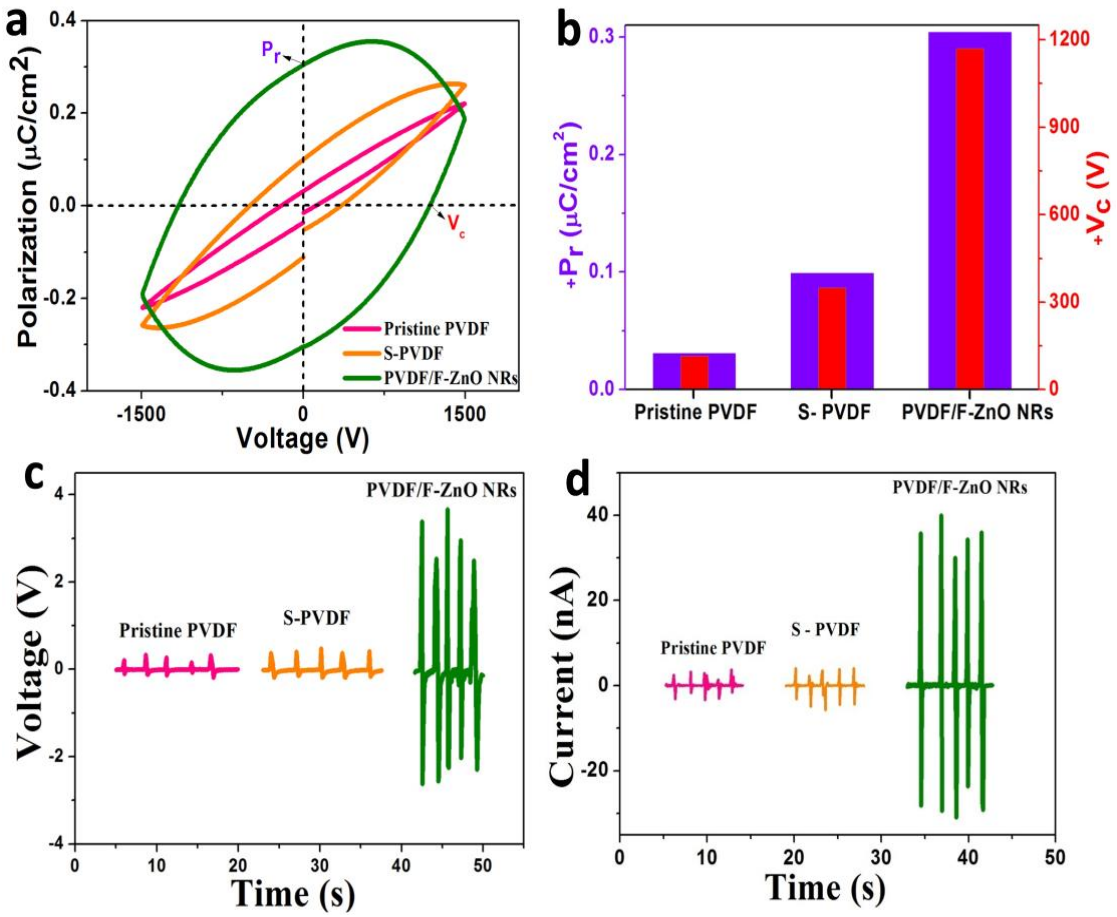

Figure 6.8 Evaluation of piezoelectric characteristics. **(a)** Hysteresis ferroelectric P-V loop analysis. **(b)** Improved remnant polarization (P_r) and coercive field (V_c) of PVDF/F-F-ZnO NRs. Piezoelectric response from the as-fabricated F-SPPD **(c)** Output voltage. **(d)** Output current.

Realization of the PD on the bases of the self-powering mechanism is demonstrated by investigating the performance of the piezoelectric nanogenerator upon irradiation of the UV light (365 nm). **Figure 6.9**(a) is the observed response in the piezoelectric output from the F-SPPD device. The working mechanism of the as-developed F-SPPD is illustrated schematically in the Figure 6.9(b) and the experimental setup is shown in Figure 6.9(c & d). Generally, in the dark condition the F-SPPD operates in its original state (~ 5 V) upon subjecting to the external bending force.

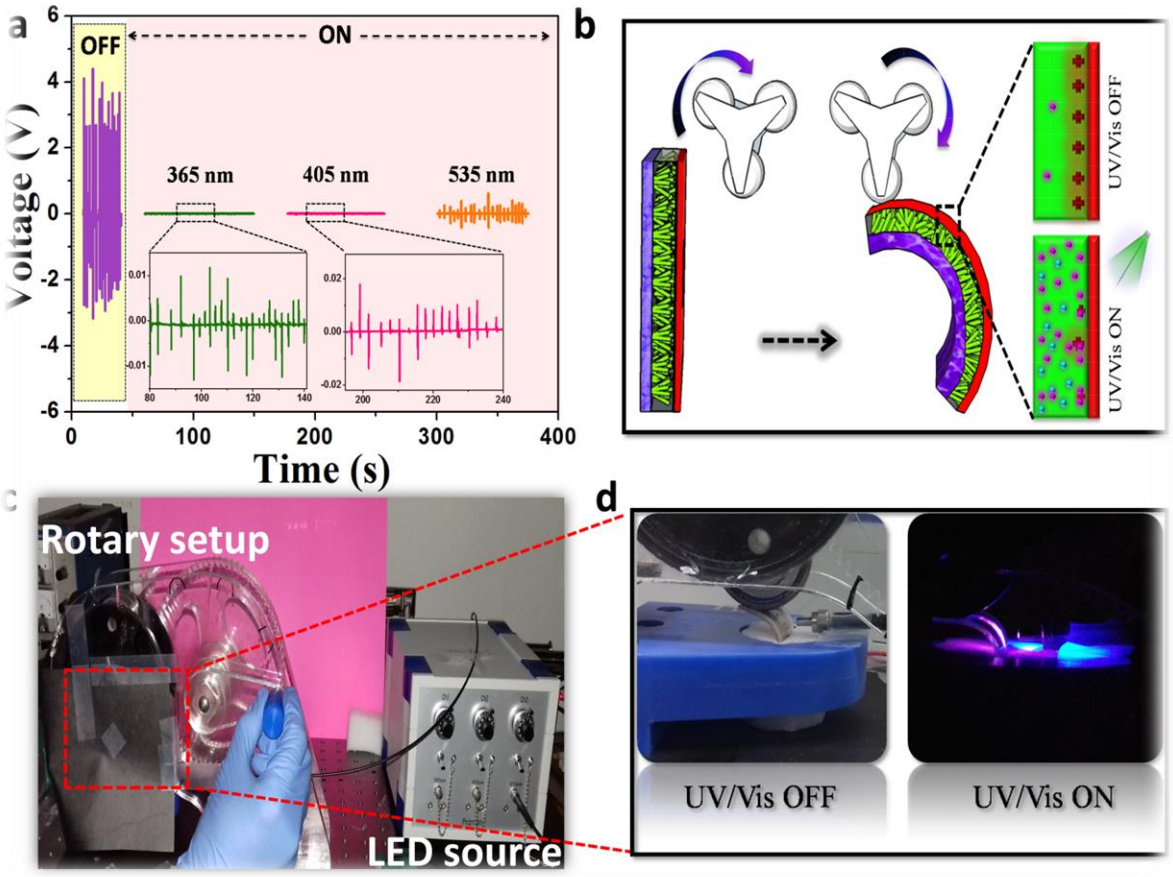

Figure 6.9 Demonstration of self-powered operation mode of internally integrated PD. **(a)** Optical detection of mechanically triggered in-built PD at varied irradiation sources (365, 405 & 535 nm). **(b)** Working mechanism of F-SPPD inherited with photodetection. **(c)** Experimental setup. **(d)** Device illustration with LED ON/OFF states.

When the device is deflected in a tensile manner (corresponding to the rotation of shaft), the piezoelectric potentials are generated near the interface making the flow of electrons between the electrodes through the circuit to balance the field imbalance produced by the dipole moments (Figure 6.9(b) – UV/Vis OFF). As there is no further moment in the dipoles, the peak gradually decays to the zero potential and hence maintained as long as the device is held in the strain position. Accounting for the strain release, the piezoelectric potential vanishes consequently causing the backflow of the electrons. This harmonizes the negative peak of the cycle (**Figure 6.10**).

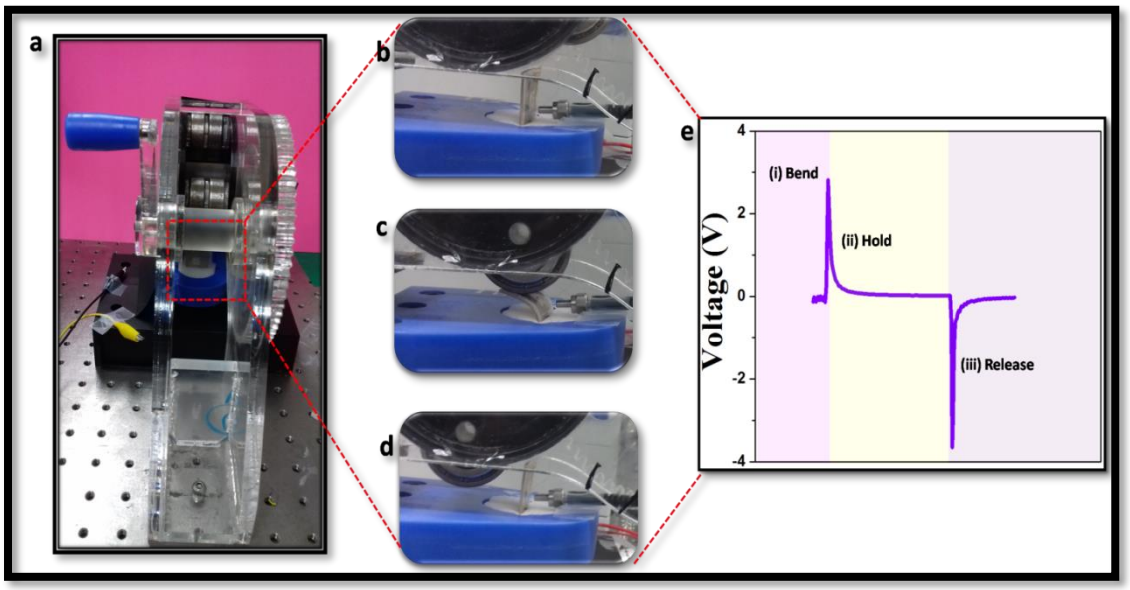

Figure 6.10 (a) Manually designed rotary setup. **(b, c, d)** Rotational force exerted on the as-fabricated F-SPPD driving the generation of piezoelectric effect. **(e)** Corresponding voltage profile.

While in the presence of UV light, the generation of e^- and h^+ takes place thus increasing the density of the charge carriers (Figure 6.9(b) – UV/Vis ON). Hence loss in the inner resistance of the device is observed causing a drastic drop in the piezoelectric output. The produced photonic charge carriers would screen or neutral the piezoelectric potentials (σ^+) at the electrode

interfaces resulting in the low piezoelectric performance of the device.[33,35] The effect of F-SPPD on various wavelengths is studied at 365 nm (24 mW/cm^2), 405 nm (17 mW/cm^2) and 535 nm (16 mW/cm^2) light irradiation. The piezoelectric voltage shows linear change depending upon the irradiated wavelengths. The results are in accordance with the I-V characteristics (Figure 6.5) where the density of photogenerated charge carriers fades as the wavelength is shifted to the visible region. The charge carrier density lies in the order where 365 nm > 405 nm > 535 nm. Henceforth, the performance of F-SPPD shows the low piezoelectric voltage (peak-peak) of ~ 0.01 V at an illumination of 365 nm that increases to ~ 0.02 V at 405 nm and ~ 0.7 V at 535 nm irradiation. This further confirms the effect of charge carrier density on the operating efficiency of the piezoelectric nanogenerator which also acts as a self-integrated photodetector. Through the results, we successfully recognized the role played by piezotronic in enhancing the photo sensing ability, and furthermost enabled its potential operation as an internally integrated flexile self-powered photodetector (F-SPPD) by dint of piezo-phototronic effect.

6.4 Conclusion

In summary, we demonstrated the internal integration of UV functioning photodetector on a flexile piezoelectric nanogenerator based on PVDF/F-F-ZnO NRs facilitating its self-powered operation. The in-build photodetector showed an enhanced UV photocurrent (I_{Ph}) of 75 μA (24 mW/cm^2) under the tensile strain condition (+ε) and also exhibited good responsivity ($R_{365\ nm}$) and detectivity (D*) in the range of 22.76 mA/W and 2.72 2×10^{10} cmH$^{1/2}$W^{-1}. As-developed F-SPPD acts as an efficient switching model for synchronously harvesting mechanical and optical energies. This work provides the platform for scaling down the device configuration and mass by virtue of actively empowering the self-integrated mechanism of piezo-phototronic towards the evolution of futuristic self-powered optoelectronic devices.

6.5 References

1 W. Tian, L. Wang, L. Li, *Small*, 2017, **13**, 1701848.

2 Z. Lou, G. Shen, *Adv. Sci.*, 2016, **3**, 1500287.

3 J. Zhou, L. Chen, Y. Wang, Y. He, X. Pan, E. Xie, *Nanoscale*, 2016, **8**, 50–73.

4 A. A. Thahe, N. Bidin, Z. Hassan, H. Bakhtiar, M. A. Qaeed, M. Bououdina, N. M. Ahmed, Z. A. Talib, M. Azawi, H. Alqaraghuli, *Mater. Res. Express*, 2017, **4**, 116203.

5 M. Zhang, Y. Wang, F. Teng, L. Chen, J. Li, J. Zhou, X. Pan, E. Xie, *Materials Letters*, 2016, **162**, 117–120.

6 J. Li, S. Yuan, G. Tang, G. Li, D. Liu, J. Li, X. Hu, J. Li, Z. Yang, Z. Liu, F. Gao, F. Yan, *ACS Appl. Mater. Interfaces*, 2017, **9 (49)**, 42779–42787.

7 X. Wan, Y. Xu, H. Guo, K. Shehzad, A. Ali, Y. Liu, J. Yang, D. Dai, C. T. Lin, L. Liu, H. C. Cheng, F. Wang, X. Wang, H. Lu, W. Hu, X. Pi, Y. Dan, J. Luo, T. Hasan, X. Duan, X. Li, J. Xu, D. Yang, T. Ren, B. Yu, *npj 2D Materials and Applications*, 2017, **1 (1)**, 4.

8 J. Qi, N. Ma, Y. Yang, *Adv. Mater. Interfaces*, 2017, **29 (46)**, 1701189

9 Z. L. Wang, *MRS Bulletin*, 2012, **37 (9)**, 814–827.

10 Z. Lin, G. Cheng, Y. Yang, Y. S. Zhou, S. Lee, Z. L. Wang, *Adv. Funct. Mater.*, 2014, **24**, 2810–2816.

11 L. Su, Z. Zhao, H. Y. Li, J. Yuan, Z. L. Wang, G. Z. Cao, G. Zhu, *Nano Energy*, 2017, **31**, 264–269.

12 W. Wu, C. Pan, Y. Zhang, X. Wen, Z. L. Wang, *Nano Today*, 2013, **8 (6)**, 619–642.

13 Y. Hu, Y. Zhang, C. Xu, L. Lin, R. L. Snyder, Z. L. Wang, *Nano Letters*, 2011, **11 (6)**, 2572–2577.

14 W. Wu, Z. L. Wang, *Nature Reviews Materials*, 2016, **1**, 16031.

15 H. Chen, K. Liu, L. Hu, A. A. Al-ghamdi, X. Fang, *Biochemical Pharmacology*, 2015, **18 (9)**, 493–502.

16 W. Wu, S. Bai, M. Yuan, Y. Qin, Z. L. Wang, T. Jing, *ACS Nano*, 2012, **6 (7)**, 6231–6235.

17 M. Lee, C. Chen, S. Wang, S. N. Cha, Y. J. Park, J. M. Kim, L. Chou, Z. L. Wang, *Adv. Mater.*, 2012, **24**, 1759–1764.

18 G. Hwang, M. Byun, C. K. Jeong, K. J. Lee, *Adv. Healthcare Mater.*, 2015, **4**, 646–658.

19 Y. Hu, C. Xu, Y. Zhang, L. Lin, R. L. Snyder, Z. L. Wang, *Adv. Mater.*, 2011, **23**, 4068–4071.

20 N. R. Alluri, Y. Purusothaman, A. Chandrasekhar, S. J. Kim, *Chemical Engineering Journal*, 2018, **334**, 1729–1739.

21 B. Saravanakumar, K. Thiyagarajan, N. R. Alluri, S. SoYoon, K. Taehyun, Z. H. Lin, S. J. Kim, *Carbon*, 2015, **84** , 56–65.

22 Y. Purusothaman, N. R. Alluri, A. Chandrasekhar, S. J. Kim, *Journal of Materials Chemistry C*, 2016, **5**, 415–426.

23 N. R. Alluri, S. Selvarajan, A. Chandrasekhar, S. Balasubramaniam, J. H. Jeong, S. J. Kim, *Sensors & Actuators: B. Chemical*, 2016, **237**, 534–544.

24 X. Yu, H. Yin, H. Li, W. Zhang, H. Zhao, C. Li, M. Zhu, *Nano Energy*, 2017, **34**, 155–163.

25 Y. Dong, Y. Zou, J. Song, Z. Zhu, J. Li, H. Zeng, *Nano Energy*, 2016, **30**, 173–179.

26 M. Peng, Y. Liu, A. Yu, Y. Zhang, C. Liu, J. Liu, W. Wu, K. Zhang, X. Shi, J. Kou, J. Zhai, Z. L. Wang, *ACS Nano*, 2016, **10 (1)**, 1572–1579.

27 L. Mandal, N. S. Chaudhari, S. Ogale, *ACS Applied Materials & Interfaces*, 2013, **5 (18)**,

9141–9147.

28 P. Martins, A. C. Lopes, S. L. Mendez, *Progress in Polymer Science*, 2013, **39 (4)**, 683–706.

29 D. Dhakras, V. Borkar, S. Ogale, J. Jog, *Nanoscale*, 2012, **4 (3)**, 752–756.

30 D. Gedamu, I. Paulowicz, S. Kaps, O. Lupan, S. Wille, G. Haidarschin, Y. K. Mishra, R. Adelung, *Adv. Mater.*, 2014, **26**, 1541–1550.

31 Y. K. Mishra, G. Modi, V. Cretu, V. Postica, O. Lupan, T. Reimer, I. Paulowicz, V. Hrkac, W. Benecke, L. Kienle, R. Adelung, R. *ACS Appl. Mater. Interfaces*, 2015, 7, 14303–14316.

32 Z. L. Wang, *Nano Today*, 2010, **5 (6)**, 540–552.

33 Y. Purusothaman, N. R. Alluri, A. Chandrasekhar, V. Vivekananthan, S. J. Kim, *Small*, 2018, 1703044.

34 Y. Hu, Y. Zhang, L. Lin, Y. Ding, G. Zhu, Z. L. Wang, *Nano Letters*, 2012, **12 (7)**, 3851–3856.

35 Y. Zhang, Y. Liu, Z. L. Wang, *Adv. Mater.*, 2011, **23**, 3004–3013.

CHAPTER VII

Photoactive Piezoelectric Energy Harvester Driven by Ternary Chalcohalides ($A_VB_{VI}C_{VII}$) towards Self-Powered Photodetection

Highlights

- A new type of ferroelectric-semiconductor material, ternary chalcohalides are explored as an efficient candidate for piezoelectric nanogenerator (S-PNG)
- Hypothesis of polymeric composite interfaces based on PDMS (Polydimethylsiloxane), PVDF (Polyvinylidene fluoride) and PMMA (Poly(methyl methacrylate) is proposed validating the suitability for the development of efficient S-PNG
- The notable piezoelectrical responses from piezoelectric-semiconducting-photoactive materials (~ 5V and ~ 150 nA, SbSI; ~2V and 60nA, SbSeI) opens up the potential for the construction of hybridized devices with multifunctional sensory units
- Further, the piezo-phototronic properties of SbSI/PMMA composite and single SbSI micro rod (SMR) were extensively investigated
- These harvesters incorporate both mechanical and optical sources, thereby providing broad opportunities for the expansion of piezoelectronic material systems for photodetection

Graphical Outline

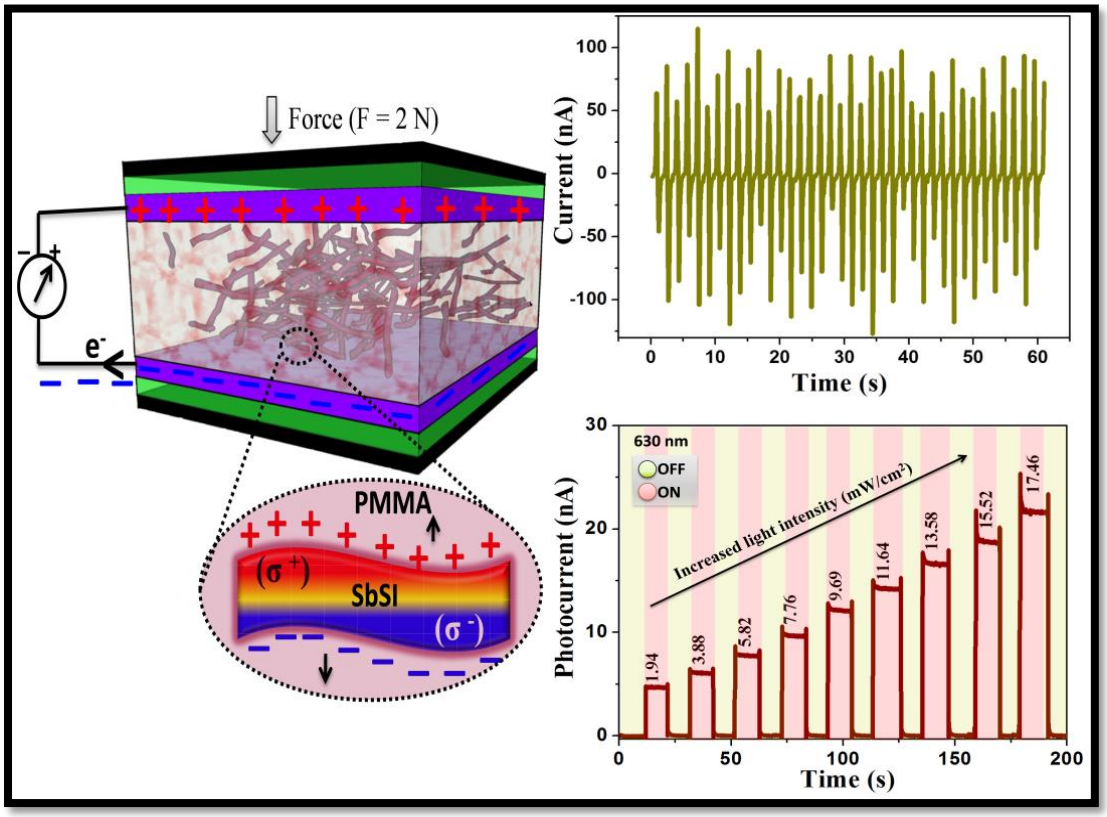

7.1 Introduction

Piezoelectric-semiconducting materials have attracted wide attention[1,2] due to the insulating nature of available energy materials such as PZT[3], Ba(Zr, Ti)O_3[4], $SrTiO_3$[5], (K, Na)NbO_3[6], (Bi, Nd)Ti_3O_{12}[7], quartz[8], and polymers like polyvinylidene fluoride (PVDF)[9] and PVDF-TrFE[10], as this restricts their potential applications to hybrid energy harvesters, human interfaces, robotics, smart sensors and self-powered optoelectronic systems[11,12]. Since the first demonstration of nanogenerator with ZnO[13], there has been increasing research interests in extracting coupling effects from materials by combining piezoelectric and semiconducting properties towards the realization of piezotronic and piezo-phototronic devices[14]. Eventually, GaN[15], CdS[16], ZnS[17], and InN[18], which is part of the wurtzite family, have been intensively investigated by researchers looking to develop devices with strong piezoelectric properties coupled with semiconducting characteristics. Recently, there have been interesting reports of the generation of piezoelectric potentials on layered semiconducting metal chalcogenide materials, such as GaSe[19] and MoS_2[20]. Reasonable performance is achieved by embedding optically active material (perovskite, $CH_3NH_3PbI_3$) into piezoelectric polymers such as PVDF, paving the way for the development of hybrid energy harvesters[21]. However, despite the efforts made thus far, there is still plenty of room to further explore semiconducting materials with piezoelectric properties[22]. The ternary V-VI-VII semiconductor group element antimony sulfoiodide (SbSI) is among the materials of greatest interest for potential energy harvesting. SbSI has many interesting characteristics, being a ferroelectric, n-type semiconductor with an indirect bandgap of 1.8–1.9 eV, pyroelectric co-efficient of ~ 6×10^{-2} $Cm^{-2}k^{-1}$ and piezoelectric co-efficient of ~ 1×10^{-9} C/N (d_{33}), along with the highest known curie temperature of ~ 22 °C[23,24]. Its physical properties have led to its role in the development of photoconductive, piezoelectric, pyroelectric

and optical devices. Several publications reporting the efficiency of SbSI for thermal imaging, nonlinear optics, and photosensors are particularly noteworthy[25,26]. However, there have not been any reports on extensively exploring the suitability of SbSI as a candidate for energy harvesting applications.

In this work, we present the first report on the development of PNGs using $A_VB_{VI}C_{VII}$ group, and demonstrate it as an emerging material for use in energy harvesting. We synthesized SbSI rods using a simple yet cost-effective and low-temperature solid state reaction (SSR) technique. We conducted a detailed investigation to optimize the reaction parameters with respect to the reaction temperature (S_T; 250 °C, 350 °C) and time (1, 15, 24 h). Our analysis of the hysteresis loop reveals SbSI as a potential mechanical energy harvesting candidate with a remnant polarization, P_r, of ~ 0.35 μC/cm^2. We determined the orientations of the dipole moments with respect to poling time (P_t ~ 15, 30, 60, 120, 180 min), and found them to exhibit an enhanced P_r of ~ 1 μC/cm^2. We further investigated a possible means of developing planar SbSI based piezoelectric nanogenerator (S-PNG) modules with widely preferred polymer matrices, such as polydimethylsiloxane (PDMS), (Polyvinylidene fluoride) PVDF and polymethyl methacrylate (PMMA). We found that an S-PNG based on an SbSI/PMMA composite serve to be the prime device configuration capable of generating a stable piezoelectrical performance of ~ 5 V and ~ 150 nA under a linear mechanical force (F) of 2 N. Supplementing, we also synthesized and developed antimony selenoiodide (SbSeI) to determine its comparison of mechanical energy harvesting capability. Further, the influence of photoactive semiconducting properties in S-PNG and single SbSI micro rod (SMR-PNG) is demonstrated with realization of piezo-phototronic effect. The generality of the reported findings indicates that SbSI has great potential for future lead-free energy harvesting applications. By means of its

multifunctional properties (ferroelectric-semiconductor-photoactive), SbSI will aid researchers in contributing to the development of hybridized self-powered devices based on multisource energy harvesting.

7.2 Methods

7.2.1. Synthesis of antimony sulfoiodide (SbSI)

The ferroelectric SbSI was prepared through a reliable, cost-effective solid-state reaction (SSR) technique using antimony (Sb), sulfur (S) and iodine (I_2) reactants sourced from Daejung chemicals. The reagents were weighed to an equal stoichiometric molar ratio (1: 1: 1~2) with an excess of I_2, then ground into a homogenous mixture using an agate mortar. Finally, the mixture was transferred to aluminum (Al) crucible and placed inside a tubular furnace, where the reaction was carried out under two different temperature conditions, 250 °C and 350 °C, for a period of 1 h with a ramping rate of 1 min/°C. At the end of the reaction, we collected the dark red colored product from the crucible and mechanically powdered it using a pestle and mortar. The product of this process was referred to as SbSI.

7.2.2. Synthesis of antimony selenoiodide (SbSeI)

To prepare SbSeI, the reagents of antimony (Sb), selenium (S) and iodine (I_2) were weighed to 1.5 g, 0.973 g, and 1.563 g and mixed with 10 ml of ethanol. Later, the solution was ultra sonicated for a period of 2 h at 70°C. This results in the formation of brown colored sol which was dried at 70°C overnight. The dried mixture is grinded using mortar to obtain fine powders of SbSeI.

7.2.3. Development of SbSI-based piezoelectric nanogenerator (S-PNG)

7.2.3.1 SbSI/PDMS composite

To develop the SbSI/PDMS composite, we first prepared the PDMS matrix by mixing Si elastomer with a curing agent to a ratio of 10: 1 (Dow Corning Sylgard 184). We obtained a homogeneously mixed transparent PDMS matrix, to which we added different weight ratios (1 and 5 wt %) of SbSI. This mixture was then magnetically stirred to ensure that the SbSI was uniformly dispersed throughout the PDMS matrix before being heated to a temperature of 70 °C for 1 h. Even after the treatment for overnight, the SbSI/PDMS composite remained uncured without causing any significant polymerization effects. The similar procedure was followed without addition of SbSI to obtained plain PDMS that eventually cured under heat treated of 70 °C for 1 h.

7.2.3.2 SbSI/PVDF composite

To form the SbSI/PVDF composite, we first prepared the PVDF matrix by dissolving 4 g of PVDF in N-Methyl-2-pyrrolidone (NMP): acetone solvent (5:3 volume ratio) followed by probe sonication for 1 h at 35 % amplitude. We acquired a clear PVDF matrix solution, to which we added different weight ratios (1, 2, 3 and 4 wt %) of SbSI and then magnetically stirred the solution for 1 h. After the SbSI was well dispersed throughout the PVDF solution, we transferred it to a petri dish and heat-treated it overnight at 70 °C. Pristine PVDF film was prepared according to the same procedure, without the addition of SbSI fillers. Highly flexible SbSI/PVDF films were obtained, which we then cut to the desired size of 2.5 cm x 2.5 cm and sandwiched between Al electrodes. This formed a PNG with a SbSI/PVDF configuration.

7.2.3.3 SbSI/PMMA composite

We demonstrated the mechanical energy harvesting capability by fabricating PNGs from the SbSI, which acted as an active layer in the PMMA polymer. In the typical procedure, the PMMA matrix was prepared by stirring 3 w/v % of PMMA in toluene at 60 °C for 1 h. To develop the SbSI/PMMA composite, 1 wt % of SbSI was added to the PMMA solution, which was then magnetically stirred for 1 h. Later, the composite solution was spin-coated on an Al electrode and dried at 70 °C/2 h. We repeated the spin coating several times to ensure that the electrode was completely covered. The active layer was sandwiched between the electrodes, with Al as a top electrode. Before packaging the device with PDMS, we attached antistatic tape to the Al electrodes to prevent electrostatic charge generation between the PDMS and Al.

7.2.3.4 SbSeI/PMMA composite

The procedure of SbSeI/PMMA composite is similar to the experimental details mentioned in 7.2.3.3 except 1 wt% of SbSeI was added to the PMMA solution instead of SbSI.

7.3. Results and discussion

7.3.1. Material analysis

The SSR SbSI synthesis method has been studied in detail, and is shown schematically in **Figure 7.1.** The X-ray diffraction (XRD) peak pattern shows that we achieved the desired SbSI product with a S_T of 250 °C. The spectrum in Figure 7.1(c) confirms that we obtained highly crystalline, well oriented orthorhombic phases of SbSI at 250 °C[25]. All of the peaks perfectly match the space group of Pnma (ICSD reference pattern: 98-004-0159). The fact that no

additional peaks were observed confirms the absence of possible byproducts or impurities, such as SbI_3 and Sb_2S_3/SbS_3.

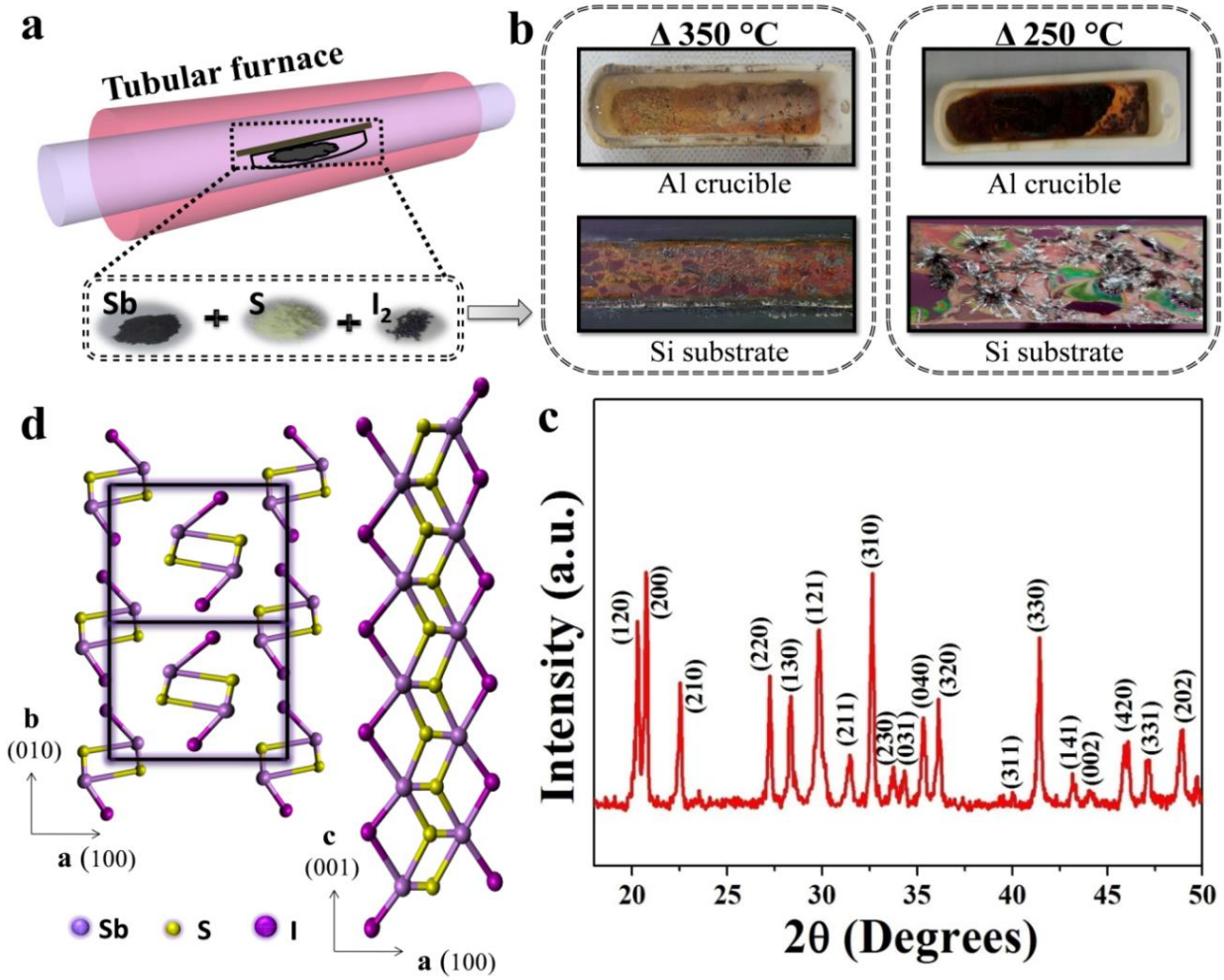

Figure 7.1 (a) Schematic illustration of the synthesis of antimony sulfoiodide (SbSI) via the solid state reaction (SSR) technique. **(b)** Formation of SbSI powder in aluminum (Al) crucible and deposited SbSI microwire on p-Si substrate. **(c)** X-ray diffraction (XRD) spectrum of as-synthesized SbSI powder at 250 °C. **(d)** Atomic arrangements of SbSI along the (010) and (001) axes, forming the crystallographic orthorhombic phase.

Meanwhile, iodine (I_2) decomposes at elevated processing temperatures (350 °C), gradually causing the formation of impure crystalline phases, as shown in **Figure 7.2**(a)[27]. The predominant peaks at (121), (310), (330), (200) indicate that, in comparison to bulk crystal, the

sizes of the SbSI crystals were reduced by SSR-assisted synthesis[25]. We further hypothesized that prolonged soaking times (S_t: 15 and 24 h) would reduce the quality of the crystals, but the desired SbSI crystal phases formed (Figure 7.2(b)). Thus, we consider the reaction at 250 °C/1 h to be the favorable processing condition for obtaining well crystallized SbSI via the SSR method.

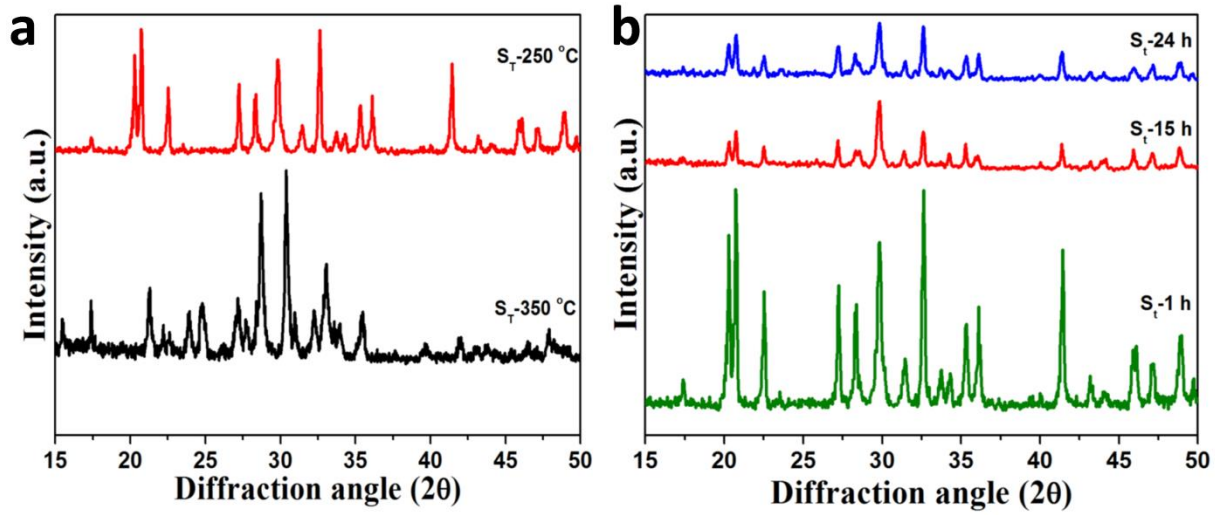

Figure 7.2 (a) XRD spectrum illustrating the soaking temperature (S_T) effects on the growth of SbSI fabricated using the SSR technique. **(b)** XRD spectrum of the soaking time (S_t) effects on the growth of SbSI fabricated using the SSR technique (250 °C).

Besides, it endorses the longer ribbon-like molecular chain arrangements in as-synthesized SbSI along its (001) plane axis which reasons the formation of SbSI in long rod-like homogeneous structures with diameter ~ 1- 2 μm and length ~ 20 - 50 μm, respectively (FESEM image, **Figure 7.3**(a)). The rods are oriented in a zigzag manner, and appear to be highly malleable. This is conventionally believed to provide stability, enabling the material to withstand high mechanical force when utilized as an energy harvesting material. SbSI exhibits lattice vibrational modes of less than 400 cm^{-1} that can be categorized into a low frequency range (LFR, < 100 cm^{-1}) and a high frequency range (HFR, > 100 cm^{-1})[28]. Figure 7.3(b) shows the Raman

active modes of the HFR measured at room temperature (R_T) showing five strong phonon modes at 106 cm^{-1}, 143 cm^{-1}, 193 cm^{-1}, 251 cm^{-1} and 315 cm^{-1} [29].

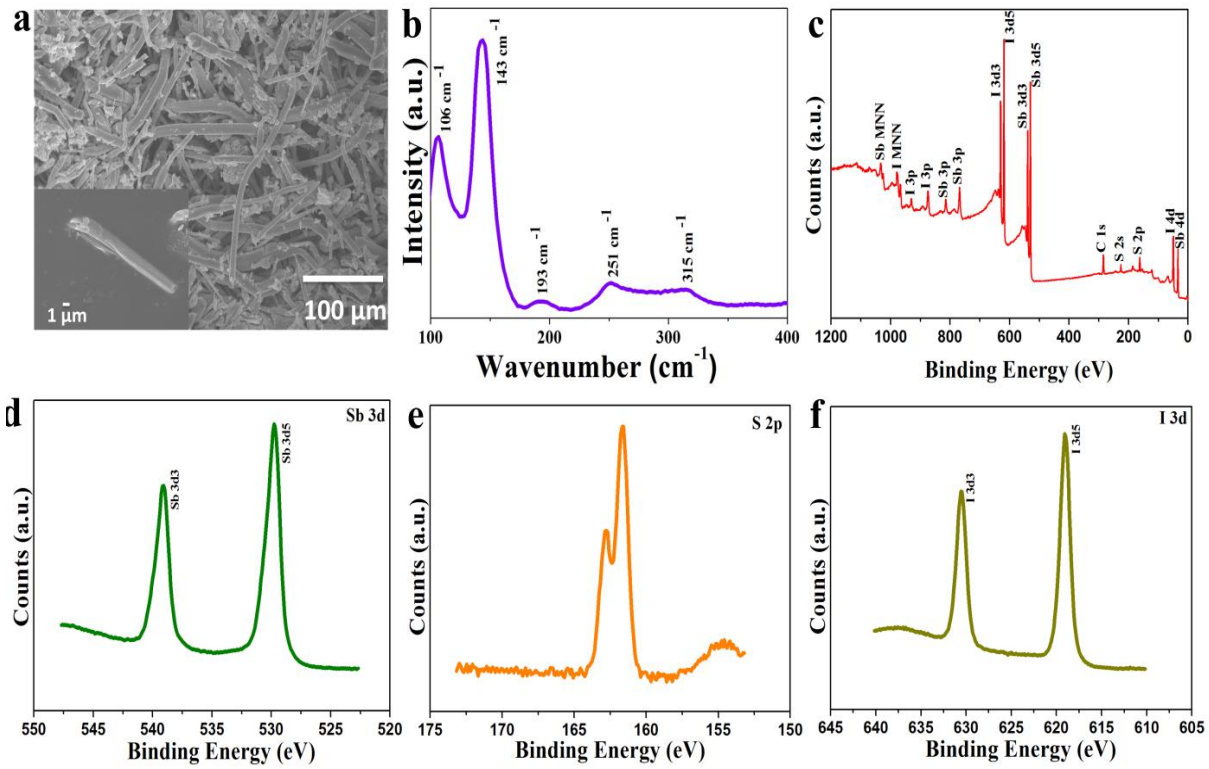

Figure 7.3 (a) Field emission scanning electron microscopy images for SbSI at 100 µm scales. Inset represents the magnified view at a scale of 1 µm. **(b)** Raman spectrum of SbSI. **(c)** XPS spectrum illustrating the core orbital levels of Sb, S and I. Enlarged regional peaks of **(d)** Sb 3d, **(e)** S 2p, and **(f)** I 3d.

The frequencies of the peaks indicate that the sample exhibits Γ_1 symmetry, which is associated with the $G_2(u)$ and $G_5(u)$ mode functions corresponding to SbSI crystals with ferroelectric polarization phases in the space group of C_{2h}^2 [28]. Figure 7.3(c) shows the XPS spectrum of SbSI measured in the binding energy range 1200–0 eV. The spectrum contains strong peaks associated with the Sb 3d5, Sb 3d3, Sb 4d, I 3d5, I 3d3, I 4d, S 2s, and S 2p orbitals. The magnified core level spectra of Sb, S and I are shown in Figure 7.3 (d, e, and f) respectively. The peaks at 539.09 and 529.77 eV correspond to, respectively, the antimony (Sb) 3d3 and 3d5

orbitals; the peaks at 162.78 and 161. 64 eV indicate the sulfur (S) 2p orbital, and those at 630.52 and 619.02 eV represent the iodine 3d3 and 3d5 orbitals. The positions of all of the peaks detected by the XPS analysis are consistent with the core-levels of SbSI[26]. Further, we conducted energy dispersive spectrometry (EDS) analysis to identify the elemental composition, as shown in **Figure 7.4**(a). The percentages of each type of atom are approximately equal, in the range of 32.77 (Sb): 33.30 (S): 33.93 (I), which proves the accuracy of the elemental ratios in the obtained product. We investigated the optical characteristics of the synthesized SbSI by conducting a ultraviolet-visible (UV-Vis) absorbance study. This revealed an indirect bandgap, which we estimated using a tauc plot analysis based on the relationship, $(\alpha h\nu)^n = A\ (h\nu - E_g)$. The exponent of the indirect interband transition, n, is equal to ½, hν is the energy of the incident photon and α is the absorption coefficient. According to Figure 7.4(b), the bandgap (E_g) is close to 1.85 eV, reflecting its semiconducting absorption potential over the visible spectrum (400–780 nm)[30].

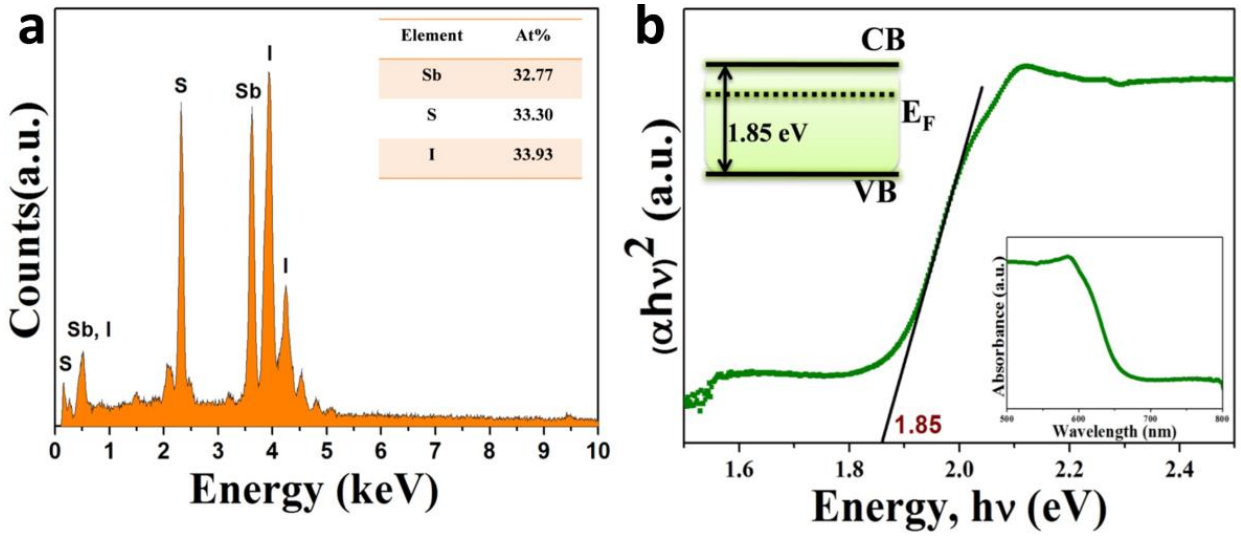

Figure 7.4 (a) Energy dispersive spectrometry analysis of SbSI. **(b)** Optical characteristics (the inset shows the ultraviolet-visible [UV-Vis] absorbance spectrum).

7.3.2. Functional dependence of polarization and applied field

We used a polarization–voltage (P–V) hysteresis loop to evaluate the ferroelectric properties of SbSI, which indicate its suitability as an energy material. The results are presented in **Figure 7.5**.

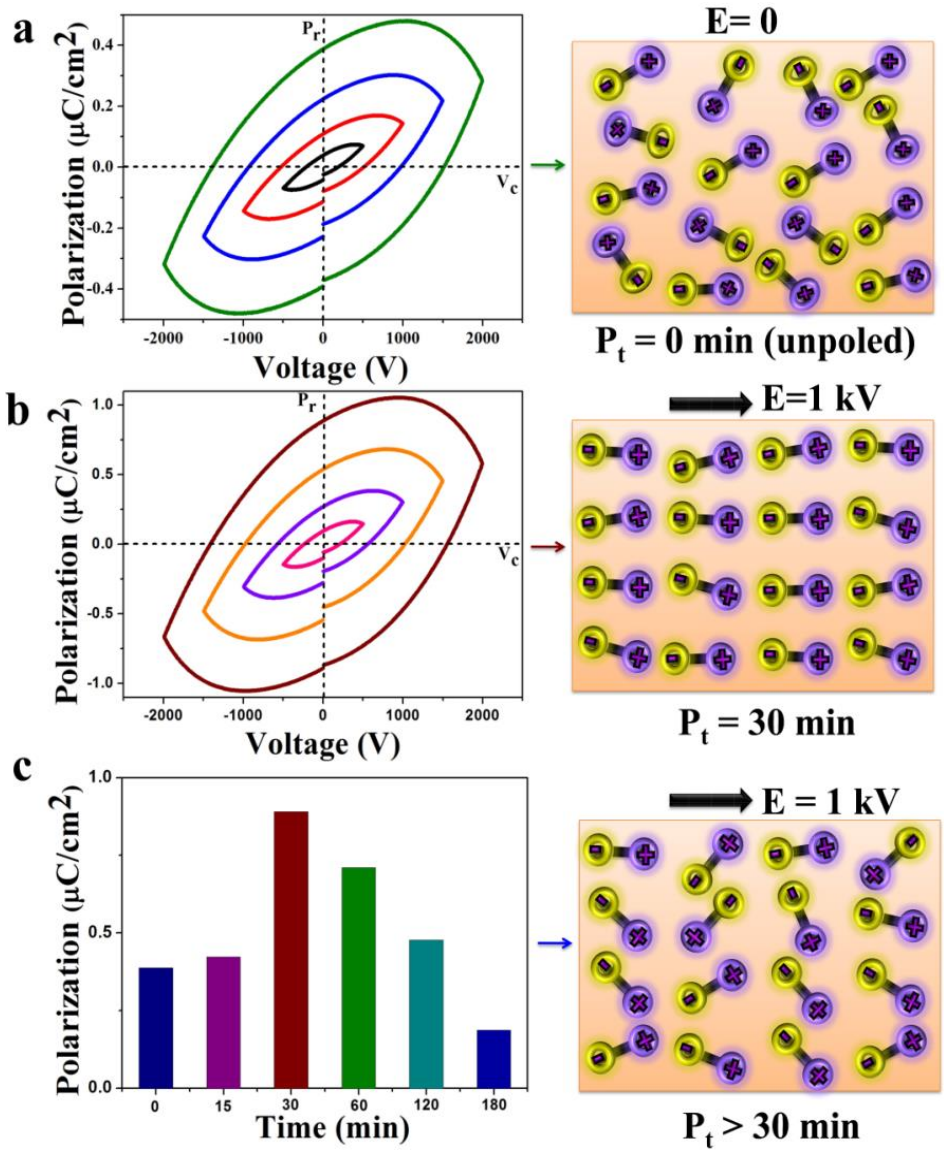

Figure 7.5 Analysis of SbSI electrical poling characteristics. **(a)** Polarization–voltage (P–V) loop before poling i.e., at zero electric field (E) when the dipoles are randomly oriented. **(b)** P–V loop after poling i.e., at applied field (E) of 1 kV for a poling time (P_t) of 30 min, causing the dipoles to be arranged in an orderly manner. **(c)** The effect of P_t as a function of dipole alignment.

All of the measurements were performed at R_T using pellets made of SbSI (with an average diameter ~ 13 mm and thickness ~ 1 mm) sandwiched between silver (Ag) electrodes. The P–V loop in Figure 7.5(a) determines the polarization efficiency at increased applied potentials, from 500–2000 V. The synthesized SbSI exhibited a remnant polarization (P_r) of ~0.35 μC/cm^2 and withstood a coercive field of (V_c) ~1590 V. The presence of the asymmetrical nodes enclosing the loop implies the existence of the leakage current associated with Schottky barrier contacts at the SbSI/Ag electrode interfaces. The curve pattern illustrates ideal ferroelectric behavior, and the non-zero P_r value confirms that SbSI exhibits spontaneous polarization. To perceive the act of time dependent polarization, the pellets were electrically poled at an applied electric field (E) of 1 kV for various time durations (P_t - 15, 30, 60, 120, 180 min). At a poling period of 30 min, the ferroelectric charges (positive and negative) tend to incline maximum along the direction of externally applied field. This signifies perfect orientation of domains with enhanced resultant polarization in SbSI producing P_r of ~ 1 μC/cm^2 (Figure 7.5(b)). Applying a constant electric field for more than 30 min, gradually declines the P_r value due to the complex space distribution features in the dipole orientation[31]. When the poling time prolongs, the dipoles tends to rotate further apparently reversing the domain motions creating an internal electric field that cancels the oriented polarizations which is typically referred as local depolarization effect[32,33]. As P_t increases, the depolarization field intensifies eventually causing more changes in the domain structural rearrangements[34]. Thus, P_r drops significantly to ~ 0.71, 0.47, and 0.18 μC/cm^2 when poled at 60, 120, and 180 min as a result of polarization decay (Figure 7.5(c)) (**Figure 7.6**)[31].

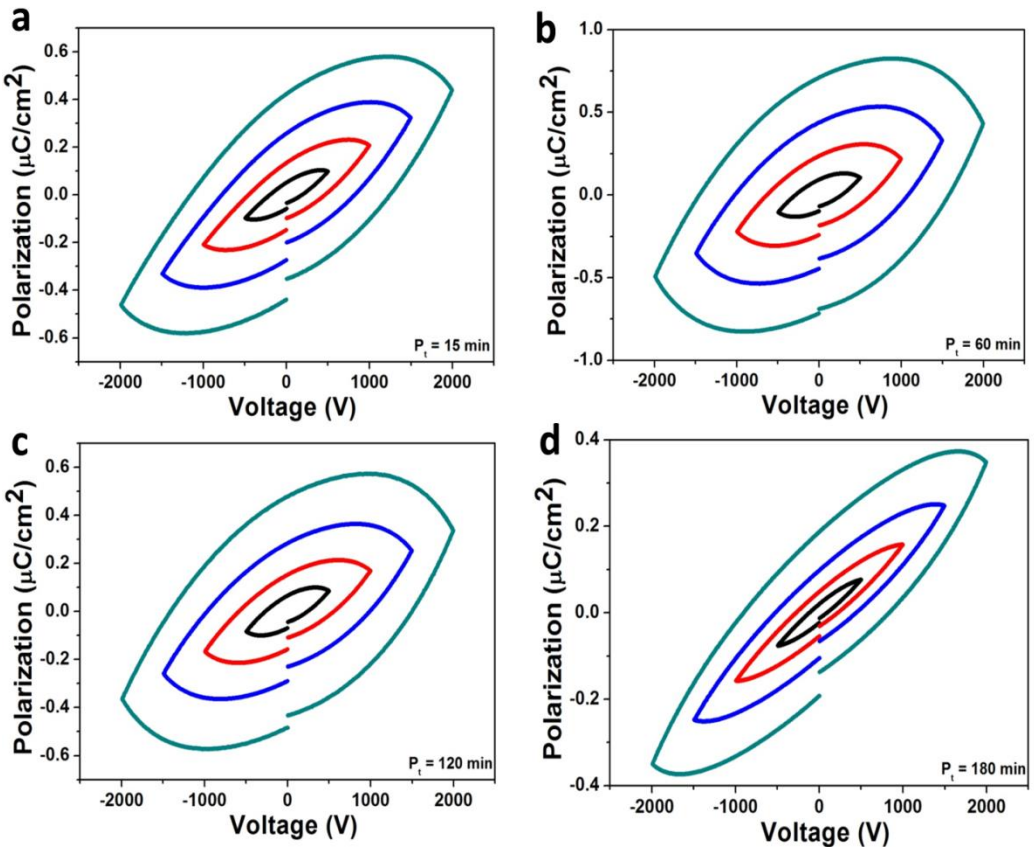

Figure 7.6 Polarization analysis (P–V loop) at various electrical P_t. **(a)** 15 min. **(b)** 60 min. **(c)** 120 min. **(d)** 180 min.

7.3.3. Evaluation of polymeric interfaces

We investigated the suitability of $A_VB_{VI}C_{VII}$ ferroelectric-semiconductor compounds as active energy harvesters by analyzing the development and performance of PNGs based on the synthesized SbSI (S-PNGs). A typical PNG includes a polymer matrix, which is employed as a medium to support the active material[22,35]. Accordingly, we evaluated the suitability of the composite using the most popular binding polymers applied for fabricating PNGs, such as (i) PDMS, (ii) PVDF, and (iii) PMMA. SbSI induced different behaviors in the polymers when impregnated as a filler material to form a composite. To begin with, we filled the uncured PDMS

matrix with different weight ratios (1 and 5 wt %) of SbSI. Even the lowest filling ratio (1 wt %) of SbSI disturbed the polymerization of PDMS, as shown in **Figure 7.7**(a)**.**

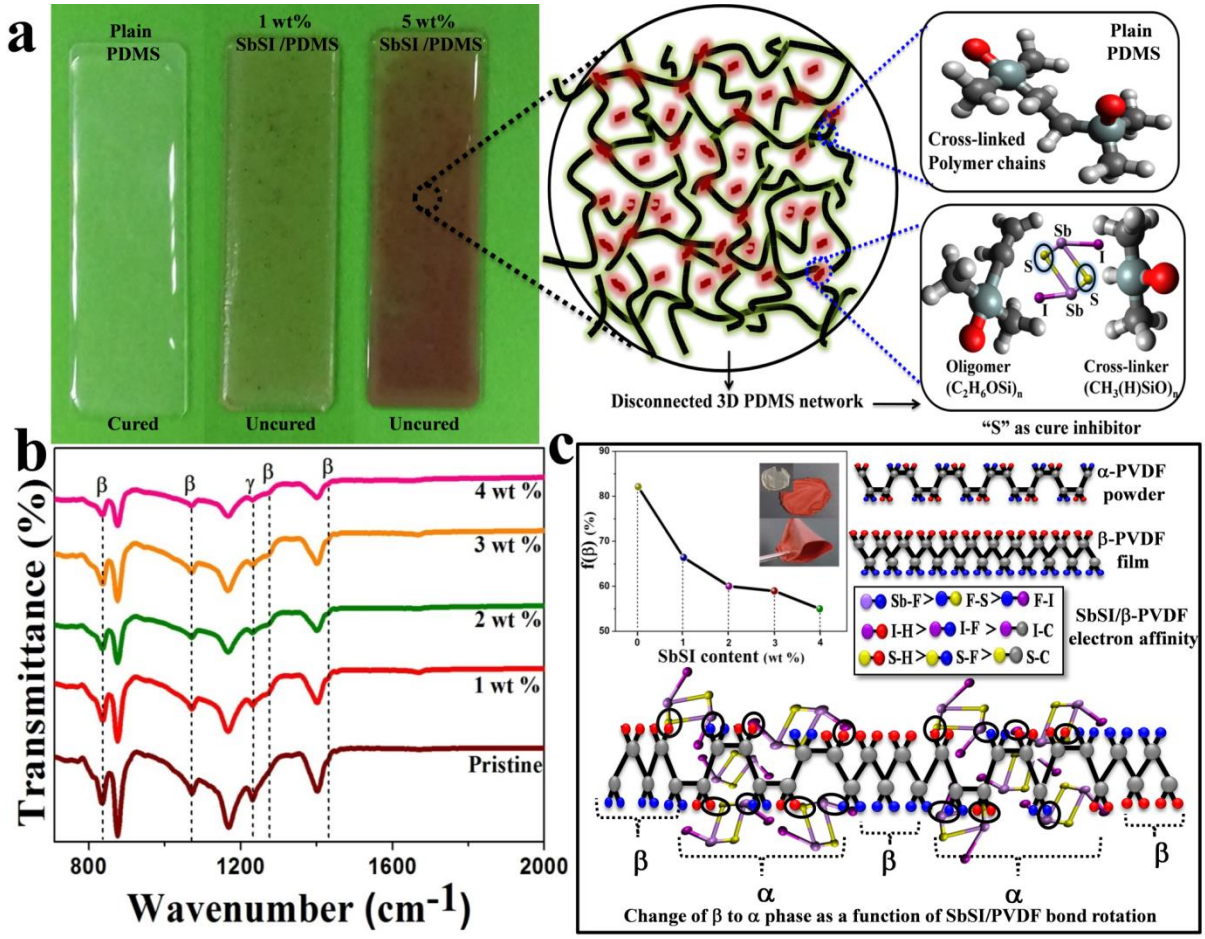

Figure 7.7 Polymer-dependent interface behavior for the development of SbSI based piezoelectric nanogenerator (S-PNG). **(a)** SbSI/PDMS composite specimens (where sulfur inhibits the cross linking of the silicone elastomer). **(b)** Fourier transform infrared spectra of SbSI/PVDF composite at various ratios of SbSI filler. **(c)** Illustration of the SbSI-PVDF interface mechanism, which caused changes to the polar chains Inset: decreased relative β fraction, f(β), versus SbSI filler content.

The presence of S in SbSI acts as a cure inhibitor and affects the formation of $–CH_2-CH_2–$ bonds between the Si elastomer-based cross-linker $(CH_3(H)SiO)_n$ and the oligomer $(C_2H_6OSi)_n$, which we sourced from Dow Corning Sylgard 184[36]. From the MSDS information,

S inhibits the catalyst present in the Sylgard 184 elastomers, thus preventing the PDMS from solidifying[37]. Following our evaluation of PDMS, we tested the ferroelectric polymer PVDF as a binding matrix. This formed a highly flexible film with various proportions of SbSI filler (1, 2, 3 and 4 wt %). The Fourier transform infrared (FTIR) spectrum of the SbSI/PVDF composite exhibits polar phase characteristics, as shown in Figure 7.7(b). The peaks at 840, 1072, 1274 and 1453 cm^{-1} correspond to the polar (β) phase, whereas the peak at 1232 cm^{-1} represents the semi polar (γ) phase. These ensure that the SbSI/PVDF composites exhibit active electric phases[35]. We promoted the β phase of the PVDF film by probe sonicating (1 h at 35 % amplitude) commercial α phase PVDF powder in an NMP: acetone solvent (5:3 volume ratio) then heat treating it overnight at 70 °C. The intensities of the β and γ phases decreased gradually upon the addition of SbSI, which shows that promotion of the ferroelectric properties of PVDF by SbSI is inversely proportional. The mechanism for this behavior is illustrated schematically in Figure 7.7(c). When the SbSI is combined with the PVDF, it interacts with the ions in its chains, such as C, F and H, via the intermolecular force between the filler and the polymer matrix. This in turn alters the bond stretching of $-CH_2-CF_2-$, which plays a crucial role in imparting the β property to PVDF[38]. The existence of SbSI/PVDF interaction is supported in **Figure 7.8**. Figure 7.8(a) represents the FTIR spectrum in the region of 2200-2600 cm^{-1}. The frequency of peak at 2500-2600 cm^{-1} corresponds to the SH stretching mode thus confirming the bonding nature between the S-H group[39]. To prove the existence of Sb-F and I-H, we carried out XPS analysis for SbSI/PVDF composite films. Figure 7.8(b) represents the spectrum over Sb 3d scan. Measured binding energy in the direct range of 542.2 eV, correlates to the SbF_3 complex ensuring the formation of Sb-F interactions[40, 41]. Higher the intensity of binding energy with increased SbSI filler content (4 wt %) confirms the higher fluorine terminations creating Sb-F[40, 41]. Since the hydrogen

bonding is equally sensitive to the presence of SH group, direct evidence of I-H is quite tedious. However, the existence of I-H is further verified by examining the C1s core levels to that of I 3d binding energy in SbSI/PVDF (Figure 7.8(c)).

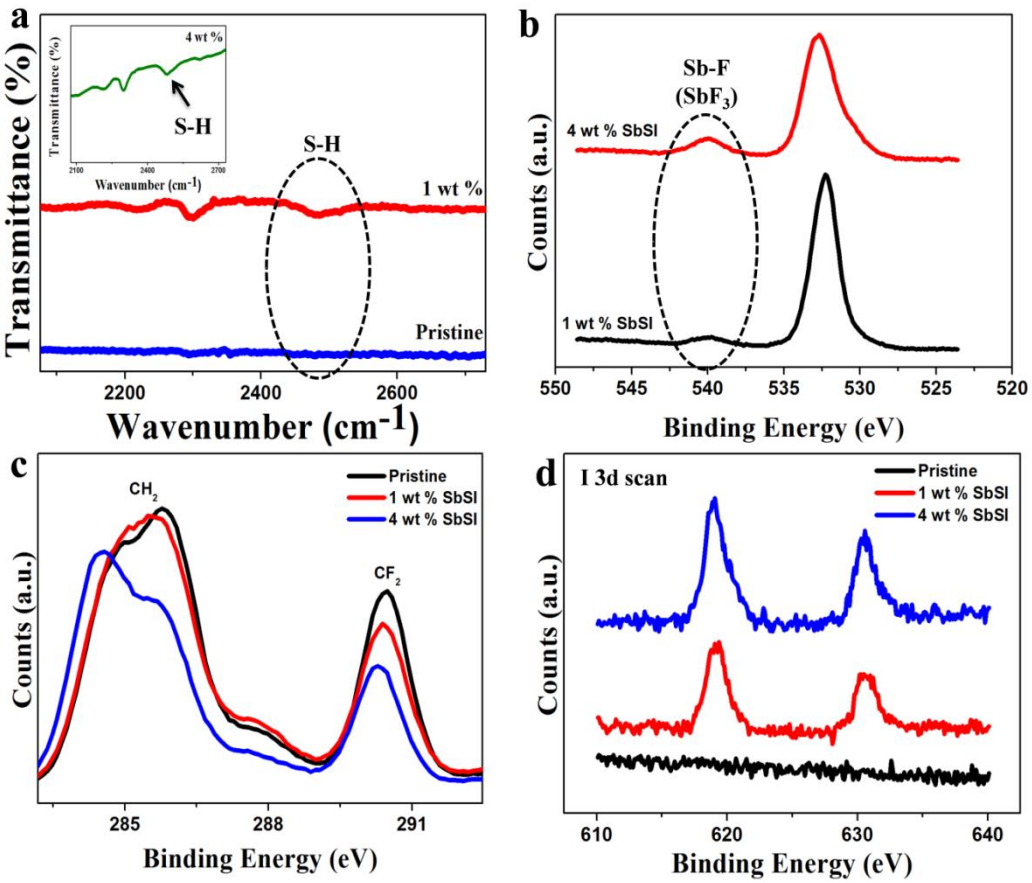

Figure 7.8 Interaction of SbSI/PVDF polymeric chains. **(a)** FTIR spectrum ensures the presence of S-H group. **(b)** Sb 3d core-level XPS spectra illustrating the possibility of bonding between Sb-F. **(c)** XPS of C1s core-level of pristine PVDF and SbSI/PVDF composites (1 wt % and 4 wt % of SbSI). **(d)** Corresponding I 3d binding energy.

The trend of decrease in CH_2 stretching with the increase in the SbSI content demonstrates that the ideal C-H bond is affected due to the filler content[42] with respect to enhanced I 3d binding energy Figure 7.8(d). This also signifies the possibility for the existence

of I-H interactions. Besides, the similar behavior in CF_2 levels equally demonstrates the changes in C-F polymeric chains due to the addition of SbSI.

In the presence of SbSI, the polymer chain stretching is based on the electron affinity in the order: Sb-F (440 KJ/mol) > F-S (284 KJ/mol) > F-I (273 KJ/mol), I-H (298 KJ/mol) > I-F (273 KJ/mol) > I-C (215 KJ/mol) and S-H (363 KJ/mol) > S-F (284 KJ/mol) > S-C (272 KJ/mol). Hence, when the SbSI/PVDF composite is formed, among all of the possible bond formations, the possibility for -CH_2-CF_2- to stretch depends on the Sb-F, I-H and S-H bonds, because it has the shortest bond length (i.e., higher energy). This rotates the β phased polar molecular chains into the non-polar α phase, thus significantly diminishing the relative β fraction content f(β) (Figure 7.7(c), inset), which we estimated as,

$$f(\beta)\ \% = \frac{A_\beta}{(k_\beta/k_\alpha)A_\alpha + A_\beta} \times 100\ \% \qquad \text{- (1)}$$

where A_α, A_β are the absorption peaks at 766 cm^{-1} and 840 cm^{-1}, respectively, and k_α, k_β corresponds to the absorption co-efficient at its phase wavelengths, with values of 6.1×10^4 cm^2/mol and 7.7×10^4 cm^2/mol, respectively[38]. We observed similar behavior in the piezoelectrical response from S-PNG devices fabricated using aluminum (Al)/SbSI-PVDF film/Al layer arrangements. All of these devices exhibited a negative effect, with a lower piezoelectric voltage (V) than that of pristine PVDF film (**Figure 7.11**). Consequently, the piezoelectric voltage declined linearly as we gradually increased the SbSI content. This clearly confirms that the incorporation of SbSI into the PVDF matrix diminishes the polarization content ((β and γ phase), rendering PVDF an inappropriate binding polymer. Furthermore, we developed an S-PNG using PMMA as a supporting medium. We fabricated the device by preparing the polymer composite, by stirring 1 wt % of SbSI in PMMA solution (3 w/v % in toluene, prepared

at 60 °C for 1 h) and then drop casting the as-prepared SbSI/PMMA matrix on the Al electrode. We ensured that the PMMA/SbSI composite was completely cured by heating it at 70 °C for 2 h. Later, covered the active layer with the top electrode (Al) and encapsulated it with an antistatic tape before packaging it in PDMS (**Figure 7.9**(a)). Cross-sectional FESEM image of as-fabricated S-PNG is provided in Figure **7.10**(a). We poled the device under the desirable condition of 1 kV for 30 min. The results of the experiment to optimize the poling are shown in Figure 7.5.

7.3.4. Demonstration of self-powered photodetection

The energy harvesting capability of the ferroelectric-semiconductor SbSI was analyzed under a constant force (F) of ~2 N with frequency (f) of 1.27 Hz, which we applied with a linearly moving shaft (mass of 2 kg, acceleration of 1 m/s^2). The responses are shown in Figure 7.9(b, c). The S-PNG device produced ~5 V and 150 nA of piezoelectric voltage and current, respectively. PMMA is an acrylic-type polymer that possesses a zero piezoelectric co-efficient of its own. Hence, the filler component (SbSI) is the only source contributing to the piezoelectric output from the S-PNG device[43]. Besides, the switching polarity test was conducted to confirm the output signals are from piezoelectric potentials rather than contribution of other effects (Figure 7.10(b)). When a force is applied, it triggers the ferroelectric SbSI crystals to induce positive and negative potentials at the top and bottom electrodes, respectively. The generation of piezoelectric potentials directs the electrons to flow through the circuit, producing a positive cycle. The electrons flow back when the applied force is released, thus resulting in a negative electrical response cycle.

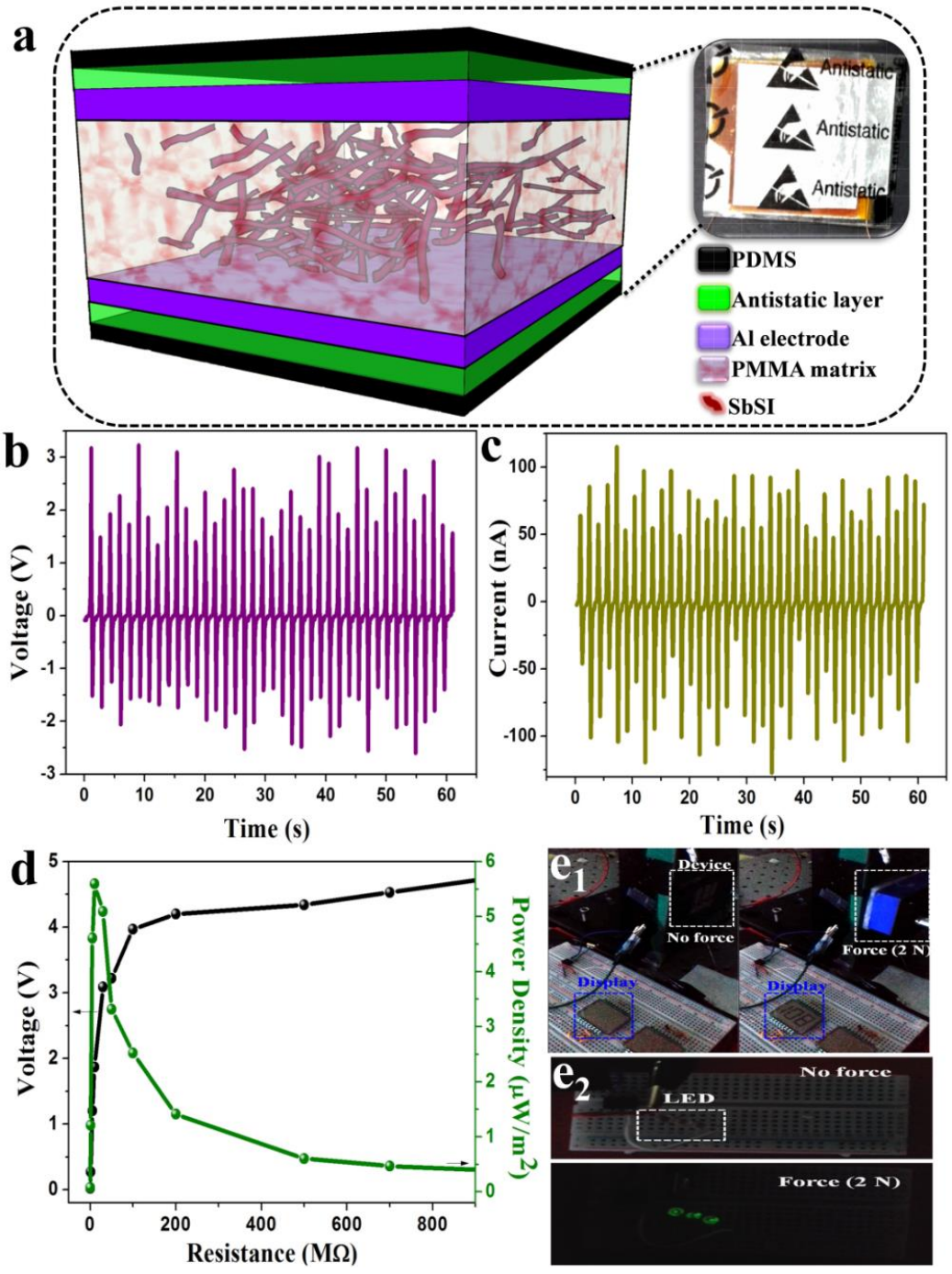

Figure 7.9 (a) Schematic of the SbSI/PMMA piezoelectric nanogenerator (S-PNG) and an optical image of the fabricated device. Piezoelectrical analysis under applied mechanical force (F) of 2 N. **(b)** Voltage (V) response. **(c)** Current (nA) profile. **(d)** Load resistance plot with equivalent power density evaluation, and real time demonstrations with **(e1)** liquid crystal display. **(e2)** Light emitting diodes.

Switching polarity test was conducted to confirm the output signals are from piezoelectric potentials rather than contributions from other effects. The electrical signals obtained for forward and reverse connections to the S-PNG device is given in Figure 7.10(b)**.** When the connections were reversed, the generated positive and negative polarity switches readily affirming the produced signal is due to the piezoelectric charges generated during the subjection of force on to the S-PNG device. The ideal polarity switching characteristics from S-PNG strongly validates the electrical performance is due to the generation of piezoelectric potentials, and not from any other effects[44].

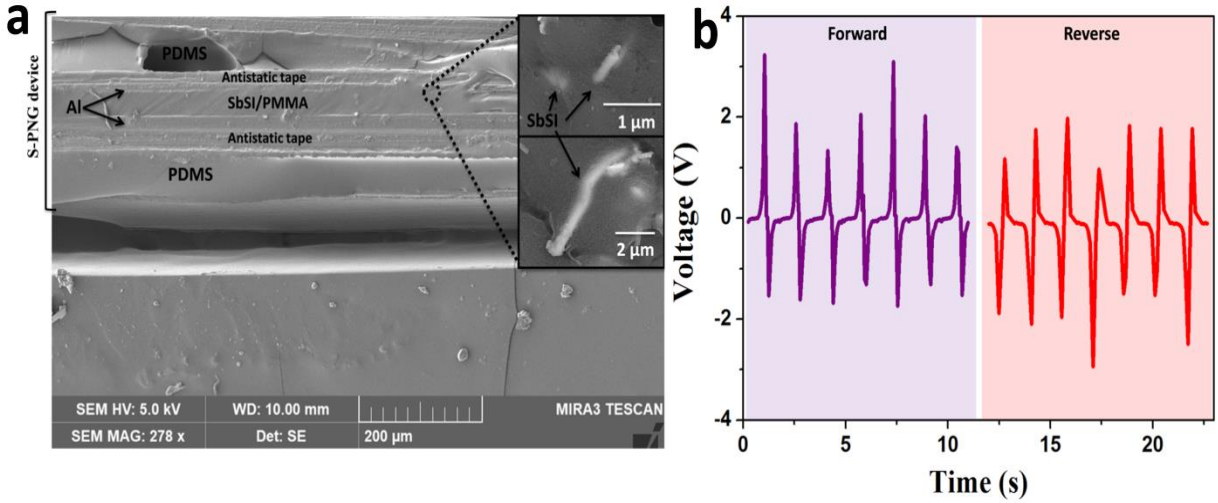

Figure 7.10 (a) Cross-sectional FESEM image of as-fabricated S-PNG (signifies the absence of air gap between the active layers). **(b)** Switching polarity analysis at force of 2 N (output voltage of S-PNG during forward and reverse connections).

We performed load resistance (R_L) and power density (P) analysis of the S-PNG as we varied the resistance from 5 MΩ to 700 MΩ and calculated P using the equation,

$$P = \frac{V^2}{R_L \times A} \qquad \text{- (2)}$$

where R_L is the load resistance, V is the piezoelectric voltage at the respective R_L, and A is the area of the S-PNG device (6.25 cm^2). As shown in Figure 7.9(d), we obtained the maximum power density (P) of 4.6 $\mu W/m^2$ when R_L was 10 MΩ. Thus, this is the optimum load matching resistance. Besides, we then demonstrated the real-time performance of the S-PNG by using the piezoelectric potentials generated by a constant F of 2 N, to drive a liquid crystal display (LCD) and green light emitting diodes (LEDs) connected in series. Figure 7.9(e_1) shows the display in the "OFF" condition when the shaft is released, and it turns "ON" when the shaft hits the device. Figure 7.9(e_2) shows the lit LEDs, which were connected through bridge rectifier circuitry. The S-PNG device was sufficient for three LEDs to glow with a good level of intensity.

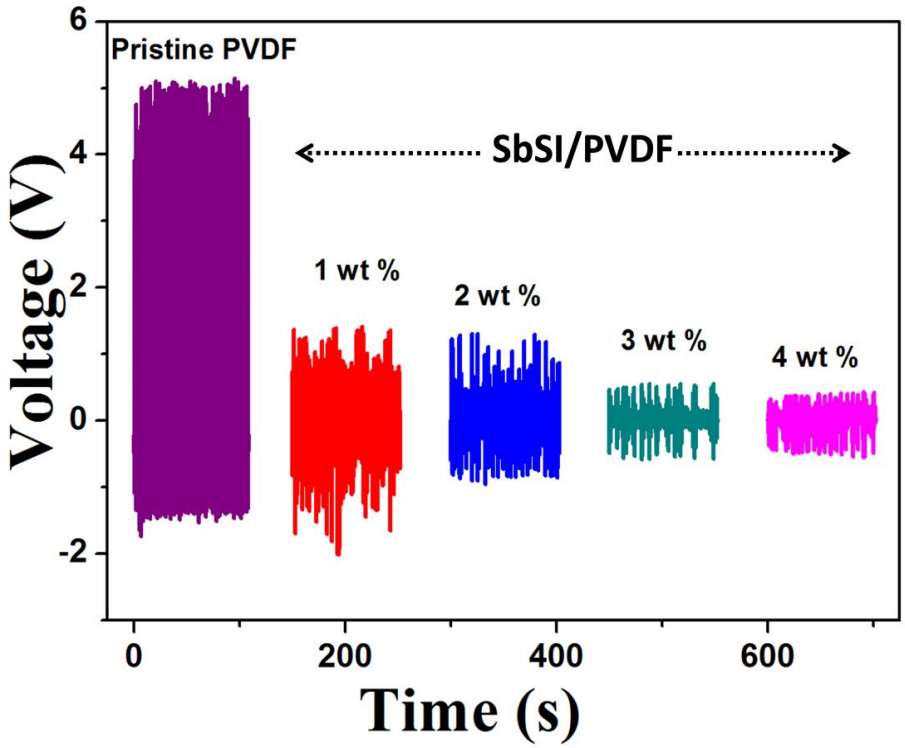

Figure 7.11 Piezoelectric performance analysis of the PNG fabricated with SbSI/PVDF composite.

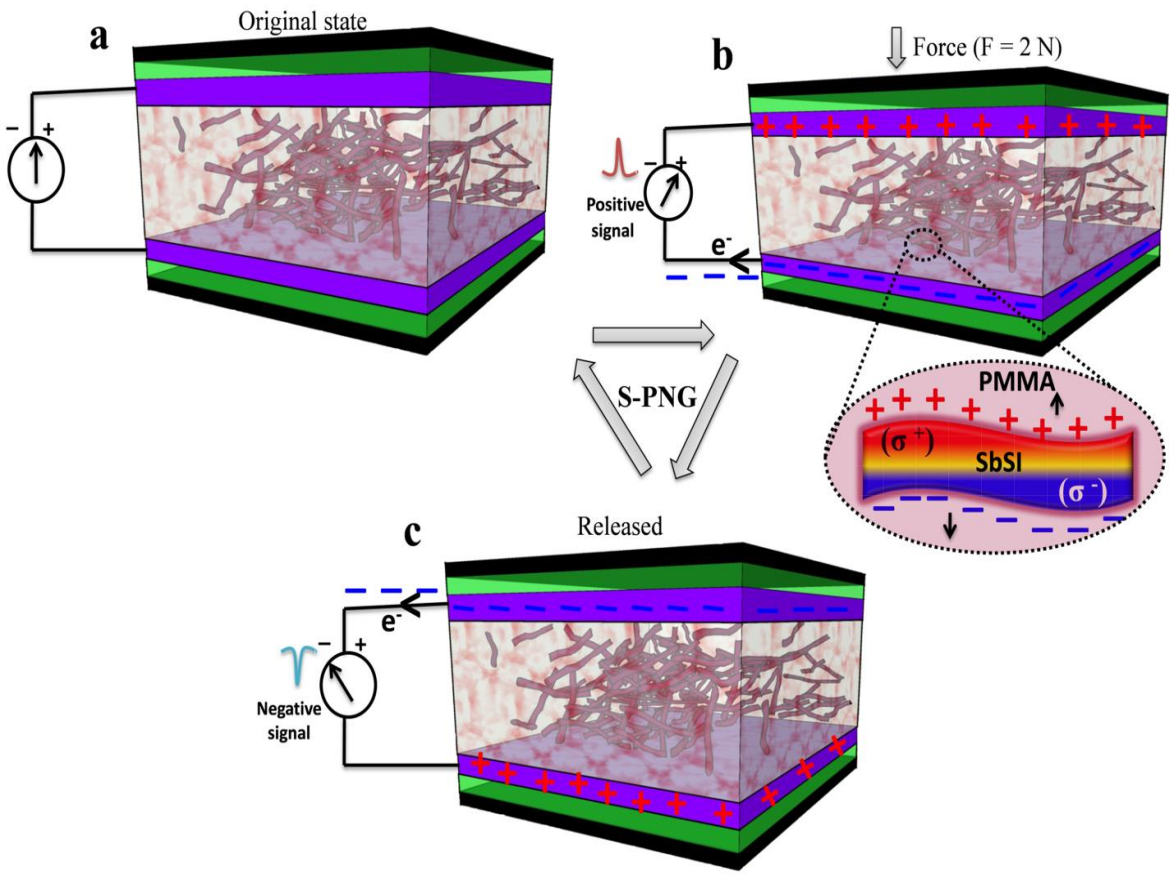

Figure 7.12 Schematic illustration of the working mechanism of S-PNG under externally applied force.

The working mechanism of S-PNG is illustrated in **Figure 7.12.** Typically the working of PNGs falls under three conditions: (a) original state (no force), (b) Under force (pressed), and (c) Released. In original state where the external force is absent, the S-PNG produces no signals. By the externally applied force, the S-PNG is activated resulting in the generation of piezoelectric field due to the released positive (σ^{+}) and negative (σ^{-}) charges in the parts of SbSI held in PMMA matrix. Here, the PMMA helps in transferring the generated piezoelectric charges towards the respective electrodes being the source of dielectric medium. At this stage of pressing, the negative charges are accumulated at the bottom electrode and positive charges at the top electrode (depending on piezoelectric potential distributions in SbSI). By establishing an electronic circuit, the accumulated electrons flow from the bottom electrode to the top electrode

to balance the generated inner piezoelectric field (Figure 7.12(b)). This results in the positive signal of the output. As the external force is released, the piezoelectric potential created inside the SbSI vanishes and the charge carriers flow back to the bottom electrode (Figure 7.12(c)). This correspond to the signal resulting in the opposite direction i.e., negative peak[45]. We assessed the electrical stability of the S-PNG by constantly subjecting the device to a force of 2 N for a period of 1500 s (**Figure 7.13**) and found it to be durable over the long run.

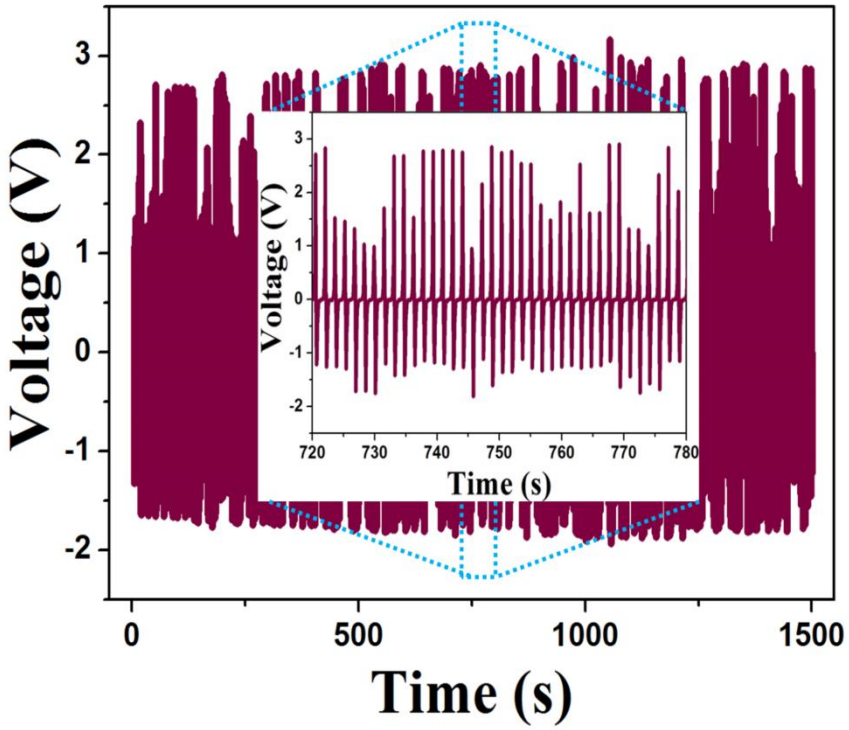

Figure 7.13 Stability graph of the PNG fabricated with the SbSI/PMMA composite for a period of 1500 s (F = 2 N).

We also estimated the capability of SbSeI to successfully scavenge mechanical energy (**Figure 7.14**). For which, we synthesized SbSeI using ultra sonication method (experimental section 7.2.3.4). The as-synthesized powder was analyzed using Raman characterization (Figure 7.14 (a)) which exhibited peaks matching the vibrational spectra of SbSeI[46]. The lower wave number peaks are assigned to the vibrational modes of Sb-I bonds and higher vibrational peaks

are assigned to Sb-Se modes (> 200 cm^{-1}). The peak below 200 cm^{-1} are halogen sensitive which corresponding to halogen atom motions with Sb-I interactions[46]. The strong peak at 206 cm^{-1} strongly activates the strengthened characteristics between Sb-Se atoms. The P-V loop shown in Figure 7.14(b) illustrates the ferroelectric nature of SbSeI with strong remnant polarization of ~0.1μC/cm^{-1} at a frequency of 444 Hz. We further proceed with determining the piezoelectric energy harvesting ability of as-synthesized SbSeI by fabricating PNG with similar device configuration as that of S-PNG where SbSeI is used as filler instead of SbSI. The obtained piezoelectric voltage response is given in Figure 7.14(c). With a mechanical actuation of 2N the fabricated SbSeI/PMMA based PNG delivered an average peak to peak potential of ~ 2V at 100 MΩ. Figure 7.14(d) illustrates the piezoelectric current profile with an average range of ~60 nA. The load matching analysis was carried out with the resistance ranging from 100 kΩ to 1 GΩ Figure 7.14(e). At an acting load resistance of 50MΩ the maximum power density of 1.6 μW/cm^2 was obtained. Further, the stability of SbSeI/PMMA based PNG device was tested for a period of 1000 s under 2 N forces. Figure 7.14(f) shows the obtained voltage profile of the device constant voltage even at 1000 s of actuation showing that the good stability. Despite the reasonable performance of SbSeI, the polarization efficiency and piezoelectric energy harvesting of SbSeI is low comparatively with SbSI. Hence, SbSI is preferred for further experiments to realize self-powered photodetection using ternary chalcohalide materials.

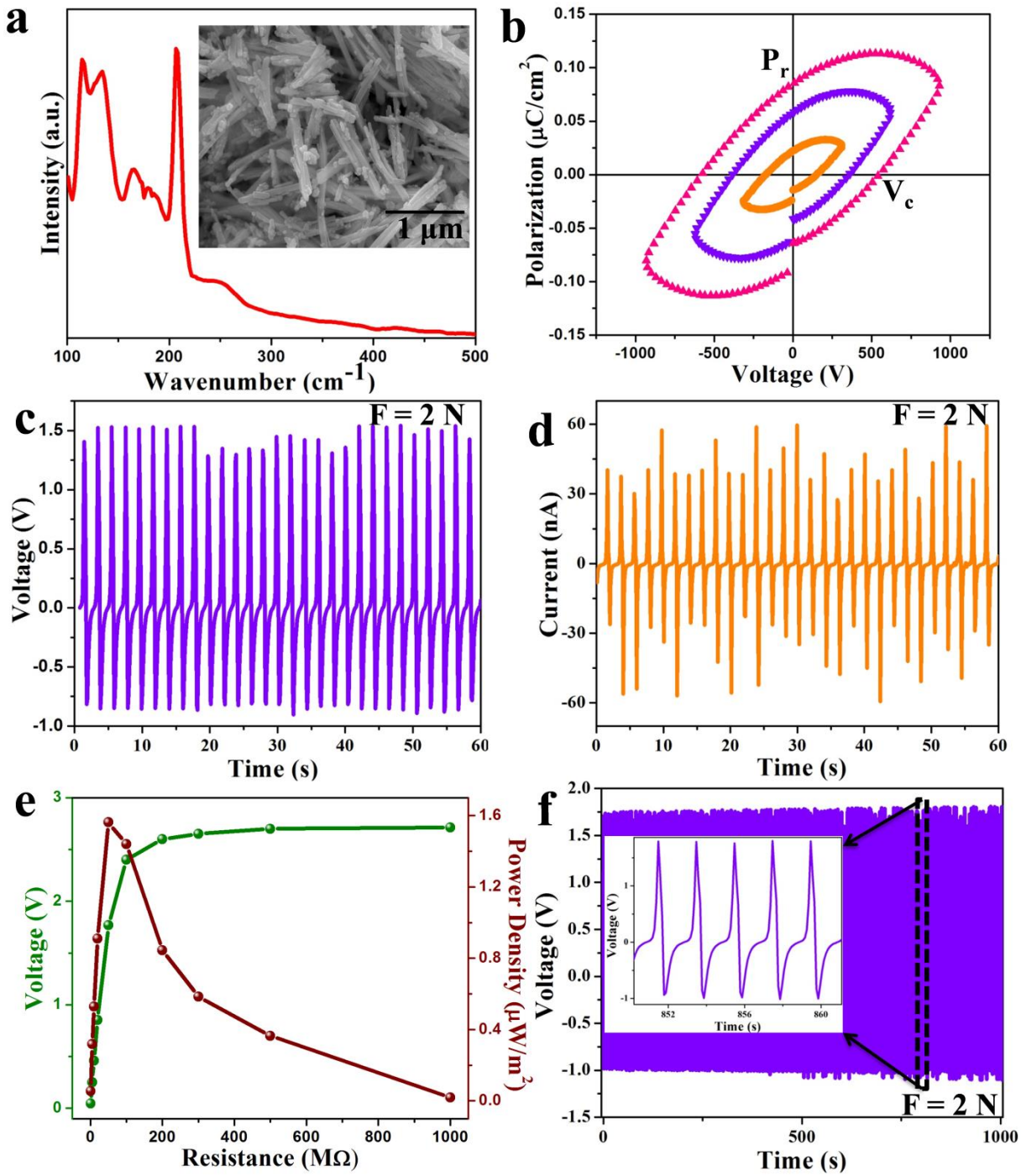

Figure 7.14 Performance evaluation of SbSeI. **(a)** Raman spectrum of synthesized SbSeI. **(b)** P-E loop. **(c)** Piezoelectric voltage of SbSeI/PMMA composite based PNG. **(d)** Current profile. **(e)** Load matching analysis. **(f)** Stability test.

In order to demonstrate the involvement of semiconducting and photoactive properties in mechanical energy harvester, we first determined the semiconducting effects through SbSI based photodetector (S-PD) with metal-semiconductor-metal (MSM) configuration **(Figure 7.15**(a) (inset)).

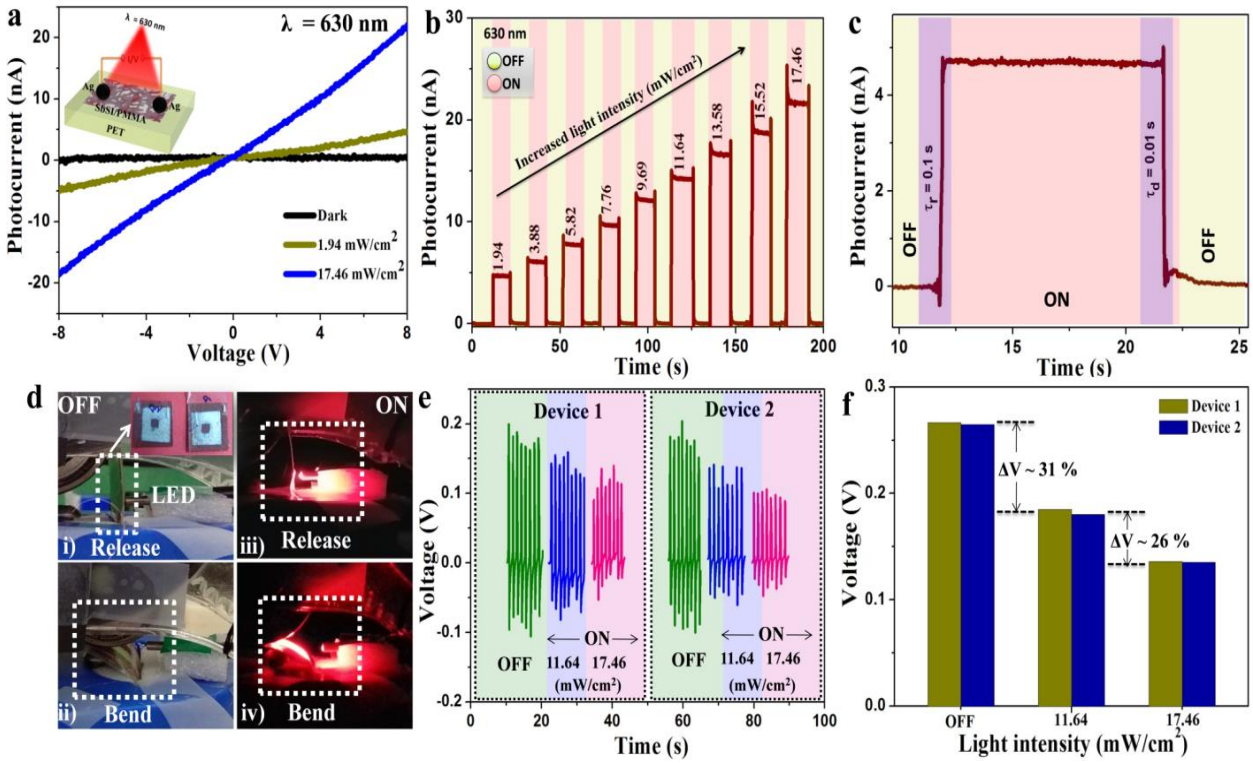

Figure 7.15 (a) I-V characteristics of SbSI/PMMA based photodetector (S-PD) at irradiation of 630 nm wavelength source (Inset: schematic illustration of as-fabricated S-PD). **(b)** Time dependent switching analysis as a function of increased light intensities. **(c)** Enlarged view of rise/decay time analysis for the switching response at an intensity of 1.94 mW/cm^2. **(d)** SbSI/PMMA based piezoelectric nanogenerator (S-PNG) mounted on a rotary stage under bending and light ON/OFF conditions. **(e)** Piezoelectrical response of S-PNG as a function of photoactivity. **(f)** Corresponding deviations in piezoelectric voltage.

The fabrication of S-PD involved the deposition of SbSI (1 wt %) / PMMA composite on a cleaned PET substrate via spin coating (device area 0.5 cm × 0.5 cm). The spin coated film was dried completely by heat treating at 70 ^{o}C in the oven. Later, silver electrodes were

established using Ag paste at the ends of the active layer in which two Cu leads were attached for the electrical measurements. Figure 7.15(a) represents the I-V spectrum of S-PD obtained at a bias voltage of $\pm$ 8 V at 630 nm LED source illumination. The photocurrent (I_{Ph}) of ~ 4.5 nA was produced from S-PD when illuminated by the light intensity of 1.94 mW/cm^2, and increases to ~ 20 nA upon increasing the light intensity to 17.46 mW/cm^2. The device responsivity (R_λ) was estimated to be 4.5 μA/W at a maximum light intensity of (17.46 mW/cm^2) calculated from the equation, $R_\lambda = (I_{Ph} - I_D)/(P_L \times A)$[40]. Figure 7.15(b) shows the time dependent switching performance of S-PD at an applied voltage of + 8 V as a function of varied light intensity levels. The as-fabricated S-PD is highly active to changes in the optical intensities which exhibited a linear increase in I_{Ph} as the light intensity increases (P_L). Also, the rise and decay time of τ_r = 0.1 s and τ_d = 0.01 s suggests that the S-PD readily responses to the irradiation of 630 nm optical source (Figure 7.15(c)). We now demonstrated the influence of conductivity in energy harvesting performance by designing SbSI based piezoelectric nanogenerator (S-PNG) provided with a bare spacing of 0.5 cm x 0.5 cm for the exposure of light source. The S-PNG was fabricated by spin coating the SbSI/PMMA active layer on to a cleaned ITO substrate, followed by deposition of Ag electrode. The optical images of as-fabricated devices are provided in the Figure 7.15(d) (i) (inset). The experiment was performed using a manually designed rotary setup to apply an external bending force as well as supporting the path for the optical irradiations to the device (Figure 7.15(d)). When the light is OFF, the S-PNG produces an output of ~ 0.26 V (Figure 7.15(e)). By employing 630 nm source illuminated at an intensity of 11.64 mW/cm^2 (i.e., ON state, 11.64 mW/cm^2), the amplitude of the piezoelectric response decreases to 0.19 V. Further increasing the light intensity (17.46 mW/cm^2), the S-PNG was capable to deliver an electrical response of ~ 0.13 V. The deviation of S-PNG performance is summarized in Figure 7.15(f)

showing a clear drop in the piezoelectric response. This is due to the changes in the improved conductivity of SbSI when irradiated by the light source. When S-PNG is subjected to light, the generation of charge carriers takes place which screens the piezoelectric potentials which were produced during bending strain. The light induced photogenerated charge carrier combines with the bending strain induced piezoelectric potential and decreases the charge density; eventually reducing the piezoelectric performance of S-PNG. As the incident light intensity increases, the enhanced conductivity in SbSI produces more charge carriers, which neutralizes more piezoelectric potentials. Hence, the S-PNG performance lowers readily upon irradiating light source of higher intensity.

Further to realize the generation of piezoelectric potentials promoted through the piezotronic/piezo-phototronic effects in SbSI (devoid of composites), we performed strain based analysis using single SbSI micro rod (Figure 7.1) with its two ends connected to Ag electrodes.

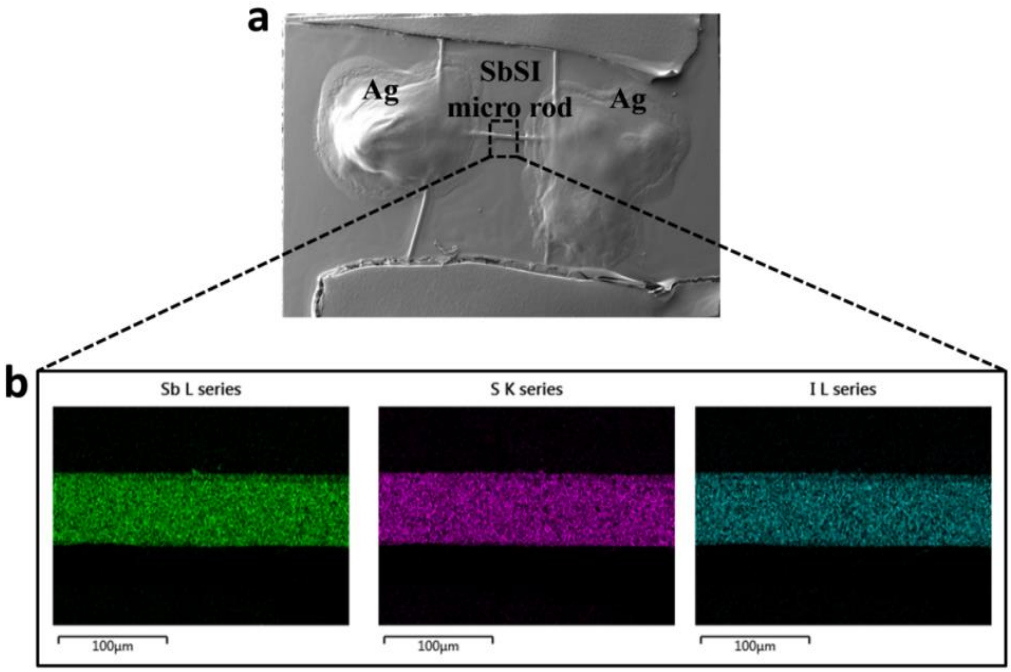

Figure 7.16 (a) FESEM image of device fabricated using SbSI micro rod (SMR). **(b**) EDS analysis corresponding to Sb, S and I elemental mapping.

The elemental purity of SMR was confirmed using EDS mapping suggesting equal proportion of Sb, S and I elements (Figure 7.16). **Figure 7.17**(a) schematically illustrates the fabricated device using SbSI micro rod (SMR) and the optical images of the devices.

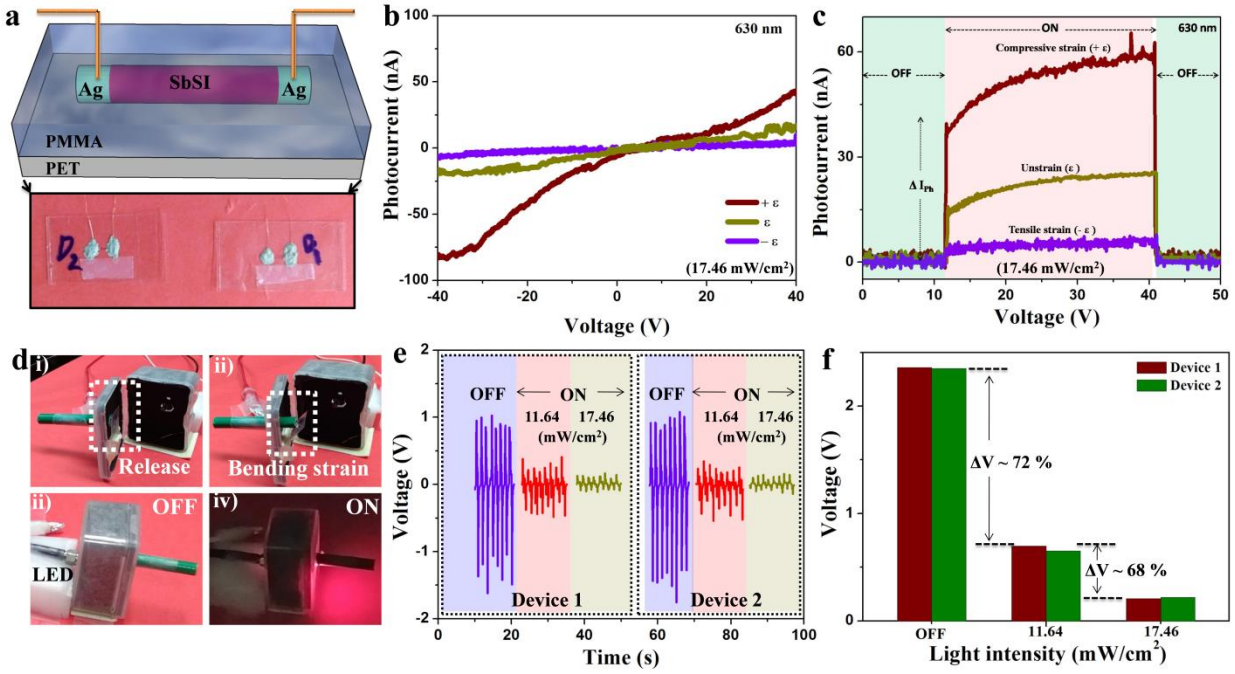

Figure 7.17 (a) Schematic illustration of as-fabricated SbSI micro rod (SMR) based device and its optical images. **(b)** I-V measurements at 630 nm (17. 46 mW/cm^2) (Inset: strain dependent piezoelectric potential distribution). **(c)** Time dependent switching analysis at varied strain conditions. **(d)** Optical images of experimental setup. **(e)** Photoactive electrical response of SMR based piezoelectric nanogenerator (SMR-PNG). **(f)** Corresponding changes in SMR-PNG performance under ON/OFF conditions.

The contribution of piezotronic effect is demonstrated under three working conditions (i) unstrain (ε), (ii) tensile strain (-ε), and (iii) compressive strain (+ε). (i) Under the normal state (unstrain, ε), where there is no external stress/force acting on the device the amount of photocurrent (I_{Ph}) generated by the SMR equals to ~ 17 nA at a bias voltage of ± 40 V (Figure 7.17(b)). In the case of applied external strain (± 1.87 %)[47], the produced I_{Ph} varies significantly

depending on the nature of the strain exerted. (ii) Upon applying compressive strain (+ε) which causes the PET substrate to bend upwards and so the SMR, I_{Ph} increases readily giving rise to generated photocurrent of ~ 40 nA. The change in I_{Ph} reveals the generated piezoelectricity when mechanical force is subjected to SbSI material causing the dipoles to align in a manner such that positive potentials are generated at the metal (Ag) - semiconductor (SbSI) interfaces which reduces the schottky barrier heights ($\Delta\Phi_{SB1}$, $\Delta\Phi_{SB2}$) allowing more photo generated charge carriers to tunnel through the interfaces (**Figure 7.18**(a, b)). (iii) In the case of tensile strain (-ε), the SMR bends downward producing an opposite phenomena of compressive strain i.e., negative potentials are generated at the MSM interfaces leading the I_{Ph} to decline (~ 5 nA) (Figure 7.18(b).

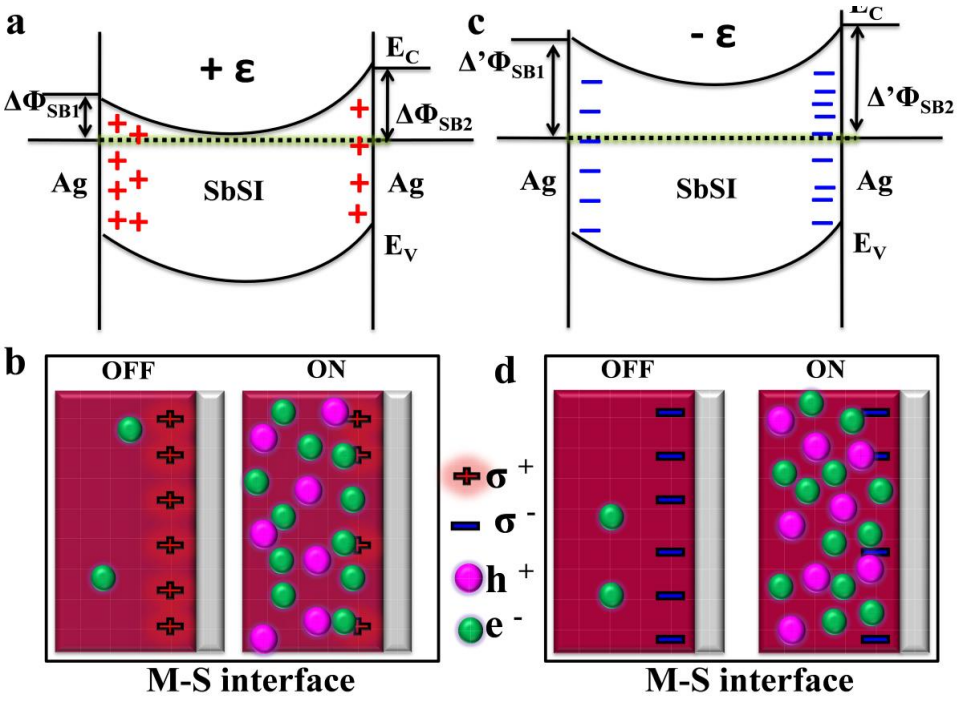

Figure 7.18 Energy band profile with piezoelectrical potentials accumulation at MSM interfaces. **(a)** Compressive strain (+ε) and **(c)** Tensile strain (-ε) conditions. Mechanism of piezopotentials screening with photogenerated charge carriers under **(b)** Compressive and **(d)** Tensile strain conditions.

The schottky barrier height increases ($\Delta'\Phi_{SB1}$, $\Delta'\Phi_{SB2}$) as a result of accumulated negative potentials (Figure 7.18 (c, d)) at the interfaces making it difficult for the transportation of photo generated charge carriers[47-49]. This behavior is further confirmed in the time dependent switching test which showed a similar behavior of I_{Ph} (Figure 7.17(c)). Figure 7.17(d) shows the experimental setup used for applying the bending force on to the device in ON/OFF states. Figure 7.17(e) represents the piezoelectric response of SMR based piezoelectric nanogenerator (SMR-PNG) under continuous bending strain conditions. At the beginning when the light is OFF, SMR-PNG delivers an output of ~ 2.4 V. Upon irradiation of LED source of 630 nm, the piezoelectric voltage drops gradually as observed in SbSI/PMMA composite based PNG. The changes in the piezoelectric responses of SMR-PNG are summarized in Figure 7.17(f) under light ON and OFF states. The photoactive sensitivity of SMR-PNG is high with 72 % and 68 % changes in piezoelectric voltage (ΔV) than SbSI/PMMA based PNG (31 % and 26 %) due to the ideal effect of employing direct MSM interface in single micro rod which was restricted by using dielectric medium (PMMA) in SbSI composite based PNG. The results provided new insights of SbSI multifunctional properties such as semiconducting-photoactive-ferroelectric properties and its involvement in harnessing the mechanical energy towards the development of next generation self-powered sensors, optical devices, and switches.

7.4. Conclusion

In summary, we have successfully demonstrated for the first time that ternary chalcohalide material (SbSI, SbSeI) serves as efficient energy harvesters. $A_VB_{VI}C_{VII}$ class compound, Antimony sulfoiodide (SbSI) synthesized via the SSR method, exhibits promising ferroelectric-semiconductor-photoactive characteristics. We tested the compatibility of SbSI with polymer matrices, such as PDMS, PVDF and PMMA, when the composites were used to

develop piezoelectric nanogenerators (S-PNG). The planar S-PNG module based on the SbSI/PMMA composite delivered a notably stable performance (voltage (V) ~5 V and current (I) ~150 nA), which was comparable to that of conventionally available lead-free piezoelectric materials. Further, demonstration of piezo-phototronic effect in SbSI/PMMA composite and single SbSI micro rod indicates that it is a viable and promising material for the development of next generation self-powered devices with internally coupled hybrid devices, such as mechanical energy harvesters and optical sensors/switches.

7.5 References

1 K. Y. Lee, J. Bae, S. Kim, J. Lee, G. C. Yoon, M. K. Gupta, S. Kim, H. Kim, J. Park, S. Kim, *Nano Energy*, 2014, **8**, 165–173.

2 B. Kumar, S. Kim, *Nano Energy*, 2012, **1**, 342–355.

3 K. I. Park, J. H. Son, G. T. Hwang, C. K. Jeong, J. Ryu, M. Koo, I. Choi, S. H. Lee, M. Byun, Z. L. Wang, K. J. Lee, *Advanced Materials*, 2014, **26**, 2514–2520.

4 N. R. Alluri, A. Chandrasekhar, V. Vivekananthan, Y. Purusothaman, S. Selvarajan, J. H. Jeong, S. Kim, *ACS Sustainable Chem. Eng.*, 2017, **5**, 4730–4738.

5 S. Maletic, D. Maletic, I. Petronijevic, J. Dojcilovic, D. M. Popovic, D. Srtio, *Chin. Phys.B*, 2014, **23**, 026102.

6 Y. Purusothaman, N. R. Alluri, A. Chandrasekhar and S. Kim, *Journal of Materials Chemistry C*, 2017, **5**, 5501–5508.

7 N. Abinnas, P. Baskaran, S. Harish, R. S. Ganesh, M. Navaneethan, K. D. Nisha, S. Ponnusamy, C. Muthamizhchelvan, H. Ikeda, Y. Hayakawa, *Applied Surface Science*, 2017, **418**, 362–368.

8 L. Liu, K. Lu, T. Wang, F. Liao, M. Peng, M. Shao, *Materials Letters*, 2015, **160**, 222–226.

9 H. H. Singh, S. Singh, N. Khare, *Polym. Adv. Technol.*, 2018, **29**, 143–150.

10 J. Kim, J. H. Lee, H. Ryu, J. Lee, U. Khan, H. Kim, S. S. Kwak, S. Kim, *Adv. Funct. Mater.*, 2017, **27**, 1700702.

11 G. Zhu, W. Q. Yang, T. Zhang, Q. Jing, J. Chen, Y. S. Zhou, P. Bai, Z. L. Wang, *Nano Letters*, 2014, **14**, 3208–3213.

12 J. Zhu, M. Dexheimer, H. Cheng, *npj Flexible Electronics*, 2017, **1**, 8.

13 Z. L. Wang, J. Song, *Science*, 2006, **312**, 242–246.

14 Z. L. Wang, *J. Phys. Chem. Lett.*, 2010, **1**, 1388–1393.

15 C. Huang, J. Song, W. Lee, Y. Ding, Z. Gao, Y. Hao, L. Chen, Z. L. Wang, *J. Am. Chem. Soc.*, 2010, **132**, 4766–4771.

16 Y. Lin, J. Song, Y. Ding, S. Lu, Z. L. Wang, *Applied Physics Letters*, 2008, **92**, 022105.

17 C. Wang, L. Cai, Y. Feng, L. Chen, W. Yan, Q. Liu, T. Yao, F. Hu, Z. Sun, S. Wei, *Applied Physics Letters*, 2014, **104**, 243112.

18 C. Huang, J. Song, C. Tsai, W. Lee, D. Lien, Z. Gao, Y. Hao, L. Chen, Z. L. Wang, *Adv. Mater.*, 2010, **22**, 4008–4013.

19 T. Jia, H. Fuh, D. Chen, M. Abid, M. Abid, D. Zhang, A. B. Sarker, J. Cho, M. Choi, B. S. Chun, H. Xu, H. Liu, C. Chang, H. Wu, *Adv. Electron. Mater.*, 2018, 1700447.

20 S. K. Kim, R. Bhatia, T. Kim, D. Seol, J. H. Kim, H. Kim, W. Seung, Y. Kim, Y. H. Lee, S. Kim, *Nano Energy*, 2016, **22**, 483–489.

21 A. Sultana, P. Sadhukhan, M. M. Alam, S. Das, T. R. Middya, D. Mandal, *ACS Appl. Mater. Interfaces*, 2018, **10**, 4121–4130.

22 J. Li, X. Wang, *APL Materials*, 2017, **5**, 073801.

23 M. K. Teng, M. Balkanski, M. Massot, M. K. Ziolkiewicz, *Phys. Stat. Sol.*, 1974, **62**, 173–182.

24 M. Balkanski, M. K. Teng, S. M. Shapiro, M. K. Ziolkiewicz, *Phys. Stat. Sol.*, 1971, **44**, 355–367.

25 K. C. Gödel, U. Steiner, *Nanoscale*, 2016, **8**, 15920–15925.

26 G. Chen, W. Li, Y. Yu, Q. Yang, *RSC Advances*, 2015, **5**, 21859–21864.

27 I. Cho, B. Min, S. W. Joo, Y. Sohn, *Materials Letters*, 2012, **86**, 132–135.

28 D. K. Agarwal, C. H. Perry, *Physical Review B*, 1971, **4**, 1893–1902.

29 A. V. Gomonnai, I. M. Voynarovych, A. M. Solomon, A. A. Kikineshi, V. P. Pinzenik, L. Daroczy, V. V. Lopushansky, *Mater. Res. Bulletin*, 2003, **38**, 1767–1772.

30 M. Nowak, B. Kauch, P. Szperlich, *AIP Rev. Sci. Instrum.*, 2009, **80**, 046107.

31 A. G. Luchaninov, A. V. Shil, L. A. Shuvalov, V. A. Malyshev, *Ferroelectrics*, 1993, **145**, 235–239.

32 R. R. Mehta, B. D. Silverman, J. T. Jacobs, *Journal of Applied Physics*, 1973, **44**, 3379–3385.

33 V. Agrawal, K. Bhattacharya, *Journal of the Mechanics and Physics of Solids*, 2018, **115**, 142–166.

34 A. Muliana, *International Journal of Solids and Structures*, 2011, **48**, 2718–2731.

35 K. Park, C. K. Jeong, N. K. Kim, K. J. Lee, *Nano Convergence*, 2016, **3**, 1–12.

36 D. Acosta, C. Densmore, *Los Alamos Nat. Laboratory report.*

37 MSDS, Product Information, Sylgard® 184, Silicone Elastomer.

38 P. Martins, A. C. Lopes, *Progress in Polymer Science*, 2013, **39**, 683–706.

39 W. Qian, S. krimm, *Biopolymers*, 1992, **32**, 1503–1518.

40 W. Morgan, W. Stec, J. R. Wazer, *Inorganic Chemistry*, 1973, **12**, 953–955.

41 F. L. Lie, W. Rachmady, A. J. Muscat, *Microelectronic Engineering*, 2009, **86**, 122–127.

42 G. Prasad, P. Sathiyanathan, A. Prabu, K. Kim, *Macromol. Res.*, 2017, **25**, 981–988.

43 R. Hinchet, S. Lee, G. Ardila, M. Mouis, Z. L. Wang, *Adv. Funct. Mater.*, 2013, **24**, 971–977.

44 S. Y. Chung, S. Kim, J. Lee, K. Kim, S. Kim, C. Kang, S. Yoon, Y. Kim, *Adv. Mater.*, 2012, **24**, 6022–6027.

45 W. Li, D. Torres, R. Diaz, Z. Wang, C. Wu, C. Wang, Z. L. Wang, N. Sepulveda, *Nature Comm.*, 2017, **8**, 15310.

46 G. Kanchana, D. Arivuoli, *Indian J. Eng and Mater. Sci.*, 2001, **8**, 373–376.

47 Y. Purusothaman, N. R. Alluri, A. Chandrasekhar, V. Vivekananthan, S. J. Kim, *Small*, 2018, 1703044.

48 Z. L. Wang, *Nano Today*, 2010, **5**, 540–552.

49 Y. Zhang, Y. Liu, Z. L. Wang, *Adv. Mater.*, 2011, **23**, 3004–3013.

CHAPTER VIII

Summary and Future Perspective

8.1 Summary

This chapter summarizes the overall thesis work, its outcomes and the possibility for its future extension. The major focus of presented thesis is to develop self-powered optical sensors (SPPD) that works on the principle of piezotronic and piezo-phototronic effects. On this basis, we explored the materials possessing multifunctional properties such as piezoelectric-semiconducting-photoexcitation and synthesized them through cost effective approaches such as solid state reaction, hydrothermal and sonochemical methods. We investigated the one way effects on synthesized materials through fabrication of mechanical energy harvesters (PNG) and optical sensors (PD). Further, we explored the mechanism of three way coupling piezo-phototronic effect and its involvement to demonstrate internally integrated SPPD. The research work presented exhibited its contribution in the field of multifunctional materials, exploration of coupling effects between piezoelectric potentials and photogenerated charge carriers, development of energy harvesters including piezoelectric nanogenerator, optical detectors and self powered sensors.

- The thesis started with providing broad knowledge and explanation on self-powered nanosystems and sensors, its potential capability to acquire optical sectors specifically focused on photodetectors, its types and drawbacks, and the role of nanogenerator to act as a power supply source. Further, the origin and gradual growth of piezo-phototronic effect is discussed up to its present status (Chapter I)

- Followed by is the informations on experimental materials, methods, measurement instruments along with its specifications, electrical characterization techniques, fabrication of devices, electrical parameters referred and precise view of modes in self-powered operations (Chapter II)
- The nanostructure of $K_{0.5}Na_{0.5}NbO_3$ was reported as filler in formulation of alkyd based composite to harvest small vibrational motions. This showed the high sensitivity of the as-fabricated cantilever beam type device to harness mechanical motion of frequency < 10 Hz which is highly commendable for scavenging biomechanical and environmental exerted actuations. However, the choice of using KNN is not highly suitable in terms of constructing self powered optical sensors. For which, with further studies we explored materials with multifunctional properties (Chapter III)
- The behaviour of ZnO nanorods (ZnO NRs) synthesized through low temperature hydrothermal method was investigated for its mechanical energy harvesting and optical sensing capabilities with cadmium (Cd) dopant. With this analysis we found that Cd introduction into the lattice sites of ZnO NRs promoted asymmetric changes in piezoelectric and semiconducting nature of ZnO NRs. The fabricated PNG produced a piezoelectric output of 36 V/284 µA (pure ZnO NRs) and 15 V/178 µA (1 wt% Cd-doped ZnO NRs).The fabricated PD showed the photoelectric response of 213 µA (pure ZnO NRs) and 330 µA (1 wt% Cd-ZnO NRs) upon incident of LED source at 365 nm wavelength at an intensity of 8mW/cm^2. Realization of self-powered UV sensor was demonstrated by parallel connections between PNG and PD (Chapter IV)
- On the other hand, the photodetection was improved through generation of piezoelectric potentials across the metal-semiconductor-metal (M-S-M) interfaces upon external

compressive/tensile strains using three way coupling mechanism, piezo-phototronic effect. For which, we constructed PD using ZnO micro-architectures such as micro wire (MW), coral like micro strip (CMS), and fibril like clustered micro wire (F-MW). The photocurrent response was significantly modulated by applying compressive strain (- ε_z = 0.37, 0.75, 1.13, 1.50 and 1.87 %) which altered the schottky barrier heights ($\Phi_{SB1,}$ Φ_{SB2}) at MSM interfaces through inner piezoelectric charges generated by ZnO material (Chapter V)

- With the realization of intrinsic behavior through piezo-phototronic effect, we demonstrated the self-powered sensor with inbuilt characteristics of mechanical and optical detection. The internal hybridization included the growth of ZnO NRs in PVDF film enabled through treating Zn^{2+} seeded film hydrothermally. The analysis ensured the ability of developed device to act as an active sensor scavenging mechanical force and respond with regards to incident optical source, thereby acting as PD with intrinsic self-powered mode without requiring bias voltage (Chapter VI)
- Finally, we identified and investigated new class of emerging multifunctional materials, ternary chalcohalides ($A^{V}B^{VI}C^{VII}$) that can be used as an efficient candidate in energy harvesting. Briefly, we analyzed antimony sulfoiodide (SbSI); one among the ternary chalcohalide group, to exhibit strong ferroelectric and semiconducting properties. The fabricated device using film and single micro rod was explored with piezo-phototronic effect and its effective utilization to empower self-powered photodetection without applying external bias voltages (Chapter VII)

The thesis provided a broad overview of utilizing piezo-phototronic concept to develop intrinsic self-powered photodetectors that can work in internal mode, devoid of power supply/batteries,

and free from issues faced through external integrations such as fabrication of two different sensing devices, interface connections, complex circuitry, and overloaded mass to sensing systems.

8.2 Suggestions for future improvement

The future direction of the research will focus on exploring the possibilities to serve the necessity/demands in self-powered optoelectronic applications. Following concerned key points will be addressed towards the future aspect.

- On the series of ternary chalcohalides ($A^{V}B^{VI}C^{VII}$), 2D ternary materials such as monolayer transition-metal chalcogenide and chalcohalides will be investigated for its efficiency to harvest mechanical and optical energies. Device level studies will be carried out to demonstrate the sensitivity and stability of the synthesized materials. Suitable measures involving structural confinements, doping and strain engineering will be explored to improve the switching rate and stability of the devices
- Device designs and electrode configurations will be improved to have better interfacial effects and sustainable performance. Flexible and stretchable characteristics will be established to the fabricated devices so that it can be used in wearable optoelectronic applications
- Real time utilization of self powered photodetectors will be explored for its potential utilization in major technologies driving toward logic gates, switching devices, and miniaturized integrate ability for implantable biomedical applications

Appendix A: List of Publications

1. **Yuvasree Purusothaman**, Nagamalleswara Rao Alluri, Arunkumar Chandrasekhar, Sang-Jae Kim, "Photoactive Piezoelectric Energy Harvester Driven by Antimony Sulfoiodide (SbSI): A $A^{V}B^{VI}C^{VII}$ Class Ferroelectric-Semiconductor Compound", **Nano Energy**, 2018, 50, 256. (IF – 13.120)

2. **Yuvasree Purusothaman**, Nagamalleswara Rao Alluri, Arunkumar Chandrasekhar, Venkateswaran Vivekananthan, Sang-Jae Kim, "Regulation of Charge Carrier Dynamics in ZnO Micro-architecture-Based UV/Visible Photodetector via Photonic-Strain Induced Effects", **Small**, 2018, 1703044. (IF – 9.598)

3. **Yuvasree Purusothaman**, Nagamalleswara Rao Alluri, Arunkumar Chandrasekhar, Sang-Jae Kim, "Elucidation of the unsymmetrical effect on the piezoelectric and semiconducting properties of Cd-doped 1D-ZnO nanorods", **Journal of Materials Chemistry C**, 2016, 5, 415. (IF – 5.976)

4. **Yuvasree Purusothaman**, Nagamalleswara Rao Alluri, Arunkumar Chandrasekhar, Sang-Jae Kim, "Harnessing low frequency-based energy using $K_{0.5}Na_{0.5}NbO_3$ (KNN) pigmented piezoelectric paint system", **Journal of Materials Chemistry C**, 2017, 5, 5501. (IF – 5.976)

5. **Yuvasree Purusothaman**, Nagamalleswara Rao Alluri, Arunkumar Chandrasekhar, Venkateswaran Vivekananthan, Sang-Jae Kim, "Direct In-Situ Hybridized Interfacial Quantification to Stimulate Highly Flexile Self-Powered Photodetector", **Journal of Physical Chemistry C**, 2018, 122 (23), 12177. (IF – 4.484)

6. Nagamalleswara Rao Alluri, **Yuvasree Purusothaman**, Arunkumar Chandrasekhar, Sang-Jae Kim, “Self-powered wire type UV sensor using in-situ radial growth of $BaTiO_3$ and TiO_2 nanostructures on human hair sized single Ti-wire”, **Chemical Engineering Journal,** 2018, 334, 1729. (IF – 6.496)

7. Venkateswaran Vivekananthan, Nagamalleswara Rao Alluri, **Yuvasree Purusothaman**, Arunkumar Chandrasekhar, Sang-Jae Kim, "Biocompatible collagen-nanofibrils: An approach for sustainable energy harvesting and battery-free humidity sensor applications", **ACS Applied Mater. Interfaces**, 2018, 10 (22), 18650. (IF – 8.097)

8. Venkateswaran Vivekananthan, Nagamalleswara Rao Alluri, Arunkumar Chandrasekhar, **Yuvasree Purusothaman**, "A flexible, planar energy harvesting device for scavenging road side waste mechanical energy via synergistic piezoelectric response of $K_{0.5}Na_{0.5}NbO_3$-$BaTiO_3$/PVDF composite films"**, Nanoscale**, 2017,9, 15122. (IF – 7.367)

9. Nagamalleswara Rao Alluri, Arunkumar Chandrasekhar, Venkateswaran Vivekananthan, **Yuvasree Purusothaman**, Sophia Selvarajan, Ji Hyun Jeong, Sang-Jae Kim, “Scavenging Biomechanical Energy using High-performance, Flexible $BaTiO_3$ Nanocube/PDMS Composite Films”, **ACS Sustainable Chem. Eng**., 2017, 5 (6), 4730. (IF – 6.140)

10. Arunkumar Chandrasekhar, Nagamalleswara Rao Alluri, Venkateswaran Vivekananthan, **Yuvasree Purusothaman**, S Sang-Jae Kim, “A sustainable freestanding biomechanical energy harvesting smart backpack as a portable-wearable power source”, **Journal of Materials Chemistry C**, 2017, **5**, 1488. (IF – 5.976)

Appendix B: List of Conferences

1. **Yuvasree Purusothaman**, Nagamalleswara Rao Alluri, Arunkumar Chandrasekhar, Sang-Jae Kim, "Tuning of Piezoelectric-Semiconducting behavior of 1D- ZnO Nanorods by Cadmium Dopant for Self-Powered UV Sensor", **4th International Conference on Electronic Materials and Nanotechnology for Green Environment (ENGE 2016)**, Nov. 06-09, Jeju, Republic of Korea.

2. **Yuvasree Purusothaman**, Nagamalleswara Rao Alluri, Arunkumar Chandrasekhar, Sang-Jae Kim, "Harnessing low frequency based energy using $K_{0.5}Na_{0.5}NbO_3$ (KNN) piezoelectric paint system", **19th Korean MEMS conference (KMEMS 2017)**, Mar. 30-Apr. 01, Jeju, Republic of Korea.

3. **Yuvasree Purusothaman**, Nagamalleswara Rao Alluri, Arunkumar Chandrasekhar, Venkateswaran Vivekananthan, Sang-Jae Kim, "Significance of ZnO Micro-Architectures in Photosensing Performance Modulated by Piezo-Phototronic Effect", **The 4th International Conference on Advanced Electromaterials (ICAE 2017)**, Nov. 21-24, Jeju, Republic of Korea.

4. **Yuvasree Purusothaman**, Nagamalleswara Rao Alluri, Arunkumar Chandrasekhar, Venkateswaran Vivekananthan, Sang-Jae Kim, "Charge Carrier Dynamics in ZnO Micro-Architectures Modulated by Piezo-phototronic Effect", **BK21+ project team workshop**, Nov. 24, 2017, Jeju, Republic of Korea.

5. **Yuvasree Purusothaman**, Nagamalleswara Rao Alluri, Arunkumar Chandrasekhar, Venkateswaran Vivekananthan, Sang-Jae Kim, "Synergistic Effect on Self-Integration of PVDF/ZnO Nanorods for Enhanced Photodetector Performance", **The 10th International**

Conference on Advanced Materials and Devices (ICAMD 2017), Dec. 05-08, Jeju, Republic of Korea.

6. **Yuvasree Purusothaman**, Nagamalleswara Rao Alluri, Arunkumar Chandrasekhar, Venkateswaran Vivekananthan, Jong Hwan Lim, Kyung-Ho Cho, Sang-Jae Kim, "ZnO Micro-Architecture Based UV/Vis Photodetector Using Piezo-Phototronic Effect", **The Korean Society of Mechanical Engineers (KSME 2018)**, Feb. 22-24, Jeju, Republic of Korea.

7. **Yuvasree Purusothaman**, Nagamalleswara Rao Alluri, Arunkumar Chandrasekhar, Venkateswaran Vivekananthan, Sang-Jae Kim, "Development of novel SbSI driven piezoelectric nanogenerator", **20th Korean MEMS conference (KMEMS 2018)**, Apr. 05-07, Jeju, Republic of Korea.

8. **Yuvasree Purusothaman**, Nagamalleswara Rao Alluri, Arunkumar Chandrasekhar, Venkateswaran Vivekananthan, Sang-Jae Kim, "An Effectual Approach for Self-Powered Photo Detection Endowed by Piezoelectric Potentials", **4th International Conference on Nanogenerator and Piezotronics (NGPT 2018)**, May 08-11, Seoul, Republic of Korea.

9. **Yuvasree Purusothaman**, Nagamalleswara Rao Alluri, Arunkumar Chandrasekhar, Venkateswaran Vivekananthan, Sang-Jae Kim, "Photoactive Piezoelectric Energy Harvester driven by $A_{V}B_{VI}C_{VII}$ class of ferroelectric- semiconductor Compound",**19th International Symposium on the Physics of Semiconductors and Applications (ISPSA 2018)**, July 01-05, Jeju, Republic of Korea.

10. **Yuvasree Purusothaman**, Nagamalleswara Rao Alluri, Arunkumar Chandrasekhar, Venkateswaran Vivekananthan, Sang-Jae Kim, "Piezo-phototronic Dependent Enhanced

Charge Transportation in SbSI Micro Rod Photodetector", **The 23rd Opto-Electronics and Communications Conference (OECC 2018)**, July 02-06, Jeju, Republic of Korea.

11. **Yuvasree Purusothaman**, Nagamalleswara Rao Alluri, Arunkumar Chandrasekhar, Venkateswaran Vivekananthan, Sang-Jae Kim, "Self-Powered Photodetector Endorsed by Piezo-phototronic effect", **Annual Meeting of the Korean Physical Society (KPS 2018)**, Aug. 06, Jeju, Republic of Korea.

12. **Yuvasree Purusothaman**, Nagamalleswara Rao Alluri, Arunkumar Chandrasekhar, Sang-Jae Kim, "Multifunctional Energy Scavenger Based on Antimony Sulfoiodide (SbSI): Mechanical-Light Triggered Piezoelectric Nanogenerator", **European Materials Research Society fall meeting (E-MRS 2018)**, Sept 17-20, Warsaw, Poland.

13. **Yuvasree Purusothaman**, Nagamalleswara Rao Alluri, Arunkumar Chandrasekhar, Venkateswaran Vivekananthan, Sang-Jae Kim, "$A^{V}B^{VI}C^{VII}$ Ternary Chalcohalides for the Development of Efficient Multifunctional Energy Harvester", **5th International Conference on Electronic Materials and Nanotechnology for Green Environment (ENGE 2018)**, Nov. 11-14, Jeju, Republic of Korea.

14. Venkateswaran Vivekananthan, Nagamalleswara Rao Alluri, **Yuvasree Purusothaman**, Arunkumar Chandrasekhar, and Sang-Jae Kim, "Structural and piezoelectric analysis of flexible (1-x)KNN-xBTO/PVDF composite film for energy harvesting applications", **Joint Symposium of Jeju National University and Nagasaki University on Science and Technology (JSST 2017)**, Nov. 11-14, Jeju, Republic of Korea.

15. Venkateswaran Vivekananthan, Nagamalleswara Rao Alluri, **Yuvasree Purusothaman**, Arunkumar Chandrasekhar, and Sang-Jae Kim, "Structural and piezoelectric analysis of

flexible (1-x)KNN-xBTO/PVDF composite film for energy harvesting applications", **The 4th International Conference on Advanced Electromaterials (ICAE 2017)**, Nov. 21-24, Jeju, Republic of Korea.

16. Venkateswaran Vivekananthan, Nagamalleswara Rao Alluri, **Yuvasree Purusothaman**, Arunkumar Chandrasekhar, and Sang-Jae Kim, "A Solution to Harness Waste Mechanical Energy in Society", **The 10th International Conference on Advanced Materials and Devices (ICAMD 2017)**, Dec. 05-08, Jeju, Republic of Korea.

17. Vivekananthan Venkateswaran , Nagamalleswara-Rao Alluri, **Yuvasree Purusothaman**, Arunkumar Chandrasekhar, Sophia Selvarajan and Kim Sang-Jae, "Bio-polymer based piezoelectric nanogenerator as a cost-effective self-powered humidity sensor", **4th International Conference on Nanogenerator and Piezotronics (NGPT 2018)**, May 08-11, Seoul, Republic of Korea.

18. Venkateswaran Vivekananthan, Nagamalleswara Rao Alluri, Arunkumar Chandrasekhar, **Yuvasree Purusothaman**, Sang-Jae Kim, "Enhanced Piezoelectricity in $K_{0.5}Na_{0.5}NbO_3$ and its Application towards a Self-powered Burglar Alarming System" **5th International Conference on Electronic Materials and Nanotechnology for Green Environment (ENGE 2018)**, Nov. 11-14, Jeju, Republic of Korea.

Appendix C: List of Awards

1. **Best Poster Presentation Award at European Materials Research Society fall meeting (E-MRS 2018),** Sept 17-20, Warsaw, Poland, "**Yuvasree Purusothaman**, Nagamalleswara Rao Alluri, Arunkumar Chandrasekhar, Sang-Jae Kim; *Multifunctional Energy Scavenger Based on Antimony Sulfoiodide (SbSI): Mechanical-Light Triggered Piezoelectric Nanogenerator*".

2. **Best Poster Paper Award at 5th International Conference on Electronic Materials and Nanotechnology for Green Environment (ENGE 2018)**, Nov. 11-14, Jeju, Republic of Korea, "**Yuvasree Purusothaman**, Nagamalleswara Rao Alluri, Arunkumar Chandrasekhar, Sang-Jae Kim; $A^{V}B^{VI}C^{VII}$ *Ternary Chalcohalides for the Development of Efficient Multifunctional Energy Harvester*".

3. **Best Poster Award at 4th International Conference on Nanogenerator and Piezotronics (NGPT 2018)**, May 08-11, Seoul, Republic of Korea, "**Yuvasree Purusothaman**, Nagamalleswara Rao Alluri, Arunkumar Chandrasekhar, Venkateswaran Vivekananthan, Sang-Jae Kim; *An Effectual Approach for Self-Powered Photo Detection Endowed by Piezoelectric Potentials*".

Appendix D: Cover Page

1. Published as journal cover article, "**Yuvasree Purusothaman**, Nagamalleswara Rao Alluri, Arunkumar Chandrasekhar, Venkateswaran Vivekananthan, Sang-Jae Kim, *"Regulation of Charge Carrier Dynamics in ZnO Micro-architecture-Based UV/Visible Photodetector via Photonic-Strain Induced Effects"*, **Small**, 2018, 1703044.

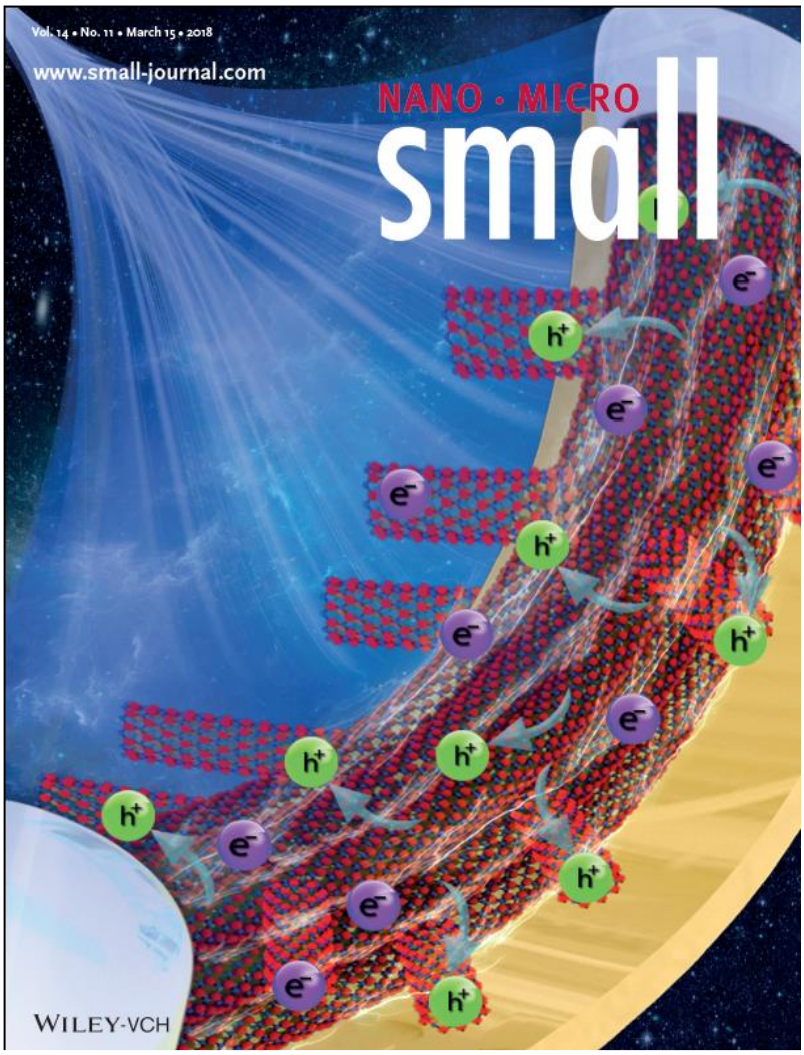

Appendix E: Patent

1. **“**Piezoelectric Nano Generator, Optical Sensor Comprising of the same, and Preparation method of Piezoelectric Nano Generator”, *Korean Patent,* **Ref. No: DP20180109**, filed on 2018.10.26. [Jointly with Prof. Kim Sang-Jae]

Declaration

I, **Yuvasree Purusothaman**, hereby declare that the thesis entitled **"Development of Intrinsic Self-Powered Photodetectors based on Piezo-Phototronic Effect"**, submitted to the **Jeju National University**, in partial fulfillment of the requirement for the award of the **Degree of Doctor of Philosophy in Department of Mechatronics Engineering** is a record of original and independent research work done and published by me during the period of September-2015 to February-2019 under the supervision of **Prof. Kim Sang-Jae**, Department of Mechatronics Engineering, Jeju National University. This thesis solely based on our publications in reputed journals, and it has not been formed for the award of any other Degree/ Diploma/ Associate ship/ Fellowship to any candidates of any university.

Yuvasree Purusothaman